UNIVERSIDADE FEDERAL DO RIO GRANDE DO SUL
INSTITUTO DE FÍSICA
DEPARTAMENTO DE ASTRONOMIA

Tese de Doutorado

Extreme Milky Way populations: from the substellar regime to the outer components

Populações extremas da Via Láctea: do regime substelar aos componentes externos

Marina Dal Ponte

PhD. dissertation taken under the supervision of Dr. Basílio Xavier Santiago submitted to the Graduate Program of Instituto de Física - Universidade Federal do Rio Grande do Sul (UFRGS) as part of the fulfilment to obtain the PhD. degree in physics with emphasis in astrophysics.

Porto Alegre, RS, Brasil
2023

⋆ This work has received financial support from Conselho Nacional de Desenvolvimento Científico e Tecnológico (CNPq)

Viver é esquisitíssimo.

Ana Cristina Cesar

Acknowledgements

This work has only been possible thanks to CNPq support. We have lived through dark times in the past years. Doing research in Brazil has become an act of resistance. I hope for a better future for science in Brazil and for all the brave souls that will follow this path. It is not easy but it is very rewarding.

To my mom Zenaide and my dad Santo for all the support and understating throughout these years. I do know that I made the most bizarre career choice for our family standards, but I was taught very early in life that I was capable of pursuing whatever I wanted in life. And dad, it is your fault that I chose Astrophysics instead of Law. It was you the one that made me lookup in the sky in the summer nights to look for Orion's belt. You left me no choice. It makes me very happy to know that you both are proud of who I have become.

To my advisor Basilio for the endless patience, to explain the same thing repeatedly until I understand. Thanks for sharing all the knowledge, trust, and support during all these years, especially in the pandemic. I always thought of you as an amazing researcher, with so much knowledge.

To my boyfriend Fabio for being by my side no matter what. The pandemic made us stay 24/7 together but I could not desire to be with anyone else. Thanks for being my best friend, and this sweet person that only sees the best in me. Despite we are living apart now, I know that soon we will be together, to divide every little moment. Love you with all my heart.

To my friends for sharing memes, listening to my complaints in long audio messages, all the video chats, and funny movie nights. Some of you are living really far away, but the friendship remains just the same.

To my little dog Antonella for being such an amazing creature. Everyday you give me just love and it is impossible to be in a bad mood around you. I just want do give you the best life that a dog can have.

Abstract

We present here the study of the properties of two different populations of our Galaxy: the very low-mass stellar and substellar regime of ultracool dwarfs and the halo stellar population. For the ultracool dwarfs, we follow the same approach as in our previous investigations presented in Carnero Rosell et al. (2019), dal Ponte et al. (2020) using the first data release of the Dark Energy Survey. Our past work resulted in two important catalogs: 11,745 ultracool dwarf candidates and 264 wide binary and multiple system candidates involving at least one ultracool dwarf. Here we present the revision and an update of the method to search for and characterize ultracool dwarfs. We obtain a sample of 19,583 ultracool dwarf candidates brighter than z $\leq$ 23 selected from the Dark Energy Survey second data release matched to VHS DR6, VIKING DR5 and AllWISE covering $\sim$ 4,800 deg^2 in the Southern Hemisphere. The ultracool candidates were first pre-selected based on their (i-z), (z-Y), and (Y-J) colors. They were further classified using a method that compares their optical, near-infrared and mid-infrared colours against templates of M, L and T dwarfs. 14,099 objects are presented as new L and T candidates and the remaining objects are from the literature, including 5,342 candidates from our previous work. We also show spectra of twelve new ultracool dwarfs discovered by our group. These spectroscopically confirmed objects are a sanity check of our selection of ultracool dwarfs and photometric classification method. Using this new and deeper sample of ultracool dwarf candidates we found: 20 new candidate members to nearby young moving groups and associations, variable candidate sources and four new wide binary systems composed of two ultracool dwarfs. We also show a method to estimate the thin disk scale height for the L dwarf population and discuss its current limitations. For the investigation of the Milky Way halo, we use a catalog with `StarHorse` stellar parameters, distances and extinctions catalog derived from Gaia EDR3 combined with photometric catalogs for stars brighter than G = 18.5. This catalog is used to select halo stars based on their tangential velocity. We also apply a geometric and an extinction cut to eliminate disk contaminants. We calculate pseudo cartesian velocities and check the consistency of our selection. We then present an initial study of the metallicity distribution for the local halo. With our sample of more than 2 million halo stars, we confirm previous measurements of metallicity presented in the literature, including an estimate for the Gaia-Enceladus component. We also show a clear metallicity gradient present in our sample.

Resumo

Apresentamos aqui o estudo das propriedades de duas populações diferentes da nossa Galáxia: o regime de estrelas de baixa massa e o regime sub-estelar de anãs ultrafrias e a população estelar do halo. Para as anãs ultrafrias, seguimos a mesma abordagem de nossos trabalhos anteriores em Carnero Rosell et al. (2019), dal Ponte et al. (2020) usando o primeiro data release do Dark Energy Survey. Nosso trabalho resultou em dois catálogos importantes: 11.745 candidatas a anãs ultrafrias e 264 candidatas a sistemas binários e múltiplos envolvendo pelo menos uma anã ultrafria. Aqui apresentamos a revisão e atualização do método de busca e caracterização de anãs ultrafrias. Obtivemos uma amostra de 19.583 candidatas mais brilhantes que z $\leq$ 23 selecionadas a partir do segundo data release do Dark Energy Survey combinado com VHS DR6, VIKING DR5 e AllWISE cobrindo $\sim 4.800\ deg^2$ no Hemisfério Sul. As candidatas a anãs ultrafrias foram primeiro pré-selecionadas com base em suas cores (i-z), (z-Y) e (Y-J). Também, foram posteriormente classificadas usando um método que compara suas cores no óptico, infravermelho próximo e infravermelho médio com modelos de anãs M, L e T. 14.099 objetos são apresentados aqui como novos candidatos a anãs L e T e os objetos restantes são da literatura, incluindo 5.342 candidatas do nosso trabalho anterior. Além disso, mostramos espectros de doze novas anãs ultrafrias descobertas por nosso grupo. Esses objetos espectroscopicamente confirmados servem como uma verificação de nossa seleção e do método de classificação fotométrico. Usando a nova amostra de candidatas, encontramos: 20 novos candidatos a membros de grupos e associações jovens próximas, candidatos a fontes variáveis e quatro novos sistemas binários de alta separação compostos por duas anãs ultrafrias. Também mostramos um método para estimar a escala de altura do disco fino para a população de anãs L e discutimos as suas limitações. Para a investigação do halo da Via Láctea, utilizamos um catálogo de parâmetros estelares, distâncias e extinções do `StarHorse` derivado do Gaia EDR3 combinado com outros catálogos fotométricos para estrelas com brilho superior a G = 18,5. Este catálogo é usado para selecionar estrelas do halo com base em sua velocidade tangencial. Aplicamos um corte geométrico e de extinção para eliminar os contaminantes do disco. Calculamos pseudo velocidades cartesianas para checar a consistência da nossa seleção. Apresentamos um estudo inicial da distribuição de metalicidade para o halo local. Com a nossa amostra de mais de 2 milhões de estrelas, confirmamos medições anteriores de metalicidade apresentadas na literatura, incluindo uma estimativa para a componente do Gaia-Enceladus. Também mostramos um claro gradiente em metalicidade presente na nossa amostra.

Contents

Chapter 1

Introduction

1.1 The Milky Way galaxy

The Milky Way (MW) is a barred spiral galaxy of intermediate size. The stellar mass of our Galaxy is around 8.5 $\times 10^{10}$ $M_\odot$, and virial mass of $\sim$ 1.5 $\times 10^{12}$ $M_\odot$ (Bland-Hawthorn & Gerhard, 2016, Watkins et al., 2019). It belongs to the Local Group, being the second more massive galaxy (the most massive is Andromeda). Currently, the MW is going through interactions with: the Small Magellanic Cloud (SMC), the Large Magellanic Cloud (LMC) and the Sagittarius (Sgr) dwarf galaxy. These systems, as many others in the past, are falling into the gravitational potential of the MW. They will be slowly disrupted through tidal and ram pressure stripping.

The MW has several visible components: a thin disk, thick disk, bulge/bar and a stellar halo as illustrated in Figure 1.1. Each component has its individual characteristics such as spatial distribution, kinematics, chemical composition and age. The thin disk contains the young metal-rich and low-α[1] stars and it is the component with ongoing star formation. It is more radially extended and have a smaller scale height than the thick disk and most stars have nearly circular orbits (Jurić et al., 2008, Bovy et al., 2016, Mackereth et al., 2019). The thick disk is more diffuse and contains older and more metal-poor stars when compared to the thin disk. It is kinematically hotter (larger vertical velocity dispersion) and has a slower rotation than the thin disk (Nidever et al., 2014, Hayden et al., 2015). Furthermore, several studies (e.g. Bensby et al., 2005, Bovy et al., 2016, Hayden et al., 2015, Vincenzo et al., 2021) suggests the existence of two separate sequences [α/Fe] vs [M/H][2] (or [Fe/H]) diagram, where the high-α is often associated to the thick disk

[1] e.g. Ca, Mg, Ti, O, S, and Si which are produced via Type II supernovae (SNII).

[2] The total metallicity is defined as [M/H] = log[N_M/N_H] - log[N_M/N_H]$_\odot$ where N_H is the

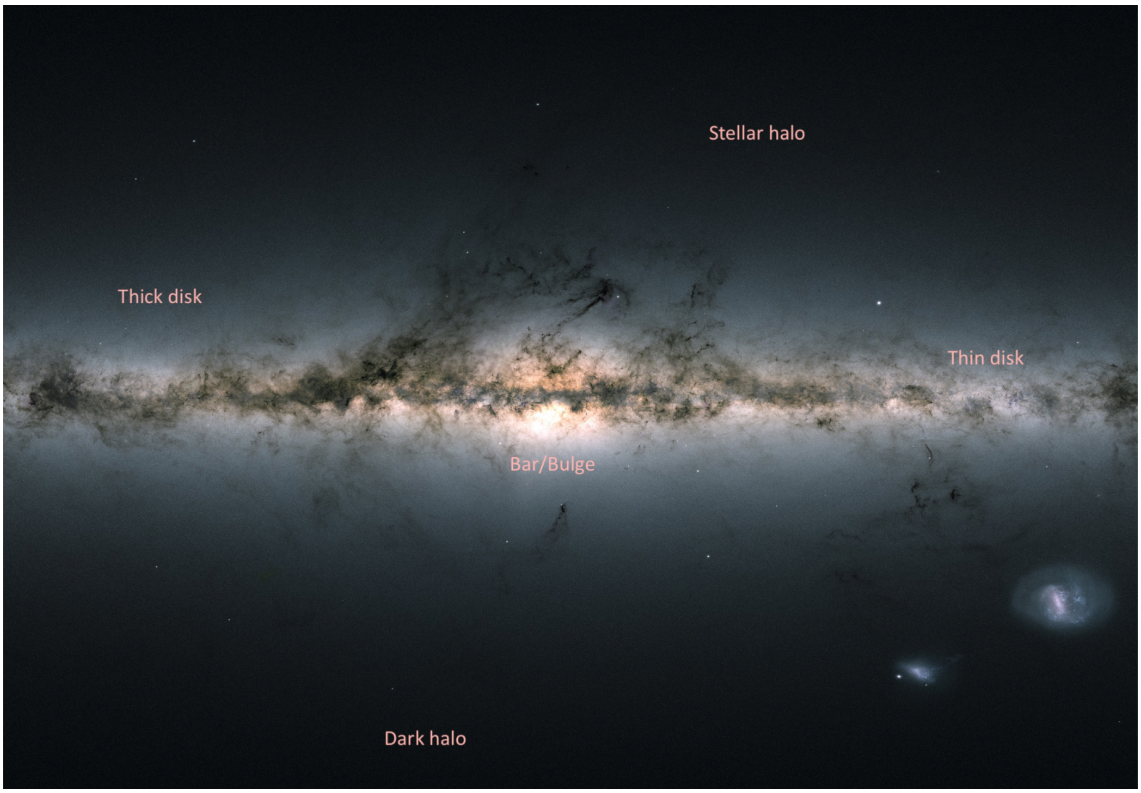

Figure 1.1: The Milky Way and its components. This image was obtained using data from the Gaia second data release. The MW components are highlighted: thin and thick disk, bulge/bar, stellar and dark halo. The Large and Small Magellanic Clouds are visible in the right lower corner. Image credit: Helmi (2020).

and the low-α with the thin disk. This chemical difference can be attributed to different star formation histories (Chiappini et al., 1997, Haywood et al., 2015). The origin of this structural, kinematical, and chemical differences between the thin and thick disk is still debated in the literature.

The bar/bulge is the central and most concentrated component. It was long thought to be a classical spheroidal bulge. However, more recently, it has been suggested to be a pseudobulge that likely formed through disk instabilities (Barbuy et al., 2018, and references therein). The central region has a spheroidal and barred metal-poor ([Fe/H] $\sim$ -0.5) population and a boxy bar metal-rich ([Fe/H] $\sim$ 0.3) population (Rojas-Arriagada et al., 2014, Zoccali et al., 2017). Lastly, the stellar halo is the most extended component and contains old and the most metal-poor stars. There is a dark matter halo embedding our Galaxy, and it is where most of the mass is located. The constituent stars from these distinct components tell us

number of hydrogen atoms and N_M the number of all atoms heavier than Hydrogen and Helium.

about the several processes that occurred over time and shaped the Galaxy as we know.

1.2 Sub/stellar populations as Milky Way tracers

Deep surveys are responsible for the enormous increase in photometric, astrometric and spectroscopic data for different types of Milky Way sub/stellar populations. These large datasets allow a clearer picture of the Galaxy, its structure and stellar content, and provide more restrictive comparisons to models of Milky Way (and galactic in general) formation and evolution.

Our motivation is to investigate the population properties of Galactic objects which have so far eluded detection in large numbers and/or at large distances. Specifically, we are interested in the substellar regime and the halo of our Galaxy. In the next sections, we will discuss the basic properties of two distinct populations, starting with the substellar population, followed by the halo.

1.3 Ultracool and brown dwarfs

Ultracool dwarfs (UCDs) are very cool ($T_{eff} < 2700$) K, low-mass ($M < 0.1$ $M_{\odot}$) objects, ranging from spectral type M7 and later. They include both very low-mass stars and brown dwarfs.

Brown dwarfs (BDs) were first theorised by Kumar (1963) and named by Tarter (1975). The first detection of a brown dwarf was made only in the 1990s with the discoveries of Gliese 229B by Oppenheimer et al. (1995) and Teide 1 by Stauffer et al. (1994), Rebolo et al. (1995). They are not massive enough to burn hydrogen in their core and their typical upper mass limit is 0.072 $M_{\odot}$ and the lower end is $\sim$ 0.012 $M_{\odot}$, approaching the planetary mass regime. Although BDs do not burn hydrogen, they have short periods of primordial deuterium burning during their early evolution. Brown dwarfs never reach thermal equilibrium, being supported by electron degeneracy pressure. Therefore, they continue to cool and dim over time across spectral types M, L, T, and Y (Kirkpatrick et al., 1999, Burgasser et al., 2002a, Cushing et al., 2011). Without sustained hydrogen fusion, there is a degeneracy between mass, age, and luminosity (and their proxies, effective temperature, absolute magnitude, and spectral type). In other words, as brown dwarfs cool continuously over time, their luminosities and temperatures depend on both age and mass. The result is that a younger, less massive brown dwarf can have the same luminosity and

temperature (and thus spectral type) as an older, more massive brown dwarf. This observational degeneracy makes evolutionary trends in brown dwarf populations difficult to identify.

Despite UCDs being a very common type of object in the Galaxy, almost over 1/6 of the local population, they are very difficult to detect at large distances. For instance, Gaia can only acquire accurate astrometry for L5 dwarfs to a distance of ∼24 pc, T0 dwarfs to ∼12 pc, T5 dwarfs to ∼10 pc, and T9 dwarfs to ∼2 pc (Smart et al., 2017). The small amount of radiation emitted by UCDs peaks typically at near-infrared/infrared (NIR/IR) wavelengths, making them extremely faint at optical wavelengths. Only with the advent of deep and wide field surveys, such as Deep Near Infrared Survey of the Southern Sky (DENIS; Epchtein et al., 1997), Sloan Digital Sky Survey (SDSS; York et al., 2000), the Two-Micron All-Sky Survey (2MASS; Skrutskie et al., 2006), the UKIRT Infrared Deep Sky Survey (UKIDSS; Lawrence et al., 2007), the VISTA Hemisphere Survey (VHS; McMahon et al., 2013), the Wide-field Infrared Survey Explorer (WISE; Wright et al., 2010), larger samples of L, T and Y dwarfs were discovered. This increase in the census allows the possibility to constrain current models for the structure, formation and evolution, especially for brown dwarfs. Also, as UCDs have a wide range of ages because of their long lifetimes (even longer than the current age of the universe), an homogeneous sample is ideal for studies of the structure, dynamics, and evolution of the stellar disk itself.

1.3.1 L and T dwarfs

The increasing discovery of cool dwarfs, lead to two new spectral types proposed by Kirkpatrick et al. (1999): L and T dwarfs. Figure 1.2 shows the Hertzsprung–Russell (HR) diagram at the H band that contains a selection from the literature of main-sequence stars and brown dwarfs with spectral types spanning from O through Y.

L dwarfs have temperatures between ∼2,300-1,400 K, with absolute magnitudes ranging from J_{2MASS} ∼11.8-14.5 (Dupuy & Liu, 2012). Even though the majority of L types are brown dwarfs, low-mass stars can be also included in the L dwarf population. Also, L dwarfs have a cool enough atmospheric temperature to favor the formation of condensate grain and droplet clouds[3] near or just below the photosphere. These condensates include liquid iron, solid VO, aluminum, calcium, magnesium, and titanium-bearing minerals such as enstatite ($MgSiO_3$), grossite ($CaAl_4O_7$), and

[3]The condensates refer to grains and drops of the condensed phase. Cloud is the region on the atmosphere within the condensed species are placed.

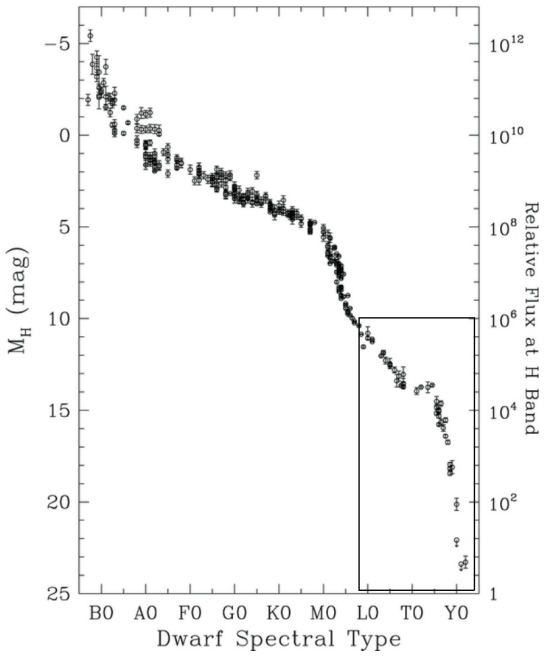

Figure 1.2: The panel shows the HR diagram from Kirkpatrick et al. (2012) showing a compilation of main-sequence stars and brown dwarfs. The box highlights the ultracool dwarfs region.

perovskite ($CaTiO_3$). The opacity of the condensates yields to red near-infrared colors (Burgasser et al., 2002b). Their spectra in the red optical region tend to exhibit strong H_2O absorption, weakening of metal-oxide (TiO and VO) which is a dominant feature in M dwarfs, strengthening of metal-hydrides (CrH and FeH) and alkali band (Na, K, Cs, Rb) features. The near-infrared spectra are dominated by H_2O and CO bands, similarly to the M dwarfs. Figure 1.3 shows example spectra of late M through L dwarfs at optical wavelengths. Some features are highlighted, including water vapour and alkali metal lines, as described above.

T dwarfs are cooler than L types, with a typical range in temperature of ∼1,400-600K or cooler. For the mid- and late T dwarfs the condensates appear to lie deep below the photosphere, providing bluer NIR colors when compared to L types. Their spectra is characterized by strong absorption features of H_2O, CH_4, and collision-induced (also called pressure induced) H_2 (Burgasser et al., 2002a). Figure 1.4 shows the infrared spectra of T dwarfs and the spectra of two L dwarfs for comparison. The strongest absorption bands of H_2O, CH_4, CO, FeH and collision-induced absorption H_2O are highlighted.

The L/T transition changes have been generally interpreted as variation in the clouds. As explained above, from the L to the T regime the cloud layers recede below the photosphere with the decreasing temperature (Burrows et al., 2006, Saumon &

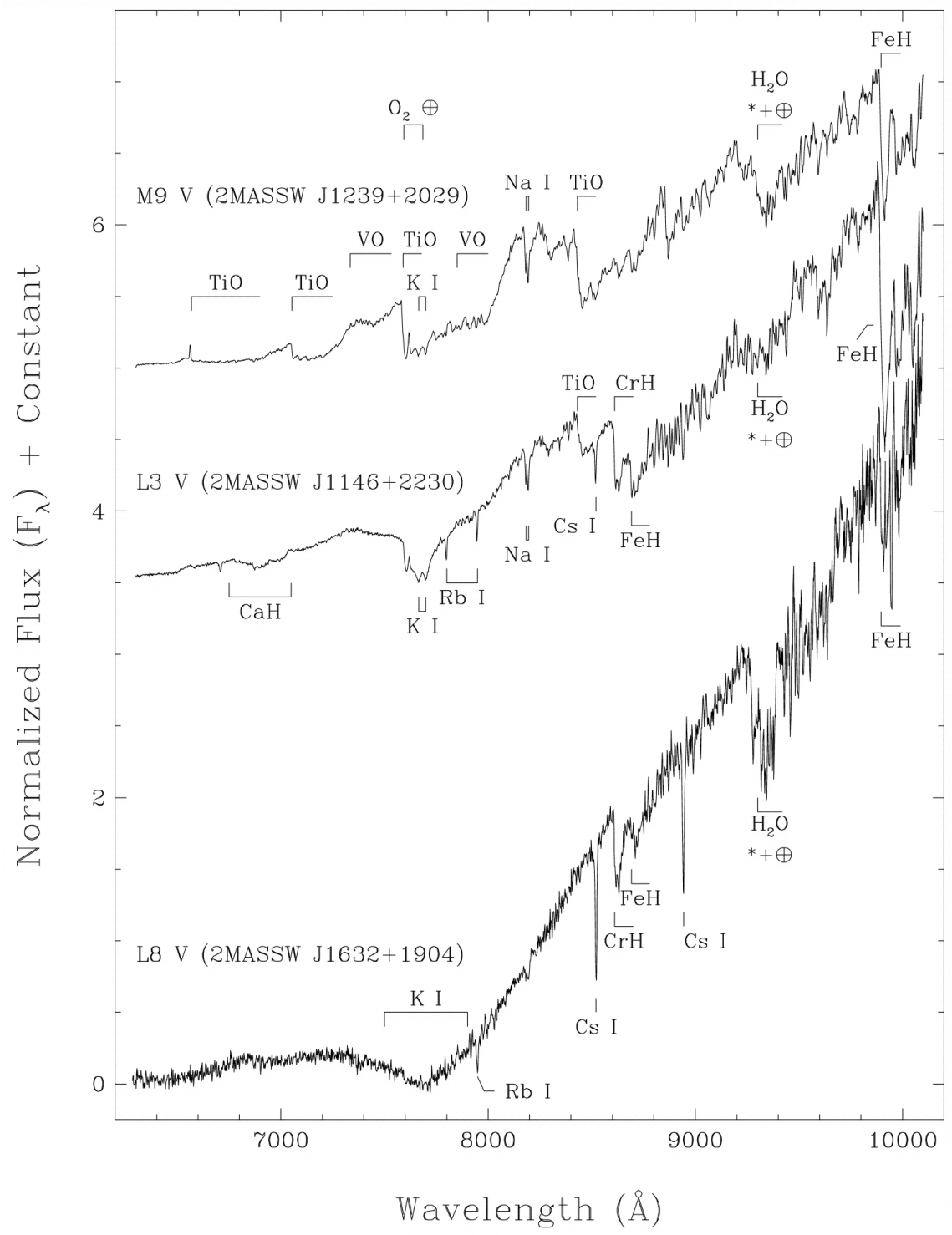

Figure 1.3: Optical spectra of an M9, L3 and L8 type from Kirkpatrick et al. (1999). Some characteristic features such as water vapour and alkali metals are highlighted.

Marley, 2008). The L/T transition has been also interpreted as being caused by chemical instability (Tremblin et al., 2015). However, this interpretation has been questioned (Leconte, 2018). With this complex debate regarding the atmosphere through L and T types, the L/T transition is still very difficult to be reproduced by evolutionary and atmospheric models.

Figure 1.5 shows that T dwarfs appear quite different from M and L dwarfs photometrically. They are significantly redder in optical colors, but they become bluer in the NIR through later types. This blueward trend followed by the T dwarfs is due to the lack of cloud opacity and also to the appearance of CH_4 bands that absorb light mostly close to the K band. However, for late T types the blueward trend diminishes as very little flux remains to be absorbed by CH_4. Also, for types later than T5 there is a large scatter in colors due to the variations in metallicity and gravity, as shown in Figure 1.5. At these temperatures, pressure induced H_2 opacity becomes important, which impacts the K band, which is very sensitive to metallicity and also gravity.

1.3.2 Evolutionary models

The atmospheres of brown dwarfs are complex, as discussed above. The cool atmosphere of a brown dwarf favors the formation of molecules which often have opacities that vary strongly with wavelength, which is another complication, ruling out the usual assumption of a gray atmosphere. Therefore, the construction of evolution model grids is a challenging task, since the atmosphere will regulate the cooling of the interior over time by connecting the convective interior with the thermal radiation emanating from the object.

Several model grids for ultracool dwarfs were developed in past years, including Burrows et al. (1997), Baraffe et al. (2003), Allard et al. (2014), Baraffe et al. (2015). In general, models rely upon the use of 1D radiative-convective equilibrium and assumptions such as thermochemical equilibrium, molecular/atomic abundances and assumed atmospheric chemistry paradigms. Moreover, these models have evolved in complexity over the years to include: clouds prescription (Ackerman & Marley, 2001), rainout (Lodders & Fegley, 2002, Marley et al., 2021) and disequilibrium chemistry (Phillips et al., 2020, Mukherjee et al., 2022). The improvement of the models also benefits as the knowledge of molecular opacities, such as water and methane, which are important absorbers in substellar atmospheres, has progressed. The improvement in molecular opacities and the increase of the complexity of the models have promoted a better description of the observed spectra by models. How-

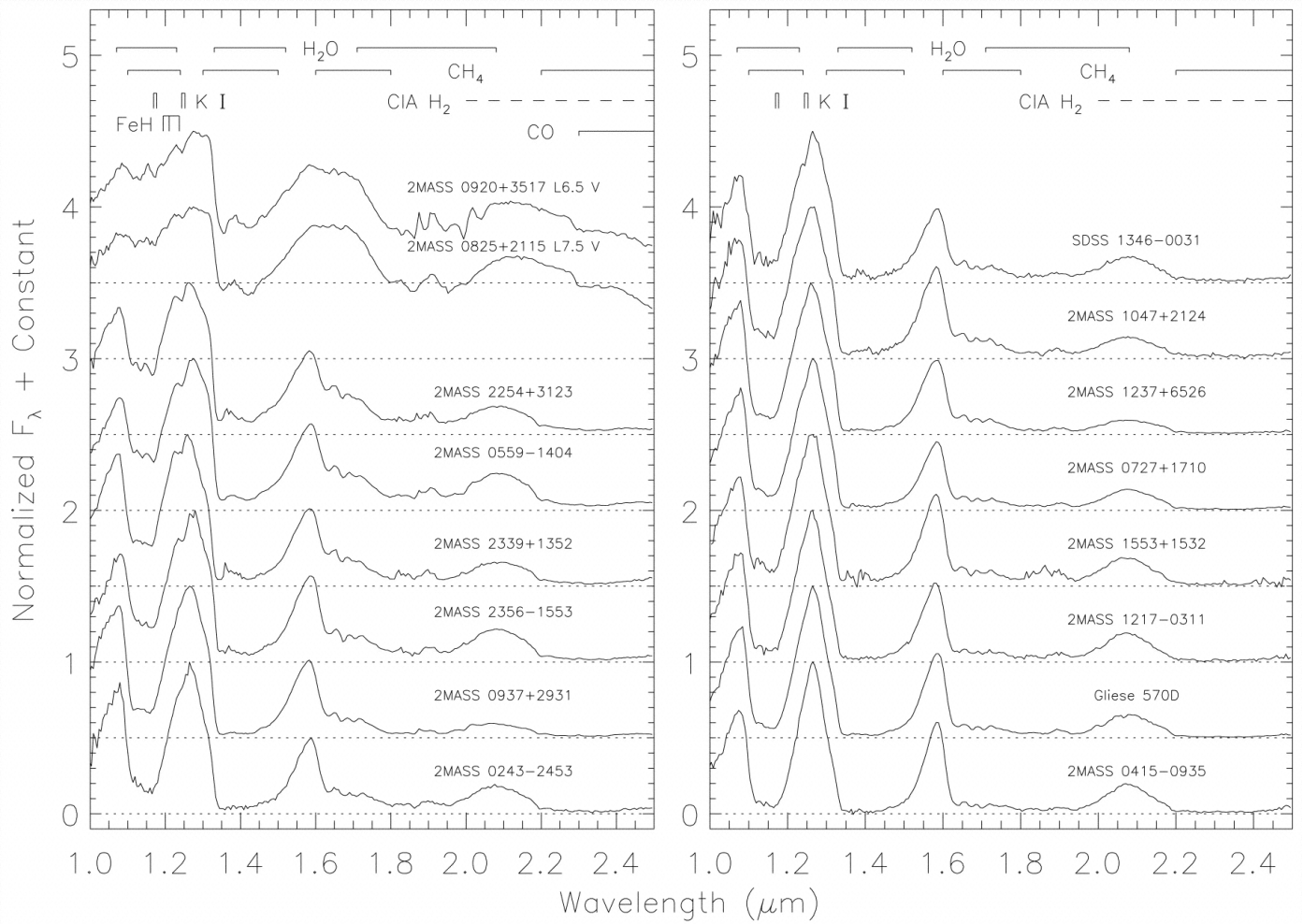

Figure 1.4: Infrared spectra of T dwarfs and of two L dwarfs, for comparison. The figure is taken from Burgasser et al. (2002a). The CO, and FeH absorption bands are indicated, as are lines of H_2O, CH_4 and the region of strongest collision-induced absorption.

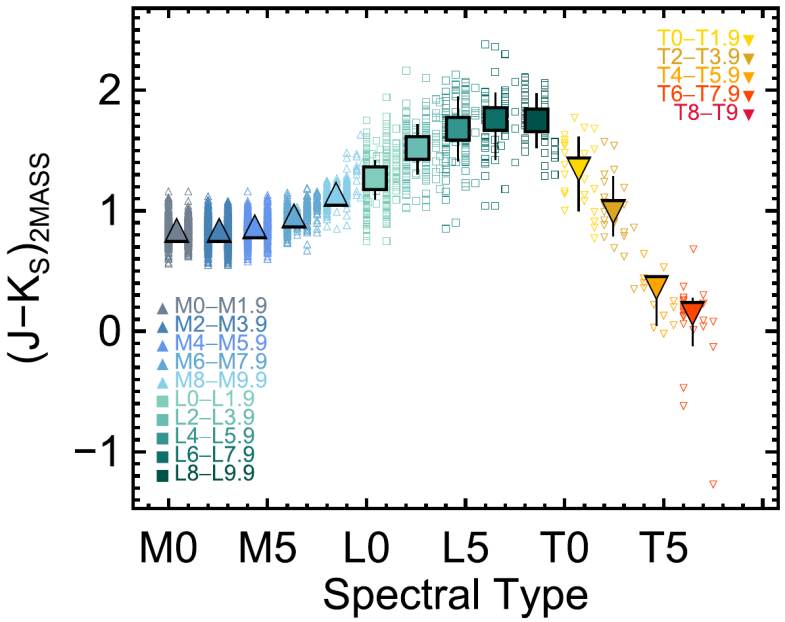

Figure 1.5: Color J-K$_s$ for M, L and T dwarfs selected by Best et al. (2018) using the PanSTARRS1 catalog. The spectral types are indicated by different symbols and colors. As we move from M to L dwarfs, they become redder. For the T types there is a change towards more blue colors.

ever, discrepancies remains, as models still fail to reproduce some key spectra features (Leggett et al., 2021).

As an example, Figure 1.6 shows the J vs. J-K color-magnitude diagram (CMD) from field ultracool dwarfs and subdwarfs from Best & et al. (2020) along with the SONORA models, developed by Marley et al. (2021). It is possible to notice that the models well reproduce the photometry for late-M and early-L dwarfs. Compared with older evolutionary models (e.g Saumon & Marley (2008)) this is an improvement due to the new sets of H_2O opacities. In J $\sim$ 12 the models turn to the blue instead of continuing to the red as observed in the L regime. In the L/T transition, even more bluer colors are predicted by the models compared to the data. This trend is due to the clearing of clouds from the L to the T regime. For the mid-T dwarfs, there is a good agreement between models and photometry. In general, it is known that T dwarfs matched with cloudless models (e.g Saumon & Marley (2008), Allard et al. (2014)).

To overcome the discrepancies still present in the model grids, as illustrated in Figure 1.6, the determination of atmospheric properties can be achieved by atmospheric retrievals. Atmospheric retrievals is a spectral inversion technique. It is complementary to model grids as it consists of minimal physical assumptions

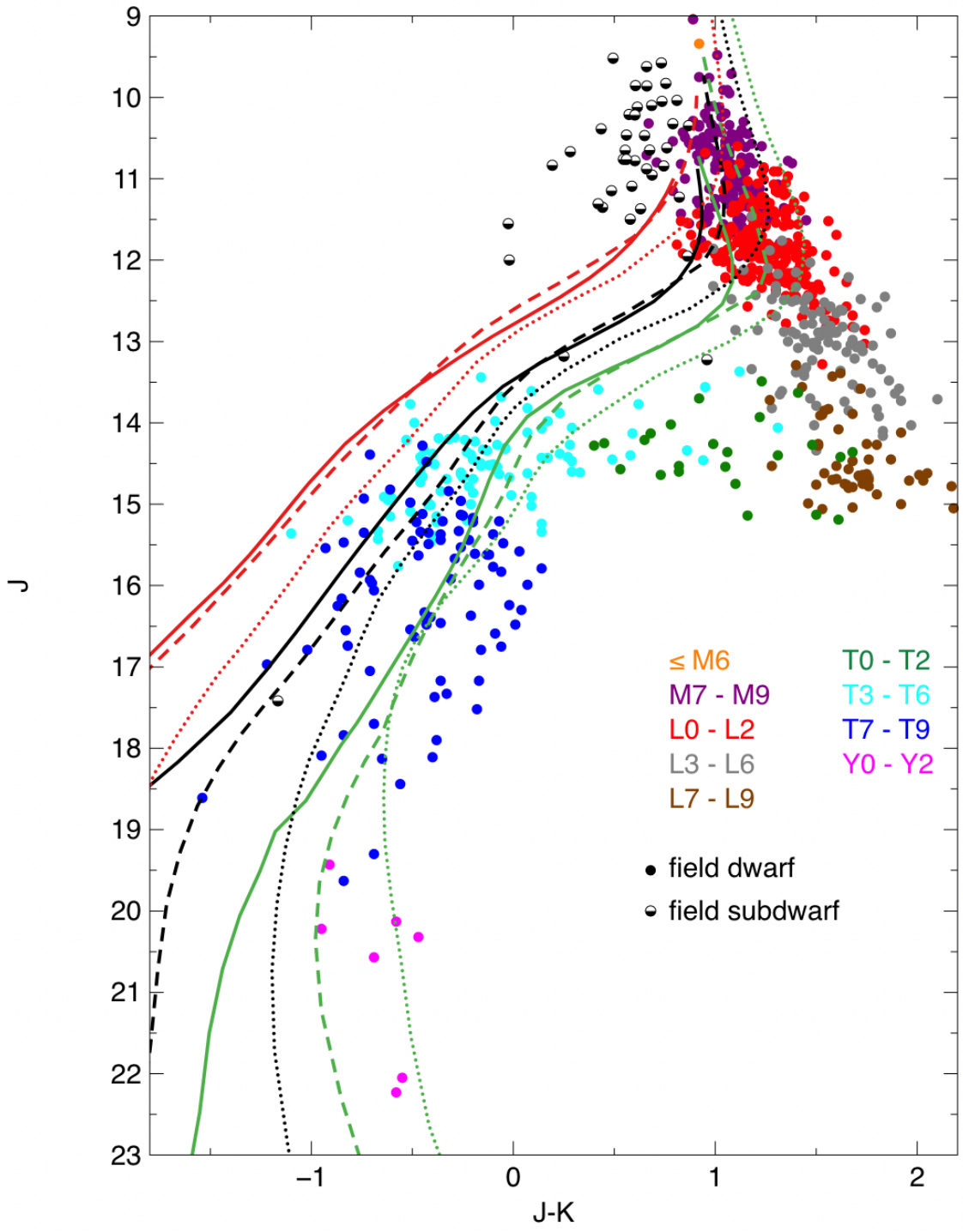

Figure 1.6: Color-magnitude diagram for nearby M, L and T dwarfs from Marley et al. (2021). The curves represent the cloudless SONORA models for different constant values of gravity and metallicity. The solid, dashed and dotted curves stand for log g (cms^{-2}) = 5, 4 and 3, respectively. The colors red, black and green are [M/H]= -0.5, 0.0 and +0.5. The colors of the dots represent the near-infrared spectral types and the half-filled circles are subdwarfs.

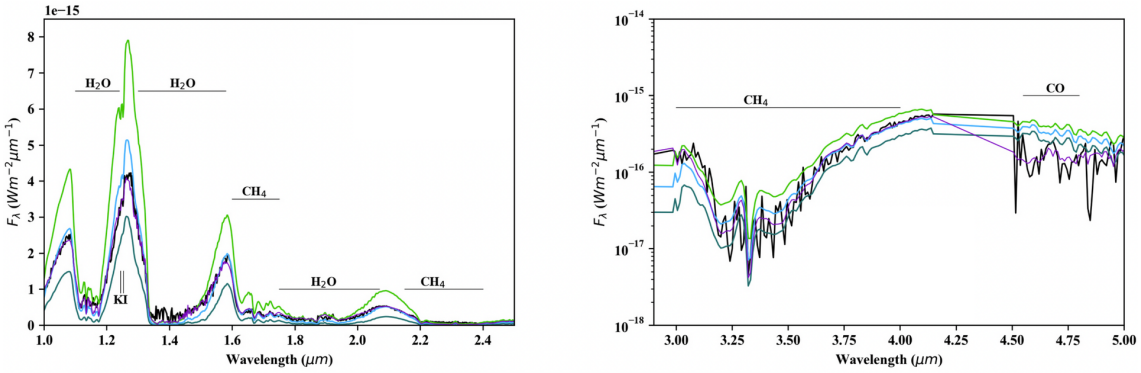

Figure 1.7: Best-fit atmospheric retrieval from Calamari et al. (2022). The black curve shows the Gl 229B spectrum. The purple curve shows the best retrieved spectrum. The blue and green curves are SONORA grid models of solar metallicity and different temperatures.

to determine atmospheric parameters when compared to those inferred by fitting synthetic to observed spectra. In order to retrieve atmospheric temperature and molecular abundances, several synthetic spectra are generated based on a set of atmospheric parameters. These will latter be compared with the observed spectra, generating a range of models that fit the actual spectra along with a statistical assessment of the goodness of the fit. The advantage of this technique is the ability to constrain abundances without relying on assumptions as made in atmospheric models. This technique has been explored for the cloudy L dwarfs by Burningham et al. (2017), cloud-free late-T regime by Line et al. (2014, 2015), Zalesky et al. (2022) and the L/T transition by Lueber et al. (2022). Figure 1.7 shows the comparison between a Gl 229B (T7 dwarf) spectra, a retrieval method presented in Calamari et al. (2022) and comparison with SONORA models that bracket the retrieved T_{eff}. Comparing with SONORA models, the retrieved spectra better fit the observed one.

1.3.3 Formation scenarios

The UCDs formation is still debated, but it is more likely that they form through a core collapse and accretion in molecular clouds. The shape of the IMF, binary fraction and multiplicity function are important discriminants to scenarios of low mass and brown dwarf formation. According to Luhman (2012), there are five basic such scenarios:

1. formation in a proto stellar cluster, where tidal shears and high internal velocities negatively affect the mass accretion by small mass cores (Bonnell et al.,

2008)

2. low mass and brown dwarfs are the least massive cores inside a proto cluster and are therefore ejected due to dynamical interaction with more massive ones, hence halting their mass growth (Boss, 2001, Bate & Bonnell, 2005)

3. massive OB stars form first and their ionizing fluxes remove the gas around least massive cores, again with a negative feedback to low mass and brown dwarf progenitors (Whitworth & Zinnecker, 2004)

4. low mass and brown dwarfs form in circumstellar disks around more massive proto stars and then are ejected into the field by interaction with other (proto)stars (Bate et al., 2002, Bate & Bonnell, 2005, Stamatellos et al., 2011)

5. a proto cluster fragments into smaller cores spanning a wide range of masses, the smallest of which turn into low mass and brown dwarfs (Padoan & Nordlund, 2002, Elmegreen, 2011)

Ruling out or even constraining these models, however, requires larger samples and more accurate estimates of the shape of the IMF, space densities, binary fractions and multiplicity functions than currently available.

1.3.4 Luminosity and Mass Function

The luminosity function (LF) measures the number density of objects as a function of luminosity (or absolute magnitude), which in turn correlates with temperature or spectral type. The luminosity function in the general field is a crucial measurement that can enable a better understanding of low-mass and brown dwarf formation, since the formation history of such objects is still lacking details and relies on many possible scenarios. The more recent and updated field luminosity function was measured by Bardalez Gagliuffi et al. (2019) using a volume-limited compilation of M7-L5 UCDs out to 25 pc from the literature. Figure 1.8 shows the comparison between several field LFs presented in the literature. The LF from Bardalez Gagliuffi et al. (2019) follows the faint end of Reid et al. (2003), pairing well within the uncertainties and had an 40% increase in the densities when compared to Cruz et al. (2007) in the 10.75–13.75 mag range. It is important to mention that the determination of the field luminosity (and also of the mass function) presented in the literature so far is based on a limited number of objects, and limited to the solar neighbourhood.

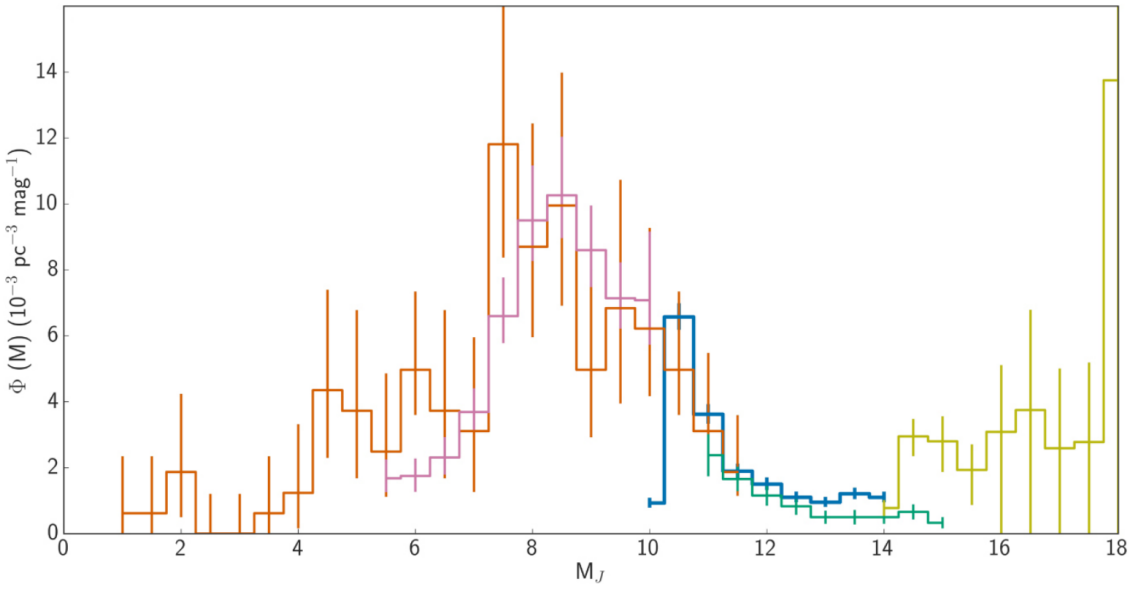

Figure 1.8: Luminosity functions for UCDs with respect to absolute magnitude in J. Figure taken from Bardalez Gagliuffi et al. (2019). The distinct colors refer to different LF measurements. The blue line is from Bardalez Gagliuffi et al. (2019), orange is from Reid et al. (2003), pink from Bochanski et al. (2010), green from Cruz et al. (2007) and yellow from Reylé et al. (2010).

The initial mass function (IMF) is defined as the number density per unit mass. For brown dwarfs there is no unique mass-luminosity (or yet mass-luminosity-metallicity) relationship that one can use to convert the luminosity function into the IMF as in the case of main-sequence stars. However, one advantage is that for very low-mass stars and brown dwarfs, that cool as they age, the observed present-day mass function (PDMF) in the field should trace the initial mass function. There are two basic factors contributing to it: i) since low-mass stars and brown dwarfs are long lived objects, with evolutionary ages similar to or larger than the age of the Galaxy itself, every field ultracool dwarf created is still present in the Galaxy; ii) dynamical effects resulting from two-body interactions, that reshape the mass function inside star clusters, are not relevant in the field because of the much lower density.

Substellar IMFs can also be determined. For field stars, assumptions about the formation history (formation rates and metal enrichment) are required to convert luminosities into masses. As mentioned in the next section, binary systems play an important role to constrain ages and metallicities, this latter parameter also being important to determine masses from luminosities.

An alternative is to investigate the census of low mass and ultracool dwarfs in

clusters and associations, where it is then possible to break the metallicity-age-mass-luminosity degeneracies (since age and metallicities are known) and, therefore, to remove the dependency of the luminosity function with the formation history that affects the field. A mass function is often described in the form of a power law $\phi(m) = dN(m)/dm \propto m^{-\alpha}$. For young clusters and associations, several measurements of α are available. For Upper Sco, $\alpha = 0.6 \pm 0.1$ (Lodieu et al., 2007), for Pleaides $\alpha = 0.6 \pm 0.1$ (Moraux et al., 2003), for σ Orionis $\alpha = 0.5 \pm 0.2$ (Lodieu et al., 2009) and for RCW 38 the slope is $\alpha = 0.8 \pm 0.8$ (Mužić et al., 2017). More recently, Mužić et al. (2019) showed that the NGC 2244 IMF is well represented by a broken power law with a break at $\sim 0.4_{\odot}$. For the low mass and brown dwarfs, the slope is $\alpha = 1.03 \pm 0.02$, which is at the high end of the typical values obtained in nearby star-forming regions but still in agreement within the uncertainties. For the field, Kirkpatrick et al. (2021a) demonstrate that a 20 pc volume-limited sample of brown dwarfs can be best described as a power law with an exponent of $\alpha = 0.6 \pm 0.1$.

1.3.5 Benchmark ultracool dwarfs

Benchmark ultracool and/or brown dwarfs are very useful because we can use them to break degeneracies in age, mass and metallicity, thus being very helpful for the characterisation of cool substellar objects. A common type of benchmark system are wide binaries, composed of resolved companions, where the primary is commonly a main sequence star and the secondary is a L or T dwarf. The metallicity and age constraints may be taken from the primary star since it is very difficult to measure these properties for the L and T dwarfs. For that purpose, one naturally has to rely on the assumption that the pair formed at the same time, from the same material, and evolved in the same environment. This is also the case of UCDs in clusters, where previously determined cluster metallicity and age are useful as benchmarks.

One issue in finding benchmark systems in wide binaries involving L or T dwarfs is that the binary fraction seems to decrease from early to late primary's spectral types (Kraus & Hillenbrand, 2012). For solar type stars, the binary fraction ranges within 50-60% (Raghavan et al., 2010) and for M stars it is in the 30-40% range (Janson et al., 2012). For brown dwarfs in the field, the resolved binary frequency ranges around 10-20% (Burgasser et al., 2006, Gelino et al., 2011, Huélamo et al., 2015).

In the case of wide binary systems, for solar type stars Tokovinin & Lépine (2012) estimates 4.4 % are wider than 2,000 AU. More recently Dhital et al. (2011) and Dhital et al. (2015) presented the Sloan Low-mass Wide Pairs of Kinematically

Equivalent Stars (SLoWPoKES), which is a catalog containing common proper motion and common distance of wide ($\sim$ 500-60,000 AU) candidate pairs. For the mid K and mid M type dwarfs presented in both catalogs, the wide binary frequency was $\sim$ 1.1%. For L and T dwarfs in wide systems this frequency still remains uncertain. Also, brown dwarfs in wide binary systems could impact the formation theories, especially the ejection model, since this type of system is not expected to survive ejection from their birth environments.

1.3.6 Spatial distribution

As discussed previously, ultracool dwarfs are a common type of object in our Galaxy. Therefore, they are expected to trace the same structural components as the stars, i.e., brown dwarfs will have a thin and thick disk and halo populations. However, measuring their spatial distribution is not an easy task, due to the faintness of the ultracool dwarf population.

There are few attempts to measure the thin disk scale height in the literature. Using 18 M and later dwarfs (spectral type M4 and later) from the Hubble Ultra Deep Field, Pirzkal et al. (2005) derived a Galactic disk scale height of 400$\pm$100 pc for M and L dwarf population. They compared the observations with Galaxy models using a luminosity function derived from Monte Carlo mass function simulations from Burgasser (2004). Ryan et al. (2005) estimated the scale height of 350$\pm$50 pc of 28 candidate L and T dwarfs identified in 15 deep parallel fields from the Hubble Space Telescope. They treated L and T dwarfs as a single population and used a local number density derived by Chabrier (2002). Jurić et al. (2008) estimate the thin disk scale height of 300 pc and the local thick-to-thin disk density normalisation of SDSS M dwarfs up to a distance of 2 kpc. More recently, Sorahana et al. (2019) have used data from the first data release from the Hyper Suprime Camera (HSC, Miyazaki et al., 2018, Aihara et al., 2018) to estimate the vertical thin disk scale height of 3,665 early L types with an estimate between 320 pc and 520 pc at 90% confidence. They assumed an exponential disk model and used the luminosity function from Cruz et al. (2007) allowing the number densities for individual magnitude bins to vary along with the scale height. Also, Carnero Rosell et al. (2019) compared the number counts from nearly 12,000 L types candidate sample along with ultracool dwarfs simulation and found a thin disk scale height of $\sim$ 450 pc. One important application is that we can convert the estimate of the scale height into a vertical velocity dispersion. The velocity dispersion could be used as an indicator of kinematics age of the population sampled.

1.4 Stellar Halo

According to the Λ-cold dark matter (ΛCDM) model, the structural formation of galaxies proceeds hierarchically, with large structures forming via mergers (Springel et al., 2005, Frenk & White, 2012, Naab & Ostriker, 2017). Therefore, a relatively large spiral galaxy such as the MW likely formed with the contribution of several accretion events involving galactic objects of various sizes and masses. In fact, the Galactic halo is a repository of most of the mass built up from accretion events. This process is observed today, through the discovery of many overdensities and streams with the aid of wide-field photometric surveys (more details in Section 1.4.3). The stellar halo is not only interesting from the mergers point of view but also because it contains the oldest (along with the bulge) and the most metal-poor stars, giving us a glimpse to the early phases of the Milky Way.

Although the Galactic halo comprises around 1% of the total stellar mass, their old metal-poor stars play an important role in the study of formation and evolution of the Galaxy. Some stars may have formed in situ and others are accreted material from merger events with satellite galaxies. The formation channel in situ refers to halo stars that were born within the Galaxy and the accreted ones being the material from tidal disruption of smaller dwarf galaxies.

The stellar halo is commonly portrayed in the literature as divided into two main components: the inner and outer halo. Several authors have identified an steepening in the stellar density profile around $R_{Gal} > 30$ kpc (Bland-Hawthorn & Gerhard, 2016, and references therein). Consistently with the apparent profile steepening, Carollo et al. (2007) have suggested that the inner halo is relatively more metal-rich, with a significant flattening and with prograde orbits and the outer halo is more metal-poor, nearly spherical in shape and with retrograde orbits. The kinematical evidence, however, was disputed as a possible bias in the stellar distances (Schönrich et al., 2011). In the last years, the inner halo (specially regions in the solar vicinity, within few kpc from the Sun) has been largely studied. However, considering that the virial radius of our Galaxy is of $\sim$ 250-300 kpc (Gómez et al., 2015), the Milky Way halo covers a vast volume that is still relatively unexplored.

1.4.1 Density profile and shape

The spatial distribution of the stellar content, specifically the density profile and the flattening of the stellar population, is crucial for understanding the formation history and dark matter distribution.

Early studies suggested that the density profile of the Milky Way halo could be described as a single power-law (SPL) $\rho \propto r^{-\alpha}$ with a flattening either constant or varying with radius. For instance, De Propris et al. (2010), using a sample of blue horizontal branch (BHB) stars up to 100 kpc, found a profile described by a SPL with index -2.5 with no evidence of a profile break. However, Sesar et al. (2011) and Deason et al. (2011) found evidence that the outer parts of the halo (>30 kpc) have a steeper stellar density profile than the inner regions. These authors also did not find strong evidence for variations in flattening with radius.

Xue et al. (2015) used a sample of giant stars and found that a broken power-law (BPL) with α_{in} = -2.1 and α_{out} = -3.8 and break radius of $\sim$ 18 kpc and constant flattening well reproduced the data. However, they also argued that if the flattening of the stellar halo varied with distance, a single power-law model with α = 4.2 described the data. Also, using a sample of giants, Slater et al. (2016) found a α = -3.5 with no signs of profile break in a 30-80 kpc range studied. More recently, Thomas et al. (2018) analyses using BHB stars favours a broken power-law profile, with an inner slope that is steeper than in the outskirt of the halo and constant flattening. The difference between the slope in the outer and inner region is $\sim$ 1, with a break around 40 kpc. Their measurement is also similar to the one found by Hernitschek et al. (2018) using RR Lyrae. These latter also found a break radius around 40 kpc, but their analyses favours a single power-low profile with constant flattening. Hernitschek et al. (2018) also allow a radius-dependent flattening, and found evidence for a distinct flattening of q $\sim$ 0.8 of the inner halo at $\sim$ 25 kpc, a similar finding to Xue et al. (2015). Xu et al. (2018) found no evidence of power-law break between 15-35 kpc. The profile for the selected giants was described by a SPL with α = -5.5 and a flattening that varies with radius (q = 0.64, 0.8 and 0.96 at r = 15, 20 and 30 kpc).

Table 1.1 summarizes the results found in the literature and discussed in this section. In the context of BPL models, the break radius between the inner and outer components is located in a range of 20-40 kpc. Regarding use of SPL/BPL models, it is difficult to determine if the difference between these measurements is due to the different tracers or methodology used. In the case of tracers, the consequence could be the differences in the spatial distribution of different stellar populations leading to different steepness in the profile.

One possible explanation for the apparent break radius is the build-up of stars at their apocenter. This build up could be caused by the accretion of a small group of dwarf satellites at a similar epoch, or by a single massive one. Deason et al. (2018)

Table 1.1: List (incomplete) of stellar halo density parameters.

Reference	Tracer	Sample size	r (kpc)	α_{in}	α_{out}	q	r_b (kpc)
De Propris et al. (2010)	BHB	666	10-100	-2.5	-	-	-
Sesar et al. (2011)	MSTO	27,544	5-35	-2.62 ± 0.04	-3.8 ± 0.1	0.70 ± 0.01	27.8 ± 0.8
Deason et al. (2011)	BS/BHB	∼ 20,000	10-45	-2.3 ± 0.1	-4.6 ± 0.15	0.59 ± 0.03	27.1 ± 1
Xue et al. (2015)	Giants	1,757	10-80	-2.1 ± 0.3	-3.8 ± 0.1	0.70 ± 0.02	18 ± 1
Slater et al. (2016)	Giants	∼ 4,000	30-80	-	-3.5 ± 0.2	0.6	-
Thomas et al. (2018)	BHB	∼ 4,800	15-220	-4.24 ± 0.08	-3.21 ± 0.07	0.86 ± 0.02	41.2 ± 2.5
Hernitschek et al. (2018)	RRab	11,025	20-131	-4.40 ± 0.05	-	0.92 ± 0.02	-
Xu et al. (2018)	Giants	5,351	15-35	-5.03 ± 0.64	-	-	-

integrated the orbits of the stars that likely belong to the Gaia-Enceladus substructure and showed that for the population with high eccentricity their apocenters lie at about ∼ 20 kpc, coincident with the break radius. More details of Gaia-Enceladus will be discussed below.

1.4.2 Metallicity distribution

The metallicity distribution function of the MW stellar halo is essential to understand the processes that were involved in its formation. For instance, the very low-metallicity component give us clues on star formation and chemical evolution at earliest epochs.

It has been shown in the literature that the halo has a metallicity that decreases with an increase in radial distance (Carollo et al., 2007). de Jong et al. (2010) measured a peak in the metallicity distribution function for the inner halo ($<$ 15 kpc) around [Fe/H] ∼ -1.6 and for the outer halo at [Fe/H] ∼ -2.2 using SEGUE data. Fernández-Alvar et al. (2017) found similar results, with peaks around [M/H] ∼ -1.5 and [M/H] ∼ -2.1 based on APOGEE DR12. Conroy et al. (2019) measured a median metallicity of [Fe/H] = -1.2 using stars at high latitudes ($|b| >$ 40°) from the H3 Survey and no discernible metallicity gradient over the range of ∼ 6–100 kpc. However, the authors admit possible evidence for a decreasing mean metallicity beyond ∼ 50 kpc. Youakim et al. (2020) used a sample of ∼ 80,000 main-sequence turnoff stars with heliocentric distances ranging from 6 to 20 kpc and found a peak at [Fe/H] = -1.6. These authors found a gradient of decreasing metallicity with increasing distance, but no clear bimodality in the halo metallicity distribution function in the range of distances probed.

Nissen & Schuster (2010) suggested that the local halo metal-poor stars have low-α and high-α abundance components. Later studies suggested that the low-α population was likely accreted through mergers whereas the high-α stars were either formed in situ or have been kicked out from the disk. With APOGEE DR13,

both Hayes et al. (2018) and Matsuno et al. (2019) showed that for the low-α halo population, the [Fe/H] peaks around -1.2 and -1.3. Considering a sample of chemically selected accreted stars from APOGEE DR14 data, Das et al. (2020) found a peak at [M/H] $\sim$ -1.3 and that they constitute over 30% of the metal-poor regime ([Fe/H] $<$ -0.8) halo stars.

Recently, studies regarding the metallicity in the stellar halo have become more focused in the Gaia-Enceladus substructure. Feuillet et al. (2020, 2021) selected the Gaia-Enceladus population using kinematics and action space, and found a peak around [Fe/H] $\sim$ -1.17 with a dispersion of 0.34 dex. Also, using dynamically selected stars from H3 survey, Naidu et al. (2020) found a similar distribution of [Fe/H] $\sim$ -1.20. These measurements are in agreement with the low-α population.

1.4.3 Substructures

In the last years, many wide-field surveys have revealed several overdensities and streams. Specially the Gaia mission, that was responsible for a true revolution and transformation in Galactic astrophysics. The access to the full phase-space information revealed a large accreted object in the local inner halo named Gaia-Enceladus-Sausage (Helmi et al., 2018, Belokurov et al., 2018). The 'Sausage-like' structure was identified by Belokurov et al. (2018) in a V_φ vs V_R velocity space, centered around $V_\varphi \sim 0$ and extended in V_R. On the other hand, Helmi et al. (2018) selected stars from the inner halo using their angular momentum L_Z and orbital energy E_n and noticed that their kinematics ranged from highly eccentric to highly retrograde. With APOGEE, Helmi et al. (2018) also showed that Gaia-Enceladus define a distinct chemical sequence from the thin and thick disk stars, being more metal-poor than the thin disk and having lower α abundances than the thick disk. The mean metallicity was obtained as [Fe/H] $\sim$ -1.6 and the age was constrained in roughly 10 Gyr. Also, they estimated a stellar mass of $\sim 6 \times 10^8$ $M_\odot$ for Gaia-Enceladus. There is still some debate in the literature about the exact nature and definition of this merger event. It is common to use the notation Gaia-Enceladus-Sausage to acknowledge the difficulty to disentangle and reconcile the substructures found in the halo by different authors.

Another structure found is the 'hot' thick disk, also known as the Splash (Belokurov et al., 2020) (more details below), which also dominates amongst stars in the solar vicinity with halo-like kinematics. For stars in the solar vicinity (within 2.5 kpc from the Sun) and with $|V\text{-}V_{LSR}| > 200$ km/s, where the velocity of the local standard of rest $V_{LSR} \sim 220$ km/s, it is estimated that roughly 44% of the

stars belong to the 'hot' thick disk. A large fraction of the remaining stars are part of the Gaia-Enceladus-Sausage structure.

The Gaia DR2 was also responsible for revealing a 'dual halo' (also known as the blue and red sequence) in a color-magnitude diagram constructed of kinematically selected Galactic components (Gaia Collaboration, Babusiaux et al., 2018). The halo selection was made using tangential velocity $v_t = 4.74/\omega\sqrt{\mu_\alpha^2 + \mu_\delta^2} > 200$ km/s. In the CMD, the halo main sequence and main sequence turn-off are clearly divided into two, with $\sim$ 0.1 mag difference in color between them. The two sequences have metallicity distributions with peaks in [Fe/H] = -1.3 and [Fe/H] = - 0.5. Also, these two sequences could be associated with the two halo components noted by Nissen & Schuster (2010) as discussed in the previous section. The more metal-poor sequence is connected to Gaia-Enceladus while the other sequence is the 'hot' thick disk, populated by stars which kinematically can be part of the thick disk, in situ halo or a mix. Gallart et al. (2019) have showed that the sequences are identical in age, where the blue and the red population formed stars at the same time, but also stopped forming at similar times. According to the mass-metallicity relation, the stars of the red sequence being more metal-rich ([Fe/H] = - 0.5) imply that they must be formed in a galaxy more massive than the ones from the blue sequence. Furthermore, the Gaia-Enceladus merger could be the responsible for the heating of a fraction of stars that were been forming in a disk-like structure. This led to extreme kinematics which lead them to be classified as halo stars.

There are other substructures identified based on kinematic, orbital properties, age, and metallicity. For instance, Myeong et al. (2019) argued that the debris presented in Helmi et al. (2018) included both mildly prograde stars and highly retrograde stars, suggesting different progenitors. Instead of one single merger event, the Gaia-Enceladus-Sausage, another merger took place roughly at the same time, named the Sequoia. The most massive globular cluster in the Galaxy, ω-Centauri, may be the remnant core of Sequoia. Also the globular cluster FRS 1758 could be associated with this substructure. Koppelman et al. (2019) used a clustering algorithm to identify substructures based on their energy, angular momentum, eccentricity and metallicity, as these quantities can retain dynamical and chemical memory of their origin. These authors found, besides Gaia-Enceladus-Sausage, Sequoia and Helmi streams, two new structures with low-energy, retrograde orbits named Thamnos 1 and 2. Figure 1.9 shows the results from Koppelman et al. (2019) based on the search for substructures using energy and angular momentum space. Recently, other small groups were reported in the literature using new releases from Gaia (see (Lövdal

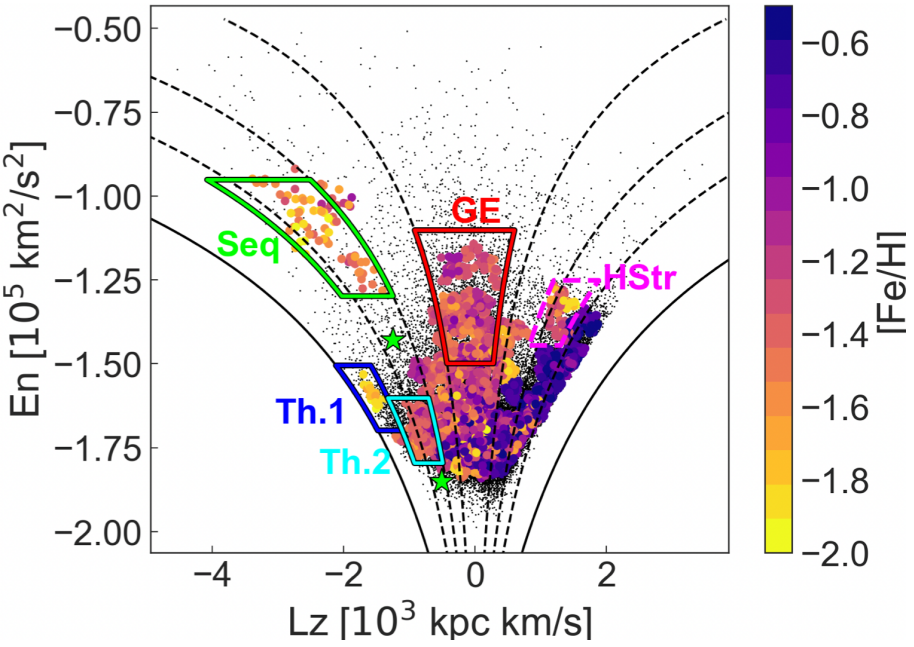

Figure 1.9: Substructures identified by Koppelman et al. (2019) using angular momentum and energy. Highlighted in the figure are: Gaia-Enceladus (GE), the Helmi streams (HStr), Sequoia (Seq) and Thamnos (Th). The green stars represents the globular clusters ω-Centauri and FRS 1758.

et al., 2022, Dodd et al., 2023, Tenachi et al., 2022)).

At larger distances from the Sun, many overdensities and streams have been also discovered. Some examples are the Sagittarius streams (Ivezić et al., 2000, Yanny et al., 2000), Hercules Aquila Cloud (Belokurov et al., 2007), the Virgo overdensity (Vivas et al., 2004, Jurić et al., 2008) and Monoceros ring (Newberg et al., 2002). Many thin streams also have been discovered, such as GD-1 (Koposov et al., 2010), Atlas (Koposov et al., 2014), Orphan (Belokurov et al., 2007) and Pal 5 (Odenkirchen et al., 2001). The Dark Energy Survey alone was responsible for the discovery of over 14 stellar streams (Drlica-Wagner et al., 2015, Balbinot et al., 2016, Shipp et al., 2018). Some of these stellar streams have been found with no clear progenitor object, probably indicating a more advanced stage of disruption. Besides the stellar streams, other dynamically hotter structures, such as galactic bridges, tidal arms and stellar clouds have been observed. Their structure and geometry (shapes, distances, widths) coupled with their kinematics, allow stringent limits on the Milky Way gravitational potential, as well as on Galactic parameters. Figure 1.10 shows the known streams and overdensities and their distribution on the sky not only for the outer but also for the inner halo.

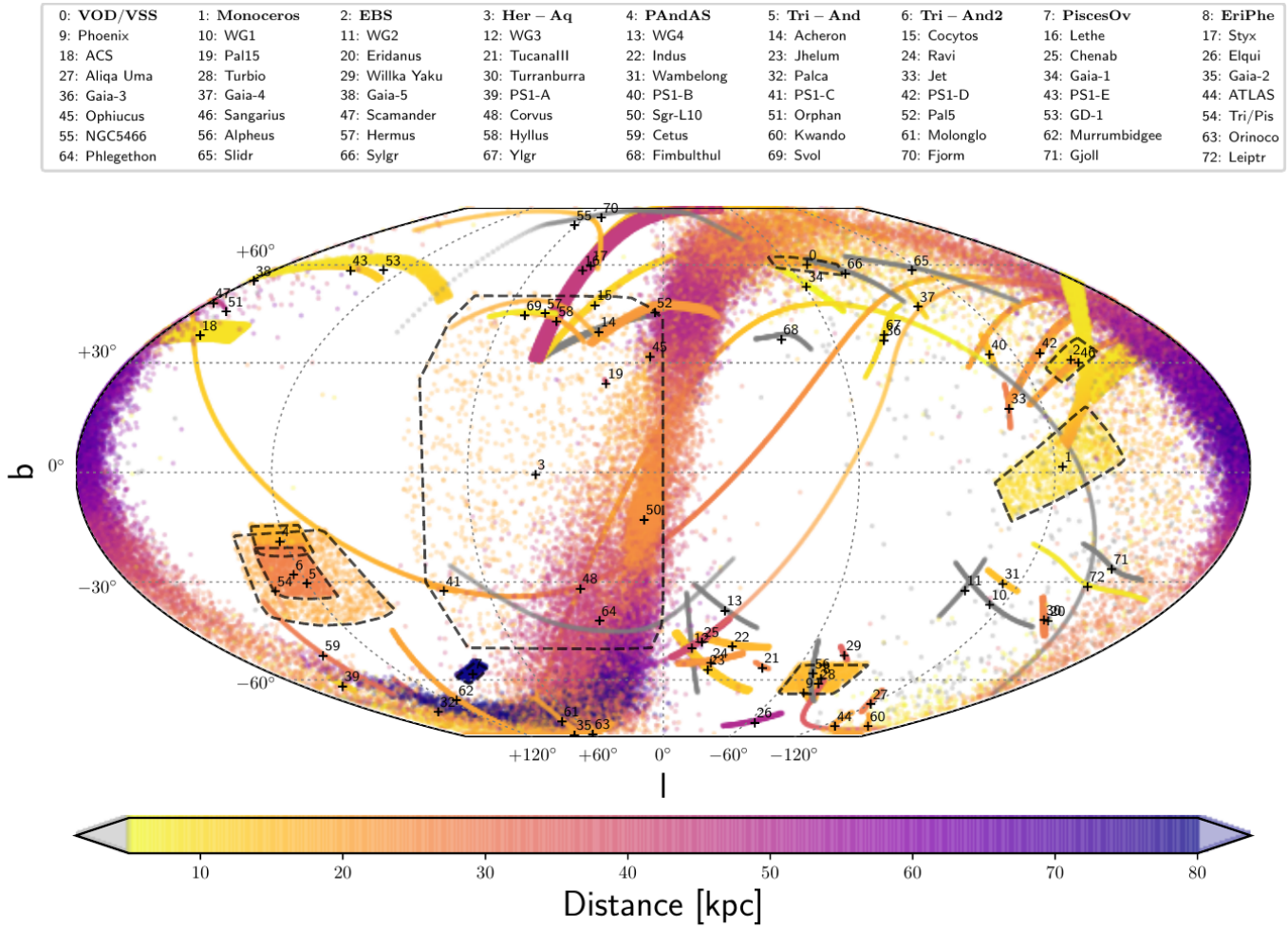

Figure 1.10: Currently known streams and overdensities from Helmi (2020). The overdensities are indicated as regions delimited by dashed lines, and in boldface in the upper panel.

1.5 Goals

Now that we discussed the substellar and very low-mass stellar regime and the halo stellar population in detail we can specify our aimed contributions towards these two topics.

For the ultracool dwarf population we plan to extend our previous analysis that was initially done with the first three years of the Dark Energy Survey (DES) science operation and presented in Carnero Rosell et al. (2019). Now, using the six years of DES data, we expand the search for ultracool dwarfs candidates. This new and updated census also allows several applications such as the search for: i) new candidate members to young moving groups and associations; ii) photometric variable objects; iii) new wide binary candidate systems composed by two ultracool dwarfs. The subsamples can help constrain formation scenarios for UCDs, as in the case of substellar members of associations and wide binary systems, and to understand atmospheric inhomogeneities in ultracool dwarfs, as in the case of variable objects. Another important use of this sample is towards the contribution of a most robust estimation of the spatial distribution of ultracool dwarfs. More details in Chapters 2 and 3.

For the halo population, it is crucial to estimate distances to individual stars, so as to map its structure. Metallicities and age estimates also help the identification of different halo populations and their variation as a function of Galactocentric distance. We are interested in using available samples of field stars with reasonably accurate distance to construct a tomography of the Milky Way outer components. We aim to explore not only their geometry and density profile, but also age and metallicity gradients and their associated spread, motivated by the ongoing debate in the literature regarding these topics. More details in Chapter 4.

Chapter 2

Ultracool dwarfs candidates discovered in the six years of the Dark Energy Survey data

In this chapter, we will present the work concerning the search and characterization of ultracool dwarfs (UCDs). This project began some years ago, and our group has already two published papers regarding a sample of UCDs selected using the first three years of Dark Energy Survey (DES) operation data that will be used as the main basis for our search.

The accurate identification and classification of UCDs in large deep ground-based surveys using only photometry enables the creation of homogeneous samples without relying on extensive spectroscopic campaigns. Such samples are essential to allow the characterization of the UCDs in the Galaxy, to enable the measurement of the luminosity and mass functions (Cruz et al., 2007, Bochanski et al., 2010), the disk scale height (Jurić et al., 2008, Sorahana et al., 2019), the frequency of close and wide binaries (Luhman, 2012, Dhital et al., 2015, Fontanive et al., 2018) and their kinematics (Faherty et al., 2010, Faherty et al., 2012, Smith et al., 2014). Taking advantage of the Dark Energy Survey (DES) depth in the optical bands i, z and Y, and combining them with infrared data from other surveys, it is possible to select a large homogeneous sample of UCD candidates to large distances.

In Carnero Rosell et al. (2019), we presented a sample of 11,745 UCDs selected using DES DR1 combined with VHS DR3 and AllWISE. This candidate sample was selected based on colors and a spectral classification using only photometry. We kept on the sample only L and T candidates. Besides the sample, we also presented a initial study of the thin disk scale height for the L dwarf population, which is by

far the most numerous in our compilation (11,545 L dwarfs). Recently, the new and latest DES data release became available. Compared to our previous work, the DES DR2 data are photometrically deeper and with more reliable/precise photometry. These deeper data have the capacity to allow us to probe fainter candidates, thus increasing the previous samples of L and T dwarfs. Furthermore, we have now available a sky coverage of almost the entire DES footprint, whereas in Carnero Rosell et al. (2019) we only had $\sim$ 2,400 deg^2. This is due to the new data releases of VHS and VIKING surveys that are also used in the analyses. This scenario implies that the UCD search and characterization can be updated.

In the next sections, we will discuss all the steps that led us to the new sample of UCDs. In Section 2.1 we present the photometric data used in this work. In Section 2.2 we introduce the updated color templates for M dwarfs and UCDs and the color cuts used to pre-select our candidates. In section 2.3 we discuss the photometric classification methodology, where we estimate a spectral type for each target using only its photometry. Once the photometric classification (Section 2.3) is carried out, we end up with what we call the UCD target sample. For this sample, in Section 2.4, we compare our photo-type to those of known candidates from the literature and discuss the contamination by extragalactic sources, to finally present the final ultracool dwarf candidate sample. In Section 2.5, we show Gemini/GMOS spectra of several UCD candidates, all of them confirmed spectroscopically as UCDs, to further corroborate our sample selection and photo-types.

All the topics discussed in this Chapter are part of an published paper (available at Appendix B) at MNRAS journal.

2.1 Data

2.1.1 DES, VHS, VIKING and AllWISE

DES is a $\sim$5,000 deg^2 optical survey in the $grizY$ bands that used the Dark Energy Camera (DECam; Flaugher et al., 2015). DECam is a wide-field (3 deg^2) imager at the prime focus of the Blanco 4m telescope at Cerro Tololo Inter-American Observatory (CTIO). DES observations started in September 2013 and were completed in January 2019, spanning nearly six years.

DES DR2 is the assembled dataset from 6 years of DES science operations, with data collected over 681 nights and which includes 691 million astronomical objects detected in 10,169 coadded image tiles of size 0.534 deg^2 produced from

76,217 single-epoch images. The estimated area loss to image defects, saturated stars, satellite trails, etc is of $\simeq$ 200 deg^2. After a basic quality selection, galaxy and stellar samples contain 543 million and 145 million objects, respectively. The typical depths (in AB system) as estimated from the magnitude at S/N = 10 in the coadd images are $g = 24.0$, $r = 23.8$, $i = 23.1$, $z = 22.13$, and $Y = 20.7$ (Abbott et al., 2021).

For the purpose of our work, we matched the DES DR2 catalog to the VHS DR6, VIKING DR5 (Edge et al., 2013) and AllWISE catalogs using a positional matching radius of 2 arcsec, keeping only the best match, i.e, the nearest object found. The DES+VHS coverage area is around 4,500 deg^2. The VHS survey is imaged with exposure time per coadded image of 120–240 seconds in J and 120 seconds in K_s. There is also partial coverage in the H band with an exposure time of 120 seconds. The median 5σ point source depths is $J_{AB} \sim 21.4$, $H_{AB} \sim 20.7$ and $K_{s,AB} \sim 20.3$. Since, by design, the VIKING and VHS footprints are complementary, we decided to use also the VIKING DR5 data in regions not covered by VHS. The DES+VIKING coverage is about 500 deg^2, providing along with VHS, almost the entire DES footprint. VIKING has a median depths at 5σ of $J_{AB} \sim 22.1$, $H_{AB} \sim 21.5$ and $K_{s,AB} \sim 21.2$ across all imaged regions ($\sim$ 1350 deg^2). Lastly, for the AllWISE survey we will use only $W1$ and $W2$ bands, which is >95% complete for sources with $W1 < 17.1$ and $W2 < 15.7$ (in the Vega system).

Quality cuts were applied to the matched catalog, such as `IMAGFLAGS_ISO_i,z,Y` = 0 from DES DR2 and `J,H,K_{s}ppErrBits` < 255, to ensure that the object has not been affected by spurious events in the images in i, z, Y, J, H and K_s bands. We also imposed a magnitude limit cut of $z < 23$ (DES) and a simultaneous 5σ level detection in the i, z, Y (DES) and J (VHS+VIKING). We did not apply any standard star/galaxy separation because they are not as efficient for relatively nearby sources with significant signature of proper motions on their coadded DES images. In this work, we adopted the `PSF_MAG_i,z,Y` magnitude type from DES and `apermag3_J,H,Ks` from VHS and VIKING catalogs. Also, all DES magnitudes and colours are in the AB system and the VHS+VIKING and AllWISE magnitudes and colours are in the Vega system.

It is important to mention that for sources with significant proper motions, a matching radius of 2 arcsec may be too small. This matching radius will work except for the very nearby ($\leq$ 6pc) or high-velocity ($>$ 50 km/s) cases. Therefore, a small percentage of ultracool dwarfs will be missing from our catalogue due to this effect. The matching between DES data and other surveys provides a broad photometric

baseline, spanning from the optical to the infrared. All these bands will be later used to construct empirical templates, perform the colour selection and photometrically estimate the spectral type of our UCDs candidates.

2.1.2 Known ultracool dwarfs

The sample from Best & et al. (2020) (hereafter B2020 sample) contains the most up-to-date compilation of ultracool dwarfs with spectroscopic confirmation. The complete sample has 2,940 sources, with spectral types ranging from M3 to Y2. This compilation includes spectral types from the optical and NIR. When both are available for a source, the authors recommend using optical types for M and L dwarfs and NIR types for T dwarfs, given that these are the spectral domains of the dominant features required for spectral classification in each case. From this catalogue there are 388 sources located in the DES footprint, and 292 of them are classified as L or T dwarfs. For the construction of the templates, we excluded objects flagged in the B2020 sample as unresolved binaries and sub-dwarfs. We first matched the B2020 sample of L and T dwarfs with the DES DR2 catalog and found 227 objects in common. Since we have a small number of objects between the B2020 sample and DES, we decided to adopt only in this step a positional match of 3 arcsec. Every matched source was inspected visually using the DES image portal tool. The remaining 65 objects were eliminated in our selection due to quality cuts or for having a positional match beyond the limit. Then we matched B2020+DES DR2 with VHS DR6 and VIKING DR5 resulting in 185 objects in common. The 42 lost objects in the match between DES and VHS+VIKING are due to lack of data or positional match beyond 2 arcsec or the VHS+VIKING quality flag applied. Finally, we matched all the B2020 sample with a combination of VHS+VIKING+AllWISE, regardless of DES data, and we end up with 658 objects. We take these three steps in order to obtain as many objects as possible to construct our colour templates. In comparison with the sample of known ultracool dwarfs in Carnero Rosell et al. (2019), there are more 19 objects with DES magnitudes, 81 more in DES+VHS+VIKING and 530 more in VHS+VIKING+AllWISE. Here, the difference between the samples with and without DES data is due to the limited area of the south where the DES footprint is located. The combination of VHS+VIKING+AllWISE covers almost the entire southern hemisphere.

2.1.3 Known contaminants

There are two main types of sources that we consider as contaminants at this stage: M dwarfs and quasars at high redshift. In Carnero Rosell et al. (2019) we used a sample of 70,841 visually inspected M dwarfs from West et al. (2011). Here we use the Kiman et al. (2019) compilation of spectroscopic confirmed 73,473 M and 743 L or later dwarfs from SDSS constructed from West et al. (2011), Schmidt et al. (2015) and Schmidt et al. (2019). The match between Kiman et al. (2019) and DES DR2, VHS DR6 and AllWISE data resulted in 19,355 objects in common. This updated M dwarfs sample, with new DES photometry, is fundamental for the update of our colour templates, used in the classification scheme. Regarding the quasars, we are now using the quasar catalogue from SDSS DR16 presented by Lyke et al. (2020). For this latter, we only kept objects with redshift $z > 4$. The reason is that the low-z quasars have much bluer colors than the UCDs and therefore are not relevant to our contamination analysis.

2.2 Templates and color selection

We updated our empirical colour templates using the samples of known M, L and T dwarfs described previously. The construction of the templates followed the same methodology described in Carnero Rosell et al. (2019). For the M dwarfs (M0 to M9), we used the median color for each spectral type as the template value. We demanded SNR $> 5\sigma$ in all bands and excluded objects that were > 2 σ from the median. The median was then recalculated after these outliers were removed in an interative process until convergence. For the L and T dwarfs, because of the smaller number of objects, we fit a n order polynomial to each colour vs. spectral type relation, using the least squares method. For (i-z), (J-K_s), (H-K_s) and (K_s-$W1$) an order 4 polynomial was used; (Y-J) and ($W1$-$W2$) an order 3 and (z-Y) an order 2 polynomial were used.

We re-estimated the intrinsic scatter for each colour index, assuming it to be the same for all spectral types. This intrinsic scatter is the spread in colour due to variations in metallicity, surface gravity, cloud cover, and also the uncertainty in the spectral classification. The procedure to estimate this intrinsic scatter followed the Skrzypek et al. (2015) prescription. We initially adopted a first guess of intrinsic scatter as 0.5 mag and added it in quadrature to the photometric errors to all templates. This new uncertainty was used to weight the points in the polynomial regression to the colour vs. spectral type relation. Then, we re-estimated the intrinsic

Table 2.1: Updated template colors of M0–T9 dwarfs.

SpT	i-z	z-Y	Y-J	J-H	H-Ks	Ks-W1	W1-W2
M0	0.28	0.08	1.12	0.59	0.17	0.09	0.01
M1	0.35	0.10	1.14	0.57	0.20	0.12	0.05
M2	0.42	0.12	1.17	0.55	0.22	0.13	0.09
M3	0.50	0.14	1.20	0.53	0.23	0.15	0.13
M4	0.58	0.16	1.23	0.52	0.25	0.17	0.15
M5	0.67	0.19	1.27	0.51	0.27	0.18	0.18
M6	0.81	0.24	1.34	0.51	0.30	0.20	0.19
M7	0.98	0.30	1.42	0.52	0.34	0.22	0.20
M8	1.18	0.37	1.53	0.54	0.37	0.23	0.19
M9	1.37	0.44	1.63	0.57	0.42	0.26	0.23
L0	1.53	0.55	1.92	0.63	0.49	0.40	0.32
L1	1.53	0.54	2.05	0.63	0.52	0.41	0.31
L2	1.54	0.54	2.15	0.68	0.56	0.47	0.31
L3	1.56	0.55	2.23	0.76	0.60	0.56	0.32
L4	1.61	0.56	2.27	0.84	0.64	0.66	0.33
L5	1.68	0.58	2.30	0.92	0.66	0.74	0.35
L6	1.78	0.60	2.32	0.97	0.67	0.81	0.38
L7	1.92	0.63	2.32	0.99	0.65	0.85	0.43
L8	2.08	0.66	2.31	0.97	0.62	0.86	0.49
L9	2.26	0.69	2.30	0.91	0.57	0.83	0.57
T0	2.46	0.74	2.29	0.80	0.50	0.78	0.68
T1	2.68	0.78	2.29	0.66	0.42	0.70	0.81
T2	2.89	0.84	2.30	0.49	0.33	0.60	0.96
T3	3.09	0.90	2.32	0.30	0.24	0.51	1.15
T4	3.26	0.96	2.36	0.09	0.15	0.42	1.36
T5	3.39	1.03	2.42	-0.09	0.07	0.38	1.61
T6	3.46	1.10	2.51	-0.25	0.02	0.40	1.90
T7	3.45	1.18	2.62	-0.36	0.01	0.50	2.22
T8	3.33	1.26	2.78	-0.39	0.04	0.72	2.59
T9	3.08	1.35	2.97	-0.30	0.15	1.10	3.00

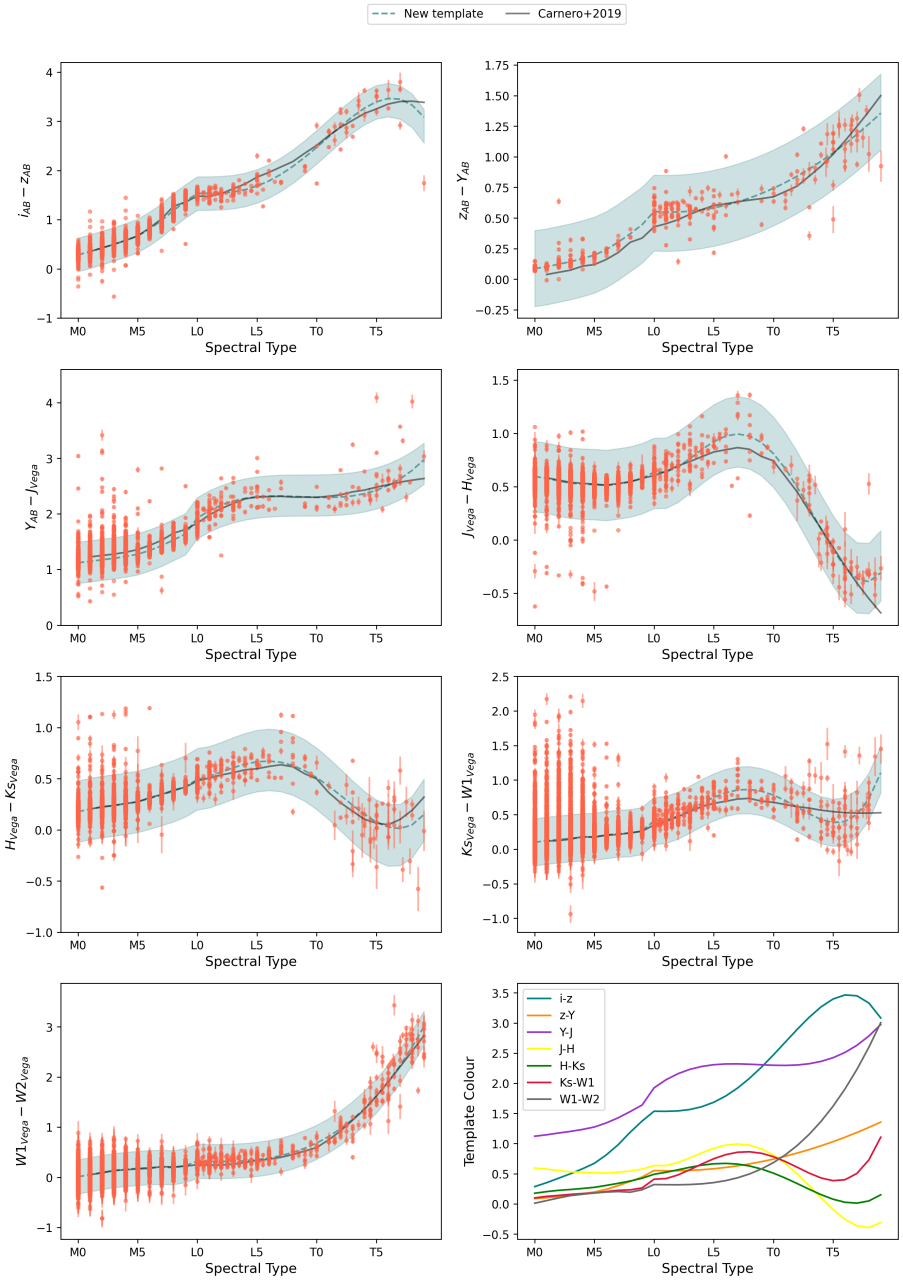

Figure 2.1: Colors as a function of the spectral type for the enlarged sample of known UCDs as described in the text. The dashed line indicates the new templates, as discussed previously in Section 2.2, and the solid line refers to the templates presented in Carnero Rosell et al. (2019). The light-shaded area corresponds to the intrinsic scatter of each color. The last panel shows all the new updated templates for each color indices used in this work.

scatter as the variance of the best-fit residuals with the rms value of the photometric errors subtracted in quadrature from it. This new value was taken as our intrinsic scatter for that colour index, irrespective of spectral type. Finally, we re-fitted the polynomial for L and T dwarfs, using the new intrinsic scatter. The intrinsic scatter values found with this method are the following: $\sigma_{i-z} = 0.34, \sigma_{z-Y} = 0.30, \sigma_{Y-J} = 0.37, \sigma_{J-H} = 0.32, \sigma_{H-Ks} = 0.30, \sigma_{Ks-W1} = 0.33, \sigma_{W1-W2} = 0.34$. These values are slightly smaller than those presented by Dupuy & Liu (2012) but more aligned with those presented recently in Kirkpatrick et al. (2021b). Even though there might be a systematic increase with spectral type, we will adopt a single value of 0.2 mag for each magnitude, corresponding to 0.3 mag for each colour index. These will later be used to perform the spectral classification of our target sample.

The templates for the several colour indices as a function of the spectral type are shown in Figure 2.1. Also shown are the templates presented in Carnero Rosell et al. (2019). In comparison to our previous templates, there are no significant changes for the M and L dwarfs. For the T dwarfs, specially for late types, color indices have changed typically by 0.1-0.2 mag, up to $\simeq 0.5$ mag in a couple of cases for T7 or later. This may be due to the clear increase in the number of objects that now contribute to the updated fit. The redder $J - H$ and $H - Ks$ colours around L4 and T0 types are a known trend caused by the effect of condensate clouds and the variability in the clouds properties. Also, there is a blueward trend from T2 to T7 types in $J - H$, $H - Ks$ and $Ks - W1$ due to the loss of the cloud decks and the onset of CH_4 absorption. However, this trend diminishes for the latest types as very little flux remains to be absorbed by CH_4 (Leggett et al., 2010). The scatter for the later T types in $H - Ks$ and $Ks - W1$ is due to the variations in metallicity and gravity. The template colours are shown in Table 2.1.

For the color selection of the UCDs, we follow the same methodology presented in Carnero Rosell et al. (2019). We analyze several color-color diagrams considering the UCDs and the contaminants samples presented earlier. The colour selection is meant to yield a sample of UCDs sources as complete as possible, at the expense of allowing some contamination by late-M dwarfs and extragalactic sources. The purity of our sample will be later improved using the photo-type classification (see section 2.3). We applied an optical band cut $(i - z) > 1.20$, in order to remove the quasars, and also $(z - Y) > 0.15$ and $(Y - J) > 1.55$ to remove M dwarfs and other contamination sources. Figure 2.2 shows the colour-colour diagrams where the colour selection was applied for known contaminants, M dwarfs and UCDs sources. Applying the color selection discussed above, the initial sample has 164,406 sources

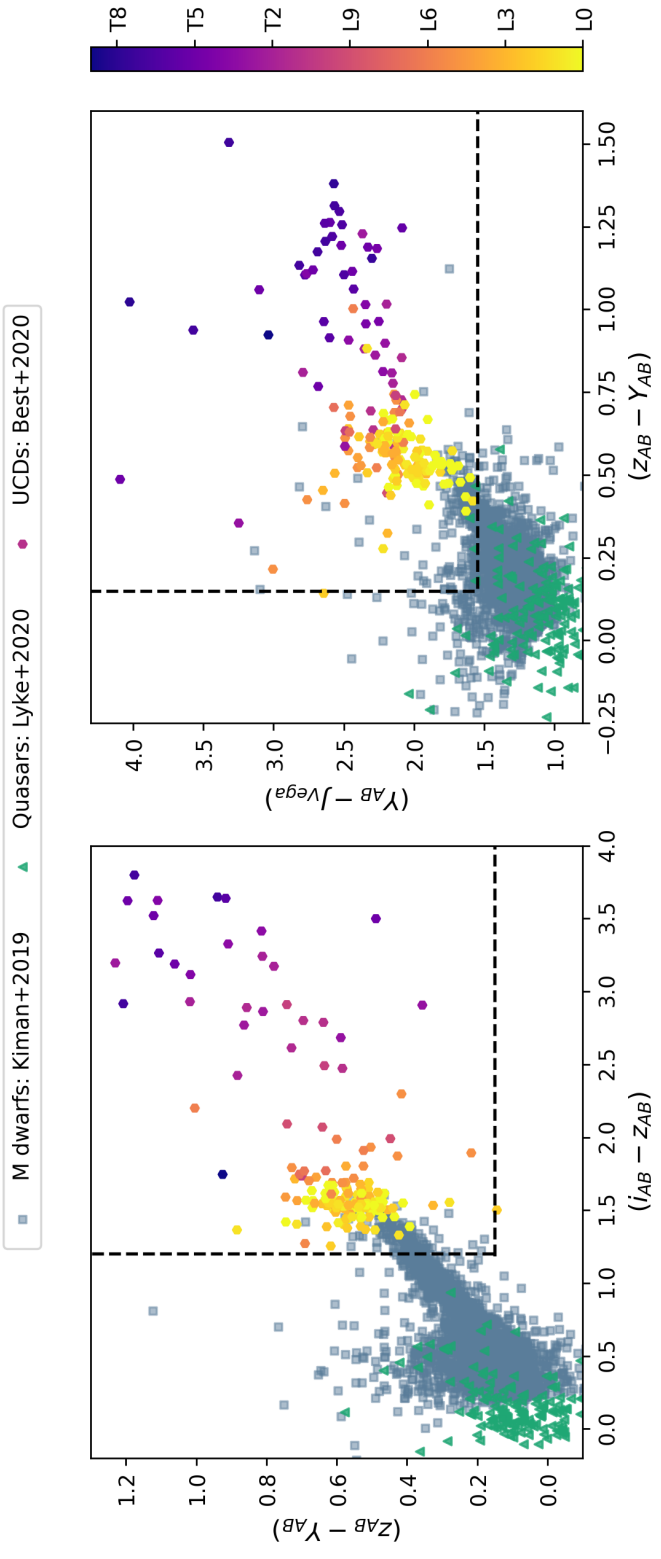

Figure 2.2: Color-color diagrams for the M dwarfs (Kiman et al., 2019) (blue squares), L and T dwarfs (Best & et al., 2020), shown as circles, and quasars with z $>$ 4 (Lyke et al., 2020) (green triangles). The color code represents objects with spectral type L0 and later. The black lines indicate the color selection.

in DES+VHS+VIKING data. Among these, 76,184 objects have AllWISE W1 and W2 bands. The next step is to infer a photo-type for each object in the target sample.

2.3 Photo-type classification

To infer a spectral type for objects in the target sample, we also closely follow the procedure described by Carnero Rosell et al. (2019), originally from Skrzypek et al. (2015). The spectral type will be assigned by the minimization of the χ^2 relative to our new empirical templates presented in Table 2.1. Only objects that have measurements in a minimum of N_{bands}= 6 bands (thus yielding 5 color indices) are considered as having a reliable photo-type. We applied this minimum of six bands because we have observed a substantial improvement in photo-type determination with the number of filters available. The χ^2 for the k-th source and the j-th spectral type is

$$\chi^2(\{m_b\},\{\sigma_b\},\hat{m}_{z,k,j},\{c_b\}) = \sum_{b=1}^{N_{bands}} \left(\frac{m_{b,k} - \hat{m}_{z,k,j} - c_{b,j}}{\sigma_{b,k}}\right)^2 \tag{2.1}$$

where $m_{b,k}$ are the measured magnitudes for the source in all available filters, and $c_{b,j}$ are the template colors for the j-th spectral type and for the same bands. These latter are measured for all templates with respect to a reference band (in our case, the z band). The $\sigma_{b,k}$ are the k-th source's photometric errors added in quadrature to the intrinsic scatter (from Section 2.2). As for $\hat{m}_{z,k,j}$ in equation 2.1, it is the inverse variance weighted estimate of the reference magnitude, computed using all the source's magnitudes, their associated uncertainties and the given template colors for the j-th type, as follows

$$\hat{m}_{z,k,j} = \frac{\sum_{b=1}^{N_{bands}} \frac{m_{b,k}-c_{b,j}}{\sigma^2_{b,k}}}{\sum_{b=1}^{N_{bands}} \frac{1}{\sigma^2_{b,k}}} \tag{2.2}$$

2.3.1 Comparison with the literature

Figure 2.3 shows the comparison between the spectral type from the literature and the photo-type method applied to the B2020 sample. As mentioned earlier, only objects with six or more valid magnitudes are shown. Only one object has a misclassification bigger than four spectral types: ULAS J223347+002214. However, this

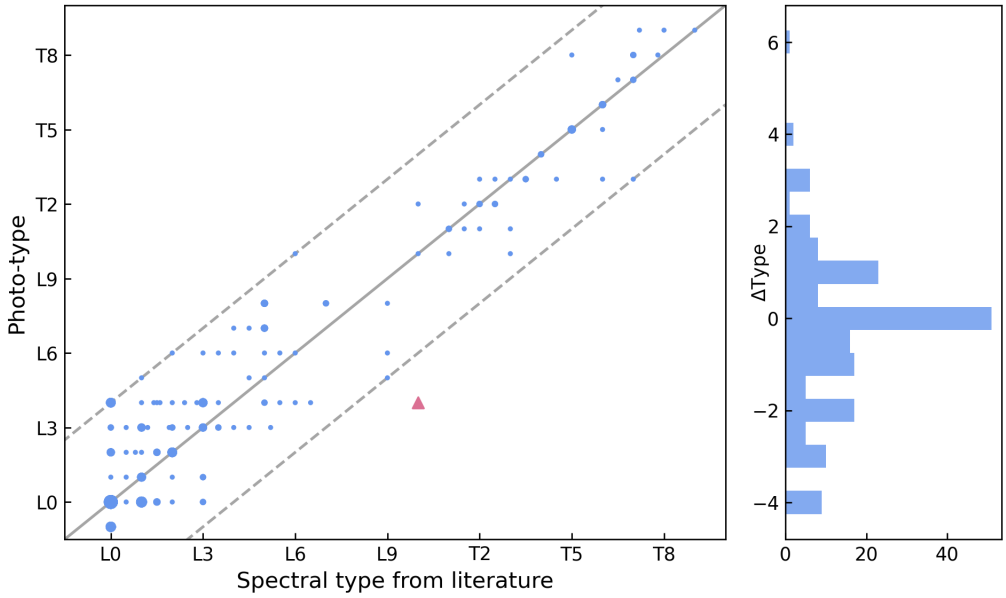

Figure 2.3: Spectral classification from the B2020 compilation versus our photo-type classification. The dashed lines represent misclassification by four spectral types. The size of the circles scales as the cube of the number of repeated points. The histogram on the right shows the differences between the spectral types from the literature and our photo-types (ΔType).

object is known as a strong binary candidate (Day-Jones et al., 2013). The accuracy[1] for the B2020 sample is $\sigma_L = 1.7$ and $\sigma_T = 1.1$ for L and T dwarfs, respectively. These values can be considered as an upper limit to the uncertainty in the assigned type. These values are compatible with those obtained by Carnero Rosell et al. (2019) and Skrzypek et al. (2015). After testing the classification code, we obtain a photo-type for each object in our target sample. We used both DES+VHS+VIKING and DES+VHS+VIKING+AllWISE catalogs to estimate a photo-type. Our target sample now has 53,565 objects with photo-type $\geq$ L0 and six or more bands.

Besides B2020, we also expect to recover in our target sample other UCDs candidates from the literature that are located in the DES footprint. As explained before, the colour selection was made considering objects that have spectroscopic confirmation, but these are currently limited in number. We thus benefit from assessing our sample selection by cross-matching our candidates to other sizeable samples of candidate sources, not only because of the increased numbers but also because this allows a direct comparison of different photo-types.

From the 1,361 objects presented by Skrzypek et al. (2016), 154 are located in

[1] $\sigma = \frac{\sum_{j=1}^{N} |\Delta Sp.T|}{N} \frac{\sqrt{2\pi}}{2}$

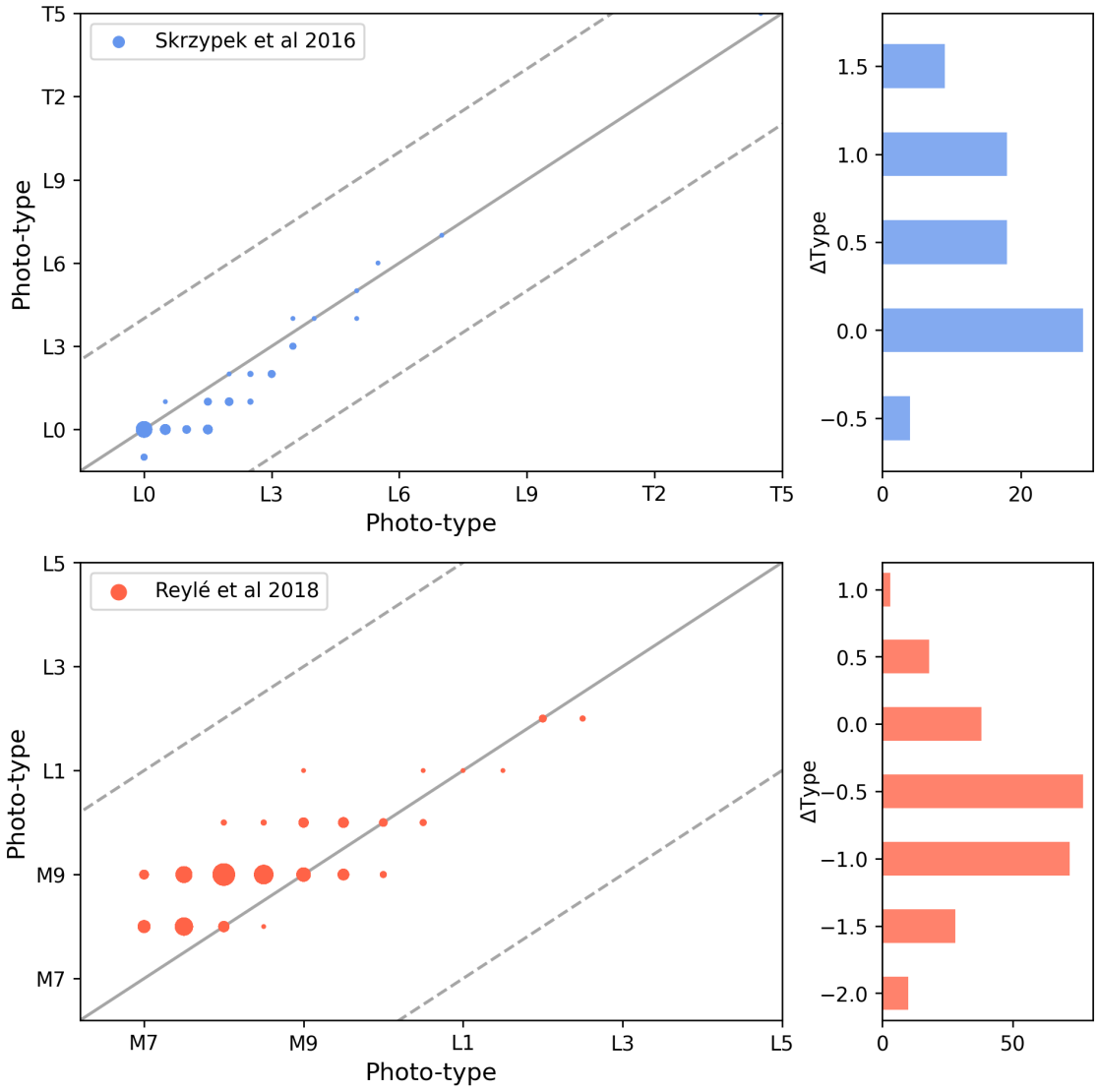

Figure 2.4: Photo-type classification from Skrzypek et al. (2016) and Reylé (2018) (x axis) and our photo-type classification (y axis). The dashed lines represent misclassification by four spectral types. The histogram on the right shows the differences between the photo-types from the literature and our photo-types (ΔType).

the DES footprint and 78 of them are present in our target sample. The missing 76 sources are due to three main reasons: i) a few objects are eliminated due to the colour selection and quality cuts applied to the DES data; ii) some are eliminated due to separation beyond 2 arcsec match radius; iii) the main reason, however, is that most of them are eliminated because of our demand on availability of VHS+VIKING data.

Reylé (2018) presented a sample of 14,915 ≥M7 and L candidates from the Gaia DR2 data, of which 2,224 are located in the DES footprint. However, only 40 of them are L dwarfs candidates and the remaining objects are M dwarfs. We end up with 248 of their objects in our target sample, 20 of which are L candidates and the remaining are M dwarfs (78 M7/M7.5, 102 M8/M8.5 and 48 M9/M9.5). The missing 20 L dwarfs were eliminated by either one of the reasons we mention above. The reduced number of M dwarfs in our sample is due to the color cuts imposed, as described in Section 2.2. Figure 2.4 shows the comparison between the photo-types estimated from our classification code and those from these two other samples of UCD candidates. The median photo-type difference is of 0.5 for both Skrzypek et al. (2016) and Reylé (2018) for objects with $z < 19$. For fainter magnitudes we can only compare to Skrzypek et al. (2016) sample as Reylé (2018) is limited in $z < 19$ in our DES sample. For $19 < z < 21$ the median discrepancy is also 0.5.

2.4 Towards the final sample: Target Validation

2.4.1 Extragalactic contamination

As in Carnero Rosell et al. (2019), we removed possible extragalactic contamination by running the `Lephare` photo-z code (Arnouts et al., 1999, Ilbert et al., 2006) on the target sample using both a galaxy and quasar templates. We considered as extragalactic all sources that satisfied the following condition: $\chi^2_{Lephare} < \chi^2_{classif}$, where $\chi^2_{Lephare}$ and $\chi^2_{classif}$ are the best fit χ^2 values from `Lephare` and from our photo-type code, respectively.

From the 164,406 objects presented in our initial sample, only 53,565 have six or more bands and have a photo-type L0 and later. From this catalog of 53,565 L and T candidates, 34,116 were flagged as an extragalatic sources by `Lephare`. Therefore, our final L and T dwarf candidate sample is constituted by a total of 19,449 objects. We also matched the 53,565 L and T dwarf candidates to SIMBAD (Wenger et al., 2000) astronomical database in order to verify if the results provided by `Lephare`

were in agreement with the literature. We found 327 objects in common, using a matching radius of 2 arcsec. From this list, only 63 were extragalactic sources and `Lephare` was able to discard 56. The 7 objects that remained in the sample were discarded. As discussed in Carnero Rosell et al. (2019), a residual contamination by extragalactic sources is estimated to be $\sim 5\%$.

We also tested running `Lephare` in the B2020 sample to verify the effect of the code on a pure UCD sample and only one object was flagged as an extragalactic: ULAS J222711-004547. ULAS J222711-004547 is known in the literature as a peculiar L dwarf. Since one ultracool dwarf was flagged as extragalatic by `Lephare` we decided to further investigate the 34,116 sources that were flagged as extragalatic sources using their proper motion information. In the next section we will discuss the details.

2.4.2 Proper motion

In addition to `Lephare`, we used available proper motion catalogs in order to assess the Galactic or extragalactic nature of our candidate L and T dwarfs. If the source has a proper motion significantly different from zero, it is likely a Galactic one. We decided to use the proper motions from Gaia DR3 (Gaia Collaboration, Vallenari et al., 2022), the CatWISE2020 catalog (Marocco et al., 2021) and the NOIRLab Source Catalog (NSC) DR2 (Nidever et al., 2021). In particular, these last two catalogues extend towards faint enough magnitudes to cover a significant fraction (96%) of our target sample of 53,565. These catalogs are responsible for several new discoveries, such as extreme T/Y subdwarfs (Kirkpatrick et al., 2021a, Meisner et al., 2021), new ultracool dwarfs members of the Solar Neighbourhood (Kota et al., 2022) and new wide binary systems (Softich et al., 2022, Kiwy et al., 2022). It is important to mention that in our sample of 53,565 L and T candidates, only 320 sources have Gaia DR3 proper motion measurements (this includes objects with RUWE < 1.4 that ensures a good astrometric solution).

We apply $\sigma_\mu/\mu < 0.5$ for all catalogs as a criterion for them to be considered Galactic sources. In the case of NSC, for some objects with large proper motion errors, $\sigma_\mu > 1{,}000$ mas yr^{-1}, we felt the need to apply a more stringent selection criterion, $\sigma_\mu/\mu < 0.1$. Considering objects with Gaia DR3 proper motion measurements, for instance, only 12 out of the 320 sources are classified as an extragalactic source by `Lephare`. However, 11 of them have proper motion from Gaia DR3 that satisfy our criteria. For the remaining objects flagged as extragalactic, 25,039 have proper motion measurements from CatWISE and NSC catalogs. In this case, 130

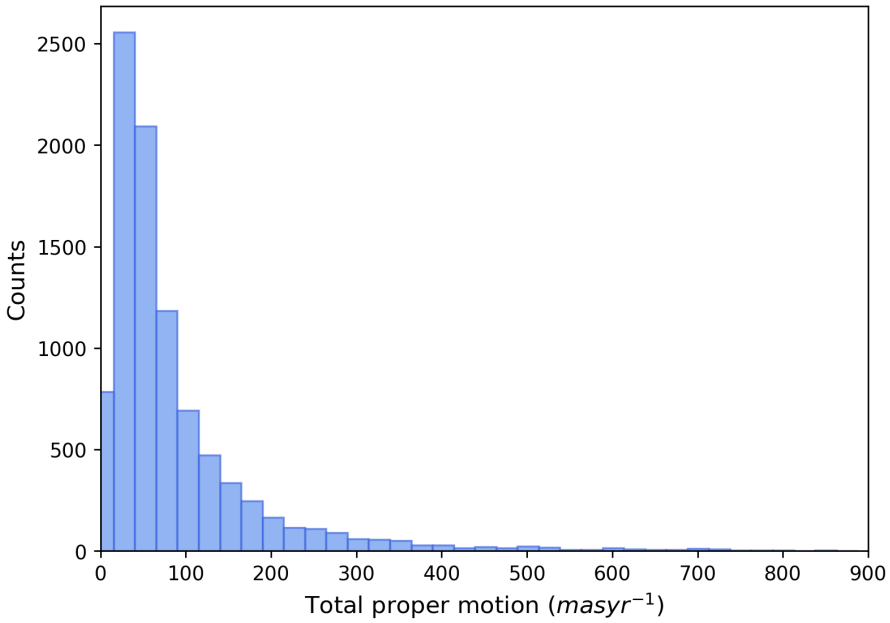

Figure 2.5: Distribution of total proper motions for ultracool dwarf candidates in our sample. We only show here objects with well-measured proper motion according to our criteria presented in Section 2.4.2.

satisfies the criteria presented above. In total, 141 objects return to the L and T candidates sample. We conclude that proper motion data in conjunction with our adopted criteria do serve as a means to recover Galactic sources mistakenly classified as extragalactic by other means. Therefore, we have now 19,583 L and T dwarf candidates in the final sample. Figure 2.5 shows the distribution of total proper motion ($\mu_{tot} = \sqrt{\mu^2_{\alpha cos\delta} + \mu^2_{\delta}}$) for the objects that satisfy the condition $\sigma_{\mu}/\mu < 0.5$ at least in one catalog (Gaia DR3, CatWISE2020 or NSC DR2). This sample has 9,278 objects.

2.4.3 Comparison with our previous work

From the objects presented in Carnero Rosell et al. (2019), 10,440 L and T dwarfs are present in the initial 164,406 sample of this paper (see Table **??**). The missing objects are due to a combination of slight changes in the DES footprint, the quality selection made in the target sample, changes in flags and photometric error criteria, and of lack of data in VHS+VIKING catalogs.

Imposing that the target must have six or more bands, something that was not applied in the past work, we end up with 8,512 in common. However, 5,342 objects

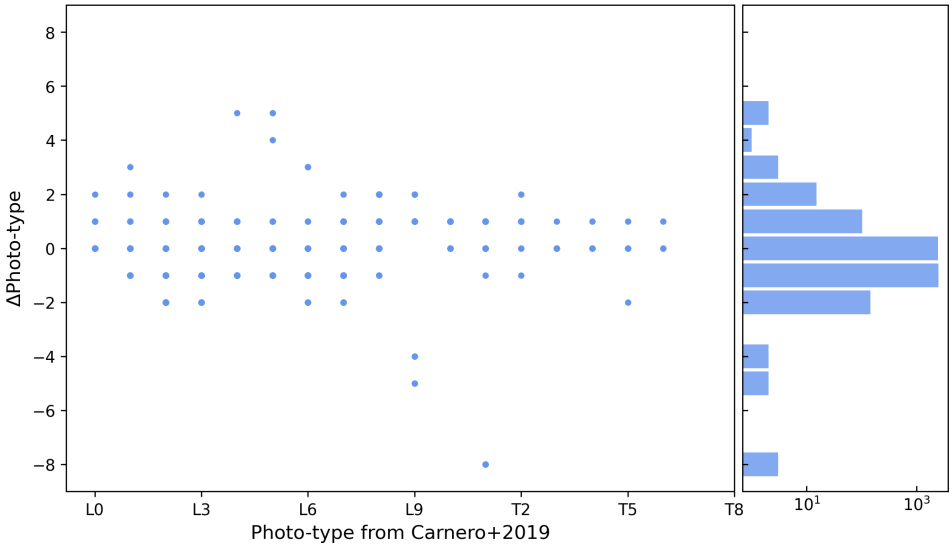

Figure 2.6: Photo-type comparison between our new classification and the results from Carnero Rosell et al. (2019) (ΔType). The histogram in the right shows that the vast majority of the objects have a difference of one spectral type, most now being classified as a slightly earlier type.

are now classified as L or later. The remaining 3,170 are now classified as M9. This large migration across the M9/L0 border is expected due to the larger intrinsic scatter adopted here when compared to the previous work, as explained in Section 2.2. Besides, we used the GalmodBD simulation code (Carnero Rosell et al., 2019) to estimate the reverse effect, namely the contamination of M dwarfs to this new sample (more details about GalmodBD in Chapter 3). We expect that $\sim$ 30% of our sample is made up of late M dwarfs, the vast majority of them of M9 type. This is again somewhat larger than the 15-20% estimated in our previous work. We should emphasize, however, that that this contamination is from sources of a very similar nature to our target L dwarfs. From the 5,342 L and T dwarfs still present on our sample, 24 were flagged as an extragalactic source either by `Lephare` or were listed in SIMBAD database. However, two flagged by `Lephare` have a proper motion measurement that satisfied our criteria. Therefore, in the end, 5,320 original L and T dwarfs from Carnero Rosell et al. (2019) remain in the new sample presented here, while most of the missing ones are now classified as late M type. Figure 2.6 shows the comparison between the photo-types from the previous work and those of the new candidate sample for objects in common.

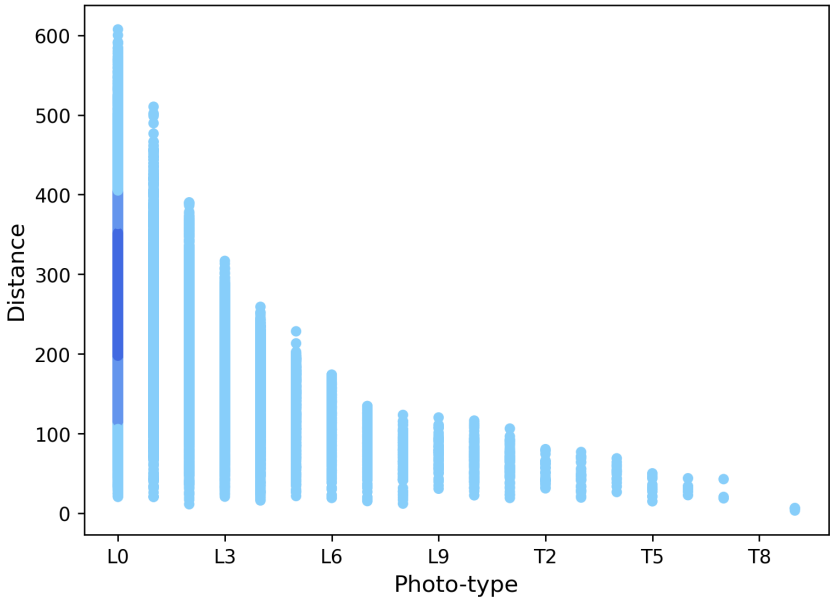

Figure 2.7: Distances as a function of photo-type. Distances have been calculated using the average value from the distance modulus obtained using all available bands. The color scale represents the density. Most ultracool dwarf candidates are early L at distances smaller than 650 parsecs.

2.4.4 New ultracool dwarf candidates

In total, 19,583 objects remain in our candidate sample, following all the criteria presented earlier. However, from this sample, 142 are included in B2020, 5,257 additional ones were presented in Carnero Rosell et al. (2019), 26 from Reylé (2018), 5 from Skrzypek et al. (2016) and 54 from SIMBAD (mostly late-M dwarfs from other references, hence surveys, than those used here). There are 14,099 new UCD candidates [2].

Figure 2.7 shows the photo-type distribution vs photometric distance of the candidate sample of UCDs from this work. The final sample has only objects with six or more bands (used to estimate the photo-type), $\chi^2_{classif} < \chi^2_{Lephare}$ (or otherwise total proper motion significantly different from zero, if available) and a photo-type $\geq$L0. Here we see that this new sample is probing larger distances than those presented in Carnero Rosell et al. (2019). We now reach over 600 pc, while in our previous work we reached $\sim$ 480 pc.

We estimate photometric distances for our candidates following the same pro-

[2]The table containing the ultracool dwarf candidates is available at: `https://des.ncsa.illinois.edu/releases/other/Y6-LTdwarfs`

cedure explained in Carnero Rosell et al. (2019). We first calculate the absolute magnitudes for the UCD templates discussed in the previous chapter for all photometric bands and spectral types. We do that by using the template colours shown in Table 2.1 and anchoring the absolute magnitude scale to the M_{W2} values presented by Dupuy & Liu (2012). The distance for each UCD candidate in our sample is then determined from all its available apparent magnitudes and the template absolute magnitudes corresponding to its assigned spectral type. The mean distance over all available bands is assigned as the UCD distance. The distance uncertainty is obtained considering the photometric errors added in quadrature with the intrinsic scatter for each available band. We did not apply any correction for extinction, since this is expected to be small for the passbands we used and towards the relatively high Galactic latitudes covered by our sample.

We checked our photometric distances comparing with those presented in B2020, which comprehends several parallax and photometric measurements from the literature, as shown in Figure 2.8. Our photometric distances tend to be slightly underestimated relative to those from B2020. This effect results from a tendency of assigning later types for the objects. Comparing our distance estimates and those from B2020 that have trigonometric parallax distances, the typical error in our photometric distances is $\sim 28\%$. Also, the systematic offset seen in the Figure, in the sense of our distances being underestimated, is 18% when we considered all objects from B2020, independent of the distance measurement method.

2.5 Spectroscopic confirmation of twelve ultracool dwarfs

We undertook a spectroscopic project to further assess our UCDs search and classification methods. We got $\sim$ 22 hours of Gemini/GMOS time to obtain spectra for a small fraction of our UCD candidates, twelve objects in total. The target sample for the spectrocopic follow up was taken from Carnero Rosell et al. (2019), limited to $z_{AB} = 22$. The Carnero Rosell et al. (2019) sample was used to search for wide binary systems composed of an UCD+UCD and UCD+star. The search for binary systems was performed based on sky position and projected distance. All details are described in the next chapter. Therefore, the spectroscopic sample prioritized these UCDs likely to be part of candidate wide binaries. The purpose is to confirm their nature, i.e. confront spectral type with our photo-type method and also re-calculate the distances. We also demanded the pair members to have a difference in distance

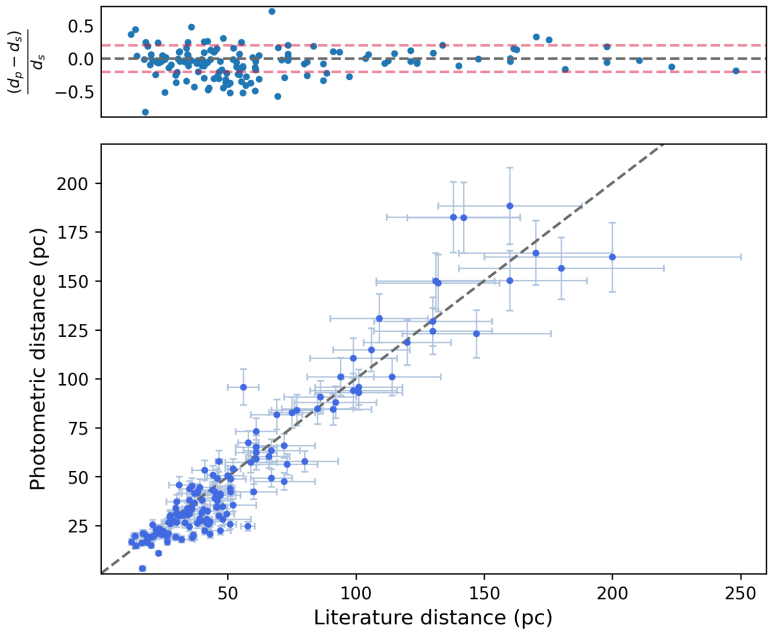

Figure 2.8: Comparison between our photometric distances (d_p) and distances from the B2020 compilation (d_s), which has a mixture of trigonometric parallaxes and photometric distances. Our photometric distances tend to be slightly underestimated compared to those presented in B2020.

modulus that was within 1.5 (1.0) from the typical expected difference given their uncertainties. Finally, we avoided the largest physical separation pairs to reach the final target sample. Our targets have magnitudes within the range $19 < z_{DES} < 21.5$ as shown in Table 2.3. The preference was given for binary systems composed of two L dwarfs because this type of system is rare. More details about this discussion will be found in Chapter 3.

2.5.1 GMOS observation and data reduction

The selected UCDs were observed using the 8-m Gemini-South telescope with the Gemini Multi-Object Spectrograph (GMOS, Hook et al., 2004). The observations were carried out through the months of September to December 2019 as part of the programs GS-2019B-Q-230 (band 2) and GS-2019B-Q-312 (band 3). We used GMOS with the R150 grating and the OG515 blocking filter to deliver a R∼600 resolution, across the 7000-10000 Å range. For all targets, three spectra, centered at 7900, 8000, 8100 Å at z' filter were taken for each source, to cover the small gaps between the three GMOS detectors, and a focal plane unit of 1 arcsec was selected. We binned both in spatial and spectral direction to 4x4 pixels to increase

Table 2.2: Observation log of the selected ultracool dwarfs. The central wavelength is in Å and the exposure time in minutes.

Name	Obs. Date	Airmass	λ	Exp. Time
	GS-2019B-Q-230			
UCD 10	2019/09/30	1.35	7900	30.0
	2019/10/07	1.37	7900	30.0
	2019/10/07	1.28	8000	45.0
	2019/10/07	1.22	8100	42.0
UCD 1	2019/10/07	1.16	7900	30.0
	2019/10/07	1.25	8000	68.8
	2019/10/07	1.25	8100	42.0
UCD 3	2019/11/30	1.06	7900	30.0
	2019/11/30	1.07	8000	45.0
	2019/11/30	1.12	8100	42.0
UCD 11	2019/12/01	1.36	7900	26.6
	2019/12/01	1.50	8000	30.0
	2019/12/01	1.73	8100	40.0

Name	Obs. Date	Airmass	λ	Exp. Time
	GS-2019B-Q-230			
UCD 36	2019/09/04	1.36	7900	60.0
	2019/09/04	1.21	8000	60.0
	2019/09/04	1.16	8100	45.0
UCD 8	2019/09/22	1.38	7900	30.0
	2019/09/28	1.33	8000	30.0
	2019/09/28	1.25	8100	30.0
UCD 6	2019/09/30	1.17	7900	60.0
	2019/09/30	1.12	8000	22.16
	2019/10/06	1.22	8000	30.0
	2019/10/08	1.26	8100	45.0
UCD 12	2019/10/06	1.13	7900	60.0
	2019/11/20	1.13	8000	15.0
	2019/11/21	1.11	8000	45.0
	2019/11/21	1.11	8100	45.0

our signal-to-noise ratio. For every change in central wavelength, a flat and a CuAr frame was taken immediately following the science exposure. Table 2.2 shows the observation log for all the objects observed with GMOS. The individual spectra for the same source were rebinned preserving flux and combined into a single coadded spectrum using standard routines. The typical signal-to-noise (SNR) per pixel for the coadded spectra is ~ 6.

The objects UCD 1, UCD 3, UCD 10 and UCD 8 are binary candidates presented previously in dal Ponte et al. (2020) as composed by two L dwarfs. As an observation strategy, we place both objects (L dwarfs) of each system on a single long-slit to obtain two spectra at the same time. The data reduction was carried out using the standard GMOS pipeline contained in the GEMINI `IRAF/PyRAF` package. We followed the standard procedure: 1) the bias was subtracted and we applied the flat-field correction in all data; 2) the wavelength calibration was constructed using a 4th order polynomial wavelength solution for the CuAr arc lamp; 3) for the final bi-dimensional combined spectra, we applied the wavelength calibration; 4) the uni-dimensional spectra for each target were extracted using the APALL pipeline; 5) we combined the uni-dimensional spectra for the individual targets. The final spectra have not being flux calibrated and corrected for telluric absorption.

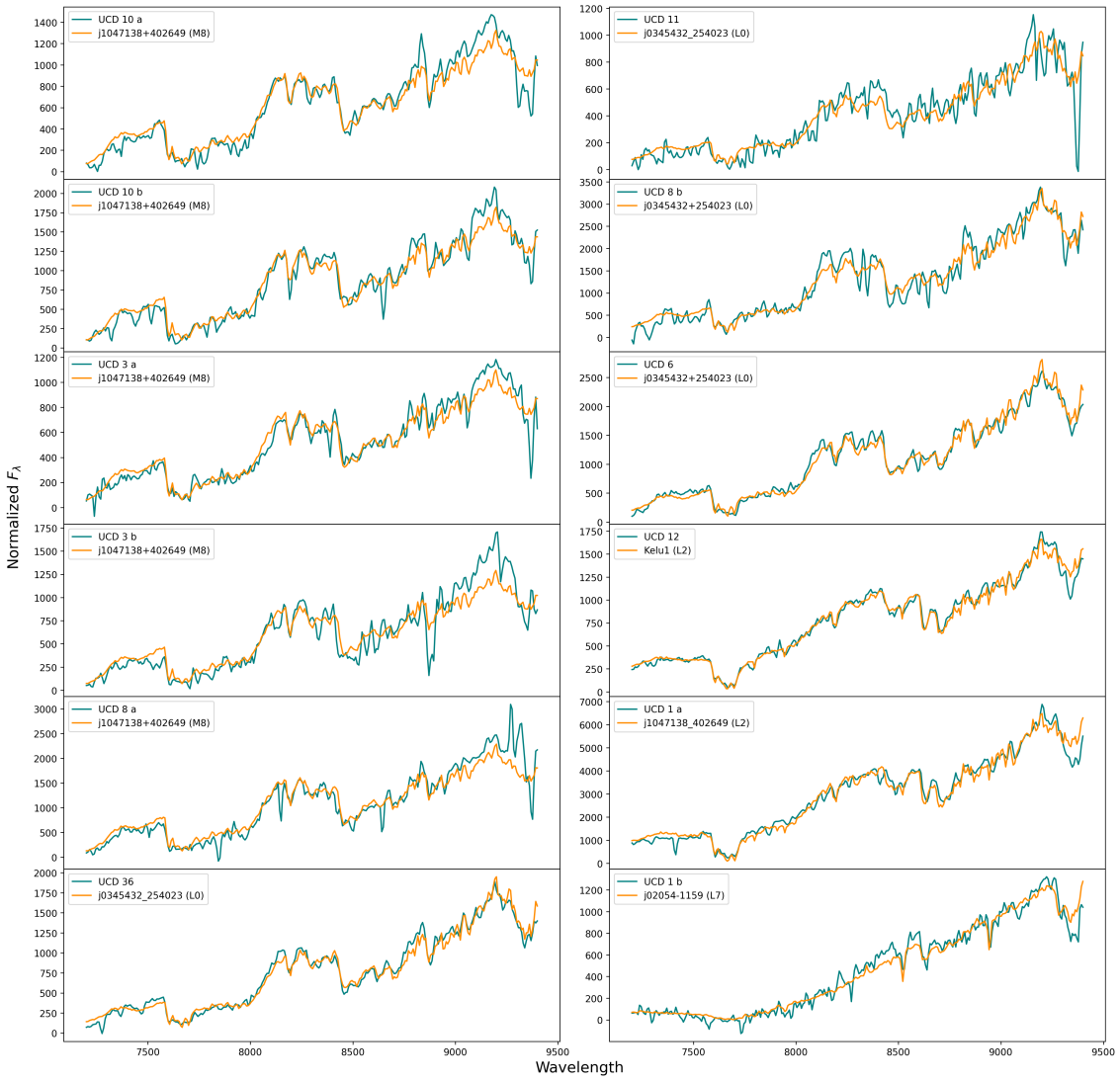

Figure 2.9: UCD spectra (blue) and the best fitting template (orange), ordered right ascension. The fluxes shown are relative F_λ in arbitrary units. The flux of the templates was multiplied by a normalization factor prior to the fit, as explained previously. The individual members of the wide binary candidates are identified by a,b labels.

2.5.2 Ultracool dwarfs spectral types

To determine the spectral type for our UCDs we use a simple χ^2 minimization relative to templates taken from Kirkpatrick et al. (1999). The templates were smoothed down and rebinned to match our resolution and wavelength range of 7200-9400 Å. We also visually inspected the five best-fitting templates to check the accuracy of the fit. For the instrumental fluxes, we attributed a Poisson fluctuation in the detector counts for every λ. We also multiplied the templates by a normalization factor before comparing them to each UCD spectrum. This normalization factor is given by

$$N = \frac{\int_{\lambda_1}^{\lambda_2} Flux_{spectra}}{\int_{\lambda_1}^{\lambda_2} Flux_{template}} \tag{2.3}$$

where the integrals in the numerator and denominator are over the instrumental fluxes of GMOS and template spectra respectively, within the spectral range of our analysis ($\lambda = 7200 - 9400$ Å).

Figure 2.9 shows the spectra and the lowest χ^2 template, along with the best match spectral type. Table 2.3 shows the photo-type estimated in Carnero Rosell et al. (2019) and the new photo type estimation as presented earlier. The photo-type previously estimated has a typical uncertainty of one or two types due to the method adopted. As discussed previously, to obtain photometric distances we compared the photo-type with our empirical model grid to estimate the absolute magnitude and then obtained the distance modulus for each object. Now, with the use of the spectral type, new distances were estimated and are shown in the last column of Table. The differences between the photometric distances presented in Carnero Rosell et al. (2019) and those calculated here using the spectral type are due to the updated template values. UCD 1, UCD 3, and UCD 10 remain wide binary candidates based on the new distances measurements whereas UCD 8 is discarded as a common distance pair. This latter, in fact, is an interesting pair of sources. Their apparent magnitudes are quite similar in most filters and they are about 1 arcmin apart from each other on the sky. Their proper motion information comes from the CatWISE2020 or NSC DR2 catalog and is not precise enough to help assessing the nature of the pair. On the other hand, their Gemini/GMOS spectra are best fit by an M8 and L0 template, respectively for the a and b components.

Also, the comoving candidate systems still have large uncertainties in their proper motion measurements, rendering current kinematical information not an efficient diagnostic. The spectra presented in this section are a basic sanity check that we

are in fact selecting ultracool dwarfs and our method to estimate spectral types works as expected, with an accuracy of $\pm$ 2 types.

Table 2.3: Objects photo-type, spectral type, magnitudes (i,z and Y) and photometric distances. The photo-type and the distance column is divided into Carnero Rosell et al. (2019) and new measurements as presented in the earlier sections. All the estimates provided by Carnero Rosell et al. (2019) have an asterisk (*) mark.

Name	RA (deg)	DEC (deg)	Ph.T	Sp. Type	i	z	Y	Distance (pc)
UCD 6	10.642	-3.531	L0*	L0	21.71 ± 0.01	20.24 ± 0.01	19.79 ± 0.05	195 ± 33*	176 ± 17
UCD 11	21.102	-44.986	L2*	L1	L0	22.45 ± 0.03	20.92 ± 0.02	20.35 ± 0.03	173 ± 8*	219 ± 22
UCD 12	22.886	-5.240	L2*	L1	L2	22.15 ± 0.03	20.83 ± 0.01	20.30 ± 0.03	158 ± 9*	149 ± 15
UCD 36	321.070	0.484	L0*	M9	L0	22.17 ± 0.03	20.63 ± 0.01	20.17 ± 0.04	246 ± 10*	222 ± 21
UCD 1 a	0.876	-0.216	L2*	L1	L2	20.62 ± 0.01	19.17 ± 0.01	18.66 ± 0.01	74 ± 2*	70 ± 6
UCD 1 b	0.876	-0.185	L7*	L8	L7	23.25 ± 0.06	21.15 ± 0.02	20.54 ± 0.04	70 ± 7*	64 ± 6
UCD 3 a	74.456	-49.567	L0*	M9	M8	22.46 ± 0.04	20.96 ± 0.02	20.45 ± 0.03	349 ± 22*	429 ± 50
UCD 3 b	74.455	-49.565	L0*	M9	M8	22.68 ± 0.05	21.13 ± 0.02	20.64 ± 0.04	371 ± 29*	457 ± 49
UCD 8 a	349.952	-52.073	L0*	M9	M8	21.40 ± 0.01	19.94 ± 0.01	19.46 ± 0.01	181 ± 7*	268 ± 26
UCD 8 b	349.929	-52.065	L0*	M9	L0	21.43 ± 0.01	19.95 ± 0.01	19.45 ± 0.01	176 ± 5*	160 ± 15
UCD 10 a	355.516	-61.588	L0*	M9	M8	22.31 ± 0.02	20.78 ± 0.01	20.34 ± 0.01	279 ± 29*	416 ± 41
UCD 10 b	355.533	-61.595	L0*	L0	M8	22.55 ± 0.03	21.17 ± 0.02	20.69 ± 0.03	286 ± 29*	445 ± 48

Chapter 3

Applications of the ultracool dwarfs sample

In this chapter we will discuss some potential applications of the ultracool dwarfs (UCDs) sample. As mentioned in the previous chapter, our group has already published a catalog of UCDs candidates using the DES DR1 data (Carnero Rosell et al., 2019). This earlier catalog is composed of 11,545 L and 200 T dwarf candidates. As also explained earlier, we now have a new and final sample of 19,583 UCDs based on DES DR2. This new compilation makes use of improved selection criteria, including better UCD templates and proper motions.

The Carnero Rosell et al. (2019) catalog was used to measure the thin disk scale height for the L dwarf population and to search for wide binary and multiple systems containing UCDs. With the new and updated sample of ultracool dwarf candidates in hand, we considered additional and/or improved early uses for this type of data. Among them we quote: i) searching for candidate members of young moving groups and associations; ii) searching for photometrically variable objects; iii) finding additional candidate binary systems constituted by two ultracool dwarfs; iv) improving the modelling of the spatial distribution of UCDs in the Galactic disk.

In the next sections, all these applications will be discussed in more detail. In Section 3.1.1 we introduce the methodology regarding the search for wide binary and multiple systems and the first compilation of such systems. In Section 3.1.2 we present the new search for wide binary systems composed by two UCDs, using the final catalog based on DES DR2. In Sections 3.2 and 3.3 we present new candidate members to young moving groups and nearby associations and candidate variable sources, respectively. Lastly, in Section 3.4 we discuss the methods and tests that we have implemented to obtain an improved estimate of the thin disc scale parameters

as traced by UCDs. The method is based on statistical inference tested and validated using realistic simulated samples. We show our results and discuss the limitations of applying it to the current sample of ultracool dwarf candidates from DES DR2 data.

3.1 Wide binary and multiple system candidates

3.1.1 DES DR1 results

During the first Ph.D. year, we published a paper focused on the study of wide binaries and multiple system candidates composed by UCD companions to stars, plus double UCD systems (L+L, L+T, T+T). These binary and multiple system candidates involving very low-mass and substellar sources are possible crucial benchmarks to evolutionary models close to or below the hydrogen burning limit, since properties such as metallicity and age, as well as masses, may be obtained for the primaries.

Using the 11,745 L and T dwarfs presented in Carnero Rosell et al. (2019), we searched for possible stellar companions in the Gaia DR2 and DES DR1 stellar data. The pairing of UCD candidates to potential primary stars was performed using a search radius that corresponds to 10,000 AU as the projected separation between the candidate pair members. Since the photometric distances of our UCD candidates are in the 20-500 pc range, these search radii cover the angular range from 20 to 500 arcsec.

To refine our search for wide binary and multiple systems, we checked if the members that have common distance also share a common proper motion, when available. The common distance criterion demanded that $|d_2 - d_1|/(\sigma_{d1}^2 + \sigma_{d2}^2)^{1/2} \leq 2$, where $d_{1,2}$ are the distances of the primary and secondary, and $\sigma_{d1,d2}$ are their associated uncertainties. The proper motions also were subjected to be within 2σ of each other. A robust binary or multiple system should satisfy $\Delta_\mu \leq 2\sigma_\mu$ where Δ_μ is the total proper motion difference $\Delta_\mu = \sqrt{\Delta_{\mu_{\alpha cos\delta}}^2 + \Delta_{\mu_\delta}^2}$ and $\Delta_{\mu_{\alpha cos\delta}}$ and Δ_{μ_δ} are the differences in proper motion between the pair members in the direction parallel and perpendicular to the Celestial Equator, respectively. In the above criterion, $\sigma_\mu = \sqrt{\delta\mu_1^2 + \delta\mu_2^2}$ is the composite uncertainty in the measured proper motions, where 1,2 again represent the primary and secondary. The individual uncertainties in proper motion also combine in quadrature the uncertainties along each on-sky direction.

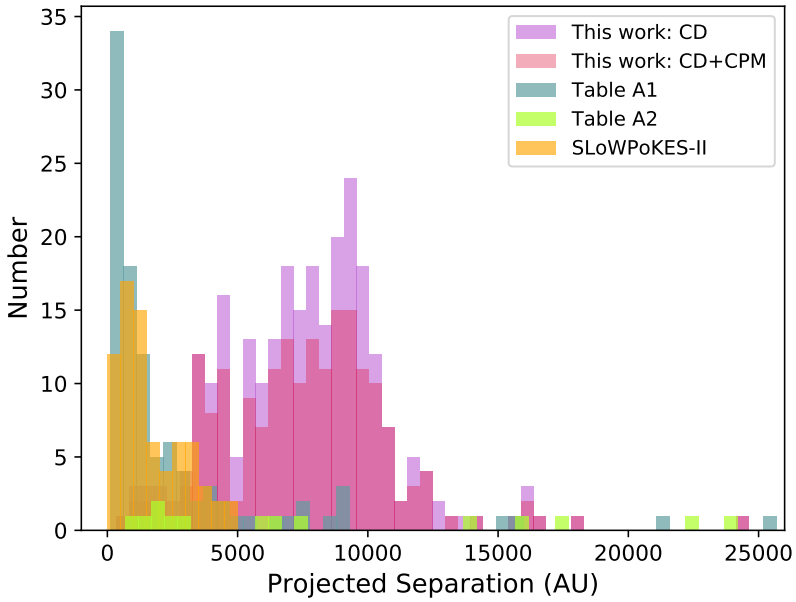

Figure 3.1: Distribution of projected separations using four different samples, as indicated in the upper right corner, from dal Ponte et al. (2020). The CD and CPM labels mean common distance and common proper motion, respectively. Our wide binary sample is the most numerous and reaches larger projected separations than the previous known samples. Table A2 lists unbound systems with very large projected separations. In order to better understand the distribution of separations, this figure only contains objects with a limiting of 26,000 AU in separation.

We found 174 common distance candidate pairs with a primary from the Gaia DR2 catalogue limited to $G < 18$, for which distances are estimated from the `StarHorse` code by Anders et al. (2019) (more details in Chapter 4). We also found 81 common distance candidate pairs with a primary from the DES DR1 sample. These latter tend to be fainter and their `StarHorse` distances are based mostly on photometry, although they have Gaia DR2 parallax information as well. In addition, we found nine systems containing two UCDs. Hence, we found in total 264 new wide binary candidates. The projected separations for the wide binary systems are spread within the $\sim$ 1,000-24,000 AU range. A sample of six candidate multiple systems were also identified and the projected separations between the UCD dwarfs and the stellar members of these higher order systems range from $\sim$ 3,000-11,000 AU.

For all these systems selected based on common distance criteria, 90% of the total sample have proper motions available and 73% of the systems also satisfy the

common proper motion criterion described above. The proper motions for the primaries were taken from Gaia DR2 and those for the UCDs were taken from the CatWISE2020 Catalog. Most of these later have large uncertainties, often comparable to the proper motion itself. Most of the systems with proper motions available, however, have proper motions within 2σ of each other.

For each possible pair, we estimate the chance alignment probability in order to assess the physical nature of each pair. This is the probability that we find a physically unrelated object with the same common distance within our uncertainties and within the search radius.

To assess the chance alignment probability, we simulate stars within a 2 deg^2 area from the UCD candidate from each pair. We randomly selected 1,000 stars within this area and calculated the fraction of common distance stars. Then we obtain the probability over all stars within the search radius by multiplying the fraction of common distance stars by the total simulated objects and making an area normalization considering the search radius area and the simulated area. In the case of the systems composed by UCD+UCD, the chance alignment probability was obtained using the `GalmodBD` simulation code, which computes expected Galactic counts of UCDs as a function of magnitude, color and direction on the sky. We computed the expected number of UCDs in a given direction and within the volume bracketed by the common range of distances and by the area within the angular separation of each possible pair. In both cases, we flagged every pair with a chance alignment probability $P_a > 5\%$ as contamination.

Figure 3.1 shows the distributions of projected separations from our wide binary candidates sample, from the 141 SLoWPoKES-II sample of wide very low mass binaries, and from other samples taken from the literature. In this context, Table A1 refers to known F/G/K/M+L or T wide systems that were spectroscopically confirmed and have an UCD as a companion. Table A2 refers to common distance and/or common proper motion known F/G/K/M+L or T wide systems identified so far. These two tables are shown in a appendix of the published paper shown in Appendix A of this text.

We also found six possible multiple systems, of which five are triples and one is a quadruple. The only potential quadruple system found is composed of an L0 dwarf associated to a star and to an M1+M1 double found previously by Dhital et al. (2015), but the L0's distance is only marginally consistent with that of the M1+M1 double, while the third star has a proper motion that is inconsistent with that of the brighter pair. One of the five triples is composed by two L dwarfs associated with a

Table 3.1: Summary of the common distance systems found. The systems with chance alignment probability >5% are not included here. CD and CPM stand for common distance and common proper motion, respectively. The PM column indicates how many CD systems have proper motion measurements.

Type of system		Total		
		CD	PM	CD+CPM
Binary	Gaia+UCD	174	153	125
	DES+UCD	81	74	61
	UCD+UCD	9	9	7
Triple		5	5	4
Quadruple		1	1	-

DES star companion. The configuration of both the quadruple and of this triple is also very atypical of multiple systems, again making their physical reality unlikely. On the other hand, the other four triple systems show a similar configuration, with a tight pair and a detached third object. This is also commonly seen in other triple systems reported in the literature, and is a favoured configuration according to models of three-body encounters (Delgado-Donate et al., 2004, Bate, 2012).

Table 3.1 summarizes all the systems found, regarding its type and the total number of systems, with and without proper motion data available. About 64% of our UCDs found in candidate binary and multiple systems are of the L0 spectral type. Still they make up only $\simeq 2\%$ of the total sample of L0 by Carnero Rosell et al. (2019). The typical wide binary fraction for the binary candidates over all spectral types ranges from $2-4\%$ in the projected separation range covered by this work. We have also added Poisson uncertainties to the binary fractions for each spectral type as shown in Figure 3.2. The candidate wide binary systems with UCDs as members presented here comprehend the largest catalogue to date.

The large number of wide binaries found is inconsistent with the formation of very low mass stars and brown dwarfs from strong dynamical interactions leading to their ejection of star forming cores, since the binding energy involved is very low and would lead in most cases to the pair dissolution.

Given the measurements of the chance alignment probabilities above, we expect some physically unrelated systems to remain in our sample. The systems identified, therefore, must all be considered as binary or multiple system candidates, pending on kinematical and spectroscopic confirmation. Still, this catalogue constitutes a significant leap in the number of candidate wide separation systems containing UCDs and in the estimates of the wide binary fraction for UCDs. Evolutionary models

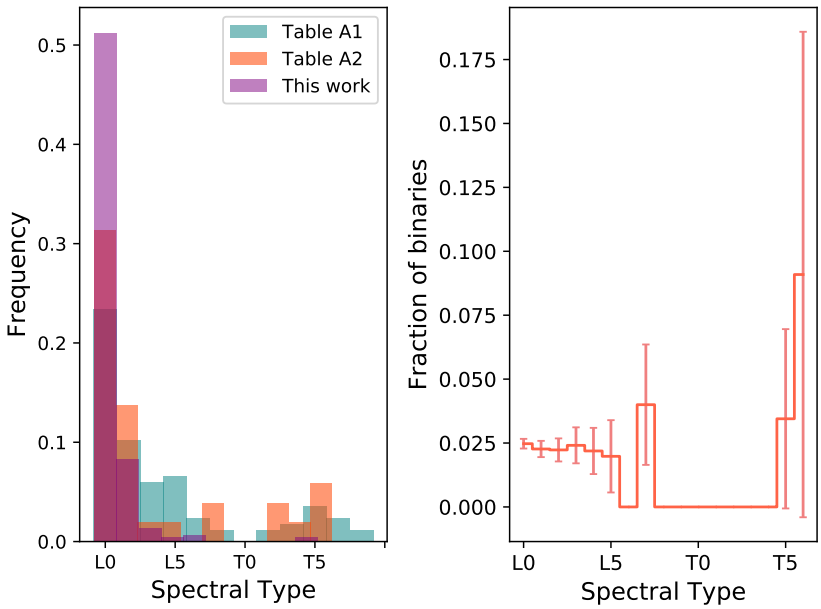

Figure 3.2: The left panel shows the frequency distribution of UCDs in wide binary systems, considering our sample and the currently known systems. The right panel shows the observed fraction of wide binaries as a function of spectral type. The error bars are Poissonian.

predict that our sample dominated by early L sources should include young or intermediate age brown dwarfs, whose benchmarking may also be very useful to constrain models.

This compilation of wide binary and multiple system candidates was done during my masters. However, the proper motion analysis using CatWISE2020 data was only made after the first referee report. Also, the paper has grown and evolved during the review, as we followed the referee suggestions. The final accepted and published paper can be found in Appendix A.

3.1.2 DES DR2 partial results

Using the new and updated compilation of 19,583 ultracool dwarfs presented Chapter 2, we decided to expand the search for wide binary systems constituted by two ultracool dwarfs. As already mentioned in the section above, this type of system is very interesting, since widely separated ultracool dwarf binaries are quite rare, especially considering field ages. A large number of wide binary systems in the Galactic field could in fact rule out formation scenarios where very low-mass and substellar objects are ejected from the protocluster due to dynamical interactions

(Reipurth et al., 2001, Bate & Bonnell, 2005). Due to their low binding energy, they are unlikely to survive this dynamical process.

Here we used the same methodology as explained in the previous section and presented new wide binary candidates composed by two UCDs. The list has four new candidates, both with common proper motion and distance. For this new search, we allowed common distance of 3σ. The criterion adopted in dal Ponte et al. (2020) was 2σ. However, only one system has a common distance beyond 2σ, but the proper motions are in clear agreement with each other. The chance alignment probability was also obtained for this new four systems using `GalmodBD` simulation code. For all the new binary candidates, the probability of chance alignment is $<$ 0.004%. The table containing the new systems and their properties can be found in Appendix B.

It is important to mention that not all systems presented in Section 3.1.1 were recovered here. The main reason is that some objects are now classified as M8 or M9 and therefore are not in the sample used for this new search, as explained in Section 2.4.4.

3.2 Young moving groups and nearby association candidates

Young moving groups and associations contain young stars ($\sim$ 10–100 Myr) and substellar objects whose similar kinematics imply that they originated in the same star-forming region. The members of a young association are a coeval population, where stars can serve as benchmarks to constrain metallicities and ages for substellar objects and to study models of star formation, for instance. Using the compilation of 19,583 ultracool dwarfs presented in the previous chapter, we used the BANYAN Σ code (Gagné et al., 2018) to estimate if any object in the sample is likely a moving group candidate member. The BANYAN Σ algorithm uses a compiled list of bonafide members of 29 young moving groups and associations within 150 pc of the Sun and field stars within 300 pc to compute membership probability given the sky position, proper motion, distance, and radial velocity of targets using Bayesian inference. In our analyses, we divided the sample into: i) targets with Gaia DR3 information; ii) targets with CatWISE or NSC proper motion. For these latter, we also demanded that $\sigma_\mu/\mu < 0.5$. Also, we added in the samples radial velocity measurements from the literature when available.

It is important to mention that we ran BANYAN Σ twice if the object has

CatWISE2020 and NSC DR2 proper motion. In this case, we only kept candidates whose BANYAN results were the same. We found that 60 objects among our list were already reported in the literature as moving groups candidate members. The young moving groups candidates (new and recovered) that we found are: 20 in AB Doradus (AB Dor, 110-150 Myr; Luhman et al., 2005, Barenfeld et al., 2013), six in β Pictoris (β Pic, 22 $\pm$ 6 Myr; Shkolnik et al., 2017), 11 in Columba (Col, 42 $^{+6}_{-4}$ Myr; Bell et al., 2015), one in Carina (Car, 45 $^{+11}_{-7}$ Myr; Bell et al., 2015), three in Carina-Near (CarN, 200 $\pm$ 50 Myr; Zuckerman et al., 2006), one in Octans (OCT, 35 $\pm$ 5 Myr; Murphy & Lawson, 2015) and 25 in Tucana-Horologium (THA, 45 $\pm$ 4 Myr; Bell et al., 2015). We did not include any candidate member from Argus association considering its high level of contamination (Bell et al., 2015).

We found 20 new candidate members to young associations with Bayesian membership probability above 90%, at least in one catalog. For objects in common with the literature, we analysed each case individually considering not only the difference in kinematics between this work and previous ones (our work probably making use of more recent and robust proper motion measurements), but also the use of BANYAN Σ (more recent and updated code) results in substitution to those presented by BANYAN II or BANYAN I, for instance. 12 objects are now classified as field members according to our results and are not presented in the following tables. The ambiguous objects were placed in the group indicated by our BANYAN Σ run.

Despite the recovered and new candidate members to younger populations, still the vast majority of 99.1% of our sample that has significant proper motion is composed of field objects. Also, it is important to mention that the comparison between our photo-type estimate and spectral type from candidate members of young associations from the literature shows a systematic discrepancy of up to +4 types in some cases. This may be the effect of deviant colors attributed to enhanced dust or thick photospheric clouds, that shift the flux to longer wavelengths in young objects (Faherty et al., 2016).

The tables containing the properties of the new and recovered objects from the literature can be found in Appendix B.

3.3 Variable ultracool dwarfs

Photometric variability can help to understand atmospheric inhomogeneities in ultracool dwarfs, as it is sensitive to the spatial distribution of condensates as the object rotates. It has been studied in the more massive field L and T dwarfs, but

still the variability of the younger and low-gravity objects is less understood. For instance, only a small sample of variability in low-gravity objects (Metchev et al., 2015, Vos et al., 2019) has been detected so far.

Here, we first used DES Y6 variability catalog described in Stringer et al. (2021) to search for variable sources among our 19,583 ultracool candidates sample and we found 291 of those. There are several available statistics to select variable sources in this particular catalog. The reduced χ^2 (`RED_CHISQ_PSF_grizy` ≥ 3.3) seems the most efficient to separate variable objects, for instance RR Lyrae, from standard stars. From these 291 variable candidate sources, 130 are also in the Transiting Exoplanet Survey Satellite (TESS) Input Catalog, 28 are young objects already identified in the literature and that were discussed in the previous section. It is out of the purpose of this work to further analyze in detail these variable candidates. However, this type of sample may be a starting point for studies regarding the cloud formation and dissipation on brown dwarf atmospheres and to assess if low-gravity objects are more likely variable than their field ultracool dwarfs counterparts (Metchev et al., 2015).

Figure 3.3 shows colour-magnitude diagrams for the entire sample of ultracool dwarf candidates presented in Chapter 2 (left panel), for ultracool dwarf candidates that have significant proper motion (satisfy the criteria from Section 2.4.2; middle panel) and for the photometrically variable candidates identified in the DES variability catalog (right panel). From these latter, the 28 young candidate objects mentioned above are highlighted. Absolute magnitudes were calculated using our photometric distance estimates. The variable sources seem to roughly follow the same colour-magnitude properties as our full sample of ultracool dwarfs. We may not see subtle redder colours for the highlighted young L types because according to our methodology we tend to attribute later spectral types for young objects, as mentioned in the previous section. Here, 10% of the young (L0-L7) candidate members to moving groups show photometric variability, a lower fraction when compared to Vos et al. (2019) that found 30^{+16}_{-8}% for the frequency of variable young objects in L0–L8.5 spectral type range. The remaining variable objects span the L0-T3 range of photo-types. We find that they correspond to 1.3% of the total populations in the range L0-L8, and 7% in the range L9-T3. These numbers are qualitatively similar to Radigan (2014), who found a higher variability of 24^{+11}_{-3}% for the L9-T3.5 range as compared to $3.2^{+2.8}_{-1.8}$% outside the L/T transition.

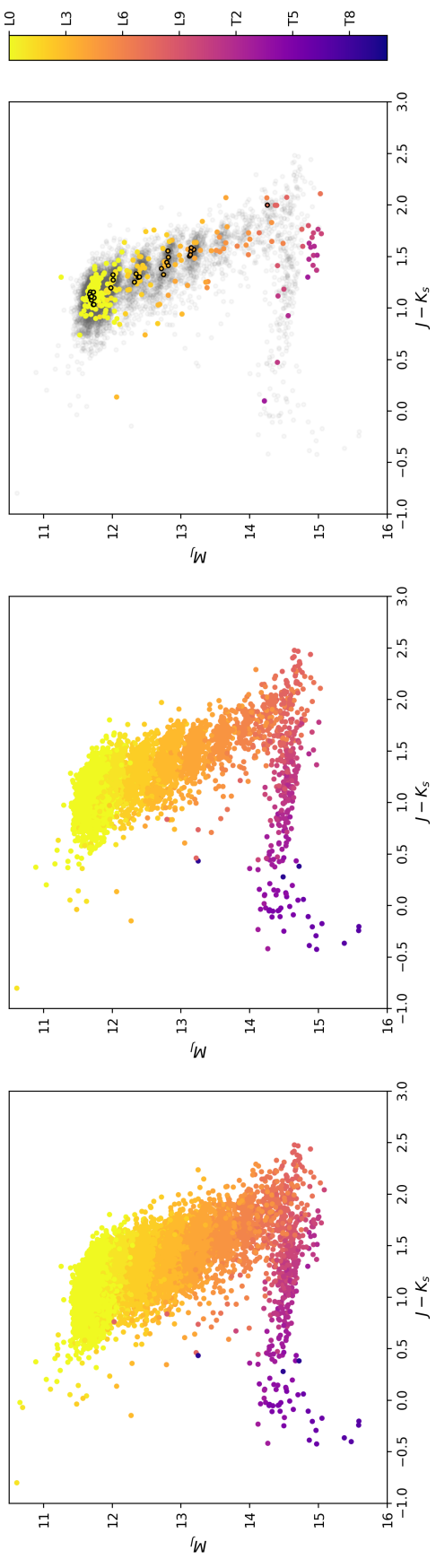

Figure 3.3: Color $J - K_s$ vs absolute magnitude in J band. The left panel shows all the 19,583 ultracool dwarf candidates. The mid panel shows only ultracool dwarfs candidates with significant proper motion. The right panel shows the photometric variable objects identified in the Dark Energy Survey Y6 variability catalog. The points with black contour represent the 28 young candidate objects among the variable sample. The shaded background is made up of all sources from the middle panel.

3.4 Ultracool dwarfs spatial distribution and profile

In Carnero Rosell et al. (2019), we compare the number of observed L and T dwarfs with different realizations of `GalmodBD` simulations to shed light on the thin disk scale parameters of the L and T population. Since T dwarfs were less than 2% of the sample and only up to 100 pc, the estimated scale height was based on the early L types (L0-L3). `GalmodBD` is a code, also presented in Carnero Rosell et al. (2019), that predicts differential number counts of L and T dwarfs as a function of apparent magnitudes and colors using the fundamental equation of stellar statistics. The code also generates a synthetic sample of such objects in a given footprint, with positions and apparent magnitudes, both true and observed ones, given a prescription for the photometric errors. To compute number counts or to generate samples, `GalmodBD` uses a model for the spatial distribution of UCDs, empirically determined space densities of these objects, plus absolute magnitudes and colours as a function of spectral type and requires several choices of structural parameters for the Galaxy, such as the density law and local normalization of each Galactic component. We generated a grid of such simulations containing the total number counts of early L types, with varying values of the main thin disk parameters. Based on their comparison to the observed numbers, we found a scale height of $h_{z,thin} \sim 450$ pc.

The idea here is to use the final and larger sample of ultracool dwarfs from DES DR2 as well as a Markov chain Monte Carlo analysis, which is a more robust method than what we have previously used. Our interest is not only for the measurement of the disk scale length and height themselves, which has so far been made in a very simplistic way. We may attempt to convert our estimated spatial height into a vertical velocity dispersion, which in turn relates to a kinematical age for the L disk population.

3.4.1 Distance and spatial distribution

Distances to our UCD candidates are needed to fit the data to a spatial density model. The description of our method to estimate photometric distances is given in Section 2.4.4. As mentioned earlier, our photometric distances tend to be slightly underestimated with respect to trigonometric distances with a typical error of $\sim$ 28%.

Figure 3.4 shows the density distribution of the ultracool dwarf candidates in the Galaxy using our distance estimates. The cartesian coordinate system used has origin at the Solar location. The XY plane is the plane of the MW disk, with negative

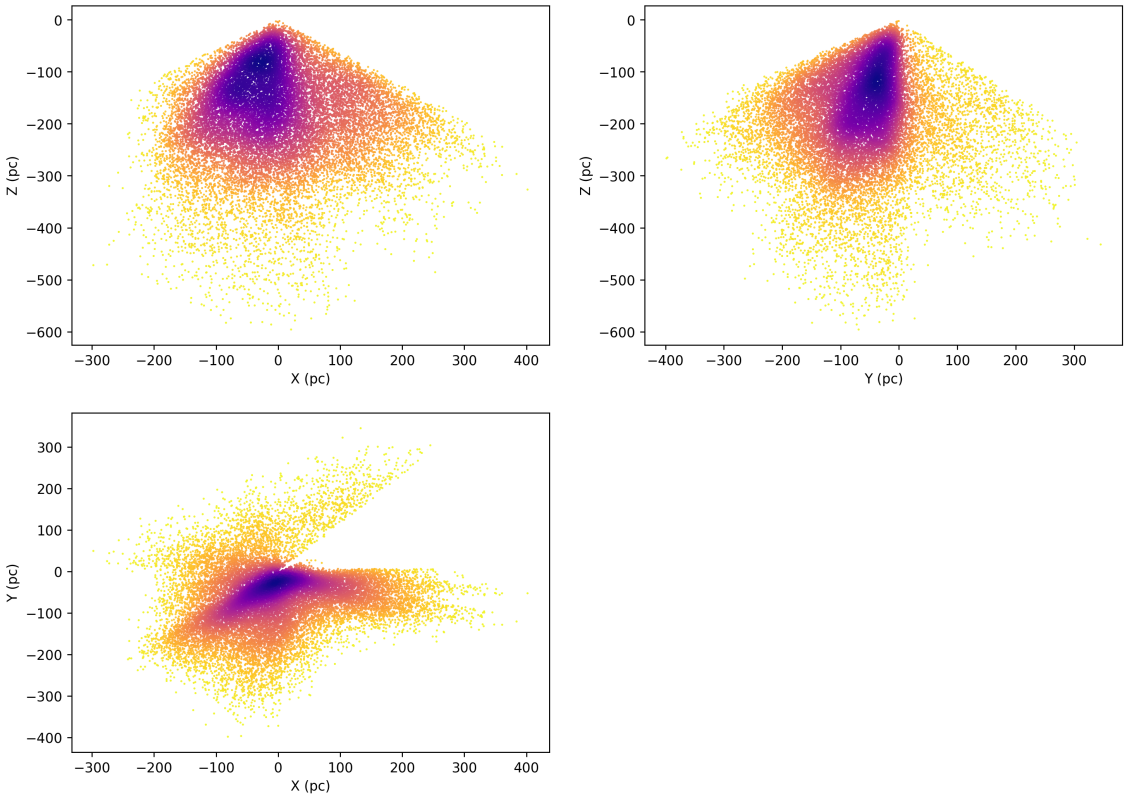

Figure 3.4: Density distribution of ultracool dwarf candidates. The projections are in Galactic Cartesian coordinates with the Sun at the origin.

(positive) X pointing towards the centre (anti-centre) of the Galaxy. Positive Z corresponds to the North Galactic Hemisphere. One clearly sees that the DES volume is entirely restricted to the Southern Galactic Hemisphere and avoids low Galactic latitudes. The sparsening of the sample for locations far from the Solar origin is partly due to selection effects in a flux-limited sample. The sparsening of the sample with increasingly negative Z, however, is also caused by the spatial density profile of the disk.

3.4.2 Analysis of the spatial profile

In order to fit the spatial number density profile we use a double exponential model for the Galactic thin disk to our sample of field sources:

$$n(\vec{r}) = n(0,0)e^{-R/R_s}e^{-|z|/z_s} \tag{3.1}$$

$$n(\vec{r}) = n(R_\odot, 0) e^{-(R-R_\odot)/R_s} e^{-|z|/z_s} \tag{3.2}$$

where R and z are Galactocentric cylindrical coordinates, R_s and z_s are the scale length and height, respectively, $R_\odot = 8$ kpc is the cylindrical radial coordinate of the Sun, also assumed to be at $z_\odot = 0$, and $n(0,0)$ (or alternatively $n(R_\odot, 0)$) is the profile normalization. The fits were carried out using the Markov Chain Monte Carlo (MCMC) method to sample parameter space and find the best model based on the maximization of likelihood or $-\chi^2$. The likelihood function evaluates the model density profile at the position of each sample object and takes the product over all sources. On the other hand, χ^2 bins the data spatially and compares the observed number of sources in each spatial bin to the predicted one given the model. The method we adopted not only fits the scale parameters R_s and z_s, but is also able to provide the density profile normalization.

The initial guess in R_s is usually in the range 1.5 - 2.5 kpc and for z_s in the range 200 - 400 pc. In some cases, as we will explain in the next sections, the initial guesses of the z_s parameter are determined using linear fits to the $ln[n(z)] = ln[n(z=0)] - |z|/z_s$ relation, where $n(z)$ is the number density of sources as a function of cylindrical z coordinate, integrated over the other coordinates.

As for the profile normalization, it is really not a free parameter. For any sample, it may in principle be obtained from the total sample size and the volume integral of the spatial profile. For example, in a hypothetical sample that covers the full Galactic volume, we get

$$N_{tot} = n(0,0) 4\pi R_s^2 z_s \tag{3.3}$$

where N_{tot} is the total number of objects. However, in real samples, limited in solid angle and distance, this volume integral becomes more complicated and has to be numerically determined. Since the integral has to be performed within the MCMC algorithm for every point in parameter space, we soon realized that it was not possible to do it for any sample resembling our DES DR2 data, due to the high computational burden. For these cases, we thus decided to treat $n(0,0)$ as a free parameter. In this case, the initial value for $n(0,0)$ is either taken from the fits to the 1D profile or from the total number of sources and the total volume integral of the profile given above. However, we still tested the fitting method for both 2 or 3 free parameters using all sky simulated samples.

Before inferring these parameters for the real sample presented in the previous

chapter, we tested the applicability of the fitting method just described to simulated data, either in an ideal sample with full sky coveraged and free of extinction or to synthetic samples subjected to similar angular censorship as DES. In all cases, a crucial preparation step is to eliminate or correct for the strong selection effect present in any flux-limited sample, where the number of sampled sources that satisfy the flux limit drops systematically towards larger distances, independently of the intrinsic spatial distribution. To account for this selection effect we adopted two alternatives:

i) volume-limit the sample out to some d_{lim}, by eliminating all sources whose distances exceed this value or which would not satisfy the flux limit if placed at d_{lim}. This second criterion translates into the cut-off of sources for which $d_{max,i} = d_i \ 10^{-0.2(z_i - z_{lim})} < d_{lim}$, where d_i and z_i are, respectively, the estimated photometric distance (see previous section) and the z-band apparent magnitude of the i-th source, and z_{lim} is the sample's magnitude limit, usually $z_{lim} = 23$;

ii) use empirical determinations of the UCD luminosity function to estimate the selection function of the sample as a function of distance:

$$\phi(d) = \frac{\int_{M_{lim}(d)}^{M_{SpT}} \Phi(M) dM}{\int_{M_{cut}}^{M_{SpT}} \Phi(M) dM} \tag{3.4}$$

where $\phi(d)$ is the sample selection function, $\Phi(M)$ is the luminosity function of UCDs. This latter was computed from the number density vs. spectral type and the M_z vs. spectral type relations in the solar neighbourhood found in Cruz et al. (2007), Marocco et al. (2015), Burningham et al. (2013). These relations are the ones used in the `GalmodBD` simulator. $M_{lim}(d) = z_{lim} - 5log[d(pc)] + 5$ is the faintest absolute magnitude of a source that is sampled at distance d, M_{cut} is the faintest absolute magnitude of UCDs in the sample and M_{SpT} is the typical absolute magnitude for the spectral type which we define as the brightest UCDs in our sample (usually M7 or M9, see next sections). In practice, to avoid too small values of $\phi(d)$, the sample is also cut at some maximum distance d_{lim}, and volume limited at some $d_{cut} << d_{lim}$, such that $M_{cut} = z_{lim} - 5log[d_{cut}(pc)] + 5$. Therefore, we call these samples as *semi volume limited.*

All Sky

The first tests include a full sky sample of M ($\geq$ M9), L and T synthetic dwarfs from `GalmodBD` simulation. The model used in `GalmodBD` has $R_s = 2.5$ kpc and $z_s =$ 250, 350 and 450 pc. The samples used have a magnitude limit of z < 23 and were

volume limited at 850 and 450 pc. The volume-limiting procedure, as described earlier, leaves mostly M9 dwarfs, since L or T dwarfs are underluminous to be kept in the sample, specially out to 850 pc. Here we tested for both likelihood and χ^2 statistics applied to the MCMC method.

As mentioned earlier, one issue with the modelling of the spatial distribution is that the global normalization of the density profile is not as simple as equation 3.3, since we do not have a sample over the entire Galactic volume. Since a spherical volume is not the most adequate for an integral with cylindrical coordinates, in the tests we ran by fitting 2 free parameters only (R_s and z_s), we decided to restrict the volume of our sample a bit further, by using the cylindrical volume fully inscribed into the sphere of radius d_{lim}. This cylindrical volume has heliocentric cylindrical coordinate ranges of ([0, + R_{max}], $[0, 2\pi]$, [-z_{max}, +z_{max}]) in (R, ϕ, z) coordinates, subject to the condition that

$$R_{max} = \sqrt{d_{lim}^2 - z_{max}^2} \tag{3.5}$$

Hence, for a given sample limiting spherical radius d_{lim} centered on the Solar position, we may then choose z_{max}, and consequently, R_{max}. The integral of the spatial density profile over this cylindrical volume is given by

$$N_{tot} = n(0,0)[z_s(1 - exp^{(-z_{max}/z_s)})] \int_0^{R_{max}} \int_0^{2\pi} exp^{[-(\sqrt{(Rcos\phi + R_\odot)^2 + R^2 sin^2\phi})/R_s]}\ R\ d\phi\ dR \tag{3.6}$$

where (R, ϕ) are again heliocentric cylindrical coordinates. In the case of fitting only the two exponential scales, this integral can be solved numerically and will then result in the appropriate normalization $n(R_\odot, 0) = n(0,0)exp(-R_\odot/R_s)$.

In Table 3.2 we show the results of fitting the horizontal exponential scale R_s and the vertical exponential scale z_s of our disk model to full sky, extinction free, `GalmodBD` simulations, while determining the profile normalization of each point in parameter space by the volume integral above. We show results for both likelihood and χ^2 statistics. The binning for the χ^2 counts was also based on cylindrical coordinates.

The recovered R_s parameter is close to the true value for both likelihood and χ^2 statistics. As for z_s, it is recovered within 10-15% of the true value for both statistics. In most cases, the best-fit z_s is larger than the true value, which reflects the contamination of the fit by simulated UCDs belonging to the thick disk and halo components of the Galaxy.

Table 3.2: Fit results for GalmodBD volume-limited true samples with a full sky coverage. The spectral type range is ≥ M9. Only the exponential scales were allowed to vary, while the profile normalization was determined for each model through a volume integral, as explained in the text. The $-\chi^2$ maximization requires binning the data, in this case using cylindrical bins, as listed.

Stats	r,z,ϕ bins	Points	d_{lim} (pc)	R_s (pc)	z_s (pc)
		z_s=250 pc			
Likelihood	-	263,274	850	2558^{+32}_{-34}	283^{+2}_{-2}
χ^2	14,12,14	263,274	850	2619^{+26}_{-25}	285^{+1}_{-1}
Likelihood	-	175,311	450	2457^{+92}_{-84}	283^{+2}_{-2}
χ^2	14,12,14	175,311	450	2537^{+67}_{-64}	286^{+2}_{-2}
		z_s=350 pc			
Likelihood	-	297,054	850	2486^{+29}_{-28}	385^{+3}_{-3}
χ^2	14,12,14	297,054	850	2543^{+21}_{-20}	386^{+3}_{-3}
Likelihood	-	197,698	450	2393^{+77}_{-78}	384^{+4}_{-4}
χ^2	14,12,14	197,698	450	2467^{+61}_{-58}	387^{+3}_{-3}
		z_s=450 pc			
Likelihood	-	318,380	850	2559^{+29}_{-27}	489^{+5}_{-5}
χ^2	14,12,14	318,380	850	2609^{+21}_{-22}	493^{+4}_{-3}
Likelihood	-	213,316	450	2562^{+89}_{-79}	495^{+6}_{-6}
χ^2	14,12,14	213,316	450	2643^{+62}_{-63}	498^{+5}_{-5}

In Table 3.3 we show the results of including the profile normalization as a free parameter to the fit. However, the likelihood function does not work with the normalization added as a free parameter. The reason is that, since the likelihood maximizes the joint probability of finding each UCD in its given spatial position, this 3 parameter fit will always diverge towards a maximum model, where $n(0,0)$, R_s, and z_s tend to large values. In the 2 parameter fit, this divergence is avoided by the compromise set by the volume integral, whereby large exponential scales result in small profile normalization values, as shown in eqs. 3.3 or 3.6. Again, the results for the χ^2 are similar to those shown in Table 3.2, which shows that the 3 parameter regression recovers the unbiased values using χ^2, despite the fact that parameters have some dependence, most specially R_s and $n(0,0)$ showing a clear anticorrelation.

In fact, the anticorrelation between R_s and $n(0,0)$ can be easily seen in Figure 3.5, where we show one of the corner plots output by the `emcee` package we used for the MCMC. It is worth pointing out that the number of UCDs used in these latter fits is larger than those shown in Table 3.2. The reason is that now we do not require a cylindrical volume to make the normalization integral tractable, so we use all sources out to d_{lim} and bin the data using spherical coordinates for the χ^2

Table 3.3: Fit results for GalmodBD volume-limited true samples with a full sky coverage. The spectral type range is ≥ M9. The fits were carried out with 3 free parameters, as explained in the text. Only the $-\chi 2$ statistic was used, now using spherical bins out to d_{lim}.

r,θ,ϕ bins	Points	d_{lim} (pc)	n (pc^{-3})	R_s (pc)	z_s (pc)
		z_s=250 pc			
14,12,14	384,270	850	0.01	2582^{+20}_{-50}	301^{+1}_{-1}
14,12,14	303,230	450	0.03	2529^{+53}_{-157}	284^{+2}_{-2}
		z_s=350 pc			
14,12,14	463,229	850	0.01	2526^{+19}_{-23}	395^{+1}_{-1}
14,12,14	344,341	450	0.03	2469^{+23}_{-59}	387^{+2}_{-2}
		z_s=450 pc			
14,12,14	522,046	850	0.01	2578^{+24}_{-54}	494^{+2}_{-2}
14,12,14	372,975	450	0.04	2435^{+6}_{-13}	486^{+3}_{-3}

computation.

As a final test using all sky samples, we added errors to the apparent magnitudes and spectral types attributed to each simulated UCD. The photometric errors were taken from a Gaussian distribution of mean equal to zero and standard deviation (std) that increases with the true apparent magnitude m according to the expression

$$\sigma(m) = A + exp[(m - B)/C] \tag{3.7}$$

where the parameters A, B and C were chosen to adequately describe typical photometric errors in DES, VHS and WISE data. Therefore for any photometric filter we now have observed magnitudes $m_{obs} = m + G(0, \sigma(m))$, where $G(\overline{x}, \sigma)$ is a Gaussian with mean $\overline{x}$ and std σ.

The errors in SpT were taken from a Gaussian of zero mean and std=1.5, $SpT_{obs} = SpT + G(0, 1.5)$, where SpT and SpT_{obs} are the true and observed spectral types. Given the *observational* versions of the magnitudes and spectral types, a new photometric distance modulus was then computed using the average of $m_{obs} - M(SpT_{obs})$ over all filters available for each simulated UCD, just as is done for the real data, where $M(SpT_{obs})$ are the absolute magnitudes for the templates, described in the previous chapter.

Table 3.4 and Table 3.5 show the results for the all sky `GalmodBD` samples cut at $m_{obs} \leq 23$ and volume limited at different d_{lim}, so that $d_{obs} \leq d_{lim}$ and $d_{max,obs} \geq d_{lim}$, where d_{obs} and $d_{max,obs}$ are observational versions of the heliocentric UCD distance and of the maximum distance out to which it is included in the sample, respectively. Table 3.4 shows the results for both likelihood and χ^2 statistics and

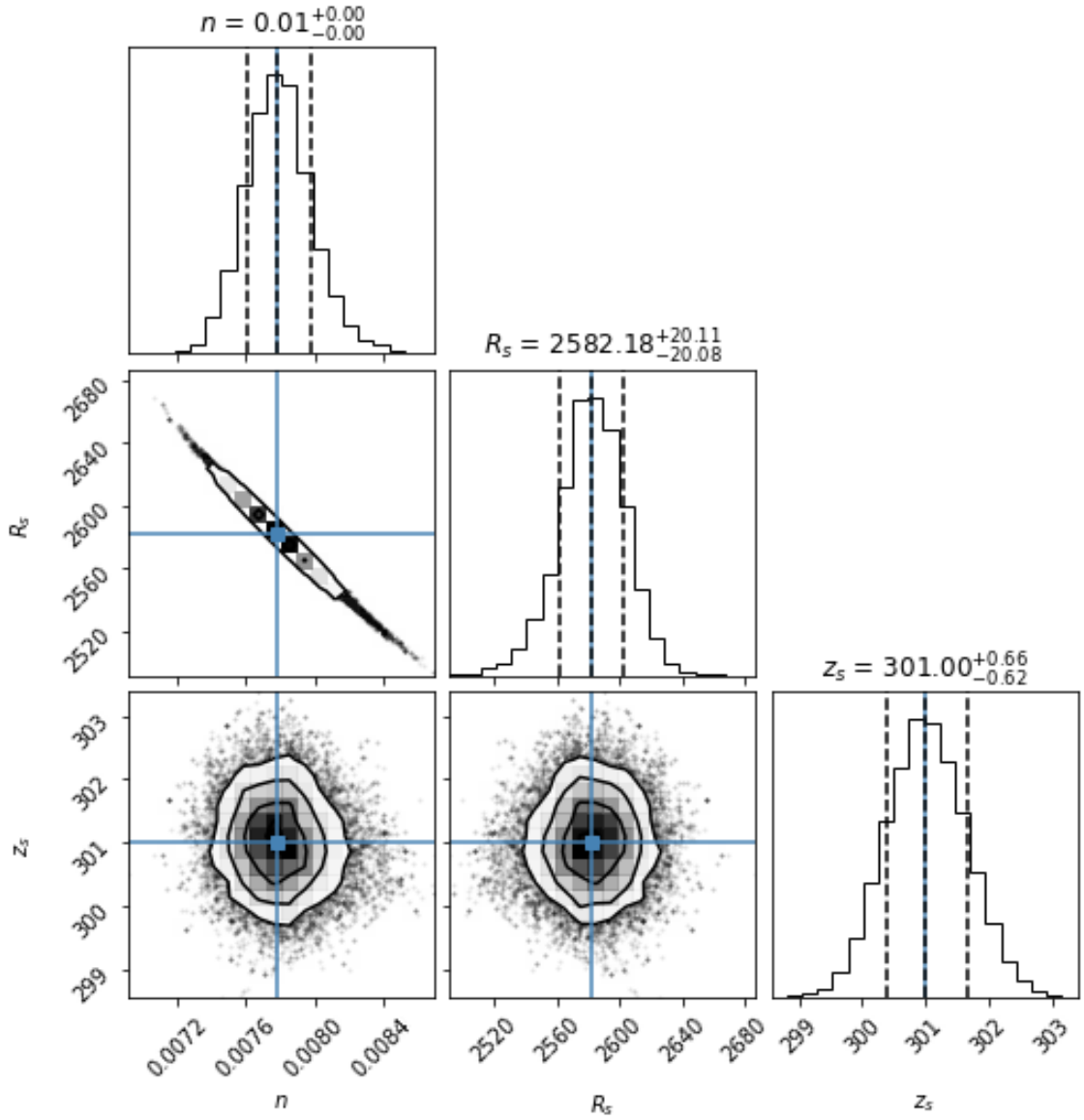

Figure 3.5: Corner plots for the true GalmodBD sample with $z_s = 250$ pc and $d_{lim} = 850$ pc. In this case, the profile normalization is treated as a free parameter, along with R_s and z_s. These results are shown in the first line of Table 3.3.

Table 3.4: Fit results for GalmodBD volume-limited *observed* samples with a full sky coverage. The spectral type range is ≥ M9. Only R_s and z_s were allowed to vary, while the profile normalization was determined for each model through a cylindrical volume integral.

Stats	r,z,ϕ bins	Points	d_{lim} (pc)	R_s (pc)	z_s (pc)
		z_s=250 pc			
Likelihood	-	277,732	850	2212^{+25}_{-23}	199^{+1}_{-1}
χ^2	14,12,14	277,732	850	2299^{+19}_{-18}	201^{+1}_{-1}
Likelihood	-	264,927	450	1586^{+31}_{-30}	170^{+1}_{-1}
χ^2	14,12,14	264,927	450	1626^{+23}_{-22}	171^{+1}_{-1}
		z_s=350 pc			
Likelihood	-	320,760	850	2188^{+20}_{-20}	257^{+1}_{-1}
χ^2	14,12,14	320,760	850	2277^{+17}_{-17}	261^{+1}_{-1}
Likelihood	-	310,967	450	1585^{+25}_{-27}	214^{+1}_{-1}
χ^2	14,12,14	310,967	450	1613^{+20}_{-20}	216^{+1}_{-1}
		z_s=450 pc			
Likelihood	-	352,358	850	2197^{+20}_{-20}	308^{+2}_{-2}
χ^2	14,12,14	352,358	850	2274^{+16}_{-16}	311^{+1}_{-1}
Likelihood	-	343,934	450	1563^{+24}_{-23}	258^{+1}_{-1}
χ^2	14,12,14	343,934	450	1601^{+18}_{-18}	260^{+1}_{-1}

only R_s and z_s as free parameters. Table 3.5 shows results for only χ^2 (computed in spherical bins) and the normalization added as free parameter. For these new fits using observed versions of the quantities both R_s and z_s are underestimated.

The effect of underestimating R_s and z_s is related to our distance estimates for the observed sample. Figure 3.6 shows the trends on the distances and spectral types as we change from true to an observed sample. Here we can see the Malmquist bias: intrinsically brighter sources will be selected in larger numbers than intrinsically fainter sources considering a magnitude-limited sample such as ours. Therefore, as shown by the lower right panel in Figure 3.6, more M dwarfs are assigned as L type than the other way around. Thus, these *observed* L dwarfs will have a much lower assigned distance than they would have as true M dwarfs. This pileup of objects with lower distances is shown in the upper panel of the Figure 3.6, being directly responsible for the biases in the profile scale parameters.

Another effect is the Eddington bias, which is caused by the photometric uncertainties on the magnitudes near our z < 23 cut. Since the number counts as a function of apparent magnitude increases for fainter magnitudes, more sources with $m > 23$ and $m_{obs} < 23$ are scattered into the sample than sources with $m < 23$ and $m_{obs} > 23$ are scattered out. This could in principle partly compensate for the

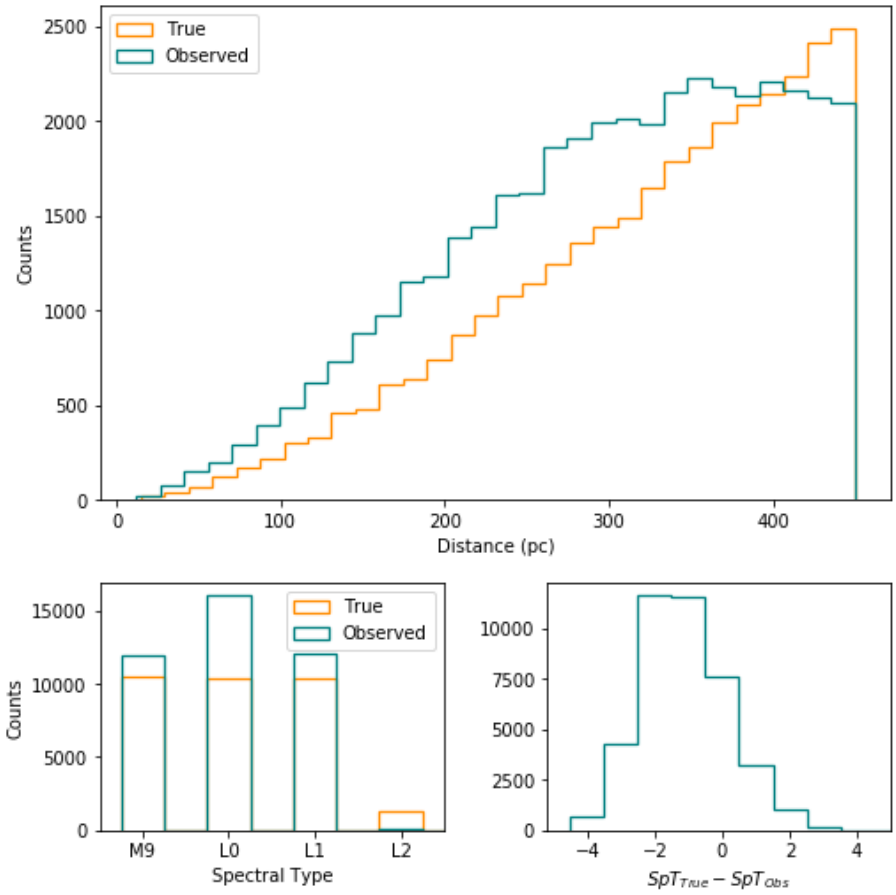

Figure 3.6: The upper panel shows the distances for a true and observed GalmodBD sample, where there are more objects in lower distances in the observed sample than the true sample. The lower left panel shows the spectral type distribution in both samples. For the observed sample, there are more objects classified as L0 dwarfs. The lower right panel, shows, only for the observed sample, the difference between the true and the observed spectral type. More M dwarfs are classified as L dwarfs than the other way around and this effect reflects on our distance estimates.

Table 3.5: Fit results for GalmodBD volume-limited *observed* samples with a full sky coverage. The spectral type range is $\geq$ M9. The fits were carried out with 3 free parameters. Only the χ^2 statistics converges in these cases.

r,θ,ϕ bins	Points	d_{lim} (pc)	n (pc^{-3})	R_s (pc)	z_s (pc)
		z_s=250 pc			
14,12,14	356,062	850	0.01	2382^{+18}_{-18}	212^{+1}_{-1}
14,12,14	419,156	450	0.26	1705^{+18}_{-17}	179^{+2}_{-2}
		z_s=350 pc			
14,12,14	432,113	850	0.01	2333^{+15}_{-15}	259^{+1}_{-1}
14,12,14	493,486	450	0.29	1682^{+22}_{-16}	225^{+2}_{-2}
		z_s=450 pc			
14,12,14	493,838	850	0.01	2346^{+15}_{-15}	301^{+1}_{-1}
14,12,14	547,660	450	0.29	1679^{+19}_{-14}	272^{+1}_{-1}

parameter biases, since we expect larger contamination by thick disk and halo UCDs (and hence an overestimated z_s at least), which tend to be fainter than their thin disk counterparts.

Angular censorship: DES footprint

The following tests were carried out using simulated `GalmodBD` samples, but now applying angular censorship to the data. Since our real candidate sample is limited to the DES footprint, we restricted also the `GalmodBD` samples to this footprint as well. Furthermore, in these cases $n(0,0)$ is considered as a free parameter and will be fitted along with R_s and z_s. As explained earlier, the normalizing volume integral for each model over a very specific footprint as is the case DES becomes computationally prohibitive. Also, since the likelihood diverges in the case when the 3 profile parameters are free to vary, all the tests were performed using χ^2, with a spherical binning out to d_{lim}. The more complicated footprint limits now also require that we compute the volume fraction of each spherical bin that is inside the DES region and scale the model counts in each bin by this factor. We again test simulations with true and observed versions of magnitudes, spectral types and photometrically derived distances.

The results for volume-limited true and observed samples are shown in Table 3.6 and Table 3.7, respectively. A novelty in these fits is that we now take a first guess of the z_s (that we call z_0) and normalization from fits in 1D

$$ln\ n(z) = ln\ n(z=0) - \frac{|z|}{z_0} \tag{3.8}$$

Table 3.6: Fit results for GalmodBD volume limited true samples restricted to the DES footprint. The spectral type range is ≥ M9. The z_0 is the initial guess **of** z_s, estimated with the 1D method. These are 3 parameter fits and only χ^2 statistics was used here.

r,θ,ϕ bins	Points	d_{lim} (pc)	$z_0(pc)$	n (pc^{-3})	R_s (pc)	z_s (pc)
			z_s=250 pc			
8,6,8	23,913	850	262	0.004	3212^{+273}_{-383}	305^{+3}_{-3}
8,6,8	25,781	450	316	0.04	2378^{+130}_{-154}	274^{+4}_{-4}
			z_s=350 pc			
8,6,8	34,066	850	370	0.01	2599^{+126}_{-138}	390^{+4}_{-4}
8,6,8	32,488	450	424	0.05	2179^{+89}_{-60}	372^{+6}_{-6}
			z_s=450 pc			
8,6,8	42,456	850	393	0.10	2764^{+132}_{-219}	481^{+5}_{-5}
8,6,8	37,031	450	539	0.05	2304^{+108}_{-99}	420^{+8}_{-8}

Table 3.7: Fit results for GalmodBD volume limited observed samples restricted to the DES footprint. The spectral type range is ≥ M9. The z_0 is the initial guess of the z_s parameter, estimated with the 1D method. These are 3 parameter fits and only χ^2 statistics was used here.

r,θ,ϕ bins	Points	d_{lim} (pc)	z_0 (pc)	n (pc^{-3})	R_s (pc)	z_s (pc)
			z_s=250 pc			
8,6,8	20,665	850	221	0.02	2545^{+131}_{-134}	191^{+2}_{-2}
8,6,8	29,969	450	184	0.01	2207^{+101}_{-73}	171^{+2}_{-2}
			z_s=350 pc			
8,6,8	29,451	850	234	0.02	2543^{+118}_{-114}	211^{+2}_{-2}
8,6,8	40,267	450	225	0.10	2167^{+30}_{-31}	196^{+2}_{-2}
			z_s=450 pc			
8,6,8	37,586	850	269	0.02	2235^{+88}_{-75}	240^{+2}_{-2}
8,6,8	48,059	450	259	0.14	2054^{+10}_{-6}	250^{+2}_{-2}

Table 3.8: Fit results for GalmodBD semi volume-limited true samples restricted to the DES footprint. The spectral type range is $\geq$ M7 and $\geq$ M9. Only χ^2 statistics were used here.

r,θ,ϕ bins	Points	d_{lim} (pc)	z_0 (pc)	n (pc^{-3})	R_s (pc)	z_s (pc)
			z_s=250 pc			
8,6,8	163,103	1102	262	0.06	3204^{+35}_{-37}	295^{+1}_{-1}
8,6,8	57,885	594	289	0.10	2691^{+93}_{-138}	250^{+1}_{-1}
			z_s=350 pc			
8,6,8	233,330	1102	311	0.09	2866^{+26}_{-71}	350^{+1}_{-1}
8,6,8	74,019	594	349	0.18	2307^{+56}_{-64}	304^{+2}_{-2}
			z_s=450 pc			
8,6,8	294,864	1102	392	0.08	3022^{+23}_{-30}	408^{+1}_{-1}
8,6,8	37,031	594	427	0.09	2923^{+111}_{-200}	351^{+2}_{-2}

These 1D fits are carried out by simply adding up the number of UCDs and the bin volumes over all bins at a fixed z value, and then computing the one-dimensional versions of the number densities.

The more restricted volume used now leads to larger discrepancies in the recovered R_s and z_s values as compared to the truth table, even in the case of Table 3.6, where the true quantities were used for each UCD. But the recovered parameters in this case are usually still within 20% of the true value. And as in the case of the full sky simulations, the trend towards overestimated z_s is due to thick disk and halo contamination.

As for the *observed* samples, as attested by comparing Table 3.7 with Table 3.5, the angular censorship has now aggravated the tendency of underestimating z_s.

An alternative attempt to recover unbiased profile parameters from an UCD sample was to consider semi volume-limited samples. Here we used the selection function presented in Equation 3.4 to weight UCDs as a function of distance. Our selection function is $\phi_d = 1$ for distances $\sim$ 80 pc, i.e., it is complete at least down to the faintest objects in the sample which correspond to an absolute magnitude $M_{z,cut}$ = 18.5 (T5) and z_{lim} = 23. Less luminous UCDs than this limit were discarded. Also, in order to avoid shot noise in the weighting of our sources by $1/\phi$, we cut the semi volume limited samples at the distance where $\phi(d_{lim}) = 0.2$. We also considered two cases of maximum luminosity (minimum absolute magnitudes) for the selection function integrals: spectral type range $M_{SpT} \geq$ M7 and $M_{SpT} \geq$ M9. For the $\geq$ M7 sample, the typical d_{lim} was 1102 pc and for the $\geq$ M9 sample, d_{lim} = 594 pc. All this results in an increased volume combined with a denser sample, at the expense of having unequal weights for the sampled objects.

Table 3.9: Fit results for GalmodBD semi volume-limited observed samples restricted to the DES footprint. The spectral type range is $\geq$ M7 and $\geq$ M9. Only χ^2 statistics were used here.

r,θ,ϕ bins	Points	d_{lim} (pc)	z_0 (pc)	n (pc^{-3})	R_s (pc)	z_s (pc)
			z_s=250 pc			
8,6,8	109,029	1102	160	0.08	3155^{+59}_{-105}	200^{+1}_{-1}
8,6,8	56,389	594	171	0.35	2112^{+35}_{-18}	169^{+1}_{-1}
			z_s=350 pc			
8,6,8	153,919	1102	184	0.12	2915^{+51}_{-346}	222^{+1}_{-1}
8,6,8	74,695	594	212	0.34	2160^{+32}_{-20}	190^{+2}_{-2}
			z_s=450 pc			
8,6,8	192,327	1102	229	0.14	2833^{+34}_{-246}	240^{+1}_{-1}
8,6,8	85,291	594	259	0.40	2193^{+31}_{-19}	215^{+1}_{-1}

The fit results are shown in Table 3.8 and Table 3.9 for the true and observed `GalmodBD` sample, respectively. Table 3.8 shows again reasonable results for the profile parameters. In most cases, they are within 20% of the truth table, although R_s tends to be systematically overestimated. As for z_s, the trend to overestimate (again largely due to contamination by non thin disk UCDs) gives place to an underestimate for the thicker thin disk models, specially when $z_s/d_{lim} > 0.5$. The situation is further agravated when the *observed* sample is used, as shown in Table 3.9. Now the bias in R_s is more pronounced and more dependent on the sample volume. Likewise for the strong underestimates of the z_s parameter.

We may thus conclude that extracting thin disk profile scales from a DES-like observed UCD sample is a challenging task, in which the measurement (photometric, spectral types, etc) errors lead to very significant errors in the photometric distances, with a strong tendency to underestimate them. Coupled with the limited volume and irregular footprint, these limitations make a reliable regression still out of our reach, at least with the models and methods discussed here. We have thus refrained from revising the disk structural parameters discussed in Carnero Rosell et al. (2019) in this work.

Chapter 4

Outer components of the Galaxy

In this chapter we will discuss the initial attempts to use the Gaia EDR3 data to study the Milky Way stellar halo. As presented in Chapter 1, there is still some debate in the literature concerning the halo density profile and metallicity distribution.

Using a catalog with 362 million sources run through the `StarHorse` code and containing stellar parameters, distances, and extinctions derived from Gaia early third data release (EDR3), we attempt to select a sample of halo stars and perform a study of the metallicity distribution covering large Galactocentric distances.

In Section 4.1 we will present the catalog used in this work and the selection imposed to avoid low quality data and disk stars. In Section 4.2 we test the consistency of our sample and, finally, in Section 4.3 we will discuss the first results regarding the metallicity distribution for our sample.

4.1 Data

One of latest releases from the Gaia mission, the Gaia Early Data Release 3 Gaia Collaboration, Brown et al. (Gaia EDR3, 2021) is based on data collected during 34 months of observations, with positions and the apparent brightness in G band for ~ 1.8 billion sources. For 1.5 billion of those sources, parallaxes and proper motions are available. Compared to Gaia DR2, the parallax precision increased by 30% and the proper motions are by a factor of 2 more precise.

Recently, Anders et al. (2022) presented a catalog of over 362 million stellar parameters, distances, and extinctions for stars brighter that G=18.5 derived from Gaia EDR3 data cross-matched with the photometric catalogues of Pan-STARRS1, AllWISE, SkyMapper (Onken et al., 2019) and 2MASS (Cutri et al., 2003). The

`StarHorse` code was used to estimate photo-astrometric parameters using high precision astrometric data from Gaia combined with the broad wavelength coverage by additional photometric surveys. The `StarHorse` code (Queiroz et al., 2018) uses a Bayesian approach to determine masses, ages, distances and extinctions for field stars through the comparison of their observed spectroscopic, photometric and astrometric parameters with those from stellar evolution models. The models used are the `PARSEC` + `COLIBRI` set of isochrones (Bressan et al., 2012, Marigo et al., 2017). The code assumes spatial priors for each structural component of the Galaxy (thin and thick disks, bulge and halo). The priors also assume Gaussian metallicity and age distribution functions for each structural component. For all components, the Chabrier Initial Mass Function (IMF; Chabrier, 2003) was assumed as a prior. The normalisation of each Galactic component, and the solar position were taken from Bland-Hawthorn & Gerhard (2016). Thus, Gaussian likelihood functions were generated using the available observed parameter set and their associated uncertainties. The code then computes the posterior distribution function over distance, marginalized for all other parameters. We take the median of this marginalized posterior as the best estimate, while the difference between the median 84th percentile and the (16th percentile) is taken as the higher (lower) 1-σ uncertainty.

In our initial selection from the Anders et al. (2022) catalog, we demanded that every source must have a distance measurement relative uncertainty lower than 30%. We also set the flag `fidelity` > 0.5 (Rybizki et al., 2022) to exclude objects with bad astrometric results and `sh_outflag` $= 0000$ to exclude objects with low number of consistent models, negative extinction, very large or very small uncertainties.

The second step is to select halo stars, which is a very challenging task. In the literature, it is possible to find several prescriptions of how to select halo stars. Prior to Gaia, the most common way to separate disk from halo stars was to use a color-magnitude diagram to select an specific tracer such as an old and metal-poor main sequence turn-off, red giant or blue horizontal branches (Carollo et al., 2007, Sesar et al., 2011, Xue et al., 2015). Soon after the Gaia release, some authors started to advocate that the selection could be done by adopting high-velocity criteria. An example of this selection is to use $|\mathrm{V\text{-}V}_{LSR}| > 200$ km/s where V is the three-dimensional velocity of the star. Another alternative is to use the tangential motion v_{tan} due to the limited availability of line-of-sight velocity information. Recently, some authors have been using the phase-space quantities as the orbital energy E, the angular momentum component parallel to the z-axis L_z and action space quantities J_R, J_ϕ, J_z to select mostly accreted halo stars. However, this also has a limitation

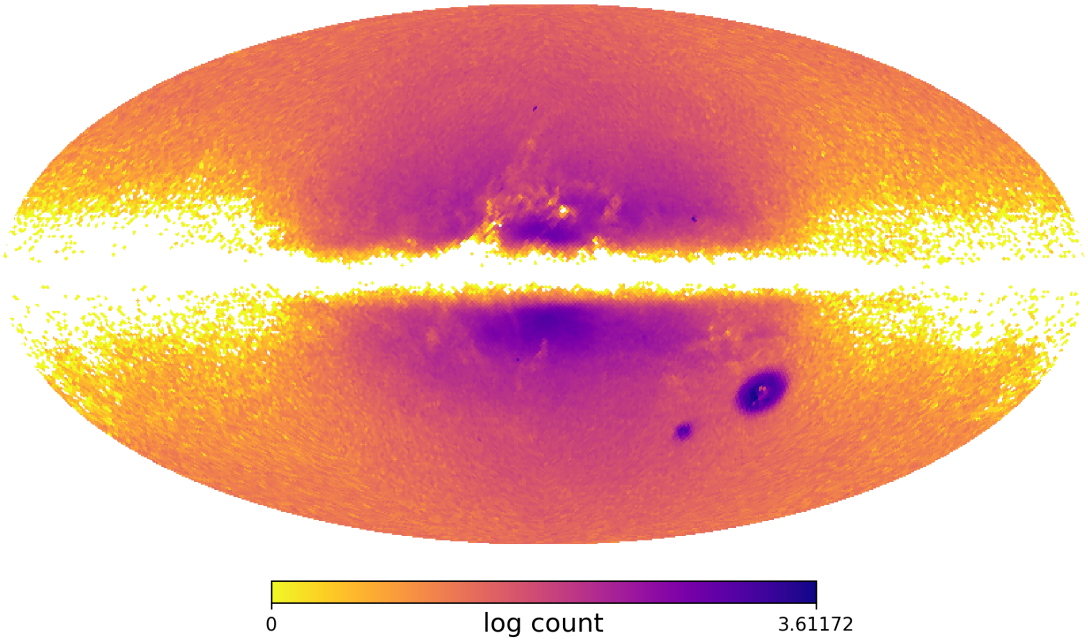

Figure 4.1: Mollweide projection map of the tentative halo stars in Galactic coordinates. The map is color-coded by the logarithm of the number of stars per HealPix. The Large and Small Magellanic Clouds are also visible on this map.

as only a small fraction of stars have the full 6D information even in the most recent releases of Gaia.

In this work, we decided to select halo stars according to the tangential velocity criteria of

$$v_t = 4.74057\,\mu\,d > 200\,km/s \tag{4.1}$$

where $\mu = \sqrt{\mu_\alpha^2 + \mu_\delta^2}$ is the total proper motion and d is the heliocentric distance. This relation was used initially in Gaia Collaboration, Babusiaux et al. (2018) to identify nearby halo stars. This type of selection is similar to a kinematical selection performed using the Toomre diagram or $|\text{V-V}_{LSR}| > 200$ km/s. However, unlike the latter, which demands a full 6D sample, a tangential velocity criterion only requires a 5D sample. We also imposed a geometrical selection of $|\text{Z}_{Gal}| > 1.5$ kpc and $A_V < 2.0$ to remove possible disk contaminants, removing stars with high extinction at lower latitudes. Here the A_V values are also from `StarHorse` catalog. The sample of tentative halo stars has initially 2,042,813 stars.

As discussed in Chapter 1, this selection of stars with high tangential velocity led to the appearance of two distinct sequences in the HRD. These sequences are

generally known in the literature as blue and red. The blue sequence is composed of more metal-poor stars on retrograde orbits, likely attributed to Gaia-Enceladus-Sausage, and the red sequence is composed of kinematically heated MW stars, either from the old thick disc, in situ halo or a mix of both these populations (Koppelman et al., 2018, Haywood et al., 2018, Di Matteo et al., 2019). The chemical abundances of the blue sequence overlap with the low-α sequence discovered by Nissen & Schuster (2010) and further studied by Hayes et al. (2018). Gallart et al. (2019) also showed that these two sequences share identical age distributions, being older than the majority of thick disc stars, with a cutoff at 10 Gyr. This cutoff could be associated with the accretion of Gaia-Enceladus.

Figure 4.1 show the on-sky density distribution of our selection of stars from `StarHorse` catalog in Galactic coordinates. The map was created using healpix level of 6, resulting in 49,152 equal area pixels. Besides the large zone of avoidance in the disk plane resulting from our geometrical and extinction cut, a few other features are clearly seen on the map: i) the clear increase in stellar density towards the Galactic centre; ii) the Large and Small Magellanic Clouds stand out clearly at intermediate southern Galactic latitudes; iii) the presence of high latitude high extinction regions in the form of plumes stretching out of the disk plane.

4.2 Velocity distribution

Even without radial velocity measurements it is possible to explore the velocity content of a sample. Here we follow the method presented in Koppelman & Helmi (2021) to calculate pseudo-3D velocities. First, we can obtain tangential velocity components in Galactic coordinates v_l^* and v_b^* corrected by the solar reflex motion using

$$v_{l,b}^* = v_{l,b} + v_{l,b\odot} \tag{4.2}$$

where $v_{l,b}$ are the heliocentric tangential velocity (as presented in Equation 4.1) for the l and b components and $v_{l,b\odot}$ are

$$v_{l,\odot} = -U_\odot sin(l) + (V_\odot + V_{LSR})cos(l) \tag{4.3}$$

$$v_{b,\odot} = W_\odot cos(b) - sin(b)[U_\odot cos(l)(V_\odot + V_{LSR})sin(l)] \tag{4.4}$$

where the velocities above are components in the heliocentric Galactic coordinate

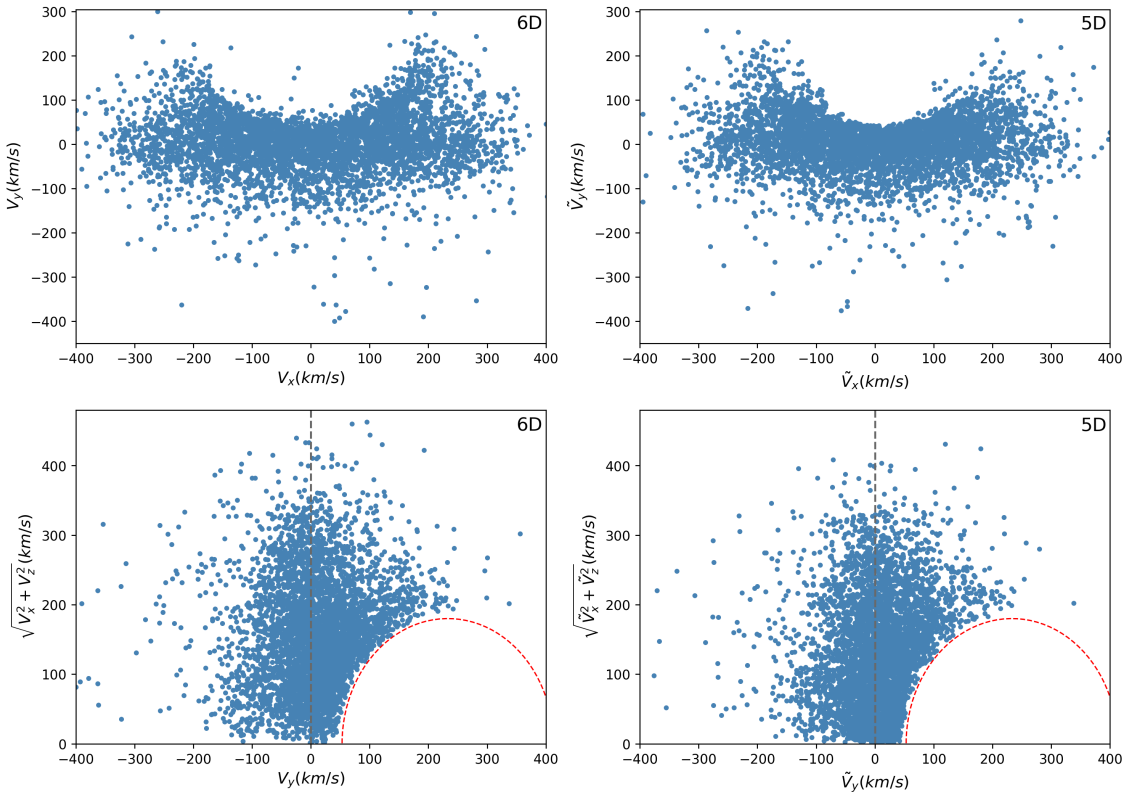

Figure 4.2: Velocity distribution of halo stars in the solar vicinity (distance < 2.5 kpc). The left panels show the velocities calculated using the full 6D phase-space information, while on the right the velocities were computed by setting the line-of-sight velocities to zero. In the bottom panels, the stars inside the dashed red line are generally labelled as disk stars.

system but in the Galactocentric reference frame. The components of the solar peculiar velocity with respect to the local standard of rest (LSR) are $(U_\odot, V_\odot, W_\odot)$ = (11.1, 12.24, 7.25) km/s (Schönrich et al., 2010) and the local standard of rest motion $V_{LSR} = 232.8$ km/s (McMillan, 2017). As mentioned, the resulting tangential velocities are in the Galactic rest frame, but as observed from the solar position. The v_l^* and v_b^* tangential velocities can now be used to calculate pseudo-3D velocities. These are not true velocities as we are assuming that the line-of-sight velocities are equal to zero. Quoting the authors Koppelman & Helmi (2021) themselves: "This assumption is valid if the velocity distribution is centred on zero in the galactocentric rest frame. However, they will not be zero on average for local regions on the sky because of the imprint of the motion of the Local Standard of Rest around the Galactic Centre, following a sin(l) cos (b) pattern." To calculate the pseudo-3D velocities we can use

$$\tilde{V_x} = -v_l^* sin(l) - v_b^* cos(b) sin(b) \tag{4.5}$$

$$\tilde{V_y} = -v_l^* cos(l) - v_b^* sin(b) sin(b) \tag{4.6}$$

$$\tilde{V_z} = v_b^* cos(b) \tag{4.7}$$

As in Koppelman & Helmi (2021) we use the notation $\tilde{V_x}, \tilde{V_y}, \tilde{V_z}$ to clarify that these are not real Cartesian velocities. In order to check the consistency of our sample selection, we can compare true and pseudo velocity distributions for the local halo.

Figure 4.2 shows the comparison between the true and pseudo velocity distributions for a sub-sample of stars with full 6D information with heliocentric distances smaller than 2.5 kpc (4,602 stars in total). Belokurov et al. (2018) found in the V_φ vs V_R space a 'Sausage' structure centered around $V_\varphi \sim 0$ and extended in V_R. Similarly, one can notice the same elongated structure in the V_x vs V_y space (top panels). The banana shaped structure is due to the stars with halo-like kinematics that are part of thick disk tail. These hot thick disk stars have likely been dynamically heated during the merger with Gaia-Enceladus (Helmi et al., 2018, Di Matteo et al., 2019). The Toomre diagram is shown in the bottom panels. The selection of presumably halo stars demands that $|V\text{-}V_{LSR}| > 200$ km/s, i.e, stars outside the dashed red line. The black dashed line divides the stars with retrograde and prograde motion. The large density of stars around $V_x = 0$ is due to the Gaia-Enceladus component. One important consideration between the two distributions is that the

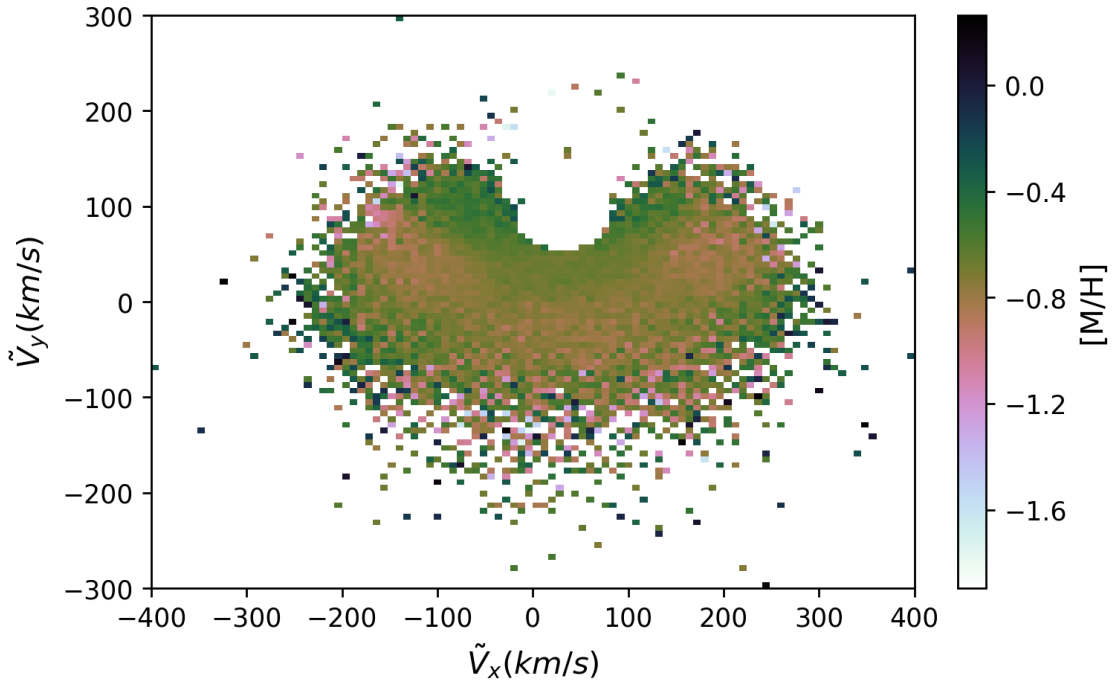

Figure 4.3: Velocity distribution color coded by the [M/H]. The Gaia-Enceladus substructure appears prominently. It seems to be the dominant component of the metal-poor population in our sample.

structures seem more diluted in the 5D case.

Figure 4.3 shows the distribution of pseudo $\tilde{V}_x$ and $\tilde{V}_y$ velocities colored by photometric metallicity [M/H] from `StarHorse` for stars in the solar vicinity (112,312 stars in total). It is possible to notice a clear metallicity gradient, in which stars from the hot thick disk region appearing to be more metal-rich than those from the halo. Again, the most prominent feature is the elongated shape around $\tilde{V}_y \sim 0$, which is the Gaia-Enceladus-Sausage component.

4.3 Metallicity distribution

For the distances probed in this study, we are mostly covering the local inner stellar halo. Also, despite the selection procedure, we still must expect some disk contamination. As discussed in Chapter 1, the outer components of the Galaxy have a complex superposition of different populations. Each population has its specific chemistry and kinematics. Here we will only explore the median metallicity [M/H] as derived by `StarHorse`. Therefore, the overall metallicity distribution will be a combination of these multiple overlapping populations.

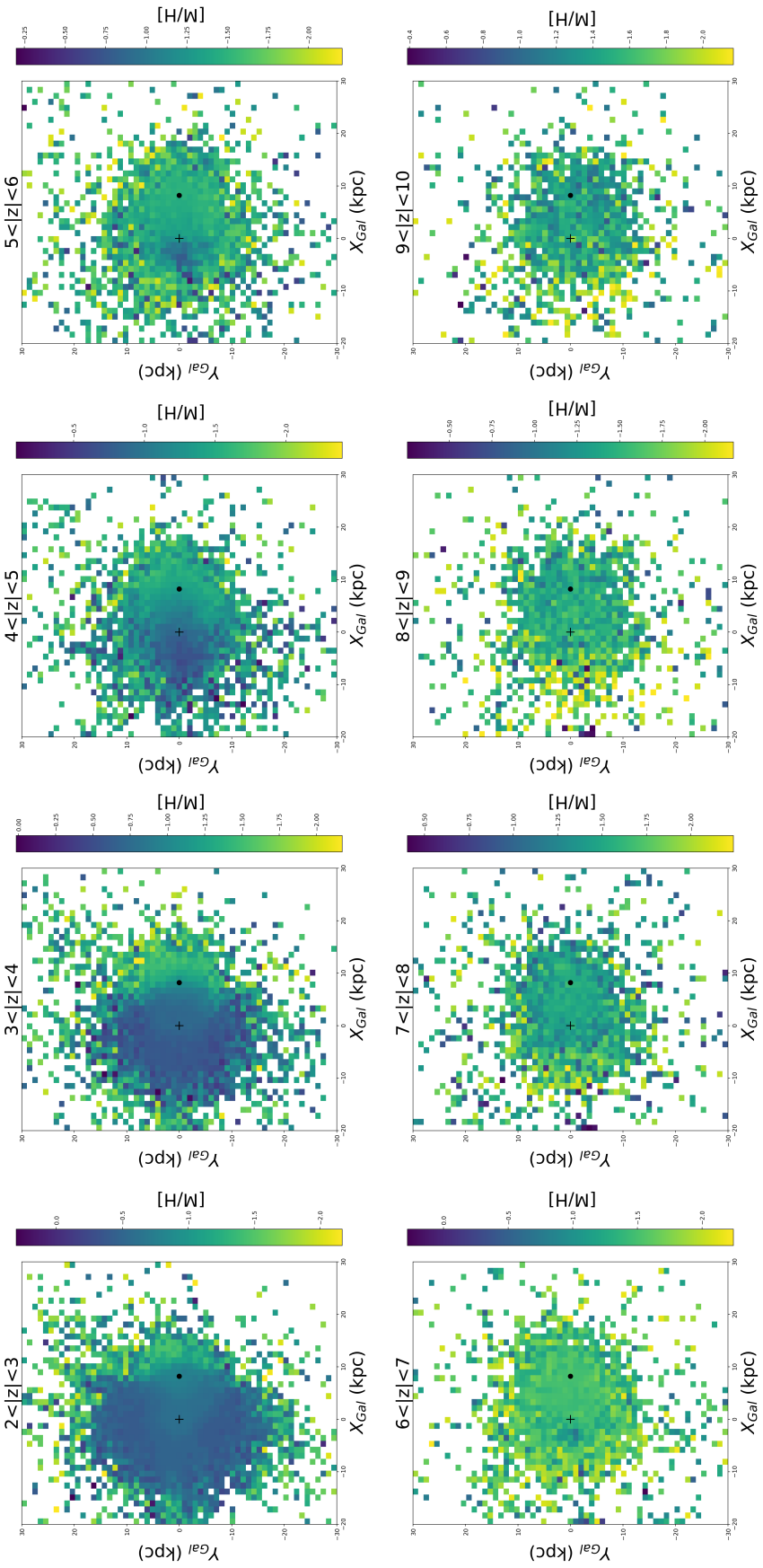

Figure 4.4: Face-on maps of our sample, showing the median metallicity [M/H] of stars in spatial bins of 1 kpc. The different panels are slices in height. The Sun's position is marked by the black dot and the position of the Galactic center is indicated by a cross sign.

Maps of the plane X_{Gal} vs Y_{Gal} as a function of [M/H] are shown in Figure 4.4. The median value of the metallicity is calculated for spatial bins of 1 kpc and shown as the color on the figure. The maps are also divided by height above the Galactic plane, from closest (top left panel with $2 < |Z| < 3$ kpc) to furthest (bottom right panel with $9 < |Z| < 10$ kpc). It is possible to notice a metallicity gradient as we move further away from the disk plane. Locations near the Galactic center also show a slightly higher median metallicity than those at larger radii.

We calculate the radial and vertical metallicity gradients for our sample restricting the sample to R_{Gal} and $|Z_{Gal}| < 10$ kpc to maintain a significant number of objects as we are dealing with photometric metallicities. We measure the median metallicity profile for the sample by separating stars into bins of Z_{Gal} and R_{Gal} 1 kpc wide. The resulting radial and vertical median metallicity profiles are shown in Figure 4.5. The radial profiles show a constant metallicity for $Z \simeq 3$ kpc and $R_{Gal} \simeq 7$ kpc. At $Z \simeq 4$ kpc, on the other hand, a continuous but mild negative radial metallicity gradient develops. The sample then shows a steeper gradient at heights of $\sim$ 4-6 kpc, which flattens out at small radii. At larger heights, the slope of the radial gradient is again generally flat. For the vertical profile, near to the Galactic plane and close to the center of the Galaxy the gradient is less steeper than at large radii. At $Z \sim 7$ the profile flattens with no significant change with radius.

As demonstrated in the literature, the local inner halo ($R_{Gal} < 15$ kpc) is predominantly composed by the hot thick disk stars, Gaia-Enceladus-Sausage debris and other small substructures (Naidu et al., 2020, Horta et al., 2022). In particular, the hot thick disk is prominent at small radii and close to the plane. In Figure 4.5 at $|Z_{Gal}| < 4$ kpc, one may notice that the mean metallicity in the radial profile is about [M/H] $\sim$ -0.6, in agreement with literature measurements, as discussed in Chapter 1. At $|Z_{Gal}| > 4$ kpc, the median metallicity drops to around [M/H] $\sim$ -1.5, again in agreement with the literature. Here, the likely main components that contribute for this lower metallicity are the superposition of accreted substructures, such as Gaia-Enceladus-Sausage, Thammos, Sequoia and Aleph.

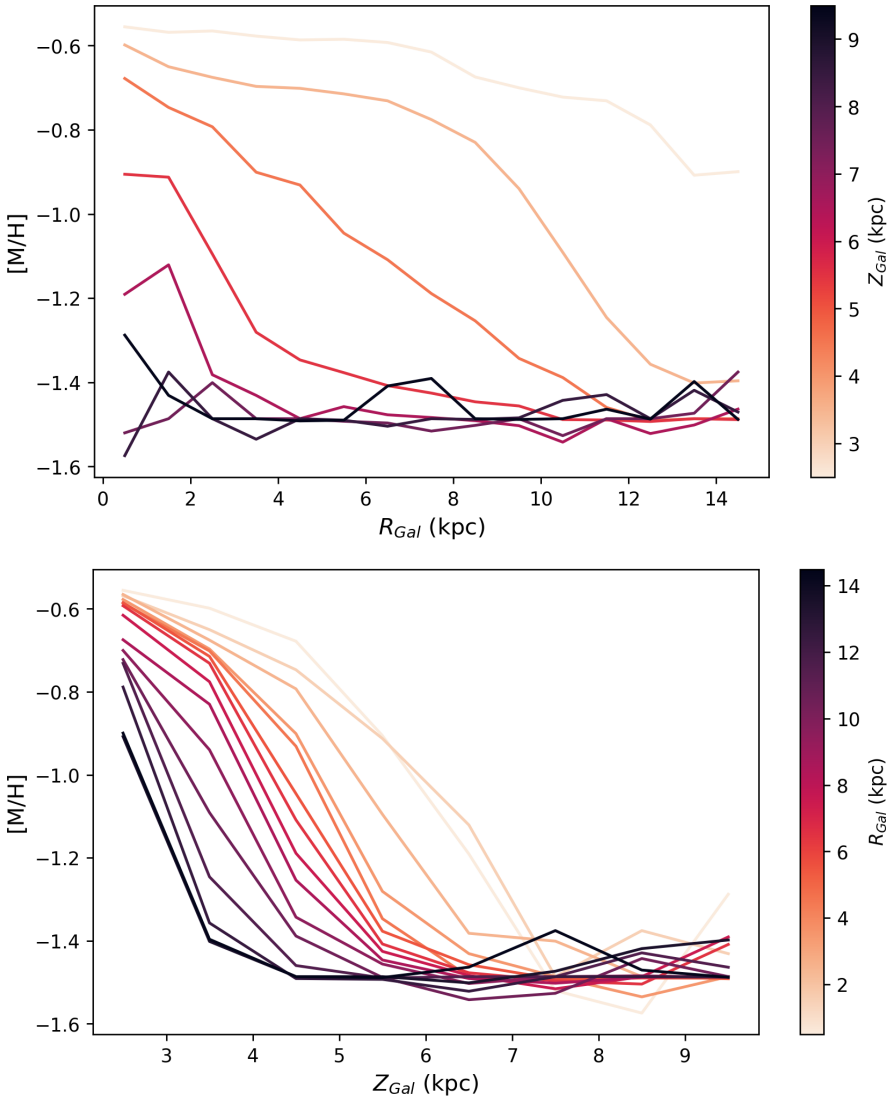

Figure 4.5: The top panel shows the radial median metallicity profile as a function of height above the plane. The bottom panel shows the vertical median metallicity profile as a function of galactocentric radius.

Chapter 5

Discussion and Conclusions

In this work we have presented the basic properties of two extreme populations in our Galaxy: the very low-mass stellar and substellar regime and the halo stellar population.

For the very low-mass stars and substellar regime, we revised ultracool dwarfs properties and the current models that try to describe their internal structure and evolution. We have also argued about the importance of larger samples of ultracool and brown dwarfs and of benchmark systems than those currently available as an important step towards improving their understanding. A large sample of L and T dwarfs will also provide a more detailed description of the spatial distribution of these sources and reliable values of the main parameters of Galactic structure as traced by this population. For the halo stellar population, we described the ongoing debate about the shape and density profile and the metallicity distribution. We also discussed about the several recent discoveries and how they revealed such a complex scenario, as a result of the mergers experienced by our Galaxy.

We have shown here the improvements towards a final and larger sample of ultracool dwarfs. In our first work, described in Carnero Rosell et al. (2019), we developed a method to select and classify ultracool dwarfs based on their photometry. Here we revised the method and updated it.

Using the recent Dark Energy Survey data release (DR2) combined with VHS DR6, VIKING DR5 and AllWISE data, we were able to identify new ultracool dwarfs candidates, probing faint and more distant objects than those presented in the literature so far. Thanks to the new VHS data release, we are currently covering 4,800 deg^2 in the southern sky. We first select these candidates based on their colors (i-z), (z-Y), and (Y-J) up to $z \leq 23$. At this stage, we allowed contamination by M dwarfs and extragalactic sources, addressed at later stages.

With more recent compilations of ultracool dwarfs and M dwarfs from the literature, we updated our color templates. These templates contain a median color for each spectral type ranging from M0 to T9 and are essential to assign a photo-type to the sources. We dubbed as photo-type the inference of a spectral type based only on photometry. We used a classification method originally proposed by Skrzypek et al. (2015). A photo-type is assigned by the minimization of the χ^2 relative to empirical templates of M, L and T dwarfs. Only objects with 5 color indices are considered as having a reliable photo-type, according to our tests, and only those are kept in the target sample. The samples from the literature, both with spectroscopic confirmation and candidates were used here to validate our method. The comparison between our estimated photo-type with those from the literature has shown us that our photo-type is accurate in ± 2 spectral types.

We also used the `Lephare` code with templates from galaxies and quasars to exclude objects that are likely extragalactic. In this case, we demanded that $\chi^2_{classif}$ should be smaller that the $\chi^2_{Lephare}$. We also matched our target sample with the SIMBAD database to exclude further contaminants and also to check `Lephare` results. Objects flagged as extragalactic were also analyzed using their proper motion measurements. Using CatWISE2020 and NSC DR2, we verified if any of these objects have a significant proper motion. This step enabled to recover likely stellar or substellar objects wrongly flagged as extragalactic.

In total, our new sample has 19,583 ultracool dwarf candidates, where 14,099 are new. The complete sample includes 142 spectroscopically confirmed objects, plus 5,342 ultracool dwarf candidates from the literature, where the vast majority (5,257 candidates) are from our previous work (Carnero Rosell et al., 2019). The final catalog of ultracool dwarf candidates presented here is the largest up to this date.

We also presented here the spectra from Gemini/GMOS of a small fraction of ultracool dwarfs compilation from Carnero Rosell et al. (2019). We obtained spectra from 12 objects and all of them were confirmed as ultracool dwarfs. This is a basic sanity check of our selection and classification method.

We have also used both samples of ultracool dwarfs, from Carnero Rosell et al. (2019) DES DR1 and the new compilation from DES DR2 presented here, into some applications. The first was the use of Carnero Rosell et al. (2019) DES DR1 sample to search for wide binary systems composed of a star + UCD and UCD + UCD. We only select systems with wide separation, with distance and proper motion (when available) in common. The final catalog contains 255 binary and six

multiple system candidates, plus nine double ultracool dwarf systems. Applying the same methodology but using the new and uptaded compilation of ultracool dwarf candidates, we search again for systems composed by UCD + UCD. Our interest in this type of system is due to their scarcity.

Using new compilation of ultracool dwarfs we also search for candidates members to nearby young groups and associations. Here we used the BANYAN Σ algorithm to investigate the likelihood of each object in our sample being a member of a young moving group. We found 20 new candidate members with membership probability $> 90\%$. We also identify 291 variable candidate sources in our sample, of which 10% are likely young objects. Also, a higher percentage of the variable sample is concentrated in the L9-T3 range.

Another application presented here was the discussion of a new method to estimate the thin disk scale height for the L and T dwarfs and its limitations. We developed a method to fit the disk spatial density profile using MCMC. The method was extensively tested on simulated samples of L and T dwarfs, validating the algorithm we developed. At the same time, these simulation tests have shown that the errors in magnitudes, photometrically determined spectral types and distances are large enough to significantly bias the inferred density profile parameters when compared to the true simulated values. Furthermore, the current sample of UCDs we have at hand suffers from spatial sampling inhomogeneities that will have to be either eliminated or incorporated into the modelling, something left for a future endeavour.

Concerning the outer components of the Galaxy, we presented here a sample of more than 2 million tentative halo stars. To select our sample, we used the `StarHorse` catalog constructed by a combination of Gaia EDR3 and photometric surveys. In order to select halo stars, we demanded that the stars should have a high tangential velocity (> 200 km/s). We also applied a geometrical cut ($|Z_{Gala}| > 1.5$ kpc) and avoided stars with high extinction ($A_V < 2.0$) to further exclude disk contaminants.

For the tentative halo stars sample, we calculated pseudo-3D velocities to check the consistency of our selection. We were able to retrieve known structures that are reported in the literature, including the gradient in metallicity seen in the V_x vs V_y space due to the Gaia-Enceladus component.

We also presented here an initial study of the metallicity distribution of the halo sample. We show here results that are in agreement with the literature and we also show a clear visible gradient in the metallicity.

The upcoming generation of new surveys, such as the LSST, will allow further identification and characterization for both substellar and halo population. For the low-mass and brown dwarf population, the LSST not only will enable the discovery of new objects but also will be able to measure parallaxes and proper motions for thousands of nearby ultracool dwarfs, improving the measurements of the brown dwarf luminosity function and spatial density profile. For the halo, spectroscopoic surveys such as WEAVE, 4MOST and MOONS on the VLT will obtain not only the missing radial velocity but also high-resolution spectra to enable better disentangling of the several overlapping accretion events in our Galaxy.

References

[1] ABBOTT, T. M. C., ADAMOW, M., AGUENA, M., ALLAM, S., AMON, A., AVILA, S., BACON, D., BANERJI, M., BECHTOL, K., BECKER, M. R., BERNSTEIN, G. M., BERTIN, E., BHARGAVA, S., BRIDLE, S. L., BROOKS, D., BURKE, D. L., ROSELL, A. CARNERO, KIND, M. CARRASCO, CARRETERO, J., CASTANDER, F. J., CAWTHON, R., CHANG, C., CHOI, A., CONSELICE, C., COSTANZI, M., CROCCE, M., COSTA, L. N.DA , DAVIS, T. M., VICENTE, J. DE, DEROSE, J., DESAI, S., DIEHL, H. T., DIETRICH, J. P., DRLICA-WAGNER, A., ECKERT, K., ELVIN-POOLE, J., EVERETT, S., EVRARD, A. E., FERRERO, I., FERTÉ, A., FLAUGHER, B., FOSALBA, P., FRIEDEL, D., FRIEMAN, J., GARCÍA-BELLIDO, J., GELMAN, L., GERDES, D. W., GIANNANTONIO, T., GILL, M., GRUEN, D., GRUENDL, R. A., GSCHWEND, J., GUTIERREZ, G., HARTLEY, W. G., HINTON, S. R., HOLLOWOOD, D. L., HUTERER, D., JAMES, D. J., JELTEMA, T., JOHNSON, M. D., KENT, S., KRON, R., KUEHN, K., KUROPATKIN, N., LAHAV, O., LI, T. S., LIDMAN, C., LIN, H., MACCRANN, N., MAIA, M. A. G., MANNING, T., MARCH, M., MARSHALL, J. L., MARTINI, P., MELCHIOR, P., MENANTEAU, F., MIQUEL, R., MORGAN, R., MYLES, J., NEILSEN, E., OGANDO, R. L. C., PALMESE, A., PAZ-CHINCHÓN, F., PETRAVICK, D., PIERES, A., PLAZAS, A. A., POND, C., RODRIGUEZ-MONROY, M., ROMER, A. K., ROODMAN, A., RYKOFF, E. S., SAKO, M., SANCHEZ, E., SANTIAGO, B., SERRANO, S., SEVILLA-NOARBE, I., SMITH, J. ALLYN., SMITH, M., SOARES-SANTOS, M., SUCHYTA, E., SWANSON, M. E. C., TARLE, G., THOMAS, D., TO, C., TREMBLAY, P. E., TROXEL, M. A., TUCKER, D. L., TURNER, D. J, VARGA, T. N., WALKER, A. R., WECHSLER, R. H., WELLER, J., WESTER, W., WILKINSON, R. D., YANNY, B., ZHANG, Y., NIKUTTA, R., FITZPATRICK, M., JACQUES, A., SCOTT, A., OLSEN, K., HUANG, L., HERRERA, D., JUNEAU, S., NIDEVER, D.,

WEAVER, B. A., ADEAN, C., CORREIA, V., FREITAS, M.DE , FREITAS, F. N., SINGULANI, C., VILA-VERDE, G. The dark energy survey data release 2, 2021.

[2] ACKERMAN, ANDREW S., MARLEY, MARK S. Precipitating Condensation Clouds in Substellar Atmospheres. **ApJ**, v. 556, n. 2, p. 872–884, August 2001.

[3] AIHARA, HIROAKI, ARMSTRONG, ROBERT, BICKERTON, STEVEN, BOSCH, JAMES, COUPON, JEAN, FURUSAWA, HISANORI, HAYASHI, YUSUKE, IKEDA, HIROYUKI, KAMATA, YUKIKO, KAROJI, HIROSHI, KAWANOMOTO, SATOSHI, KOIKE, MICHITARO, KOMIYAMA, YUTAKA, LANG, DUSTIN, LUPTON, ROBERT H., MINEO, SOGO, MIYATAKE, HIRONAO, MIYAZAKI, SATOSHI, MOROKUMA, TOMOKI, OBUCHI, YOSHIYUKI, OISHI, YUKIE, OKURA, YUKI, PRICE, PAUL A., TAKATA, TADAFUMI, TANAKA, MANOBU M., TANAKA, MASAYUKI, TANAKA, YOKO, UCHIDA, TOMOHISA, URAGUCHI, FUMIHIRO, UTSUMI, YOUSUKE, WANG, SHIANG YU, YAMADA, YOSHIHIKO, YAMANOI, HITOMI, YASUDA, NAOKI, ARIMOTO, NOBUO, CHIBA, MASASHI, FINET, FRANCOIS, FUJIMORI, HIROKI, FUJIMOTO, SEIJI, FURUSAWA, JUNKO, GOTO, TOMOTSUGU, GOULDING, ANDY, GUNN, JAMES E., HARIKANE, YUICHI, HATTORI, TAKASHI, HAYASHI, MASAO, HELMINIAK, KRZYSZTOF G., HIGUCHI, RYO, HIKAGE, CHIAKI, HO, PAUL T.P., HSIEH, BAU CHING, HUANG, KUIYUN, HUANG, SONG, IMANISHI, MASATOSHI, IWATA, IKURU, JAELANI, ANTON T., JIAN, HUNG YU, KASHIKAWA, NOBUNARI, KATAYAMA, NOBUHIKO, KOJIMA, TAKASHI, KONNO, AKIRA, KOSHIDA, SHINTARO, KUSAKABE, HARUKA, LEAUTHAUD, ALEXIE, LEE, CHIEN HSIU, LIN, LIHWAI, LIN, YEN TING, MANDELBAUM, RACHEL, MATSUOKA, YOSHIKI, MEDEZINSKI, ELINOR, MIYAMA, SHOKEN, MOMOSE, RIEKO, MORE, ANUPREETA, MORE, SURHUD, MUKAE, SHIRO, MURATA, RYOMA, MURAYAMA, HITOSHI, NAGAO, TOHRU, NAKATA, FUMIAKI, NIIDA, MANA, NIIKURA, HIROKO, NISHIZAWA, ATSUSHI J., OGURI, MASAMUNE, OKABE, NOBUHIRO, ONO, YOSHIAKI, ONODERA, MASATO, ONOUE, MASAFUSA, OUCHI, MASAMI, PYO, TAE SOO, SHIBUYA, TAKATOSHI, SHIMASAKU, KAZUHIRO, SIMET, MELANIE, SPEAGLE, JOSHUA, SPERGEL, DAVID

N., STRAUSS, MICHAEL ABRAM, SUGAHARA, YUMA, SUGIYAMA, NAOSHI, SUTO, YASUSHI, SUZUKI, NAO, TAIT, PHILIP J., TAKADA, MASAHIRO, TERAI, TSUYOSHI, TOBA, YOSHIKI, TURNER, EDWIN LEWIS, UCHIYAMA, HISAKAZU, UMETSU, KEIICHI, URATA, YUJI, USUDA, TOMONORI, YEH, SHERRY, YUMA, SURAPHONG. First data release of the hyper suprime-cam subaru strategic program. **Publication of the Astronomical Society of Japan**, v. 70, n. Special Issue 1, 1 2018.

[4] ALLARD, F., HOMEIER, D., FREYTAG, B. Synthetic spectral libraries. In: ASTRONOMICAL SOCIETY OF INDIA CONFERENCE SERIES, v. 11 of **Astronomical Society of India Conference Series**, p. 33–45, January 2014.

[5] ANDERS, F., KHALATYAN, A., CHIAPPINI, C., QUEIROZ, A. B., SANTIAGO, B. X., JORDI, C., GIRARDI, L., BROWN, A. G. A., MATIJEVIČ, G., MONARI, G., CANTAT-GAUDIN, T., WEILER, M., KHAN, S., MIGLIO, A., CARRILLO, I., ROMERO-GÓMEZ, M., MINCHEV, I., DE JONG, R. S., ANTOJA, T., RAMOS, P., STEINMETZ, M., ENKE, H. Photo-astrometric distances, extinctions, and astrophysical parameters for Gaia DR2 stars brighter than G = 18. **A&A**, v. 628, p. A94, Aug 2019.

[6] ANDERS, F., KHALATYAN, A., QUEIROZ, A. B. A., CHIAPPINI, C., ARDÈVOL, J., CASAMIQUELA, L., FIGUERAS, F., JIMÉNEZ-ARRANZ, Ó., JORDI, C., MONGUIÓ, M., ROMERO-GÓMEZ, M., ALTAMIRANO, D., ANTOJA, T., ASSAAD, R., CANTAT-GAUDIN, T., CASTRO-GINARD, A., ENKE, H., GIRARDI, L., GUIGLION, G., KHAN, S., LURI, X., MIGLIO, A., MINCHEV, I., RAMOS, P., SANTIAGO, B. X., STEINMETZ, M. Photo-astrometric distances, extinctions, and astrophysical parameters for Gaia EDR3 stars brighter than G = 18.5. **A&A**, v. 658, p. A91, February 2022.

[7] ARNOUTS, S., CRISTIANI, S., MOSCARDINI, L., MATARRESE, S., LUCCHIN, F., FONTANA, A., GIALLONGO, E. Measuring and modelling the redshift evolution of clustering: the Hubble Deep Field North. **MNRAS**, v. 310, n. 2, p. 540–556, December 1999.

[8] BALBINOT, E., YANNY, B., LI, T. S., SANTIAGO, B., MARSHALL, J. L., FINLEY, D. A., PIERES, A., ABBOTT, T. M. C., ABDALLA, F. B., ALLAM, S., BENOIT-LÉVY, A., BERNSTEIN, G. M., BERTIN, E., BROOKS,

D., BURKE, D. L., CARNERO ROSELL, A., CARRASCO KIND, M., CARRETERO, J., CUNHA, C. E., DA COSTA, L. N., DEPOY, D. L., DESAI, S., DIEHL, H. T., DOEL, P., ESTRADA, J., FLAUGHER, B., FRIEMAN, J., GERDES, D. W., GRUEN, D., GRUENDL, R. A., HONSCHEID, K., JAMES, D. J., KUEHN, K., KUROPATKIN, N., LAHAV, O., MARCH, M., MARTINI, P., MIQUEL, R., NICHOL, R. C., OGANDO, R., ROMER, A. K., SANCHEZ, E., SCHUBNELL, M., SEVILLA-NOARBE, I., SMITH, R. C., SOARES-SANTOS, M., SOBREIRA, F., SUCHYTA, E., TARLE, G., THOMAS, D., TUCKER, D., WALKER, A. R., DES COLLABORATION, . The Phoenix Stream: A Cold Stream in the Southern Hemisphere. **ApJ**, v. 820, n. 1, p. 58, March 2016.

[9] BARAFFE, I., CHABRIER, G., BARMAN, T. S., ALLARD, F., HAUSCHILDT, P. H. Evolutionary models for cool brown dwarfs and extrasolar giant planets. The case of HD 209458. **A&A**, v. 402, p. 701–712, May 2003.

[10] BARAFFE, ISABELLE, HOMEIER, DEREK, ALLARD, FRANCE, CHABRIER, GILLES. New evolutionary models for pre-main sequence and main sequence low-mass stars down to the hydrogen-burning limit. **A&A**, v. 577, p. A42, May 2015.

[11] BARBUY, BEATRIZ, CHIAPPINI, CRISTINA, GERHARD, ORTWIN. Chemodynamical History of the Galactic Bulge. **ARA&A**, v. 56, p. 223–276, September 2018.

[12] BARDALEZ GAGLIUFFI, DANIELLA C., BURGASSER, ADAM J., SCHMIDT, SARAH J., THEISSEN, CHRISTOPHER, GAGNÉ, JONATHAN, GILLON, MICHAEL, SAHLMANN, JOHANNES, FAHERTY, JACQUELINE K., GELINO, CHRISTOPHER, CRUZ, KELLE L., SKRZYPEK, NATHALIE, LOOPER, DAGNY. The Ultracool SpeXtroscopic Survey. I. Volume-limited Spectroscopic Sample and Luminosity Function of M7-L5 Ultracool Dwarfs. **ApJ**, v. 883, n. 2, p. 205, October 2019.

[13] BARENFELD, SCOTT A., BUBAR, ERIC J., MAMAJEK, ERIC E., YOUNG, PATRICK A. A Kine-chemical Investigation of the AB Dor Moving Group "Stream". **ApJ**, v. 766, n. 1, p. 6, March 2013.

[14] BATE, M. R., BONNELL, I. A. The origin of the initial mass function and its dependence on the mean Jeans mass in molecular clouds. **MNRAS**, v. 356, p. 1201–1221, February 2005.

[15] BATE, M. R., OGILVIE, G. I., LUBOW, S. H., PRINGLE, J. E. The excitation, propagation and dissipation of waves in accretion discs: the non-linear axisymmetric case. **MNRAS**, v. 332, p. 575–600, May 2002.

[16] BATE, MATTHEW R. Stellar, brown dwarf and multiple star properties from a radiation hydrodynamical simulation of star cluster formation. **MNRAS**, v. 419, n. 4, p. 3115–3146, February 2012.

[17] BELL, CAMERON P. M., MAMAJEK, ERIC E., NAYLOR, TIM. A self-consistent, absolute isochronal age scale for young moving groups in the solar neighbourhood. **MNRAS**, v. 454, n. 1, p. 593–614, November 2015.

[18] BELOKUROV, V., ERKAL, D., EVANS, N. W., KOPOSOV, S. E., DEASON, A. J. Co-formation of the disc and the stellar halo. **MNRAS**, v. 478, n. 1, p. 611–619, July 2018.

[19] BELOKUROV, V., EVANS, N. W., BELL, E. F., IRWIN, M. J., HEWETT, P. C., KOPOSOV, S., ROCKOSI, C. M., GILMORE, G., ZUCKER, D. B., FELLHAUER, M., WILKINSON, M. I., BRAMICH, D. M., VIDRIH, S., RIX, H. W., BEERS, T. C., SCHNEIDER, D. P., BARENTINE, J. C., BREWINGTON, H., BRINKMANN, J., HARVANEK, M., KRZESINSKI, J., LONG, D., PAN, K., SNEDDEN, S. A., MALANUSHENKO, O., MALANUSHENKO, V. The Hercules-Aquila Cloud. **ApJ**, v. 657, n. 2, p. L89–L92, March 2007.

[20] BELOKUROV, VASILY, SANDERS, JASON L., FATTAHI, AZADEH, SMITH, MARTIN C., DEASON, ALIS J., EVANS, N. WYN, GRAND, ROBERT J. J. The biggest splash. **MNRAS**, v. 494, n. 3, p. 3880–3898, May 2020.

[21] BENSBY, T., FELTZING, S., LUNDSTRÖM, I., ILYIN, I. α-, r-, and s-process element trends in the Galactic thin and thick disks. **A&A**, v. 433, n. 1, p. 185–203, April 2005.

[22] BEST, WILLIAM M. J., AL., ET . The UltracoolSheet: Photometry, Astrometry, Spectroscopy, and Multiplicity for 3000+ Ultracool Dwarfs and Imaged Exoplanets. 2020.

[23] BEST, WILLIAM M. J., MAGNIER, EUGENE A., LIU, MICHAEL C., ALLER, KIMBERLY M., ZHANG, ZHOUJIAN, BURGETT, W. S., CHAMBERS, K. C., DRAPER, P., FLEWELLING, H., KAISER, N., KUDRITZKI, R. P.,

METCALFE, N., TONRY, J. L., WAINSCOAT, R. J., WATERS, C. Photometry and Proper Motions of M, L, and T Dwarfs from the Pan-STARRS1 3π Survey. **ApJS**, v. 234, n. 1, p. 1, January 2018.

[24] BLAND-HAWTHORN, JOSS, GERHARD, ORTWIN. The Galaxy in Context: Structural, Kinematic, and Integrated Properties. **ARA&A**, v. 54, p. 529–596, Sep 2016.

[25] BOCHANSKI, JOHN J., HAWLEY, SUZANNE L., COVEY, KEVIN R., WEST, ANDREW A., REID, I. NEILL, GOLIMOWSKI, DAVID A., IVEZIĆ, ŽELJKO. The Luminosity and Mass Functions of Low-mass Stars in the Galactic Disk. II. The Field. **AJ**, v. 139, n. 6, p. 2679–2699, June 2010.

[26] BONNELL, I. A., CLARK, P., BATE, M. R. Gravitational fragmentation and the formation of brown dwarfs in stellar clusters. **MNRAS**, v. 389, p. 1556–1562, October 2008.

[27] BOSS, A. P. Formation of Planetary-Mass Objects by Protostellar Collapse and Fragmentation. **ApJ**, v. 551, p. L167–L170, April 2001.

[28] BOVY, JO, RIX, HANS-WALTER, SCHLAFLY, EDWARD F., NIDEVER, DAVID L., HOLTZMAN, JON A., SHETRONE, MATTHEW, BEERS, TIMOTHY C. The Stellar Population Structure of the Galactic Disk. **ApJ**, v. 823, n. 1, p. 30, May 2016.

[29] BRESSAN, A., MARIGO, P., GIRARDI, L., SALASNICH, B., DAL CERO, C., RUBELE, S., NANNI, A. PARSEC: stellar tracks and isochrones with the PAdova and TRieste Stellar Evolution Code. **MNRAS**, v. 427, p. 127–145, November 2012.

[30] BURGASSER, A. J., KIRKPATRICK, J. D., CRUZ, K. L., REID, I. N., LEGGETT, S. K., LIEBERT, J., BURROWS, A., BROWN, M. E. Hubble Space Telescope NICMOS Observations of T Dwarfs: Brown Dwarf Multiplicity and New Probes of the L/T Transition. **ApJS**, v. 166, p. 585–612, October 2006.

[31] BURGASSER, ADAM J. T Dwarfs and the Substellar Mass Function. I. Monte Carlo Simulations. **ApJS**, v. 155, n. 1, p. 191–207, November 2004.

[32] BURGASSER, ADAM J., KIRKPATRICK, J. DAVY, BROWN, MICHAEL E., REID, I. NEILL, BURROWS, ADAM, LIEBERT, JAMES, MATTHEWS,

KEITH, GIZIS, JOHN E., DAHN, CONARD C., MONET, DAVID G., CUTRI, ROC M., SKRUTSKIE, MICHAEL F. The Spectra of T Dwarfs. I. Near-Infrared Data and Spectral Classification. **ApJ**, v. 564, n. 1, p. 421–451, January 2002a.

[33] BURGASSER, ADAM J., MARLEY, MARK S., ACKERMAN, ANDREW S., SAUMON, DIDIER, LODDERS, KATHARINA, DAHN, CONARD C., HARRIS, HUGH C., KIRKPATRICK, J. DAVY. Evidence of Cloud Disruption in the L/T Dwarf Transition. **ApJ**, v. 571, n. 2, p. L151–L154, June 2002b.

[34] BURNINGHAM, BEN, CARDOSO, C. V., SMITH, L., LEGGETT, S. K., SMART, R. L., MANN, A. W., DHITAL, S., LUCAS, P. W., TINNEY, C. G., PINFIELD, D. J., ZHANG, Z., MORLEY, C., SAUMON, D., ALLER, K., LITTLEFAIR, S. P., HOMEIER, D., LODIEU, N., DEACON, N., MARLEY, M. S., VAN SPAANDONK, L., BAKER, D., ALLARD, F., ANDREI, A. H., CANTY, J., CLARKE, J., DAY-JONES, A. C., DUPUY, T., FORTNEY, J. J., GOMES, J., ISHII, M., JONES, H. R. A., LIU, M., MAGAZZÚ, A., MAROCCO, F., MURRAY, D. N., ROJAS-AYALA, B., TAMURA, M. 76 T dwarfs from the UKIDSS LAS: benchmarks, kinematics and an updated space density. **MNRAS**, v. 433, n. 1, p. 457–497, July 2013.

[35] BURNINGHAM, BEN, MARLEY, M. S., LINE, M. R., LUPU, R., VISSCHER, C., MORLEY, C. V., SAUMON, D., FREEDMAN, R. Retrieval of atmospheric properties of cloudy L dwarfs. **MNRAS**, v. 470, n. 1, p. 1177–1197, September 2017.

[36] BURROWS, A., MARLEY, M., HUBBARD, W. B., LUNINE, J. I., GUILLOT, T., SAUMON, D., FREEDMAN, R., SUDARSKY, D., SHARP, C. A Nongray Theory of Extrasolar Giant Planets and Brown Dwarfs. **ApJ**, v. 491, n. 2, p. 856–875, December 1997.

[37] BURROWS, ADAM, SUDARSKY, DAVID, HUBENY, IVAN. L and T Dwarf Models and the L to T Transition. **ApJ**, v. 640, n. 2, p. 1063–1077, April 2006.

[38] CALAMARI, EMILY, FAHERTY, JACQUELINE K., BURNINGHAM, BEN, GONZALES, EILEEN, BARDALEZ-GAGLIUFFI, DANIELLA, VOS, JOHANNA M., GEMMA, MARINA, WHITEFORD, NIALL, GAARN, JOSEFINE. An Atmospheric Retrieval of the Brown Dwarf Gliese 229B. **ApJ**, v. 940, n. 2, p. 164, December 2022.

[39] CARNERO ROSELL, A., SANTIAGO, B., DAL PONTE, M., BURNINGHAM, B., DA COSTA, L. N., JAMES, D. J., MARSHALL, J. L., MCMAHON, R. G., BECHTOL, K., DE PARIS, L., LI, T., PIERES, A., GARCíA-BELLIDO, J., ABBOTT, T. M. C., ANNIS, J., AVILA, S., BERNSTEIN, G. M., BROOKS, D., BURKE, D. L., CARRASCO KIND, M., CARRETERO, J., DE VICENTE, J., DRLICA-WAGNER, A., FOSALBA, P., FRIEMAN, J., GAZTANAGA, E., GRUENDL, R. A., GSCHWEND, J., GUTIERREZ, G., HOLLOWOOD, D. L., MAIA, M. A. G., MENANTEAU, F., MIQUEL, R., PLAZAS, A. A., ROODMAN, A., SANCHEZ, E., SCARPINE, V., SCHINDLER, R., SERRANO, S., SEVILLA-NOARBE, I., SMITH, M., SOBREIRA, F., SOARES-SANTOS, M., SUCHYTA, E., SWANSON, M. E. C., TARLE, G., VIKRAM, V., WALKER, A. R., DES COLLABORATION, . Brown dwarf census with the Dark Energy Survey year 3 data and the thin disc scale height of early L types. **MNRAS**, v. 489, n. 4, p. 5301–5325, November 2019.

[40] CAROLLO, DANIELA, BEERS, TIMOTHY C., LEE, YOUNG SUN, CHIBA, MASASHI, NORRIS, JOHN E., WILHELM, RONALD, SIVARANI, THIRUPATHI, MARSTELLER, BRIAN, MUNN, JEFFREY A., BAILER-JONES, CORYN A. L. Two stellar components in the halo of the Milky Way. **Nature**, v. 450, n. 7172, p. 1020–1025, Dec 2007.

[41] CHABRIER, GILLES. The Galactic Disk Mass Budget. II. Brown Dwarf Mass Function and Density. **ApJ**, v. 567, n. 1, p. 304–313, March 2002.

[42] CHABRIER, GILLES. Galactic Stellar and Substellar Initial Mass Function. **Publications of the Astronomical Society of the Pacific**, v. 115, p. 763–795, July 2003.

[43] CHIAPPINI, C., MATTEUCCI, F., GRATTON, R. The Chemical Evolution of the Galaxy: The Two-Infall Model. **ApJ**, v. 477, n. 2, p. 765–780, March 1997.

[44] CONROY, CHARLIE, NAIDU, ROHAN P., ZARITSKY, DENNIS, BONACA, ANA, CARGILE, PHILLIP, JOHNSON, BENJAMIN D., CALDWELL, NELSON. Resolving the Metallicity Distribution of the Stellar Halo with the H3 Survey. **ApJ**, v. 887, n. 2, p. 237, December 2019.

[45] CRUZ, KELLE L., REID, I. NEILL, KIRKPATRICK, J. DAVY, BURGASSER, ADAM J., LIEBERT, JAMES, SOLOMON, ADAM R., SCHMIDT,

SARAH J., ALLEN, PETER R., HAWLEY, SUZANNE L., COVEY, KEVIN R. Meeting the Cool Neighbors. IX. The Luminosity Function of M7-L8 Ultracool Dwarfs in the Field. **AJ**, v. 133, n. 2, p. 439–467, Feb 2007.

[46] CUSHING, MICHAEL C., KIRKPATRICK, J. DAVY, GELINO, CHRISTOPHER R., GRIFFITH, ROGER L., SKRUTSKIE, MICHAEL F., MAINZER, A., MARSH, KENNETH A., BEICHMAN, CHARLES A., BURGASSER, ADAM J., PRATO, LISA A., SIMCOE, ROBERT A., MARLEY, MARK S., SAUMON, D., FREEDMAN, RICHARD S., EISENHARDT, PETER R., WRIGHT, EDWARD L. The Discovery of Y Dwarfs using Data from the Wide-field Infrared Survey Explorer (WISE). **ApJ**, v. 743, n. 1, p. 50, December 2011.

[47] CUTRI, R. M., SKRUTSKIE, M. F., VAN DYK, S., BEICHMAN, C. A., CARPENTER, J. M., CHESTER, T., CAMBRESY, L., EVANS, T., FOWLER, J., GIZIS, J., HOWARD, E., HUCHRA, J., JARRETT, T., KOPAN, E. L., KIRKPATRICK, J. D., LIGHT, R. M., MARSH, K. A., MCCALLON, H., SCHNEIDER, S., STIENING, R., SYKES, M., WEINBERG, M., WHEATON, W. A., WHEELOCK, S., ZACARIAS, N. **2MASS All Sky Catalog of point sources.**: 2003.

[48] DAL PONTE, M., SANTIAGO, B., CARNERO ROSELL, A., BURNINGHAM, B., YANNY, B., MARSHALL, J. L., BECHTOL, K., MARTINI, P., LI, T. S., DE PARIS, L., ABBOTT, T. M. C., AGUENA, M., ALLAM, S., AVILA, S., BERTIN, E., BHARGAVA, S., BROOKS, D., BUCKLEY-GEER, E., KIND, M. CARRASCO, CARRETERO, J., DA COSTA, L. N., DE VICENTE, J., DIEHL, H. T., DOEL, P., EIFLER, T. F., EVERETT, S., FLAUGHER, B., FOSALBA, P., FRIEMAN, J., GARCíA-BELLIDO, J., GAZTANAGA, E., GERDES, D. W., GRUEN, D., GRUENDL, R. A., GSCHWEND, J., GUTIERREZ, G., HINTON, S. R., HOLLOWOOD, D. L., HONSCHEID, K., JAMES, D. J., KUEHN, K., KUROPATKIN, N., MAIA, M. A. G., MARCH, M., MENANTEAU, F., MIQUEL, R., PALMESE, A., PAZ-CHINCHÓN, F., PLAZAS, A. A., SANCHEZ, E., SCARPINE, V., SERRANO, S., SEVILLA-NOARBE, I., SMITH, M., SUCHYTA, E., SWANSON, M. E. C., TARLE, G., THOMAS, D., VARGA, T. N., WALKER, A. R., WALKER, A. R., DES COLLABORATION, . Increasing the census of ultracool dwarfs in wide binary and multiple systems using Dark Energy Survey DR1 and Gaia DR2 data. **MNRAS**, v. 499, n. 4, p. 5302–5317, December 2020.

[49] DAS, PAYEL, HAWKINS, KEITH, JOFRÉ, PAULA. Ages and kinematics of chemically selected, accreted Milky Way halo stars. **MNRAS**, v. 493, n. 4, p. 5195–5207, April 2020.

[50] DAY-JONES, A. C., MAROCCO, F., PINFIELD, D. J., ZHANG, Z. H., BURNINGHAM, B., DEACON, N., RUIZ, M. T., GALLARDO, J., JONES, H. R. A., LUCAS, P. W. L., JENKINS, J. S., GOMES, J., FOLKES, S. L., CLARKE, J. R. A. The sub-stellar birth rate from UKIDSS. **MNRAS**, v. 430, n. 2, p. 1171–1187, April 2013.

[51] DE JONG, JELTE T. A., YANNY, BRIAN, RIX, HANS-WALTER, DOLPHIN, ANDREW E., MARTIN, NICOLAS F., BEERS, TIMOTHY C. Mapping the Stellar Structure of the Milky Way Thick Disk and Halo Using SEGUE Photometry. **ApJ**, v. 714, n. 1, p. 663–674, May 2010.

[52] DE PROPRIS, R., HARRISON, C. D., MARES, P. J. Mapping the Galactic Halo with Blue Horizontal Branch Stars from the Two-degree Field Quasar Redshift Survey. **ApJ**, v. 719, p. 1582–1587, August 2010.

[53] DEASON, A. J., BELOKUROV, V., EVANS, N. W. The Milky Way stellar halo out to 40 kpc: squashed, broken but smooth. **MNRAS**, v. 416, n. 4, p. 2903–2915, October 2011.

[54] DEASON, ALIS J., BELOKUROV, VASILY, KOPOSOV, SERGEY E., LANCASTER, LACHLAN. Apocenter Pile-up: Origin of the Stellar Halo Density Break. **ApJ**, v. 862, n. 1, p. L1, July 2018.

[55] DELGADO-DONATE, E. J., CLARKE, C. J., BATE, M. R. The dependence of the substellar initial mass function on the initial conditions for star formation. **MNRAS**, v. 347, n. 3, p. 759–770, January 2004.

[56] DHITAL, S., WEST, A. A., STASSUN, K. G., SCHLUNS, K. J., MASSEY, A. P. SLoWPoKES-II: 100,000 Wide Binaries Identified in SDSS without Proper Motions. **AJ**, v. 150, p. 57, August 2015.

[57] DHITAL, SAURAV, BURGASSER, ADAM J., LOOPER, DAGNY L., STASSUN, KEIVAN G. Resolved Spectroscopy of M Dwarf/L Dwarf Binaries. IV. Discovery of AN M9 + L6 Binary Separated by Over 100 AU. **AJ**, v. 141, p. 7, January 2011.

[58] DI MATTEO, P., HAYWOOD, M., LEHNERT, M. D., KATZ, D., KHOPERSKOV, S., SNAITH, O. N., GÓMEZ, A., ROBICHON, N. The Milky Way has no in-situ halo other than the heated thick disc. Composition of the stellar halo and age-dating the last significant merger with Gaia DR2 and APOGEE. **A&A**, v. 632, p. A4, December 2019.

[59] DODD, EMMA, CALLINGHAM, THOMAS M., HELMI, AMINA, MATSUNO, TADAFUMI, RUIZ-LARA, TOMÁS, BALBINOT, EDUARDO, LÖVDAL, SOFIE. Gaia DR3 view of dynamical substructure in the stellar halo near the Sun. **A&A**, v. 670, p. L2, February 2023.

[60] DRLICA-WAGNER, A., BECHTOL, K., RYKOFF, E. S., LUQUE, E., QUEIROZ, A., MAO, Y. Y., WECHSLER, R. H., SIMON, J. D., SANTIAGO, B., YANNY, B., BALBINOT, E., DODELSON, S., FAUSTI NETO, A., JAMES, D. J., LI, T. S., MAIA, M. A. G., MARSHALL, J. L., PIERES, A., STRINGER, K., WALKER, A. R., ABBOTT, T. M. C., ABDALLA, F. B., ALLAM, S., BENOIT-LÉVY, A., BERNSTEIN, G. M., BERTIN, E., BROOKS, D., BUCKLEY-GEER, E., BURKE, D. L., CARNERO ROSELL, A., CARRASCO KIND, M., CARRETERO, J., CROCCE, M., DA COSTA, L. N., DESAI, S., DIEHL, H. T., DIETRICH, J. P., DOEL, P., EIFLER, T. F., EVRARD, A. E., FINLEY, D. A., FLAUGHER, B., FOSALBA, P., FRIEMAN, J., GAZTANAGA, E., GERDES, D. W., GRUEN, D., GRUENDL, R. A., GUTIERREZ, G., HONSCHEID, K., KUEHN, K., KUROPATKIN, N., LAHAV, O., MARTINI, P., MIQUEL, R., NORD, B., OGANDO, R., PLAZAS, A. A., REIL, K., ROODMAN, A., SAKO, M., SANCHEZ, E., SCARPINE, V., SCHUBNELL, M., SEVILLA-NOARBE, I., SMITH, R. C., SOARES-SANTOS, M., SOBREIRA, F., SUCHYTA, E., SWANSON, M. E. C., TARLE, G., TUCKER, D., VIKRAM, V., WESTER, W., ZHANG, Y., ZUNTZ, J., DES COLLABORATION, . Eight Ultra-faint Galaxy Candidates Discovered in Year Two of the Dark Energy Survey. **ApJ**, v. 813, n. 2, p. 109, November 2015.

[61] DUPUY, T. J., LIU, M. C. **Apjs**, v. 201, p. 19, August 2012.

[62] EDGE, A., SUTHERLAND, W., KUIJKEN, K., DRIVER, S., MCMAHON, R., EALES, S., EMERSON, J. P. The VISTA Kilo-degree Infrared Galaxy (VIKING) Survey: Bridging the Gap between Low and High Redshift. **The Messenger**, v. 154, p. 32–34, December 2013.

[63] ELMEGREEN, B. G. On the Initial Conditions for Star Formation and the Initial Mass Function. **ApJ**, v. 731, p. 61, April 2011.

[64] EPCHTEIN, N., DE BATZ, B., CAPOANI, L., CHEVALLIER, L., COPET, E., FOUQUÉ, P., LACOMBE, P., LE BERTRE, T., PAU, S., ROUAN, D., RUPHY, S., SIMON, G., TIPHÈNE, D., BURTON, W. B., BERTIN, E., DEUL, E., HABING, H., BORSENBERGER, J., DENNEFELD, M., GUGLIELMO, F., LOUP, C., MAMON, G., NG, Y., OMONT, A., PROVOST, L., RENAULT, J. C., TANGUY, F., KIMESWENGER, S., KIENEL, C., GARZON, F., PERSI, P., FERRARI-TONIOLO, M., ROBIN, A., PATUREL, G., VAUGLIN, I., FORVEILLE, T., DELFOSSE, X., HRON, J., SCHULTHEIS, M., APPENZELLER, I., WAGNER, S., BALAZS, L., HOLL, A., LÉPINE, J., BOSCOLO, P., PICAZZIO, E., DUC, P. A., MENNESSIER, M. O. The deep near-infrared southern sky survey (DENIS). **The Messenger**, v. 87, p. 27–34, Mar 1997.

[65] FAHERTY, J. K., BURGASSER, A. J., WALTER, F. M., BLIEK, N.VAN DER , SHARA, M. M., CRUZ, K. L., WEST, A. A., VRBA, F. J., ANGLADA-ESCUDÉ, G. The Brown Dwarf Kinematics Project (BDKP). III. Parallaxes for 70 Ultracool Dwarfs. **ApJ**, v. 752, p. 56, June 2012.

[66] FAHERTY, J. K., BURGASSER, A. J., WEST, A. A., BOCHANSKI, J. J., CRUZ, K. L., SHARA, M. M., WALTER, F. M. The Brown Dwarf Kinematics Project. II. Details on Nine Wide Common Proper Motion Very Low Mass Companions to Nearby Stars. **AJ**, v. 139, p. 176–194, January 2010.

[67] FAHERTY, JACQUELINE K., RIEDEL, ADRIC R., CRUZ, KELLE L., GAGNE, JONATHAN, FILIPPAZZO, JOSEPH C., LAMBRIDES, ERINI, FICA, HALEY, WEINBERGER, ALYCIA, THORSTENSEN, JOHN R., TINNEY, C. G., BALDASSARE, VIVIENNE, LEMONIER, EMILY, RICE, EMILY L. Population Properties of Brown Dwarf Analogs to Exoplanets. **ApJS**, v. 225, n. 1, p. 10, July 2016.

[68] FERNÁNDEZ-ALVAR, E., CARIGI, L., ALLENDE PRIETO, C., HAYDEN, M. R., BEERS, T. C., FERNÁNDEZ-TRINCADO, J. G., MEZA, A., SCHULTHEIS, M., SANTIAGO, B. X., QUEIROZ, A. B., ANDERS, F., DA COSTA, L. N., CHIAPPINI, C. Chemical trends in the Galactic halo from APOGEE data. **MNRAS**, v. 465, n. 2, p. 1586–1600, February 2017.

[69] FEUILLET, DIANE K., FELTZING, SOFIA, SAHLHOLDT, CHRISTIAN L., CASAGRANDE, LUCA. The SkyMapper-Gaia RVS view of the Gaia-Enceladus-Sausage - an investigation of the metallicity and mass of the Milky Way's last major merger. **MNRAS**, v. 497, n. 1, p. 109–124, September 2020.

[70] FEUILLET, DIANE K., SAHLHOLDT, CHRISTIAN L., FELTZING, SOFIA, CASAGRANDE, LUCA. Selecting accreted populations: metallicity, elemental abundances, and ages of the Gaia-Sausage-Enceladus and Sequoia populations. **MNRAS**, v. 508, n. 1, p. 1489–1508, November 2021.

[71] FLAUGHER, B., DIEHL, H. T., HONSCHEID, K., ABBOTT, T. M. C., ALVAREZ, O., ANGSTADT, R., ANNIS, J. T., ANTONIK, M., BALLESTER, O., BEAUFORE, L., BERNSTEIN, G. M., BERNSTEIN, R. A., BIGELOW, B., BONATI, M., BOPRIE, D., BROOKS, D., BUCKLEY-GEER, E. J., CAMPA, J., CARDIEL-SAS, L., CASTANDER, F. J., CASTILLA, J., CEASE, H., CELA-RUIZ, J. M., CHAPPA, S., CHI, E., COOPER, C., DA COSTA, L. N., DEDE, E., DERYLO, G., DEPOY, D. L., DE VICENTE, J., DOEL, P., DRLICA-WAGNER, A., EITING, J., ELLIOTT, A. E., EMES, J., ESTRADA, J., FAUSTI NETO, A., FINLEY, D. A., FLORES, R., FRIEMAN, J., GERDES, D., GLADDERS, M. D., GREGORY, B., GUTIERREZ, G. R., HAO, J., HOLLAND, S. E., HOLM, S., HUFFMAN, D., JACKSON, C., JAMES, D. J., JONAS, M., KARCHER, A., KARLINER, I., KENT, S., KESSLER, R., KOZLOVSKY, M., KRON, R. G., KUBIK, D., KUEHN, K., KUHLMANN, S., KUK, K., LAHAV, O., LATHROP, A., LEE, J., LEVI, M. E., LEWIS, P., LI, T. S., MANDRICHENKO, I., MARSHALL, J. L., MARTINEZ, G., MERRITT, K. W., MIQUEL, R., MUÑOZ, F., NEILSEN, E. H., NICHOL, R. C., NORD, B., OGANDO, R., OLSEN, J., PALAIO, N., PATTON, K., PEOPLES, J., PLAZAS, A. A., RAUCH, J., REIL, K., RHEAULT, J.-P., ROE, N. A., ROGERS, H., ROODMAN, A., SANCHEZ, E., SCARPINE, V., SCHINDLER, R. H., SCHMIDT, R., SCHMITT, R., SCHUBNELL, M., SCHULTZ, K., SCHURTER, P., SCOTT, L., SERRANO, S., SHAW, T. M., SMITH, R. C., SOARES-SANTOS, M., STEFANIK, A., STUERMER, W., SUCHYTA, E., SYPNIEWSKI, A., TARLE, G., THALER, J., TIGHE, R., TRAN, C., TUCKER, D., WALKER, A. R., WANG, G., WATSON, M., WEAVERDYCK, C., WESTER, W., WOODS, R., YANNY, B., DES COLLABORATION, . The Dark Energy Camera. **AJ**, v. 150, p. 150, November 2015.

[72] FONTANIVE, C., BILLER, B., BONAVITA, M., ALLERS, K. Constraining the multiplicity statistics of the coolest brown dwarfs: binary fraction continues to decrease with spectral type. **MNRAS**, v. 479, p. 2702–2727, September 2018.

[73] FRENK, C. S., WHITE, S. D. M. Dark matter and cosmic structure. **Annalen der Physik**, v. 524, n. 9-10, p. 507–534, October 2012.

[74] GAGNÉ, JONATHAN, MAMAJEK, ERIC E., MALO, LISON, RIEDEL, ADRIC, RODRIGUEZ, DAVID, LAFRENIÈRE, DAVID, FAHERTY, JACQUELINE K., ROY-LOUBIER, OLIVIER, PUEYO, LAURENT, ROBIN, ANNIE C., DOYON, RENÉ. BANYAN. XI. The BANYAN Σ Multivariate Bayesian Algorithm to Identify Members of Young Associations with 150 pc. **ApJ**, v. 856, n. 1, p. 23, March 2018.

[75] GAIA COLLABORATION, BABUSIAUX, C., VAN LEEUWEN, F., BARSTOW, M. A., JORDI, C., VALLENARI, A., BOSSINI, D., BRESSAN, A., CANTAT-GAUDIN, T., VAN LEEUWEN, M., BROWN, A. G. A., PRUSTI, T., DE BRUIJNE, J. H. J., BAILER-JONES, C. A. L., BIERMANN, M., EVANS, D. W., EYER, L., JANSEN, F., KLIONER, S. A., LAMMERS, U., LINDEGREN, L., LURI, X., MIGNARD, F., PANEM, C., POURBAIX, D., RANDICH, S., SARTORETTI, P., SIDDIQUI, H. I., SOUBIRAN, C., WALTON, N. A., ARENOU, F., BASTIAN, U., CROPPER, M., DRIMMEL, R., KATZ, D., LATTANZI, M. G., BAKKER, J., CACCIARI, C., CASTAÑEDA, J., CHAOUL, L., CHEEK, N., DE ANGELI, F., FABRICIUS, C., GUERRA, R., HOLL, B., MASANA, E., MESSINEO, R., MOWLAVI, N., NIENARTOWICZ, K., PANUZZO, P., PORTELL, J., RIELLO, M., SEABROKE, G. M., TANGA, P., THÉVENIN, F., GRACIA-ABRIL, G., COMORETTO, G., GARCIA-REINALDOS, M., TEYSSIER, D., ALTMANN, M., ANDRAE, R., AUDARD, M., BELLAS-VELIDIS, I., BENSON, K., BERTHIER, J., BLOMME, R., BURGESS, P., BUSSO, G., CARRY, B., CELLINO, A., CLEMENTINI, G., CLOTET, M., CREEVEY, O., DAVIDSON, M., DE RIDDER, J., DELCHAMBRE, L., DELL'ORO, A., DUCOURANT, C., FERNÁNDEZ-HERNÁNDEZ, J., FOUESNEAU, M., FRÉMAT, Y., GALLUCCIO, L., GARCíA-TORRES, M., GONZÁLEZ-NÚÑEZ, J., GONZÁLEZ-VIDAL, J. J., GOSSET, E., GUY, L. P., HALBWACHS, J. L., HAMBLY, N. C., HARRISON, D. L., HERNÁNDEZ, J., HESTROFFER, D., HODGKIN, S. T., HUTTON, A.,

JASNIEWICZ, G., JEAN-ANTOINE-PICCOLO, A., JORDAN, S., KORN, A. J., KRONE-MARTINS, A., LANZAFAME, A. C., LEBZELTER, T., LÖFFLER, W., MANTEIGA, M., MARRESE, P. M., MARTíN-FLEITAS, J. M., MOITINHO, A., MORA, A., MUINONEN, K., OSINDE, J., PANCINO, E., PAUWELS, T., PETIT, J. M., RECIO-BLANCO, A., RICHARDS, P. J., RIMOLDINI, L., ROBIN, A. C., SARRO, L. M., SIOPIS, C., SMITH, M., SOZZETTI, A., SÜVEGES, M., TORRA, J., VAN REEVEN, W., ABBAS, U., ABREU ARAMBURU, A., ACCART, S., AERTS, C., ALTAVILLA, G., ÁLVAREZ, M. A., ALVAREZ, R., ALVES, J., ANDERSON, R. I., ANDREI, A. H., ANGLADA VARELA, E., ANTICHE, E., ANTOJA, T., ARCAY, B., ASTRAATMADJA, T. L., BACH, N., BAKER, S. G., BALAGUER-NÚÑEZ, L., BALM, P., BARACHE, C., BARATA, C., BARBATO, D., BARBLAN, F., BARKLEM, P. S., BARRADO, D., BARROS, M., BARTHOLOMÉ MUÑOZ, L., BASSILANA, J. L., BECCIANI, U., BELLAZZINI, M., BERIHUETE, A., BERTONE, S., BIANCHI, L., BIENAYMÉ, O., BLANCO-CUARESMA, S., BOCH, T., BOECHE, C., BOMBRUN, A., BORRACHERO, R., BOUQUILLON, S., BOURDA, G., BRAGAGLIA, A., BRAMANTE, L., BREDDELS, M. A., BROUILLET, N., BRÜSEMEISTER, T., BRUGALETTA, E., BUCCIARELLI, B., BURLACU, A., BUSONERO, D., BUTKEVICH, A. G., BUZZI, R., CAFFAU, E., CANCELLIERE, R., CANNIZZARO, G., CARBALLO, R., CARLUCCI, T., CARRASCO, J. M., CASAMIQUELA, L., CASTELLANI, M., CASTRO-GINARD, A., CHARLOT, P., CHEMIN, L., CHIAVASSA, A., COCOZZA, G., COSTIGAN, G., COWELL, S., CRIFO, F., CROSTA, M., CROWLEY, C., CUYPERS, J., DAFONTE, C., DAMERDJI, Y., DAPERGOLAS, A., DAVID, P., DAVID, M., DE LAVERNY, P., DE LUISE, F., DE MARCH, R., DE MARTINO, D., DE SOUZA, R., DE TORRES, A., DEBOSSCHER, J., DEL POZO, E., DELBO, M., DELGADO, A., DELGADO, H. E., DIAKITE, S., DIENER, C., DISTEFANO, E., DOLDING, C., DRAZINOS, P., DURÁN, J., EDVARDSSON, B., ENKE, H., ERIKSSON, K., ESQUEJ, P., EYNARD BONTEMPS, G., FABRE, C., FABRIZIO, M., FAIGLER, S., FALCÃO, A. J., FARRÀS CASAS, M., FEDERICI, L., FEDORETS, G., FERNIQUE, P., FIGUERAS, F., FILIPPI, F., FINDEISEN, K., FONTI, A., FRAILE, E., FRASER, M., FRÉZOULS, B., GAI, M., GALLETI, S., GARABATO, D., GARCíA-SEDANO, F., GAROFALO, A., GARRALDA, N., GAVEL, A., GAVRAS, P., GERSSEN, J., GEYER, R., GIACOBBE, P., GILMORE, G.,

GIRONA, S., GIUFFRIDA, G., GLASS, F., GOMES, M., GRANVIK, M., GUEGUEN, A., GUERRIER, A., GUIRAUD, J., GUTIÉ, R., HAIGRON, R., HATZIDIMITRIOU, D., HAUSER, M., HAYWOOD, M., HEITER, U., HELMI, A., HEU, J., HILGER, T., HOBBS, D., HOFMANN, W., HOLLAND, G., HUCKLE, H. E., HYPKI, A., ICARDI, V., JANßEN, K., JEVARDAT DE FOMBELLE, G., JONKER, P. G., JUHÁSZ, Á. L., JULBE, F., KARAMPELAS, A., KEWLEY, A., KLAR, J., KOCHOSKA, A., KOHLEY, R., KOLENBERG, K., KONTIZAS, M., KONTIZAS, E., KOPOSOV, S. E., KORDOPATIS, G., KOSTRZEWA-RUTKOWSKA, Z., KOUBSKY, P., LAMBERT, S., LANZA, A. F., LASNE, Y., LAVIGNE, J. B., LE FUSTEC, Y., LE PONCIN-LAFITTE, C., LEBRETON, Y., LECCIA, S., LECLERC, N., LECOEUR-TAIBI, I., LENHARDT, H., LEROUX, F., LIAO, S., LICATA, E., LINDSTRøM, H. E. P., LISTER, T. A., LIVANOU, E., LOBEL, A., LÓPEZ, M., MANAGAU, S., MANN, R. G., MANTELET, G., MARCHAL, O., MARCHANT, J. M., MARCONI, M., MARINONI, S., MARSCHALKÓ, G., MARSHALL, D. J., MARTINO, M., MARTON, G., MARY, N., MASSARI, D., MATIJEVIČ, G., MAZEH, T., MCMILLAN, P. J., MESSINA, S., MICHALIK, D., MILLAR, N. R., MOLINA, D., MOLINARO, R., MOLNÁR, L., MONTEGRIFFO, P., MOR, R., MORBIDELLI, R., MOREL, T., MORRIS, D., MULONE, A. F., MURAVEVA, T., MUSELLA, I., NELEMANS, G., NICASTRO, L., NOVAL, L., O'MULLANE, W., ORDÉNOVIC, C., ORDÓÑEZ-BLANCO, D., OSBORNE, P., PAGANI, C., PAGANO, I., PAILLER, F., PALACIN, H., PALAVERSA, L., PANAHI, A., PAWLAK, M., PIERSIMONI, A. M., PINEAU, F. X., PLACHY, E., PLUM, G., POGGIO, E., POUJOULET, E., PRŠA, A., PULONE, L., RACERO, E., RAGAINI, S., RAMBAUX, N., RAMOS-LERATE, M., REGIBO, S., REYLÉ, C., RICLET, F., RIPEPI, V., RIVA, A., RIVARD, A., RIXON, G., ROEGIERS, T., ROELENS, M., ROMERO-GÓMEZ, M., ROWELL, N., ROYER, F., RUIZ-DERN, L., SADOWSKI, G., SAGRISTÀ SELLÉS, T., SAHLMANN, J., SALGADO, J., SALGUERO, E., SANNA, N., SANTANA-ROS, T., SARASSO, M., SAVIETTO, H., SCHULTHEIS, M., SCIACCA, E., SEGOL, M., SEGOVIA, J. C., SÉGRANSAN, D., SHIH, I. C., SILTALA, L., SILVA, A. F., SMART, R. L., SMITH, K. W., SOLANO, E., SOLITRO, F., SORDO, R., SORIA NIETO, S., SOUCHAY, J., SPAGNA, A., SPOTO, F., STAMPA, U., STEELE, I. A., STEIDELMÜLLER, H., STEPHENSON, C. A., STOEV,

H., SUESS, F. F., SURDEJ, J., SZABADOS, L., SZEGEDI-ELEK, E., TAPIADOR, D., TARIS, F., TAURAN, G., TAYLOR, M. B., TEIXEIRA, R., TERRETT, D., TEYSSANDIER, P., THUILLOT, W., TITARENKO, A., TORRA CLOTET, F., TURON, C., ULLA, A., UTRILLA, E., UZZI, S., VAILLANT, M., VALENTINI, G., VALETTE, V., VAN ELTEREN, A., VAN HEMELRYCK, E., VASCHETTO, M., VECCHIATO, A., VELJANOSKI, J., VIALA, Y., VICENTE, D., VOGT, S., VON ESSEN, C., VOSS, H., VOTRUBA, V., VOUTSINAS, S., WALMSLEY, G., WEILER, M., WERTZ, O., WEVERS, T., WYRZYKOWSKI, Ł., YOLDAS, A., ŽERJAL, M., ZIAEEPOUR, H., ZOREC, J., ZSCHOCKE, S., ZUCKER, S., ZURBACH, C., ZWITTER, T. Gaia Data Release 2. Observational Hertzsprung-Russell diagrams. **A&A**, v. 616, p. A10, August 2018.

[76] GAIA COLLABORATION, BROWN, A. G. A., VALLENARI, A., PRUSTI, T., DE BRUIJNE, J. H. J., BABUSIAUX, C., BIERMANN, M., CREEVEY, O. L., EVANS, D. W., EYER, L., HUTTON, A., JANSEN, F., JORDI, C., KLIONER, S. A., LAMMERS, U., LINDEGREN, L., LURI, X., MIGNARD, F., PANEM, C., POURBAIX, D., RANDICH, S., SARTORETTI, P., SOUBIRAN, C., WALTON, N. A., ARENOU, F., BAILER-JONES, C. A. L., BASTIAN, U., CROPPER, M., DRIMMEL, R., KATZ, D., LATTANZI, M. G., VAN LEEUWEN, F., BAKKER, J., CACCIARI, C., CASTAÑEDA, J., DE ANGELI, F., DUCOURANT, C., FABRICIUS, C., FOUESNEAU, M., FRÉMAT, Y., GUERRA, R., GUERRIER, A., GUIRAUD, J., JEAN-ANTOINE PICCOLO, A., MASANA, E., MESSINEO, R., MOWLAVI, N., NICOLAS, C., NIENARTOWICZ, K., PAILLER, F., PANUZZO, P., RICLET, F., ROUX, W., SEABROKE, G. M., SORDO, R., TANGA, P., THÉVENIN, F., GRACIA-ABRIL, G., PORTELL, J., TEYSSIER, D., ALTMANN, M., ANDRAE, R., BELLAS-VELIDIS, I., BENSON, K., BERTHIER, J., BLOMME, R., BRUGALETTA, E., BURGESS, P. W., BUSSO, G., CARRY, B., CELLINO, A., CHEEK, N., CLEMENTINI, G., DAMERDJI, Y., DAVIDSON, M., DELCHAMBRE, L., DELL'ORO, A., FERNÁNDEZ-HERNÁNDEZ, J., GALLUCCIO, L., GARCíA-LARIO, P., GARCIA-REINALDOS, M., GONZÁLEZ-NÚÑEZ, J., GOSSET, E., HAIGRON, R., HALBWACHS, J. L., HAMBLY, N. C., HARRISON, D. L., HATZIDIMITRIOU, D., HEITER, U., HERNÁNDEZ, J., HESTROFFER, D., HODGKIN, S. T., HOLL, B., JANßEN, K., JEVARDAT DE FOMBELLE, G., JORDAN, S., KRONE-MARTINS, A., LANZAFAME, A. C., LÖF-

FLER, W., LORCA, A., MANTEIGA, M., MARCHAL, O., MARRESE, P. M., MOITINHO, A., MORA, A., MUINONEN, K., OSBORNE, P., PANCINO, E., PAUWELS, T., PETIT, J. M., RECIO-BLANCO, A., RICHARDS, P. J., RIELLO, M., RIMOLDINI, L., ROBIN, A. C., ROEGIERS, T., RYBIZKI, J., SARRO, L. M., SIOPIS, C., SMITH, M., SOZZETTI, A., ULLA, A., UTRILLA, E., VAN LEEUWEN, M., VAN REEVEN, W., ABBAS, U., ABREU ARAMBURU, A., ACCART, S., AERTS, C., AGUADO, J. J., AJAJ, M., ALTAVILLA, G., ÁLVAREZ, M. A., ÁLVAREZ CID-FUENTES, J., ALVES, J., ANDERSON, R. I., ANGLADA VARELA, E., ANTOJA, T., AUDARD, M., BAINES, D., BAKER, S. G., BALAGUER-NÚÑEZ, L., BALBINOT, E., BALOG, Z., BARACHE, C., BARBATO, D., BARROS, M., BARSTOW, M. A., BARTOLOMÉ, S., BASSILANA, J. L., BAUCHET, N., BAUDESSON-STELLA, A., BECCIANI, U., BELLAZZINI, M., BERNET, M., BERTONE, S., BIANCHI, L., BLANCO-CUARESMA, S., BOCH, T., BOMBRUN, A., BOSSINI, D., BOUQUILLON, S., BRAGAGLIA, A., BRAMANTE, L., BREEDT, E., BRESSAN, A., BROUILLET, N., BUCCIARELLI, B., BURLACU, A., BUSONERO, D., BUTKEVICH, A. G., BUZZI, R., CAFFAU, E., CANCELLIERE, R., CÁNOVAS, H., CANTAT-GAUDIN, T., CARBALLO, R., CARLUCCI, T., CARNERERO, M. I., CARRASCO, J. M., CASAMIQUELA, L., CASTELLANI, M., CASTRO-GINARD, A., CASTRO SAMPOL, P., CHAOUL, L., CHARLOT, P., CHEMIN, L., CHIAVASSA, A., CIONI, M. R. L., COMORETTO, G., COOPER, W. J., CORNEZ, T., COWELL, S., CRIFO, F., CROSTA, M., CROWLEY, C., DAFONTE, C., DAPERGOLAS, A., DAVID, M., DAVID, P., DE LAVERNY, P., DE LUISE, F., DE MARCH, R., DE RIDDER, J., DE SOUZA, R., DE TEODORO, P., DE TORRES, A., DEL PELOSO, E. F., DEL POZO, E., DELBO, M., DELGADO, A., DELGADO, H. E., DELISLE, J. B., DI MATTEO, P., DIAKITE, S., DIENER, C., DISTEFANO, E., DOLDING, C., EAPPACHEN, D., EDVARDSSON, B., ENKE, H., ESQUEJ, P., FABRE, C., FABRIZIO, M., FAIGLER, S., FEDORETS, G., FERNIQUE, P., FIENGA, A., FIGUERAS, F., FOURON, C., FRAGKOUDI, F., FRAILE, E., FRANKE, F., GAI, M., GARABATO, D., GARCIA-GUTIERREZ, A., GARCíA-TORRES, M., GAROFALO, A., GAVRAS, P., GERLACH, E., GEYER, R., GIACOBBE, P., GILMORE, G., GIRONA, S., GIUFFRIDA, G., GOMEL, R., GOMEZ, A., GONZALEZ-SANTAMARIA, I., GONZÁLEZ-VIDAL, J. J., GRANVIK,

M., GUTIÉRREZ-SÁNCHEZ, R., GUY, L. P., HAUSER, M., HAYWOOD, M., HELMI, A., HIDALGO, S. L., HILGER, T., HŁADCZUK, N., HOBBS, D., HOLLAND, G., HUCKLE, H. E., JASNIEWICZ, G., JONKER, P. G., JUARISTI CAMPILLO, J., JULBE, F., KARBEVSKA, L., KERVELLA, P., KHANNA, S., KOCHOSKA, A., KONTIZAS, M., KORDOPATIS, G., KORN, A. J., KOSTRZEWA-RUTKOWSKA, Z., KRUSZYŃSKA, K., LAMBERT, S., LANZA, A. F., LASNE, Y., LE CAMPION, J. F., LE FUSTEC, Y., LEBRETON, Y., LEBZELTER, T., LECCIA, S., LECLERC, N., LECOEUR-TAIBI, I., LIAO, S., LICATA, E., LINDSTRøM, E. P., LISTER, T. A., LIVANOU, E., LOBEL, A., MADRERO PARDO, P., MANAGAU, S., MANN, R. G., MARCHANT, J. M., MARCONI, M., MARCOS SANTOS, M. M. S., MARINONI, S., MAROCCO, F., MARSHALL, D. J., MARTIN POLO, L., MARTíN-FLEITAS, J. M., MASIP, A., MASSARI, D., MASTROBUONO-BATTISTI, A., MAZEH, T., MCMILLAN, P. J., MESSINA, S., MICHALIK, D., MILLAR, N. R., MINTS, A., MOLINA, D., MOLINARO, R., MOLNÁR, L., MONTEGRIFFO, P., MOR, R., MORBIDELLI, R., MOREL, T., MORRIS, D., MULONE, A. F., MUNOZ, D., MURAVEVA, T., MURPHY, C. P., MUSELLA, I., NOVAL, L., ORDÉNOVIC, C., ORRÙ, G., OSINDE, J., PAGANI, C., PAGANO, I., PALAVERSA, L., PALICIO, P. A., PANAHI, A., PAWLAK, M., PEÑALOSA ESTELLER, X., PENTTILÄ, A., PIERSIMONI, A. M., PINEAU, F. X., PLACHY, E., PLUM, G., POGGIO, E., PORETTI, E., POUJOULET, E., PRŠA, A., PULONE, L., RACERO, E., RAGAINI, S., RAINER, M., RAITERI, C. M., RAMBAUX, N., RAMOS, P., RAMOS-LERATE, M., RE FIORENTIN, P., REGIBO, S., REYLÉ, C., RIPEPI, V., RIVA, A., RIXON, G., ROBICHON, N., ROBIN, C., ROELENS, M., ROHRBASSER, L., ROMERO-GÓMEZ, M., ROWELL, N., ROYER, F., RYBICKI, K. A., SADOWSKI, G., SAGRISTÀ SELLÉS, A., SAHLMANN, J., SALGADO, J., SALGUERO, E., SAMARAS, N., SANCHEZ GIMENEZ, V., SANNA, N., SANTOVEÑA, R., SARASSO, M., SCHULTHEIS, M., SCIACCA, E., SEGOL, M., SEGOVIA, J. C., SÉGRANSAN, D., SEMEUX, D., SHAHAF, S., SIDDIQUI, H. I., SIEBERT, A., SILTALA, L., SLEZAK, E., SMART, R. L., SOLANO, E., SOLITRO, F., SOUAMI, D., SOUCHAY, J., SPAGNA, A., SPOTO, F., STEELE, I. A., STEIDELMÜLLER, H., STEPHENSON, C. A., SÜVEGES, M., SZABADOS, L., SZEGEDI-ELEK, E., TARIS, F., TAURAN, G., TAYLOR, M. B., TEIXEIRA, R., THUILLOT, W., TONELLO, N., TORRA, F., TORRA, J., TURON, C., UNGER,

N., VAILLANT, M., VAN DILLEN, E., VANEL, O., VECCHIATO, A., VIALA, Y., VICENTE, D., VOUTSINAS, S., WEILER, M., WEVERS, T., WYRZYKOWSKI, Ł., YOLDAS, A., YVARD, P., ZHAO, H., ZOREC, J., ZUCKER, S., ZURBACH, C., ZWITTER, T. Gaia Early Data Release 3. Summary of the contents and survey properties. **A&A**, v. 649, p. A1, May 2021.

[77] GAIA COLLABORATION, VALLENARI, A., BROWN, A. G. A., PRUSTI, T., DE BRUIJNE, J. H. J., ARENOU, F., BABUSIAUX, C., BIERMANN, M., CREEVEY, O. L., DUCOURANT, C., EVANS, D. W., EYER, L., GUERRA, R., HUTTON, A., JORDI, C., KLIONER, S. A., LAMMERS, U. L., LINDEGREN, L., LURI, X., MIGNARD, F., PANEM, C., POURBAIX, D., RANDICH, S., SARTORETTI, P., SOUBIRAN, C., TANGA, P., WALTON, N. A., BAILER-JONES, C. A. L., BASTIAN, U., DRIMMEL, R., JANSEN, F., KATZ, D., LATTANZI, M. G., VAN LEEUWEN, F., BAKKER, J., CACCIARI, C., CASTAÑEDA, J., DE ANGELI, F., FABRICIUS, C., FOUESNEAU, M., FRÉMAT, Y., GALLUCCIO, L., GUERRIER, A., HEITER, U., MASANA, E., MESSINEO, R., MOWLAVI, N., NICOLAS, C., NIENARTOWICZ, K., PAILLER, F., PANUZZO, P., RICLET, F., ROUX, W., SEABROKE, G. M., SORDOøRCIT, R., THÉVENIN, F., GRACIA-ABRIL, G., PORTELL, J., TEYSSIER, D., ALTMANN, M., ANDRAE, R., AUDARD, M., BELLAS-VELIDIS, I., BENSON, K., BERTHIER, J., BLOMME, R., BURGESS, P. W., BUSONERO, D., BUSSO, G., CÁNOVAS, H., CARRY, B., CELLINO, A., CHEEK, N., CLEMENTINI, G., DAMERDJI, Y., DAVIDSON, M., DE TEODORO, P., NUÑEZ CAMPOS, M., DELCHAMBRE, L., DELL'ORO, A., ESQUEJ, P., FERNÁNDEZ-HERNÁNDEZ, J., FRAILE, E., GARABATO, D., GARCíA-LARIO, P., GOSSET, E., HAIGRON, R., HALBWACHS, J. L., HAMBLY, N. C., HARRISON, D. L., HERNÁNDEZ, J., HESTROFFER, D., HODGKIN, S. T., HOLL, B., JANßEN, K., JEVARDAT DE FOMBELLE, G., JORDAN, S., KRONE-MARTINS, A., LANZAFAME, A. C., LÖFFLER, W., MARCHAL, O., MARRESE, P. M., MOITINHO, A., MUINONEN, K., OSBORNE, P., PANCINO, E., PAUWELS, T., RECIOBLANCO, A., REYLÉ, C., RIELLO, M., RIMOLDINI, L., ROEGIERS, T., RYBIZKI, J., SARRO, L. M., SIOPIS, C., SMITH, M., SOZZETTI, A., UTRILLA, E., VAN LEEUWEN, M., ABBAS, U., ÁBRAHÁM, P., ABREU ARAMBURU, A., AERTS, C., AGUADO, J. J., AJAJ, M., ALDEAMONTERO, F., ALTAVILLA, G., ÁLVAREZ, M. A., ALVES, J., AN-

DERS, F., ANDERSON, R. I., ANGLADA VARELA, E., ANTOJA, T., BAINES, D., BAKER, S. G., BALAGUER-NÚÑEZ, L., BALBINOT, E., BALOG, Z., BARACHE, C., BARBATO, D., BARROS, M., BARSTOW, M. A., BARTOLOMÉ, S., BASSILANA, J. L., BAUCHET, N., BECCIANI, U., BELLAZZINI, M., BERIHUETE, A., BERNET, M., BERTONE, S., BIANCHI, L., BINNENFELD, A., BLANCO-CUARESMA, S., BLAZERE, A., BOCH, T., BOMBRUN, A., BOSSINI, D., BOUQUILLON, S., BRAGAGLIA, A., BRAMANTE, L., BREEDT, E., BRESSAN, A., BROUILLET, N., BRUGALETTA, E., BUCCIARELLI, B., BURLACU, A., BUTKEVICH, A. G., BUZZI, R., CAFFAU, E., CANCELLIERE, R., CANTAT-GAUDIN, T., CARBALLO, R., CARLUCCI, T., CARNERERO, M. I., CARRASCO, J. M., CASAMIQUELA, L., CASTELLANI, M., CASTRO-GINARD, A., CHAOUL, L., CHARLOT, P., CHEMIN, L., CHIARAMIDA, V., CHIAVASSA, A., CHORNAY, N., COMORETTO, G., CONTURSI, G., COOPER, W. J., CORNEZ, T., COWELL, S., CRIFO, F., CROPPER, M., CROSTA, M., CROWLEY, C., DAFONTE, C., DAPERGOLAS, A., DAVID, M., DAVID, P., DE LAVERNY, P., DE LUISE, F., DE MARCH, R., DE RIDDER, J., DE SOUZA, R., DE TORRES, A., DEL PELOSO, E. F., DEL POZO, E., DELBO, M., DELGADO, A., DELISLE, J. B., DEMOUCHY, C., DHARMAWARDENA, T. E., DI MATTEO, P., DIAKITE, S., DIENER, C., DISTEFANO, E., DOLDING, C., EDVARDSSON, B., ENKE, H., FABRE, C., FABRIZIO, M., FAIGLER, S., FEDORETS, G., FERNIQUE, P., FIENGA, A., FIGUERAS, F., FOURNIER, Y., FOURON, C., FRAGKOUDI, F., GAI, M., GARCIA-GUTIERREZ, A., GARCIA-REINALDOS, M., GARCíA-TORRES, M., GAROFALO, A., GAVEL, A., GAVRAS, P., GERLACH, E., GEYER, R., GIACOBBE, P., GILMORE, G., GIRONA, S., GIUFFRIDA, G., GOMEL, R., GOMEZ, A., GONZÁLEZ-NÚÑEZ, J., GONZÁLEZ-SANTAMARíA, I., GONZÁLEZ-VIDAL, J. J., GRANVIK, M., GUILLOUT, P., GUIRAUD, J., GUTIÉRREZ-SÁNCHEZ, R., GUY, L. P., HATZIDIMITRIOU, D., HAUSER, M., HAYWOOD, M., HELMER, A., HELMI, A., SARMIENTO, M. H., HIDALGO, S. L., HILGER, T., HŁADCZUK, N., HOBBS, D., HOLLAND, G., HUCKLE, H. E., JARDINE, K., JASNIEWICZ, G., JEAN-ANTOINE PICCOLO, A., JIMÉNEZ-ARRANZ, Ó., JORISSEN, A., JUARISTI CAMPILLO, J., JULBE, F., KARBEVSKA, L., KERVELLA, P., KHANNA, S., KONTIZAS, M., KORDOPATIS, G., KORN, A. J., KÓSPÁL, Á, KOSTRZEWA-RUTKOWSKA,

Z., KRUSZYŃSKA, K., KUN, M., LAIZEAU, P., LAMBERT, S., LANZA, A. F., LASNE, Y., LE CAMPION, J. F., LEBRETON, Y., LEBZELTER, T., LECCIA, S., LECLERC, N., LECOEUR-TAIBI, I., LIAO, S., LICATA, E. L., LINDSTRøM, H. E. P., LISTER, T. A., LIVANOU, E., LOBEL, A., LORCA, A., LOUP, C., MADRERO PARDO, P., MAGDALENO ROMEO, A., MANAGAU, S., MANN, R. G., MANTEIGA, M., MARCHANT, J. M., MARCONI, M., MARCOS, J., MARCOS SANTOS, M. M. S., MARíN PINA, D., MARINONI, S., MAROCCO, F., MARSHALL, D. J., POLO, L. MARTIN, MARTíN-FLEITAS, J. M., MARTON, G., MARY, N., MASIP, A., MASSARI, D., MASTROBUONO-BATTISTI, A., MAZEH, T., MCMILLAN, P. J., MESSINA, S., MICHALIK, D., MILLAR, N. R., MINTS, A., MOLINA, D., MOLINARO, R., MOLNÁR, L., MONARI, G., MONGUIÓ, M., MONTEGRIFFO, P., MONTERO, A., MOR, R., MORA, A., MORBIDELLI, R., MOREL, T., MORRIS, D., MURAVEVA, T., MURPHY, C. P., MUSELLA, I., NAGY, Z., NOVAL, L., OCAÑA, F., OGDEN, A., ORDENOVIC, C., OSINDE, J. O., PAGANI, C., PAGANO, I., PALAVERSA, L., PALICIO, P. A., PALLAS-QUINTELA, L., PANAHI, A., PAYNE-WARDENAAR, S., PEÑALOSA ESTELLER, X., PENTTILÄ, A., PICHON, B., PIERSIMONI, A. M., PINEAU, F. X., PLACHY, E., PLUM, G., POGGIO, E., PRŠA, A., PULONE, L., RACERO, E., RAGAINI, S., RAINER, M., RAITERI, C. M., RAMBAUX, N., RAMOS, P., RAMOS-LERATE, M., RE FIORENTIN, P., REGIBO, S., RICHARDS, P. J., RIOS DIAZ, C., RIPEPI, V., RIVA, A., RIX, H. W., RIXON, G., ROBICHON, N., ROBIN, A. C., ROBIN, C., ROELENS, M., ROGUES, H. R. O., ROHRBASSER, L., ROMERO-GÓMEZ, M., ROWELL, N., ROYER, F., RUZ MIERES, D., RYBICKI, K. A., SADOWSKI, G., SÁEZ NÚÑEZ, A., SAGRISTÀ SELLÉS, A., SAHLMANN, J., SALGUERO, E., SAMARAS, N., SANCHEZ GIMENEZ, V., SANNA, N., SANTOVEÑA, R., SARASSO, M., SCHULTHEIS, M., SCIACCA, E., SEGOL, M., SEGOVIA, J. C., SÉGRANSAN, D., SEMEUX, D., SHAHAF, S., SIDDIQUI, H. I., SIEBERT, A., SILTALA, L., SILVELO, A., SLEZAK, E., SLEZAK, I., SMART, R. L., SNAITH, O. N., SOLANO, E., SOLITRO, F., SOUAMI, D., SOUCHAY, J., SPAGNA, A., SPINA, L., SPOTO, F., STEELE, I. A., STEIDELMÜLLER, H., STEPHENSON, C. A., SÜVEGES, M., SURDEJ, J., SZABADOS, L., SZEGEDI-ELEK, E., TARIS, F., TAYLO, M. B., TEIXEIRA, R., TOLOMEI, L., TONELLO, N., TORRA, F., TORRA, J., TORRALBA ELIPE, G., TRABUCCHI, M., TSOUNIS, A. T., TURON,

C., ULLA, A., UNGER, N., VAILLANT, M. V., VAN DILLEN, E., VAN REEVEN, W., VANEL, O., VECCHIATO, A., VIALA, Y., VICENTE, D., VOUTSINAS, S., WEILER, M., WEVERS, T., WYRZYKOWSKI, L., YOLDAS, A., YVARD, P., ZHAO, H., ZOREC, J., ZUCKER, S., ZWITTER, T. Gaia Data Release 3: Summary of the content and survey properties. **arXiv e-prints**, p. arXiv:2208.00211, July 2022.

[78] GALLART, CARME, BERNARD, EDOUARD J., BROOK, CHRIS B., RUIZ-LARA, TOMÁS, CASSISI, SANTI, HILL, VANESSA, MONELLI, MATTEO. Uncovering the birth of the Milky Way through accurate stellar ages with Gaia. **Nature Astronomy**, v. 3, p. 932–939, July 2019.

[79] GELINO, C. R., KIRKPATRICK, J. D., CUSHING, M. C., EISENHARDT, P. R., GRIFFITH, R. L., MAINZER, A. K., MARSH, K. A., SKRUTSKIE, M. F., WRIGHT, E. L. WISE Brown Dwarf Binaries: The Discovery of a T5+T5 and a T8.5+T9 System. **AJ**, v. 142, p. 57, August 2011.

[80] GÓMEZ, F. A., BESLA, G., CARPINTERO, D. D., VILLALOBOS, Á., O'SHEA, B. W., BELL, E. F. And Yet it Moves: The Dangers of Artificially Fixing the Milky Way Center of Mass in the Presence of a Massive Large Magellanic Cloud. **ApJ**, v. 802, p. 128, April 2015.

[81] HAYDEN, MICHAEL R., BOVY, JO, HOLTZMAN, JON A., NIDEVER, DAVID L., BIRD, JONATHAN C., WEINBERG, DAVID H., ANDREWS, BRETT H., MAJEWSKI, STEVEN R., ALLENDE PRIETO, CARLOS, ANDERS, FRIEDRICH, BEERS, TIMOTHY C., BIZYAEV, DMITRY, CHIAPPINI, CRISTINA, CUNHA, KATIA, FRINCHABOY, PETER, GARCíA-HERŃANDEZ, D. A., GARCíA PÉREZ, ANA E., GIRARDI, LÉO, HARDING, PAUL, HEARTY, FRED R., JOHNSON, JENNIFER A., MÉSZÁROS, SZABOLCS, MINCHEV, IVAN, O'CONNELL, ROBERT, PAN, KAIKE, ROBIN, ANNIE C., SCHIAVON, RICARDO P., SCHNEIDER, DONALD P., SCHULTHEIS, MATHIAS, SHETRONE, MATTHEW, SKRUTSKIE, MICHAEL, STEINMETZ, MATTHIAS, SMITH, VERNE, WILSON, JOHN C., ZAMORA, OLGA, ZASOWSKI, GAIL. Chemical Cartography with APOGEE: Metallicity Distribution Functions and the Chemical Structure of the Milky Way Disk. **ApJ**, v. 808, n. 2, p. 132, August 2015.

[82] HAYES, CHRISTIAN R., MAJEWSKI, STEVEN R., SHETRONE, MATTHEW, FERNÁNDEZ-ALVAR, EMMA, ALLENDE PRIETO, CARLOS, SCHUS-

TER, WILLIAM J., CARIGI, LETICIA, CUNHA, KATIA, SMITH, VERNE V., SOBECK, JENNIFER, ALMEIDA, ANDRES, BEERS, TIMOTHY C., CARRERA, RICARDO, FERNÁNDEZ-TRINCADO, J. G., GARCíA-HERNÁNDEZ, D. A., GEISLER, DOUG, LANE, RICHARD R., LUCATELLO, SARA, MATTHEWS, ALLISON M., MINNITI, DANTE, NITSCHELM, CHRISTIAN, TANG, BAITIAN, TISSERA, PATRICIA B., ZAMORA, OLGA. Disentangling the Galactic Halo with APOGEE. I. Chemical and Kinematical Investigation of Distinct Metal-poor Populations. **ApJ**, v. 852, n. 1, p. 49, January 2018.

[83] HAYWOOD, M., DI MATTEO, P., LEHNERT, M. D., SNAITH, O., KHOPERSKOV, S., GÓMEZ, A. In Disguise or Out of Reach: First Clues about In Situ and Accreted Stars in the Stellar Halo of the Milky Way from Gaia DR2. **ApJ**, v. 863, n. 2, p. 113, August 2018.

[84] HAYWOOD, M., DI MATTEO, P., SNAITH, O., LEHNERT, M. D. Clues to the formation of the Milky Way's thick disk. **A&A**, v. 579, p. A5, July 2015.

[85] HELMI, AMINA. Streams, Substructures, and the Early History of the Milky Way. **ARA&A**, v. 58, p. 205–256, August 2020.

[86] HELMI, AMINA, BABUSIAUX, CARINE, KOPPELMAN, HELMER H., MASSARI, DAVIDE, VELJANOSKI, JOVAN, BROWN, ANTHONY G. A. The merger that led to the formation of the Milky Way's inner stellar halo and thick disk. **Nature**, v. 563, n. 7729, p. 85–88, October 2018.

[87] HERNITSCHEK, NINA, COHEN, JUDITH G., RIX, HANS-WALTER, SESAR, BRANIMIR, MARTIN, NICOLAS F., MAGNIER, EUGENE, WAINSCOAT, RICHARD, KAISER, NICK, TONRY, JOHN L., KUDRITZKI, ROLF-PETER, HODAPP, KLAUS, CHAMBERS, KEN, FLEWELLING, HEATHER, BURGETT, WILLIAM. The Profile of the Galactic Halo from Pan-STARRS1 3π RR Lyrae. **ApJ**, v. 859, n. 1, p. 31, May 2018.

[88] HOOK, I. M., JøRGENSEN, INGER, ALLINGTON-SMITH, J. R., DAVIES, R. L., METCALFE, N., MUROWINSKI, R. G., CRAMPTON, D. The Gemini-North Multi-Object Spectrograph: Performance in Imaging, Long-Slit, and Multi-Object Spectroscopic Modes. **PASP**, v. 116, n. 819, p. 425–440, May 2004.

[89] HORTA, DANNY, SCHIAVON, RICARDO P., MACKERETH, J. TED, WEINBERG, DAVID H., HASSELQUIST, STEN, FEUILLET, DIANE, O'CONNELL, ROBERT W., ANGUIANO, BORJA, ALLENDE-PRIETO, CARLOS, BEATON, RACHAEL L., BIZYAEV, DMITRY, CUNHA, KATIA, GEISLER, DOUG, GARCíA-HERNÁNDEZ, D. A., HOLTZMAN, JON, JÖNSSON, HENRIK, LANE, RICHARD R., MAJEWSKI, STEVE R., MÉSZÁROS, SZABOLCS, MINNITI, DANTE, NITSCHELM, CHRISTIAN, SHETRONE, MATTHEW, SMITH, VERNE V., ZASOWSKI, GAIL. The chemical characterisation of halo substructure in the Milky Way based on APOGEE. **MNRAS**, November 2022.

[90] HUÉLAMO, N., IVANOV, V. D., KURTEV, R., GIRARD, J. H., BORISSOVA, J., MAWET, D., MUŽIĆ, K., CÁCERES, C., MELO, C. H. F., STERZIK, M. F., MINNITI, D. WISE J061213.85-303612.5: a new T-dwarf binary candidate. **A&A**, v. 578, p. A1, June 2015.

[91] ILBERT, O., ARNOUTS, S., MCCRACKEN, H. J., BOLZONELLA, M., BERTIN, E., LE FÈVRE, O., MELLIER, Y., ZAMORANI, G., PELLÒ, R., IOVINO, A., TRESSE, L., LE BRUN, V., BOTTINI, D., GARILLI, B., MACCAGNI, D., PICAT, J. P., SCARAMELLA, R., SCODEGGIO, M., VETTOLANI, G., ZANICHELLI, A., ADAMI, C., BARDELLI, S., CAPPI, A., CHARLOT, S., CILIEGI, P., CONTINI, T., CUCCIATI, O., FOUCAUD, S., FRANZETTI, P., GAVIGNAUD, I., GUZZO, L., MARANO, B., MARINONI, C., MAZURE, A., MENEUX, B., MERIGHI, R., PALTANI, S., POLLO, A., POZZETTI, L., RADOVICH, M., ZUCCA, E., BONDI, M., BONGIORNO, A., BUSARELLO, G., DE LA TORRE, S., GREGORINI, L., LAMAREILLE, F., MATHEZ, G., MERLUZZI, P., RIPEPI, V., RIZZO, D., VERGANI, D. Accurate photometric redshifts for the CFHT legacy survey calibrated using the VIMOS VLT deep survey. **A&A**, v. 457, n. 3, p. 841–856, October 2006.

[92] IVEZIĆ, ŽELJKO, GOLDSTON, JOSH, FINLATOR, KRISTIAN, KNAPP, GILLIAN R., YANNY, BRIAN, MCKAY, TIMOTHY A., AMROSE, SUSAN, KRISCIUNAS, KEVIN, WILLMAN, BETH, ANDERSON, SCOTT, SCHABER, CHRIS, ERB, DAWN, LOGAN, CHELSEA, STUBBS, CHRIS, CHEN, BING, NEILSEN, ERIC, UOMOTO, ALAN, PIER, JEFFREY R., FAN, XIAOHUI, GUNN, JAMES E., LUPTON, ROBERT H., ROCKOSI, CONSTANCE M., SCHLEGEL, DAVID, STRAUSS, MICHAEL A., AN-

NIS, JAMES, BRINKMANN, JON, CSABAI, ISTVÁN, DOI, MAMORU, FUKUGITA, MASATAKA, HENNESSY, GREGORY S., HINDSLEY, ROBERT B., MARGON, BRUCE, MUNN, JEFFREY A., NEWBERG, HEIDI JO, SCHNEIDER, DONALD P., SMITH, J. ALLYN, SZOKOLY, GYULA P., THAKAR, ANIRUDDHA R., VOGELEY, MICHAEL S., WADDELL, PATRICK, YASUDA, NAOKI, YORK, DONALD G., SDSS COLLABORATION, . Candidate RR Lyrae Stars Found in Sloan Digital Sky Survey Commissioning Data. **AJ**, v. 120, n. 2, p. 963–977, August 2000.

[93] JANSON, M., HORMUTH, F., BERGFORS, C., BRANDNER, W., HIPPLER, S., DAEMGEN, S., KUDRYAVTSEVA, N., SCHMALZL, E., SCHNUPP, C., HENNING, T. The AstraLux Large M-dwarf Multiplicity Survey. **ApJ**, v. 754, p. 44, July 2012.

[94] JURIĆ, MARIO, IVEZIĆ, ŽELJKO, BROOKS, ALYSON, LUPTON, ROBERT H., SCHLEGEL, DAVID, FINKBEINER, DOUGLAS, PADMANABHAN, NIKHIL, BOND, NICHOLAS, SESAR, BRANIMIR, ROCKOSI, CONSTANCE M., KNAPP, GILLIAN R., GUNN, JAMES E., SUMI, TAKAHIRO, SCHNEIDER, DONALD P., BARENTINE, J. C., BREWINGTON, HOWARD J., BRINKMANN, J., FUKUGITA, MASATAKA, HARVANEK, MICHAEL, KLEINMAN, S. J., KRZESINSKI, JUREK, LONG, DAN, NEILSEN, JR., ERIC H., NITTA, ATSUKO, SNEDDEN, STEPHANIE A., YORK, DONALD G. The Milky Way Tomography with SDSS. I. Stellar Number Density Distribution. **ApJ**, v. 673, n. 2, p. 864–914, February 2008.

[95] KIMAN, ROCIO, SCHMIDT, SARAH J., ANGUS, RUTH, CRUZ, KELLE L., FAHERTY, JACQUELINE K., RICE, EMILY. Exploring the Age-dependent Properties of M and L Dwarfs Using Gaia and SDSS. **AJ**, v. 157, n. 6, p. 231, June 2019.

[96] KIRKPATRICK, J. DAVY, GELINO, CHRISTOPHER R., CUSHING, MICHAEL C., MACE, GREGORY N., GRIFFITH, ROGER L., SKRUTSKIE, MICHAEL F., MARSH, KENNETH A., WRIGHT, EDWARD L., EISENHARDT, PETER R., MCLEAN, IAN S., MAINZER, AMANDA K., BURGASSER, ADAM J., TINNEY, C. G., PARKER, STEPHEN, SALTER, GRAEME. Further Defining Spectral Type "Y" and Exploring the Low-mass

End of the Field Brown Dwarf Mass Function. **ApJ**, v. 753, n. 2, p. 156, July 2012.

[97] KIRKPATRICK, J. DAVY, GELINO, CHRISTOPHER R., FAHERTY, JACQUELINE K., MEISNER, AARON M., CASELDEN, DAN, SCHNEIDER, ADAM C., MAROCCO, FEDERICO, CAYAGO, ALFRED J., SMART, R. L., EISENHARDT, PETER R., KUCHNER, MARC J., WRIGHT, EDWARD L., CUSHING, MICHAEL C., ALLERS, KATELYN N., BARDALEZ GAGLIUFFI, DANIELLA C., BURGASSER, ADAM J., GAGNÉ, JONATHAN, LOGSDON, SARAH E., MARTIN, EMILY C., INGALLS, JAMES G., LOWRANCE, PATRICK J., ABRAHAMS, ELLIANNA S., AGANZE, CHRISTIAN, GERASIMOV, ROMAN, GONZALES, EILEEN C., HSU, CHIH-CHUN, KAMRAJ, NIKITA, KIMAN, ROCIO, REES, JON, THEISSEN, CHRISTOPHER, AMMAR, KAREEM, ANDERSEN, NIKOLAJ STEVNBAK, BEAULIEU, PAUL, COLIN, GUILLAUME, ELACHI, CHARLES A., GOODMAN, SAMUEL J., GRAMAIZE, LÉOPOLD, HAMLET, LESLIE K., HONG, JUSTIN, JONKEREN, ALEXANDER, KHALIL, MOHAMMED, MARTIN, DAVID W., PENDRILL, WILLIAM, PUMPHREY, BENJAMIN, ROTHERMICH, AUSTIN, SAINIO, ARTTU, STENNER, ANDRES, TANNER, CHRISTOPHER, THÉVENOT, MELINA, VOLOSHIN, NIKITA V., WALLA, JIM, WĘDRACKI, ZBIGNIEW, COLLABORATION, BACKYARD WORLDS: PLANET 9. The Field Substellar Mass Function Based on the Full-sky 20 pc Census of 525 L, T, and Y Dwarfs. **ApJS**, v. 253, n. 1, p. 7, March 2021a.

[98] KIRKPATRICK, J. DAVY, GELINO, CHRISTOPHER R., FAHERTY, JACQUELINE K., MEISNER, AARON M., CASELDEN, DAN, SCHNEIDER, ADAM C., MAROCCO, FEDERICO, CAYAGO, ALFRED J., SMART, R. L., EISENHARDT, PETER R., KUCHNER, MARC J., WRIGHT, EDWARD L., CUSHING, MICHAEL C., ALLERS, KATELYN N., BARDALEZ GAGLIUFFI, DANIELLA C., BURGASSER, ADAM J., GAGNÉ, JONATHAN, LOGSDON, SARAH E., MARTIN, EMILY C., INGALLS, JAMES G., LOWRANCE, PATRICK J., ABRAHAMS, ELLIANNA S., AGANZE, CHRISTIAN, GERASIMOV, ROMAN, GONZALES, EILEEN C., HSU, CHIH-CHUN, KAMRAJ, NIKITA, KIMAN, ROCIO, REES, JON, THEISSEN, CHRISTOPHER, AMMAR, KAREEM, ANDERSEN, NIKOLAJ STEVNBAK, BEAULIEU, PAUL, COLIN, GUIL-

LAUME, ELACHI, CHARLES A., GOODMAN, SAMUEL J., GRAMAIZE, LÉOPOLD, HAMLET, LESLIE K., HONG, JUSTIN, JONKEREN, ALEXANDER, KHALIL, MOHAMMED, MARTIN, DAVID W., PENDRILL, WILLIAM, PUMPHREY, BENJAMIN, ROTHERMICH, AUSTIN, SAINIO, ARTTU, STENNER, ANDRES, TANNER, CHRISTOPHER, THÉVENOT, MELINA, VOLOSHIN, NIKITA V., WALLA, JIM, WĘDRACKI, ZBIGNIEW, BACKYARD WORLDS: PLANET 9 COLLABORATION, . The Field Substellar Mass Function Based on the Full-sky 20 pc Census of 525 L, T, and Y Dwarfs. **ApJS**, v. 253, n. 1, p. 7, March 2021b.

[99] KIRKPATRICK, J. DAVY, REID, I. NEILL, LIEBERT, JAMES, CUTRI, ROC M., NELSON, BRANT, BEICHMAN, CHARLES A., DAHN, CONARD C., MONET, DAVID G., GIZIS, JOHN E., SKRUTSKIE, MICHAEL F. Dwarfs Cooler than "M": The Definition of Spectral Type "L" Using Discoveries from the 2 Micron All-Sky Survey (2MASS). **ApJ**, v. 519, n. 2, p. 802–833, Jul 1999.

[100] KIWY, FRANK, FAHERTY, JACQUELINE K., MEISNER, AARON, SCHNEIDER, ADAM C., KIRKPATRICK, J. DAVY, KUCHNER, MARC J., BURGASSER, ADAM J., CASEWELL, SARAH, KIMAN, ROCIO, CALAMARI, EMILY, AGANZE, CHRISTIAN, HSU, CHIH-CHUN, SAINIO, ARTTU, THAKUR, VINOD, BACKYARD WORLDS: PLANET 9 COLLABORATION, . Discovery of 34 Low-mass Comoving Systems Using NOIRLab Source Catalog DR2. **AJ**, v. 164, n. 1, p. 3, July 2022.

[101] KOPOSOV, S. E., IRWIN, M., BELOKUROV, V., GONZALEZ-SOLARES, E., YOLDAS, A. K., LEWIS, J., METCALFE, N., SHANKS, T. Discovery of a cold stellar stream in the ATLAS DR1 data. **MNRAS**, v. 442, p. L85–L89, July 2014.

[102] KOPOSOV, SERGEY E., RIX, HANS-WALTER, HOGG, DAVID W. Constraining the Milky Way Potential with a Six-Dimensional Phase-Space Map of the GD-1 Stellar Stream. **ApJ**, v. 712, n. 1, p. 260–273, March 2010.

[103] KOPPELMAN, HELMER, HELMI, AMINA, VELJANOSKI, JOVAN. One Large Blob and Many Streams Frosting the nearby Stellar Halo in Gaia DR2. **ApJ**, v. 860, n. 1, p. L11, June 2018.

[104] KOPPELMAN, HELMER H., HELMI, AMINA. The reduced proper motion selected halo: Methods and description of the catalogue. **A&A**, v. 645, p. A69, January 2021.

[105] KOPPELMAN, HELMER H., HELMI, AMINA, MASSARI, DAVIDE, PRICE-WHELAN, ADRIAN M., STARKENBURG, TJITSKE K. Multiple retrograde substructures in the Galactic halo: A shattered view of Galactic history. **A&A**, v. 631, p. L9, November 2019.

[106] KOTA, TARUN, KIRKPATRICK, J. DAVY, CASELDEN, DAN, MAROCCO, FEDERICO, SCHNEIDER, ADAM C., GAGNÉ, JONATHAN, FAHERTY, JACQUELINE K., MEISNER, AARON M., KUCHNER, MARC J., CASEWELL, SARAH, KACHOLIA, KANISHK, BICKLE, TOM, BEAULIEU, PAUL, COLIN, GUILLAUME, HAMLET, LESLIE K., SCHÜMANN, JÖRG, TANNER, CHRISTOPHER, BACKYARD WORLDS: PLANET 9 COLLABORATION, . Discovery of 16 New Members of the Solar Neighborhood Using Proper Motions from CatWISE2020. **AJ**, v. 163, n. 3, p. 116, March 2022.

[107] KRAUS, A. L., HILLENBRAND, L. A. Multiple Star Formation to the Bottom of the Initial Mass Function. **ApJ**, v. 757, p. 141, October 2012.

[108] KUMAR, S. S. The Structure of Stars of Very Low Mass. **ApJ**, v. 137, p. 1121, May 1963.

[109] LAWRENCE, A., WARREN, S.J., ALMAINI, O., EDGE, A.C., HAMBLY, N.C., JAMESON, R.F., LUCAS, P., CASALI, M., ADAMSON, A., DYE, S., EMERSON, J.P., FOUCAUD, S., HEWETT, P., HIRST, P., HODGKIN, S.T., IRWIN, M.J., LODIEU, N., MCMAHON, R.G., SIMPSON, C., SMAIL, I., MORTLOCK, D., FOLGER, M. The ukirt infrared deep sky survey (ukidss). **Monthly Notices of the Royal Astronomical Society**, v. 379, n. 4, p. 1599–1617, 2007.

[110] LECONTE, JÉRÉMY. Why Compositional Convection Cannot Explain Substellar Objects' Sharp Spectral-type Transitions. **ApJ**, v. 853, n. 2, p. L30, February 2018.

[111] LEGGETT, S. K., BURNINGHAM, BEN, SAUMON, D., MARLEY, M. S., WARREN, S. J., SMART, R. L., JONES, H. R. A., LUCAS, P. W., PINFIELD, D. J., TAMURA, MOTOHIDE. Mid-Infrared Photometry of Cold

Brown Dwarfs: Diversity in Age, Mass, and Metallicity. **ApJ**, v. 710, n. 2, p. 1627–1640, February 2010.

[112] LEGGETT, S. K., TREMBLIN, PASCAL, PHILLIPS, MARK W., DUPUY, TRENT J., MARLEY, MARK, MORLEY, CAROLINE, SCHNEIDER, ADAM, CASELDEN, DAN, GUILLAUME, COLIN, LOGSDON, SARAH E. Measuring and Replicating the 1-20 μm Energy Distributions of the Coldest Brown Dwarfs: Rotating, Turbulent, and Nonadiabatic Atmospheres. **ApJ**, v. 918, n. 1, p. 11, September 2021.

[113] LINE, MICHAEL R., FORTNEY, JONATHAN J., MARLEY, MARK S., SORAHANA, SATOKO. A Data-driven Approach for Retrieving Temperatures and Abundances in Brown Dwarf Atmospheres. **ApJ**, v. 793, n. 1, p. 33, September 2014.

[114] LINE, MICHAEL R., TESKE, JOHANNA, BURNINGHAM, BEN, FORTNEY, JONATHAN J., MARLEY, MARK S. Uniform Atmospheric Retrieval Analysis of Ultracool Dwarfs. I. Characterizing Benchmarks, Gl 570D and HD 3651B. **ApJ**, v. 807, n. 2, p. 183, July 2015.

[115] LODDERS, KATHARINA, FEGLEY, BRUCE. Atmospheric Chemistry in Giant Planets, Brown Dwarfs, and Low-Mass Dwarf Stars. I. Carbon, Nitrogen, and Oxygen. **Icarus**, v. 155, n. 2, p. 393–424, February 2002.

[116] LODIEU, N., HAMBLY, N. C., JAMESON, R. F., HODGKIN, S. T., CARRARO, G., KENDALL, T. R. New brown dwarfs in Upper Sco using UKIDSS Galactic Cluster Survey science verification data. **MNRAS**, v. 374, p. 372–384, January 2007.

[117] LODIEU, N., ZAPATERO OSORIO, M. R., REBOLO, R., MARTíN, E. L., HAMBLY, N. C. A census of very-low-mass stars and brown dwarfs in the σ Orionis cluster. **A&A**, v. 505, p. 1115–1127, October 2009.

[118] LÖVDAL, S. S., RUIZ-LARA, T., KOPPELMAN, H. H., MATSUNO, T., DODD, E., HELMI, A. Substructure in the stellar halo near the Sun. I. Data-driven clustering in integrals-of-motion space. **A&A**, v. 665, p. A57, September 2022.

[119] LUEBER, ANNA, KITZMANN, DANIEL, BOWLER, BRENDAN P., BURGASSER, ADAM J., HENG, KEVIN. Retrieval Study of Brown Dwarfs across the L-T Sequence. **ApJ**, v. 930, n. 2, p. 136, May 2022.

[120] LUHMAN, K. L. The Formation and Early Evolution of Low-Mass Stars and Brown Dwarfs. **ARA&A**, v. 50, p. 65–106, September 2012.

[121] LUHMAN, K. L., STAUFFER, JOHN R., MAMAJEK, E. E. The Age of AB Doradus. **ApJ**, v. 628, n. 1, p. L69–L72, July 2005.

[122] LYKE, BRAD W., HIGLEY, ALEXANDRA N., MCLANE, J. N., SCHURHAMMER, DANIELLE P., MYERS, ADAM D., ROSS, ASHLEY J., DAWSON, KYLE, CHABANIER, SOLÈNE, MARTINI, PAUL, BUSCA, NICOLÁS G., MAS DES BOURBOUX, HÉLION DU, SALVATO, MARA, STREBLYANSKA, ALINA, ZARROUK, PAULINE, BURTIN, ETIENNE, ANDERSON, SCOTT F., BAUTISTA, JULIAN, BIZYAEV, DMITRY, BRANDT, W. N., BRINKMANN, JONATHAN, BROWNSTEIN, JOEL R., COMPARAT, JOHAN, GREEN, PAUL, DE LA MACORRA, AXEL, MUÑOZ GUTIÉRREZ, ANDREA, HOU, JIAMIN, NEWMAN, JEFFREY A., PALANQUE-DELABROUILLE, NATHALIE, PÂRIS, ISABELLE, PERCIVAL, WILL J., PETITJEAN, PATRICK, RICH, JAMES, ROSSI, GRAZIANO, SCHNEIDER, DONALD P., SMITH, ALEXANDER, VIVEK, M., WEAVER, BENJAMIN ALAN. The Sloan Digital Sky Survey Quasar Catalog: Sixteenth Data Release. **ApJS**, v. 250, n. 1, p. 8, September 2020.

[123] MACKERETH, J. TED, BOVY, JO, LEUNG, HENRY W., SCHIAVON, RICARDO P., TRICK, WILMA H., CHAPLIN, WILLIAM J., CUNHA, KATIA, FEUILLET, DIANE K., MAJEWSKI, STEVEN R., MARTIG, MARIE, MIGLIO, ANDREA, NIDEVER, DAVID, PINSONNEAULT, MARC H., AGUIRRE, VICTOR SILVA, SOBECK, JENNIFER, TAYAR, JAMIE, ZASOWSKI, GAIL. Dynamical heating across the Milky Way disc using APOGEE and Gaia. **MNRAS**, v. 489, n. 1, p. 176–195, October 2019.

[124] MARIGO, PAOLA, GIRARDI, LÉO, BRESSAN, ALESSANDRO, ROSENFIELD, PHILIP, ARINGER, BERNHARD, CHEN, YANG, DUSSIN, MARCO, NANNI, AMBRA, PASTORELLI, GIADA, RODRIGUES, THAíSE S., TRABUCCHI, MICHELE, BLADH, SARA, DALCANTON, JULIANNE, GROENEWEGEN, MARTIN A. T., MONTALBÁN, JOSEFINA, WOOD, PETER R. A New Generation of PARSEC-COLIBRI Stellar Isochrones Including the TP-AGB Phase. **ApJ**, v. 835, n. 1, p. 77, January 2017.

[125] MARLEY, MARK S., SAUMON, DIDIER, VISSCHER, CHANNON, LUPU, ROXANA, FREEDMAN, RICHARD, MORLEY, CAROLINE, FORTNEY, JONATHAN J., SEAY, CHRISTOPHER, SMITH, ADAM J. R. W., TEAL, D. J., WANG, RUOYAN. The Sonora Brown Dwarf Atmosphere and Evolution Models. I. Model Description and Application to Cloudless Atmospheres in Rainout Chemical Equilibrium. **ApJ**, v. 920, n. 2, p. 85, October 2021.

[126] MAROCCO, F., JONES, H. R. A., DAY-JONES, A. C., PINFIELD, D. J., LUCAS, P. W., BURNINGHAM, B., ZHANG, Z. H., SMART, R. L., GOMES, J. I., SMITH, L. A large spectroscopic sample of L and T dwarfs from UKIDSS LAS: peculiar objects, binaries, and space density. **MNRAS**, v. 449, n. 4, p. 3651–3692, June 2015.

[127] MAROCCO, FEDERICO, EISENHARDT, PETER R. M., FOWLER, JOHN W., KIRKPATRICK, J. DAVY, MEISNER, AARON M., SCHLAFLY, EDWARD F., STANFORD, S. A., GARCIA, NELSON, CASELDEN, DAN, CUSHING, MICHAEL C., CUTRI, ROC M., FAHERTY, JACQUELINE K., GELINO, CHRISTOPHER R., GONZALEZ, ANTHONY H., JARRETT, THOMAS H., KOONTZ, RENATA, MAINZER, AMANDA, MARCHESE, ELIJAH J., MOBASHER, BAHRAM, SCHLEGEL, DAVID J., STERN, DANIEL, TEPLITZ, HARRY I., WRIGHT, EDWARD L. The CatWISE2020 Catalog. **ApJS**, v. 253, n. 1, p. 8, March 2021.

[128] MATSUNO, TADAFUMI, AOKI, WAKO, SUDA, TAKUMA. Origin of the Excess of High-energy Retrograde Stars in the Galactic Halo. **ApJ**, v. 874, n. 2, p. L35, April 2019.

[129] MCMAHON, R. G., BANERJI, M., GONZALEZ, E., KOPOSOV, S. E., BEJAR, V. J., LODIEU, N., REBOLO, R., VHS COLLABORATION, . First Scientific Results from the VISTA Hemisphere Survey (VHS). **The Messenger**, v. 154, p. 35–37, December 2013.

[130] MCMILLAN, PAUL J. The mass distribution and gravitational potential of the Milky Way. **MNRAS**, v. 465, n. 1, p. 76–94, February 2017.

[131] MEISNER, AARON M., SCHNEIDER, ADAM C., BURGASSER, ADAM J., MAROCCO, FEDERICO, LINE, MICHAEL R., FAHERTY, JACQUELINE K., KIRKPATRICK, J. DAVY, CASELDEN, DAN, KUCHNER,

MARC J., GELINO, CHRISTOPHER R., GAGNÉ, JONATHAN, THEISSEN, CHRISTOPHER, GERASIMOV, ROMAN, AGANZE, CHRISTIAN, HSU, CHIH-CHUN, WISNIEWSKI, JOHN P., CASEWELL, SARAH L., BARDALEZ GAGLIUFFI, DANIELLA C., LOGSDON, SARAH E., EISENHARDT, PETER R. M., ALLERS, KATELYN, DEBES, JOHN H., ALLEN, MICHAELA B., STEVNBAK ANDERSEN, NIKOLAJ, GOODMAN, SAM, GRAMAIZE, LÉOPOLD, MARTIN, DAVID W., SAINIO, ARTTU, CUSHING, MICHAEL C., BACKYARD WORLDS: PLANET 9 COLLABORATION, . New Candidate Extreme T Subdwarfs from the Backyard Worlds: Planet 9 Citizen Science Project. **ApJ**, v. 915, n. 2, p. 120, July 2021.

[132] METCHEV, STANIMIR A., HEINZE, AREN, APAI, DÁNIEL, FLATEAU, DAVIN, RADIGAN, JACQUELINE, BURGASSER, ADAM, MARLEY, MARK S., ARTIGAU, ÉTIENNE, PLAVCHAN, PETER, GOLDMAN, BERTRAND. Weather on Other Worlds. II. Survey Results: Spots are Ubiquitous on L and T Dwarfs. **ApJ**, v. 799, n. 2, p. 154, February 2015.

[133] MIYAZAKI, S., KOMIYAMA, Y., KAWANOMOTO, S., DOI, Y., FURUSAWA, H., HAMANA, T., HAYASHI, Y., IKEDA, H., KAMATA, Y., KAROJI, H., KOIKE, M., KURAKAMI, T., MIYAMA, S., MOROKUMA, T., NAKATA, F., NAMIKAWA, K., NAKAYA, H., NARIAI, K., OBUCHI, Y., OISHI, Y., OKADA, N., OKURA, Y., TAIT, P., TAKATA, T., TANAKA, Y., TANAKA, M., TERAI, T., TOMONO, D., URAGUCHI, F., USUDA, T., UTSUMI, Y., YAMADA, Y., YAMANOI, H., AIHARA, H., FUJIMORI, H., MINEO, S., MIYATAKE, H., OGURI, M., UCHIDA, T., TANAKA, M. M., YASUDA, N., TAKADA, M., MURAYAMA, H., NISHIZAWA, A. J., SUGIYAMA, N., CHIBA, M., FUTAMASE, T., WANG, S.-Y., CHEN, H.-Y., HO, P. T. P., LIAW, E. J. Y., CHIU, C.-F., HO, C.-L., LAI, T.-C., LEE, Y.-C., JENG, D.-Z., IWAMURA, S., ARMSTRONG, R., BICKERTON, S., BOSCH, J., GUNN, J. E., LUPTON, R. H., LOOMIS, C., PRICE, P., SMITH, S., STRAUSS, M. A., TURNER, E. L., SUZUKI, H., MIYAZAKI, Y., MURAMATSU, M., YAMAMOTO, K., ENDO, M., EZAKI, Y., ITO, N., KAWAGUCHI, N., SOFUKU, S., TANIIKE, T., AKUTSU, K., DOJO, N., KASUMI, K., MATSUDA, T., IMOTO, K., MIWA, Y., SUZUKI, M., TAKESHI, K., YOKOTA, H. Hyper Suprime-Cam: System design and verification of image quality. **PASJ**, v. 70, p. S1, January 2018.

[134] MORAUX, E., BOUVIER, J., STAUFFER, J. R., CUILLANDRE, J.-C. Brown dwarfs in the Pleiades cluster: Clues to the substellar mass function. **A&A**, v. 400, p. 891–902, March 2003.

[135] MUKHERJEE, SAGNICK, FORTNEY, JONATHAN J., BATALHA, NATASHA E., KARALIDI, THEODORA, MARLEY, MARK S., VISSCHER, CHANNON, MILES, BRITTANY E., SKEMER, ANDREW J. I. Probing the Extent of Vertical Mixing in Brown Dwarf Atmospheres with Disequilibrium Chemistry. **ApJ**, v. 938, n. 2, p. 107, October 2022.

[136] MURPHY, SIMON J., LAWSON, WARRICK A. New low-mass members of the Octans stellar association and an updated 30-40 Myr lithium age. **MNRAS**, v. 447, n. 2, p. 1267–1281, February 2015.

[137] MUŽIĆ, KORALJKA, SCHÖDEL, RAINER, SCHOLZ, ALEXANDER, GEERS, VINCENT C., JAYAWARDHANA, RAY, ASCENSO, JOANA, CIEZA, LUCAS A. The low-mass content of the massive young star cluster RCW 38. **MNRAS**, v. 471, n. 3, p. 3699–3712, November 2017.

[138] MUŽIĆ, KORALJKA, SCHOLZ, ALEXANDER, PEÑA RAMíREZ, KARLA, JAYAWARDHANA, RAY, SCHÖDEL, RAINER, GEERS, VINCENT C., CIEZA, LUCAS A., BAYO, AMELIA. Looking Deep into the Rosette Nebula's Heart: The (Sub)stellar Content of the Massive Young Cluster NGC 2244. **ApJ**, v. 881, n. 1, p. 79, August 2019.

[139] MYEONG, G. C., VASILIEV, E., IORIO, G., EVANS, N. W., BELOKUROV, V. Evidence for two early accretion events that built the Milky Way stellar halo. **MNRAS**, v. 488, n. 1, p. 1235–1247, September 2019.

[140] NAAB, THORSTEN, OSTRIKER, JEREMIAH P. Theoretical Challenges in Galaxy Formation. **ARA&A**, v. 55, n. 1, p. 59–109, August 2017.

[141] NAIDU, ROHAN P., CONROY, CHARLIE, BONACA, ANA, JOHNSON, BENJAMIN D., TING, YUAN-SEN, CALDWELL, NELSON, ZARITSKY, DENNIS, CARGILE, PHILLIP A. Evidence from the H3 Survey That the Stellar Halo Is Entirely Comprised of Substructure. **ApJ**, v. 901, n. 1, p. 48, September 2020.

[142] NEWBERG, HEIDI JO, YANNY, BRIAN, ROCKOSI, CONNIE, GREBEL, EVA K., RIX, HANS-WALTER, BRINKMANN, JON, CSABAI, ISTVAN, HENNESSY, GREG, HINDSLEY, ROBERT B., IBATA, RODRIGO,

IVEZIĆ, ZELJKO, LAMB, DON, NASH, E. THOMAS, ODENKIRCHEN, MICHAEL, RAVE, HEATHER A., SCHNEIDER, D. P., SMITH, J. ALLYN, STOLTE, ANDREA, YORK, DONALD G. The Ghost of Sagittarius and Lumps in the Halo of the Milky Way. **ApJ**, v. 569, n. 1, p. 245–274, April 2002.

[143] NIDEVER, DAVID L., BOVY, JO, BIRD, JONATHAN C., ANDREWS, BRETT H., HAYDEN, MICHAEL, HOLTZMAN, JON, MAJEWSKI, STEVEN R., SMITH, VERNE, ROBIN, ANNIE C., GARCíA PÉREZ, ANA E., CUNHA, KATIA, ALLENDE PRIETO, CARLOS, ZASOWSKI, GAIL, SCHIAVON, RICARDO P., JOHNSON, JENNIFER A., WEINBERG, DAVID H., FEUILLET, DIANE, SCHNEIDER, DONALD P., SHETRONE, MATTHEW, SOBECK, JENNIFER, GARCíA-HERNÁNDEZ, D. A., ZAMORA, O., RIX, HANS-WALTER, BEERS, TIMOTHY C., WILSON, JOHN C., O'CONNELL, ROBERT W., MINCHEV, IVAN, CHIAPPINI, CRISTINA, ANDERS, FRIEDRICH, BIZYAEV, DMITRY, BREWINGTON, HOWARD, EBELKE, GARRETT, FRINCHABOY, PETER M., GE, JIAN, KINEMUCHI, KAREN, MALANUSHENKO, ELENA, MALANUSHENKO, VIKTOR, MARCHANTE, MOSES, MÉSZÁROS, SZABOLCS, ORAVETZ, DANIEL, PAN, KAIKE, SIMMONS, AUDREY, SKRUTSKIE, MICHAEL F. Tracing Chemical Evolution over the Extent of the Milky Way's Disk with APOGEE Red Clump Stars. **ApJ**, v. 796, n. 1, p. 38, November 2014.

[144] NIDEVER, DAVID L., DEY, ARJUN, FASBENDER, KATIE, JUNEAU, STÉPHANIE, MEISNER, AARON M., WISHART, JOSEPH, SCOTT, ADAM, MATT, KYLE, NIKUTTA, ROBERT, PUCHA, RAGADEEPIKA. Second Data Release of the All-sky NOIRLab Source Catalog. **AJ**, v. 161, n. 4, p. 192, April 2021.

[145] NISSEN, P. E., SCHUSTER, W. J. Two distinct halo populations in the solar neighborhood. Evidence from stellar abundance ratios and kinematics. **A&A**, v. 511, p. L10, February 2010.

[146] ODENKIRCHEN, MICHAEL, GREBEL, EVA K., ROCKOSI, CONSTANCE M., DEHNEN, WALTER, IBATA, RODRIGO, RIX, HANS-WALTER, STOLTE, ANDREA, WOLF, CHRISTIAN, ANDERSON, JR., JOHN E., BAHCALL, NETA A., BRINKMANN, JON, CSABAI, ISTVÁN,

HENNESSY, G., HINDSLEY, ROBERT B., IVEZIĆ, ŽELJKO, LUPTON, ROBERT H., MUNN, JEFFREY A., PIER, JEFFREY R., STOUGHTON, CHRIS, YORK, DONALD G. Detection of Massive Tidal Tails around the Globular Cluster Palomar 5 with Sloan Digital Sky Survey Commissioning Data. **ApJ**, v. 548, n. 2, p. L165–L169, February 2001.

[147] ONKEN, CHRISTOPHER A., WOLF, CHRISTIAN, BESSELL, MICHAEL S., CHANG, SEO-WON, DA COSTA, GARY S., LUVAUL, LANCE C., MACKEY, DOUGAL, SCHMIDT, BRIAN P., SHAO, LI. SkyMapper Southern Survey: Second data release (DR2). **Publ. Astron. Soc. Australia**, v. 36, p. e033, August 2019.

[148] OPPENHEIMER, B. R., KULKARNI, S. R., MATTHEWS, K., NAKAJIMA, T. Infrared Spectrum of the Cool Brown Dwarf Gl 229B. **Science**, v. 270, p. 1478–1479, December 1995.

[149] PADOAN, P., NORDLUND, Å. The Stellar Initial Mass Function from Turbulent Fragmentation. **ApJ**, v. 576, p. 870–879, September 2002.

[150] PHILLIPS, M. W., TREMBLIN, P., BARAFFE, I., CHABRIER, G., ALLARD, N. F., SPIEGELMAN, F., GOYAL, J. M., DRUMMOND, B., HÉBRARD, E. A new set of atmosphere and evolution models for cool T-Y brown dwarfs and giant exoplanets. **A&A**, v. 637, p. A38, May 2020.

[151] PIRZKAL, N., SAHU, K. C., BURGASSER, A., MOUSTAKAS, L. A., XU, C., MALHOTRA, S., RHOADS, J. E., KOEKEMOER, A. M., NELAN, E. P., WINDHORST, R. A., PANAGIA, N., GRONWALL, C., PASQUALI, A., WALSH, J. R. Stars in the Hubble Ultra Deep Field. **ApJ**, v. 622, n. 1, p. 319–332, March 2005.

[152] QUEIROZ, A. B. A., ANDERS, F., SANTIAGO, B. X., CHIAPPINI, C., STEINMETZ, M., DAL PONTE, M., STASSUN, K. G., DA COSTA, L. N., MAIA, M. A. G., CRESTANI, J., BEERS, T. C., FERNÁNDEZ-TRINCADO, J. G., GARCíA-HERNÁNDEZ, D. A., ROMAN-LOPES, A., ZAMORA, O. StarHorse: a Bayesian tool for determining stellar masses, ages, distances, and extinctions for field stars. **MNRAS**, v. 476, p. 2556–2583, May 2018.

[153] RADIGAN, JACQUELINE. An Independent Analysis of the Brown Dwarf Atmosphere Monitoring (BAM) Data: Large-amplitude Variability is Rare Outside the L/T Transition. **ApJ**, v. 797, n. 2, p. 120, December 2014.

[154] RAGHAVAN, D., MCALISTER, H. A., HENRY, T. J., LATHAM, D. W., MARCY, G. W., MASON, B. D., GIES, D. R., WHITE, R. J., TEN BRUMMELAAR, T. A. A Survey of Stellar Families: Multiplicity of Solar-type Stars. **ApJS**, v. 190, p. 1–42, September 2010.

[155] REBOLO, R., ZAPATERO OSORIO, M. R., MARTíN, E. L. Discovery of a brown dwarf in the Pleiades star cluster. **Nature**, v. 377, p. 129–131, September 1995.

[156] REID, I. NEILL, CRUZ, K. L., LAURIE, STEPHEN P., LIEBERT, JAMES, DAHN, CONARD C., HARRIS, HUGH C., GUETTER, HARRY H., STONE, RONALD C., CANZIAN, BLAISE, LUGINBUHL, CHRISTIAN B., LEVINE, STEPHEN E., MONET, ALICE K. B., MONET, DAVID G. Meeting the Cool Neighbors. IV. 2MASS 1835+32, a Newly Discovered M8.5 Dwarf within 6 Parsecs of the Sun. **AJ**, v. 125, n. 1, p. 354–358, January 2003.

[157] REIPURTH, BO, CLARKE, CATHIE, DELGADO-DONATE, EDUARDO. A Dynamical Origin for Brown Dwarfs. **arXiv e-prints**, p. astro–ph/0110481, October 2001.

[158] REYLÉ, C. New ultra-cool and brown dwarf candidates in Gaia DR2. **A&A**, v. 619, p. L8, November 2018.

[159] REYLÉ, C., DELORME, P., WILLOTT, C. J., ALBERT, L., DELFOSSE, X., FORVEILLE, T., ARTIGAU, E., MALO, L., HILL, G. J., DOYON, R. The ultracool-field dwarf luminosity-function and space density from the Canada-France Brown Dwarf Survey. **A&A**, v. 522, p. A112, November 2010.

[160] ROJAS-ARRIAGADA, A., RECIO-BLANCO, A., HILL, V., DE LAVERNY, P., SCHULTHEIS, M., BABUSIAUX, C., ZOCCALI, M., MINNITI, D., GONZALEZ, O. A., FELTZING, S., GILMORE, G., RANDICH, S., VALLENARI, A., ALFARO, E. J., BENSBY, T., BRAGAGLIA, A., FLACCOMIO, E., LANZAFAME, A. C., PANCINO, E., SMILJANIC, R., BERGEMANN, M., COSTADO, M. T., DAMIANI, F., HOURIHANE, A., JOFRÉ, P., LARDO, C., MAGRINI, L., MAIORCA, E., MORBIDELLI, L., SBORDONE, L., WORLEY, C. C., ZAGGIA, S., WYSE, R. The Gaia-ESO Survey: metallicity and kinematic trends in the Milky Way bulge. **A&A**, v. 569, p. A103, September 2014.

[161] RYAN, JR., R. E., HATHI, N. P., COHEN, S. H., WINDHORST, R. A. Constraining the Distribution of L and T Dwarfs in the Galaxy. **ApJ**, v. 631, n. 2, p. L159–L162, October 2005.

[162] RYBIZKI, JAN, GREEN, GREGORY M., RIX, HANS-WALTER, EL-BADRY, KAREEM, DEMLEITNER, MARKUS, ZARI, ELEONORA, UDALSKI, ANDRZEJ, SMART, RICHARD L., GOULD, ANDREW. A classifier for spurious astrometric solutions in Gaia eDR3. **MNRAS**, v. 510, n. 2, p. 2597–2616, February 2022.

[163] SAUMON, D., MARLEY, MARK S. The Evolution of L and T Dwarfs in Color-Magnitude Diagrams. **ApJ**, v. 689, n. 2, p. 1327–1344, December 2008.

[164] SCHMIDT, SARAH J., HAWLEY, SUZANNE L., WEST, ANDREW A., BOCHANSKI, JOHN J., DAVENPORT, JAMES R. A., GE, JIAN, SCHNEIDER, DONALD P. BOSS Ultracool Dwarfs. I. Colors and Magnetic Activity of M and L Dwarfs. **AJ**, v. 149, n. 5, p. 158, May 2015.

[165] SCHMIDT, SARAH J., SHAPPEE, BENJAMIN J., VAN SADERS, JENNIFER L., STANEK, K. Z., BROWN, JONATHAN S., KOCHANEK, C. S., DONG, SUBO, DROUT, MARIA R., FRANK, STEPHAN, HOLOIEN, T. W. S., JOHNSON, SEAN, MADORE, BARRY F., PRIETO, J. L., SEIBERT, MARK, SEIDEL, MARJA K., SIMONIAN, GREGORY V. A. The Largest M Dwarf Flares from ASAS-SN. **ApJ**, v. 876, n. 2, p. 115, May 2019.

[166] SCHÖNRICH, RALPH, ASPLUND, MARTIN, CASAGRANDE, LUCA. On the alleged duality of the Galactic halo. **MNRAS**, v. 415, n. 4, p. 3807–3823, Aug 2011.

[167] SCHÖNRICH, RALPH, BINNEY, JAMES, DEHNEN, WALTER. Local kinematics and the local standard of rest. **MNRAS**, v. 403, n. 4, p. 1829–1833, April 2010.

[168] SESAR, BRANIMIR, JURIĆ, MARIO, IVEZIĆ, ŽELJKO. The Shape and Profile of the Milky Way Halo as Seen by the Canada-France-Hawaii Telescope Legacy Survey. **ApJ**, v. 731, n. 1, p. 4, Apr 2011.

[169] SHIPP, N., DRLICA-WAGNER, A., BALBINOT, E., FERGUSON, P., ERKAL, D., LI, T. S., BECHTOL, K., BELOKUROV, V., BUNCHER, B., CAROLLO, D., CARRASCO KIND, M., KUEHN, K., MARSHALL, J. L., PACE,

A. B., RYKOFF, E. S., SEVILLA-NOARBE, I., SHELDON, E., STRIGARI, L., VIVAS, A. K., YANNY, B., ZENTENO, A., ABBOTT, T. M. C., ABDALLA, F. B., ALLAM, S., AVILA, S., BERTIN, E., BROOKS, D., BURKE, D. L., CARRETERO, J., CASTANDER, F. J., CAWTHON, R., CROCCE, M., CUNHA, C. E., D'ANDREA, C. B., DA COSTA, L. N., DAVIS, C., DE VICENTE, J., DESAI, S., DIEHL, H. T., DOEL, P., EVRARD, A. E., FLAUGHER, B., FOSALBA, P., FRIEMAN, J., GARCíABELLIDO, J., GAZTANAGA, E., GERDES, D. W., GRUEN, D., GRUENDL, R. A., GSCHWEND, J., GUTIERREZ, G., HARTLEY, W., HONSCHEID, K., HOYLE, B., JAMES, D. J., JOHNSON, M. D., KRAUSE, E., KUROPATKIN, N., LAHAV, O., LIN, H., MAIA, M. A. G., MARCH, M., MARTINI, P., MENANTEAU, F., MILLER, C. J., MIQUEL, R., NICHOL, R. C., PLAZAS, A. A., ROMER, A. K., SAKO, M., SANCHEZ, E., SANTIAGO, B., SCARPINE, V., SCHINDLER, R., SCHUBNELL, M., SMITH, M., SMITH, R. C., SOBREIRA, F., SUCHYTA, E., SWANSON, M. E. C., TARLE, G., THOMAS, D., TUCKER, D. L., WALKER, A. R., WECHSLER, R. H., DES COLLABORATION, . Stellar Streams Discovered in the Dark Energy Survey. **ApJ**, v. 862, n. 2, p. 114, August 2018.

[170] SHKOLNIK, EVGENYA L., ALLERS, KATELYN N., KRAUS, ADAM L., LIU, MICHAEL C., FLAGG, LAURA. All-sky Co-moving Recovery Of Nearby Young Members (ACRONYM). II. The β Pictoris Moving Group. **AJ**, v. 154, n. 2, p. 69, August 2017.

[171] SKRUTSKIE, M. F., CUTRI, R. M., STIENING, R., WEINBERG, M. D., SCHNEIDER, S., CARPENTER, J. M., BEICHMAN, C., CAPPS, R., CHESTER, T., ELIAS, J., HUCHRA, J., LIEBERT, J., LONSDALE, C., MONET, D. G., PRICE, S., SEITZER, P., JARRETT, T., KIRKPATRICK, J. D., GIZIS, J. E., HOWARD, E., EVANS, T., FOWLER, J., FULLMER, L., HURT, R., LIGHT, R., KOPAN, E. L., MARSH, K. A., MCCALLON, H. L., TAM, R., VAN DYK, S., WHEELOCK, S. The Two Micron All Sky Survey (2MASS). **AJ**, v. 131, p. 1163–1183, Feb 2006.

[172] SKRZYPEK, N., WARREN, S. J., FAHERTY, J. K. Photometric brown-dwarf classification. II. A homogeneous sample of 1361 L and T dwarfs brighter than J = 17.5 with accurate spectral types. **A&A**, v. 589, p. A49, May 2016.

[173] SKRZYPEK, N., WARREN, S. J., FAHERTY, J. K., MORTLOCK, D. J., BURGASSER, A. J., HEWETT, P. C. **A&A**, v. 574, p. A78, February 2015.

[174] SLATER, COLIN T., NIDEVER, DAVID L., MUNN, JEFFREY A., BELL, ERIC F., MAJEWSKI, STEVEN R. The Stellar Density Profile of the Distant Galactic Halo. **ApJ**, v. 832, n. 2, p. 206, Dec 2016.

[175] SMART, R. L., MAROCCO, F., CABALLERO, J. A., JONES, H. R. A., BARRADO, D., BEAMíN, J. C., PINFIELD, D. J., SARRO, L. M. The Gaia ultracool dwarf sample - I. Known L and T dwarfs and the first Gaia data release. **MNRAS**, v. 469, n. 1, p. 401–415, July 2017.

[176] SMITH, L., LUCAS, P. W., BURNINGHAM, B., JONES, H. R. A., SMART, R. L., ANDREI, A. H., CATALÁN, S., PINFIELD, D. J. A 1500 deg^2 near infrared proper motion catalogue from the UKIDSS Large Area Survey. **MNRAS**, v. 437, p. 3603–3625, February 2014.

[177] SOFTICH, EMMA, SCHNEIDER, ADAM C., PATIENCE, JENNIFER, BURGASSER, ADAM J., SHKOLNIK, EVGENYA, FAHERTY, JACQUELINE K., CASELDEN, DAN, MEISNER, AARON M., KIRKPATRICK, J. DAVY, KUCHNER, MARC J., GAGNÉ, JONATHAN, GAGLIUFFI, DANIELLA BARDALEZ, CUSHING, MICHAEL C., CASEWELL, SARAH L., AGANZE, CHRISTIAN, HSU, CHIH-CHUN, ANDERSEN, NIKOLAJ STEVNBAK, KIWY, FRANK, THÉVENOT, MELINA, BACKYARD WORLDS: PLANET 9 COLLABORATION, . CWISE J014611.20-050850.0AB: The Widest Known Brown Dwarf Binary in the Field. **ApJ**, v. 926, n. 2, p. L12, February 2022.

[178] SORAHANA, SATOKO, NAKAJIMA, TADASHI, MATSUOKA, YOSHIKI. Evaluation of the Vertical Scale Height of L Dwarfs in the Galactic Thin Disk. **ApJ**, v. 870, n. 2, p. 118, January 2019.

[179] SPRINGEL, VOLKER, WHITE, SIMON D. M., JENKINS, ADRIAN, FRENK, CARLOS S., YOSHIDA, NAOKI, GAO, LIANG, NAVARRO, JULIO, THACKER, ROBERT, CROTON, DARREN, HELLY, JOHN, PEACOCK, JOHN A., COLE, SHAUN, THOMAS, PETER, COUCHMAN, HUGH, EVRARD, AUGUST, COLBERG, JÖRG, PEARCE, FRAZER. Simulations of the formation, evolution and clustering of galaxies and quasars. **Nature**, v. 435, n. 7042, p. 629–636, June 2005.

[180] STAMATELLOS, D., MAURY, A., WHITWORTH, A., ANDRÉ, P. The lower limits of disc fragmentation and the prospects for observing fragmenting discs. **MNRAS**, v. 413, p. 1787–1796, May 2011.

[181] STAUFFER, J. R., HAMILTON, D., PROBST, R. G. A CCD-based search for very low mass members of the Pleiades cluster. **AJ**, v. 108, p. 155–159, July 1994.

[182] STRINGER, K. M., DRLICA-WAGNER, A., MACRI, L., MARTíNEZ-VÁZQUEZ, C. E., VIVAS, A. K., FERGUSON, P., PACE, A. B., WALKER, A. R., NEILSEN, E., TAVANGAR, K., WESTER, W., ABBOTT, T. M. C., AGUENA, M., ALLAM, S., BACON, D., BECHTOL, K., BERTIN, E., BROOKS, D., BURKE, D. L., CARNERO ROSELL, A., CARRASCO KIND, M., CARRETERO, J., COSTANZI, M., CROCCE, M., DA COSTA, L. N., PEREIRA, M. E. S., DE VICENTE, J., DESAI, S., DIEHL, H. T., DOEL, P., FERRERO, I., GARCíA-BELLIDO, J., GAZTANAGA, E., GERDES, D. W., GRUEN, D., GRUENDL, R. A., GSCHWEND, J., GUTIERREZ, G., HINTON, S. R., HOLLOWOOD, D. L., HONSCHEID, K., HOYLE, B., JAMES, D. J., KUEHN, K., KUROPATKIN, N., LI, T. S., MAIA, M. A. G., MARSHALL, J. L., MENANTEAU, F., MIQUEL, R., MORGAN, R., OGANDO, R. L. C., PALMESE, A., PAZ-CHINCHÓN, F., PLAZAS, A. A., ROODMAN, A., SANCHEZ, E., SCHUBNELL, M., SERRANO, S., SEVILLA-NOARBE, I., SMITH, M., SOARES-SANTOS, M., SUCHYTA, E., TARLE, G., THOMAS, D., TO, C., VARGA, T. N., WILKINSON, R. D., ZHANG, Y., DES COLLABORATION, . Identifying RR Lyrae Variable Stars in Six Years of the Dark Energy Survey. **ApJ**, v. 911, n. 2, p. 109, April 2021.

[183] TARTER, J. C. **The interaction of gas and galaxies within galaxy clusters**. 1975. Tese de Doutoramento – California Univ., Berkeley.

[184] TENACHI, WASSIM, ORIA, PIERRE-ANTOINE, IBATA, RODRIGO, FAMAEY, BENOIT, YUAN, ZHEN, ARENTSEN, ANKE, MARTIN, NICOLAS, VISWANATHAN, AKSHARA. Typhon: A Polar Stream from the Outer Halo Raining through the Solar Neighborhood. **ApJ**, v. 935, n. 2, p. L22, August 2022.

[185] THOMAS, GUILLAUME F., MCCONNACHIE, ALAN W., IBATA, RODRIGO A., CÔTÉ, PATRICK, MARTIN, NICOLAS, STARKENBURG, ELSE, CARLBERG, RAYMOND, CHAPMAN, SCOTT, FABBRO,

SÉBASTIEN, FAMAEY, BENOIT, FANTIN, NICHOLAS, GWYN, STEPHEN, HÉNAULT-BRUNET, VINCENT, MALHAN, KHYATI, NAVARRO, JULIO, ROBIN, ANNIE C., SCOTT, DOUGLAS. A-type stars in the Canada-France Imaging Survey I. The stellar halo of the Milky Way traced to large radius by blue horizontal branch stars. **MNRAS**, v. 481, n. 4, p. 5223–5235, December 2018.

[186] TOKOVININ, A., LÉPINE, S. Wide Companions to Hipparcos Stars within 67 pc of the Sun. **AJ**, v. 144, p. 102, October 2012.

[187] TREMBLIN, P., AMUNDSEN, D. S., MOURIER, P., BARAFFE, I., CHABRIER, G., DRUMMOND, B., HOMEIER, D., VENOT, O. Fingering Convection and Cloudless Models for Cool Brown Dwarf Atmospheres. **ApJ**, v. 804, n. 1, p. L17, May 2015.

[188] VINCENZO, FIORENZO, WEINBERG, DAVID H., MIGLIO, ANDREA, LANE, RICHARD R., ROMAN-LOPES, ALEXANDRE. The distribution of [α/Fe] in the Milky Way disc. **MNRAS**, v. 508, n. 4, p. 5903–5920, December 2021.

[189] VIVAS, A. K., ZINN, R., ABAD, C., ANDREWS, P., BAILYN, C., BALTAY, C., BONGIOVANNI, A., BRICEÑO, C., BRUZUAL, G., COPPI, P., DELLA PRUGNA, F., ELLMAN, N., FERRíN, I., GEBHARD, M., GIRARD, T., HERNANDEZ, J., HERRERA, D., HONEYCUTT, R., MAGRIS, G., MUFSON, S., MUSSER, J., NARANJO, O., RABINOWITZ, D., RENGSTORF, A., ROSENZWEIG, P., SÁNCHEZ, GE., SÁNCHEZ, GU., SCHAEFER, B., SCHENNER, H., SNYDER, J. A., SOFIA, S., STOCK, J., VAN ALTENA, W., VICENTE, B., VIEIRA, K. The QUEST RR Lyrae Survey. I. The First Catalog. **AJ**, v. 127, n. 2, p. 1158–1175, February 2004.

[190] VOS, JOHANNA M., BILLER, BETH A., BONAVITA, MARIANGELA, ERIKSSON, SIMON, LIU, MICHAEL C., BEST, WILLIAM M. J., METCHEV, STANIMIR, RADIGAN, JACQUELINE, ALLERS, KATELYN N., JANSON, MARKUS, BUENZLI, ESTHER, DUPUY, TRENT J., BONNEFOY, MICKAËL, MANJAVACAS, ELENA, BRANDNER, WOLFGANG, CROSSFIELD, IAN, DEACON, NIALL, HENNING, THOMAS, HOMEIER, DEREK, KOPYTOVA, TAISIYA, SCHLIEDER, JOSHUA. A search for variability in exoplanet analogues and low-gravity brown dwarfs. **MNRAS**, v. 483, n. 1, p. 480–502, February 2019.

[191] WATKINS, LAURA L., VAN DER MAREL, ROELAND P., SOHN, SANGMO TONY, EVANS, N. WYN. Evidence for an Intermediate-mass Milky Way from Gaia DR2 Halo Globular Cluster Motions. **ApJ**, v. 873, n. 2, p. 118, March 2019.

[192] WENGER, M., OCHSENBEIN, F., EGRET, D., DUBOIS, P., BONNAREL, F., BORDE, S., GENOVA, F., JASNIEWICZ, G., LALOË, S., LESTEVEN, S., MONIER, R. The SIMBAD astronomical database. The CDS reference database for astronomical objects. **A&AS**, v. 143, p. 9–22, April 2000.

[193] WEST, A. A., MORGAN, D. P., BOCHANSKI, J. J., ANDERSEN, J. M., ET AL., . The Sloan Digital Sky Survey Data Release 7 Spectroscopic M Dwarf Catalog. I. Data. **Aj**, v. 141, p. 97, March 2011.

[194] WHITWORTH, A. P., ZINNECKER, H. The formation of free-floating brown dwarves and planetary-mass objects by photo-erosion of prestellar cores. **A&A**, v. 427, p. 299–306, November 2004.

[195] WRIGHT, E. L., EISENHARDT, P. R. M., MAINZER, A. K., RESSLER, M. E., CUTRI, R. M., JARRETT, T., KIRKPATRICK, J. D., PADGETT, D., MCMILLAN, R. S., SKRUTSKIE, M., STANFORD, S. A., COHEN, M., WALKER, R. G., MATHER, J. C., LEISAWITZ, D., GAUTIER, T. N., III, MCLEAN, I., BENFORD, D., LONSDALE, C. J., BLAIN, A., MENDEZ, B., IRACE, W. R., DUVAL, V., LIU, F., ROYER, D., HEINRICHSEN, I., HOWARD, J., SHANNON, M., KENDALL, M., WALSH, A. L., LARSEN, M., CARDON, J. G., SCHICK, S., SCHWALM, M., ABID, M., FABINSKY, B., NAES, L., TSAI, C.-W. The Wide-field Infrared Survey Explorer (WISE): Mission Description and Initial On-orbit Performance. **AJ**, v. 140, p. 1868–1881, December 2010.

[196] XU, YAN, LIU, CHAO, XUE, XIANG-XIANG, NEWBERG, HEIDI JO, CARLIN, JEFFREY L., XIA, QI-RAN, DENG, LI-CAI, LI, JING, ZHANG, YONG, HOU, YONGHUI, WANG, YUEFEI, CAO, ZIHUANG. Mapping the Milky Way with LAMOST - II. The stellar halo. **MNRAS**, v. 473, n. 1, p. 1244–1257, January 2018.

[197] XUE, XIANG-XIANG, RIX, HANS-WALTER, MA, ZHIBO, MORRISON, HEATHER, BOVY, JO, SESAR, BRANIMIR, JANESH, WILLIAM. The Radial Profile and Flattening of the Milky Way's Stellar Halo to 80 kpc from the SEGUE K-giant Survey. **ApJ**, v. 809, n. 2, p. 144, August 2015.

[198] YANNY, BRIAN, NEWBERG, HEIDI JO, KENT, STEVE, LAURENT-MUEHLEISEN, SALLY A., PIER, JEFFREY R., RICHARDS, GORDON T., STOUGHTON, CHRIS, ANDERSON, JR., JOHN E., ANNIS, JAMES, BRINKMANN, J., CHEN, BING, CSABAI, ISTVÁN, DOI, MAMORU, FUKUGITA, MASATAKA, HENNESSY, G. S., IVEZIĆ, ŽELJKO, KNAPP, G. R., LUPTON, ROBERT, MUNN, JEFFREY A., NASH, THOMAS, ROCKOSI, CONSTANCE M., SCHNEIDER, DONALD P., SMITH, J. ALLYN, YORK, DONALD G. Identification of A-colored Stars and Structure in the Halo of the Milky Way from Sloan Digital Sky Survey Commissioning Data. **ApJ**, v. 540, n. 2, p. 825–841, September 2000.

[199] YORK, DONALD G., ADELMAN, J., ANDERSON, JR., JOHN E., ANDERSON, SCOTT F., ANNIS, JAMES, BAHCALL, NETA A., BAKKEN, J. A., BARKHOUSER, ROBERT, BASTIAN, STEVEN, BERMAN, EILEEN, BOROSKI, WILLIAM N., BRACKER, STEVE, BRIEGEL, CHARLIE, BRIGGS, JOHN W., BRINKMANN, J., BRUNNER, ROBERT, BURLES, SCOTT, CAREY, LARRY, CARR, MICHAEL A., CASTANDER, FRANCISCO J., CHEN, BING, COLESTOCK, PATRICK L., CONNOLLY, A. J., CROCKER, J. H., CSABAI, ISTVÁN, CZARAPATA, PAUL C., DAVIS, JOHN ERIC, DOI, MAMORU, DOMBECK, TOM, EISENSTEIN, DANIEL, ELLMAN, NANCY, ELMS, BRIAN R., EVANS, MICHAEL L., FAN, XIAOHUI, FEDERWITZ, GLENN R., FISCELLI, LARRY, FRIEDMAN, SCOTT, FRIEMAN, JOSHUA A., FUKUGITA, MASATAKA, GILLESPIE, BRUCE, GUNN, JAMES E., GURBANI, VIJAY K., DE HAAS, ERNST, HALDEMAN, MERLE, HARRIS, FREDERICK H., HAYES, J., HECKMAN, TIMOTHY M., HENNESSY, G. S., HINDSLEY, ROBERT B., HOLM, SCOTT, HOLMGREN, DONALD J., HUANG, CHI-HAO, HULL, CHARLES, HUSBY, DON, ICHIKAWA, SHIN-ICHI, ICHIKAWA, TAKASHI, IVEZIĆ, ŽELJKO, KENT, STEPHEN, KIM, RITA S. J., KINNEY, E., KLAENE, MARK, KLEINMAN, A. N., KLEINMAN, S., KNAPP, G. R., KORIENEK, JOHN, KRON, RICHARD G., KUNSZT, PETER Z., LAMB, D. Q., LEE, B., LEGER, R. FRENCH, LIMMONGKOL, SIRILUK, LINDENMEYER, CARL, LONG, DANIEL C., LOOMIS, CRAIG, LOVEDAY, JON, LUCINIO, RICH, LUPTON, ROBERT H., MACKINNON, BRYAN, MANNERY, EDWARD J., MANTSCH, P. M., MARGON, BRUCE, MCGEHEE, PEREGRINE, MCKAY, TIMOTHY A., MEIKSIN, AVERY, MERELLI, ARONNE, MONET, DAVID G., MUNN, JEF-

FREY A., NARAYANAN, VIJAY K., NASH, THOMAS, NEILSEN, ERIC, NESWOLD, RICH, NEWBERG, HEIDI JO, NICHOL, R. C., NICINSKI, TOM, NONINO, MARIO, OKADA, NORIO, OKAMURA, SADANORI, OSTRIKER, JEREMIAH P., OWEN, RUSSELL, PAULS, A. GEORGE, PEOPLES, JOHN, PETERSON, R. L., PETRAVICK, DONALD, PIER, JEFFREY R., POPE, ADRIAN, PORDES, RUTH, PROSAPIO, ANGELA, RECHENMACHER, RON, QUINN, THOMAS R., RICHARDS, GORDON T., RICHMOND, MICHAEL W., RIVETTA, CLAUDIO H., ROCKOSI, CONSTANCE M., RUTHMANSDORFER, KURT, SAND FORD, DALE, SCHLEGEL, DAVID J., SCHNEIDER, DONALD P., SEKIGUCHI, MAKI, SERGEY, GARY, SHIMASAKU, KAZUHIRO, SIEGMUND, WALTER A., SMEE, STEPHEN, SMITH, J. ALLYN, SNEDDEN, S., STONE, R., STOUGHTON, CHRIS, STRAUSS, MICHAEL A., STUBBS, CHRISTOPHER, SUBBARAO, MARK, SZALAY, ALEXANDER S., SZAPUDI, ISTVAN, SZOKOLY, GYULA P., THAKAR, ANIRUDDA R., TREMONTI, CHRISTY, TUCKER, DOUGLAS L., UOMOTO, ALAN, VANDEN BERK, DAN, VOGELEY, MICHAEL S., WADDELL, PATRICK, WANG, SHU-I., WATANABE, MASARU, WEINBERG, DAVID H., YANNY, BRIAN, YASUDA, NAOKI, SDSS COLLABORATION, . The Sloan Digital Sky Survey: Technical Summary. **AJ**, v. 120, p. 1579–1587, Sep 2000.

[200] YOUAKIM, K., STARKENBURG, E., MARTIN, N. F., MATIJEVIČ, G., AGUADO, D. S., ALLENDE PRIETO, C., ARENTSEN, A., BONIFACIO, P., CARLBERG, R. G., GONZÁLEZ HERNÁNDEZ, J. I., HILL, V., KORDOPATIS, G., LARDO, C., NAVARRO, J. F., JABLONKA, P., SÁNCHEZ JANSSEN, R., SESTITO, F., THOMAS, G. F., VENN, K. The Pristine Survey - VIII. The metallicity distribution function of the Milky Way halo down to the extremely metal-poor regime. **MNRAS**, v. 492, n. 4, p. 4986–5002, March 2020.

[201] ZALESKY, JOSEPH A., SABOI, KEZMAN, LINE, MICHAEL R., ZHANG, ZHOUJIAN, SCHNEIDER, ADAM C., LIU, MICHAEL C., BEST, WILLIAM M. J., MARLEY, MARK S. A Uniform Retrieval Analysis of Ultra-cool Dwarfs. IV. A Statistical Census from 50 Late-T Dwarfs. **ApJ**, v. 936, n. 1, p. 44, September 2022.

[202] ZOCCALI, M., VASQUEZ, S., GONZALEZ, O. A., VALENTI, E., ROJAS-ARRIAGADA, A., MINNITI, J., REJKUBA, M., MINNITI, D.,

MCWILLIAM, A., BABUSIAUX, C., HILL, V., RENZINI, A. The GIRAFFE Inner Bulge Survey (GIBS). III. Metallicity distributions and kinematics of 26 Galactic bulge fields. **A&A**, v. 599, p. A12, March 2017.

[203] ZUCKERMAN, B., BESSELL, M. S., SONG, INSEOK, KIM, S. The Carina-Near Moving Group. **ApJ**, v. 649, n. 2, p. L115–L118, October 2006.

Appendix A

Monthly Notices
of the
ROYAL ASTRONOMICAL SOCIETY

MNRAS **499,** 5302–5317 (2020)
Advance Access publication 2020 October 9

doi:10.1093/mnras/staa3118

Increasing the census of ultracool dwarfs in wide binary and multiple systems using Dark Energy Survey DR1 and Gaia DR2 data

M. dal Ponte,[1,2]★ B. Santiago,[1,2] A. Carnero Rosell,[2,3] B. Burningham,[4] B. Yanny,[5] J. L. Marshall,[6] K. Bechtol,[7,8] P. Martini,[9,10] T. S. Li,[11,5,12,13] L. De Paris,[1] T. M. C. Abbott,[14] M. Aguena,[15,2] S. Allam,[5] S. Avila,[16] E. Bertin,[17,18] S. Bhargava,[19] D. Brooks,[20] E. Buckley-Geer,[5] M. Carrasco Kind,[21,22] J. Carretero,[23] L. N. da Costa,[2,24] J. De Vicente,[3] H. T. Diehl,[5] P. Doel,[20] T. F. Eifler,[25,26] S. Everett,[27] B. Flaugher,[5] P. Fosalba,[28,29] J. Frieman,[5,12] J. García-Bellido,[16] E. Gaztanaga,[28,29] D. W. Gerdes,[30,31] D. Gruen,[32,12,33] R. A. Gruendl,[21,22] J. Gschwend,[2,24] G. Gutierrez,[5] S. R. Hinton,[32,34] D. L. Hollowood,[27] K. Honscheid,[9,35] D. J. James,[36] K. Kuehn,[37,38] N. Kuropatkin,[5] M. A. G. Maia,[2,24] M. March,[39] F. Menanteau,[21,22] R. Miquel,[23,40] A. Palmese,[5,12] F. Paz-Chinchón,[21,22] A. A. Plazas,[11] E. Sanchez,[3] V. Scarpine,[5] S. Serrano,[28,29] I. Sevilla-Noarbe,[3] M. Smith,[41] E. Suchyta,[42] M. E. C. Swanson,[22] G. Tarle,[31] D. Thomas,[43] T. N. Varga,[44,45] and A. R. Walker[14] DES Collaboration

Affiliations are listed at the end of the paper

Accepted 2020 October 1. Received 2020 September 18; in original form 2020 January 25

ABSTRACT

We present the discovery of 255 binary and 6 multiple system candidates with wide (> 5 arcsec) separation composed by ultracool dwarfs (UCDs) companions to stars, plus nine double ultracool dwarf systems. These systems were selected based on common distance criteria. About 90 per cent of the total sample has proper motions available and 73 per cent of the systems also satisfy a common proper motion criterion. The sample of ultracool candidates was taken from the Dark Energy Survey (DES) and the candidate stellar primaries are from Gaia DR2 and DES data. We compute chance alignment probabilities in order to assess the physical nature of each pair. We find that 174 candidate pairs with Gaia DR2 primaries and 81 pairs with a DES star as a primary have chance alignment probabilities < 5 per cent. Only nine candidate systems composed of two UCDs were identified. The sample of candidate multiple systems is made up of five triple systems and one quadruple system. The majority of the UCDs found in binaries and multiples are of early L type and the typical wide binary fraction over the L spectral types is 2–4 per cent. Our sample of candidate wide binaries with UCDs as secondaries constitutes a substantial increase over the known number of such systems, which are very useful to constrain the formation and evolution of UCDs.

Key words: binaries: general – brown dwarfs – stars: low-mass.

1 INTRODUCTION

Ultracool dwarfs (UCDs) are presumed to be common objects in the Milky Way. But due to their very low masses, temperatures ($T_{\rm eff}$ < 2300 K) and hence luminosities, they are difficult sources to detect. Interest on them has increased in recent years. Very low-mass stars have been found to harbour planetary systems, some of them similar to Earth (Gillon et al. 2017). Dust discs that could harbour protoplanetary systems have also been reported around young substellar sources (brown dwarfs) (Sanchis et al. 2020). And the incomplete census of such ultracool objects in the Galactic field, even close to the Sun, makes their initial mass function (IMF), spatial distribution, and binary fraction relatively unconstrained and hard to place into the general context of Galactic star formation and evolution.

Large samples of M dwarfs, close to the H-burning limit already exist (Lépine & Gaidos 2011; West et al. 2011). Also, the census of L and T dwarfs has greatly improved since the appearance of infrared surveys, such as the Two-Micron All-Sky Survey (2MASS; Skrutskie et al. 2006), the Deep Near Infrared Survey of the Southern Sky (DENIS; Epchtein et al. 1997), the UKIRT Infrared Deep Sky Survey (UKIDSS; Lawrence et al. 2007), the *Wide-field Infrared Survey Explorer* (*WISE*; Wright et al. 2010) and the VISTA Hemisphere Survey (VHS; McMahon et al. 2013). Among the optical surveys that unveiled substantial numbers of such ultracool sources are the Sloan Digital Sky Survey (SDSS; York et al. 2000), and, more recently, the Dark Energy Survey (DES; Abbott et al. 2018) and Gaia DR2 (Reylé 2018).

On the theoretical side, uncertainties about the interiors, and, most especially, the atmospheres and evolution of L and T dwarfs still remain (Pinfield et al. 2012; Leggett et al. 2013; Baraffe et al. 2015). As in the case of higher mass stars, L and T dwarf formation and evolution models should benefit from the knowledge of chemical composition, masses and ages of a sizeable sample of such objects. Binary systems are ideal for this purpose since the physical properties of the primary star can be applied to the UCD companion, assuming

★ E-mail: mari.dalponte@gmail.com

© 2020 The Author(s)
Published by Oxford University Press on behalf of the Royal Astronomical Society

Downloaded from https://academic.oup.com/mnras/article/499/4/5302/5920232 by guest on 02 May 2023

that the pair formed at the same time, of the same material and evolved in the same environment (Faherty et al. 2010). Also, large statistical samples could constrain intrinsic variations of the formation process of the L and T dwarf population relative to more massive stars.

In terms of binary statistics, there is evidence that the binary frequency decreases as a function of spectral type and separation. For solar-type stars, Raghavan et al. (2010) found that ∼ 25 per cent have a companion with separation wider than 100 au, ∼11 per cent wider than 1000 au and Tokovinin & Lépine (2012) estimate 4.4 per cent wider than 2000 au. However, searches for M, L, or T dwarfs in wide binary systems remain incomplete. Recently Dhital et al. (2011) and Dhital et al. (2015) presented the Sloan Low-mass Wide Pairs of Kinematically Equivalent Stars (SLoWPoKES), a catalogue containing common proper motion and common distance wide candidate pairs. For the mid-K and mid-M type dwarfs presented in both catalogues, the wide binary frequency was ∼1.1 per cent. The binary fraction for L and T dwarfs in wide systems is still uncertain. The fraction of L and T dwarfs found in binary and multiple systems, the distributions of mass ratios, primary spectral types, and separations may constrain different scenarios proposed for the formation of very low-mass stars and brown dwarfs in general, and of binary and multiple systems involving these sources in particular (Reipurth, Clarke & Delgado-Donate 2001; Whitworth & Zinnecker 2004; Bate & Bonnell 2005; Bonnell, Clark & Bate 2008; Elmegreen 2011; Jumper & Fisher 2013).

In this paper, we present the search for wide binary and multiple systems which contain UCD companions, using the sample of 11 745 UCD candidates from Carnero Rosell et al. (2019). We analyse the properties of this sample, including the distribution of projected separations and the binary fraction, and compare them to previous works.

In Section 2, we describe the catalogues used and the criteria used to select the samples. In Section 3, we discuss the photometric distance measurement for the candidates and the spectrophotometric distance for the primary stars selected in the Gaia DR2 and DES data. In Section 4, we present the properties of candidate binaries and multiples and also we address the estimation of chance alignment probability. In Section 5, we show our analysis and comparisons to samples of wide binaries. Finally, we present our summary and concluding remarks in Section 6.

2 CANDIDATE SELECTION OF UCDS AND PRIMARY STARS

2.1 DES, VHS, and *WISE* data

DES is a (∼5000 deg^2) optical survey in the *grizY* bands used the Dark Energy Camera (DECam; Flaugher et al. 2015). DECam is a wide-field (3 deg^2) imager at the prime focus of the Blanco 4m telescope in Cerro Tololo Inter-American Observatory (CTIO).

The DES footprint was selected to obtain an overlap with the South Pole Telescope survey (Carlstrom et al. 2011) and Stripe 82 from SDSS (Abazajian et al. 2009). The Galactic plane was avoided to minimize stellar foregrounds and extinction from interstellar dust in order to maintain the DES cosmological goals. Even though the main driver for DES is cosmological, the stellar data have been extensively used by the collaboration to identify new star clusters, streams and satellite galaxies in the MW Halo and beyond (Bechtol et al. 2015; Drlica-Wagner et al. 2015; Luque et al. 2017).

The first public data release of the Dark Energy Survey, DES DR1 (DR1; Abbott et al. 2018) is composed of 345 distinct nights spread over the first three years of DES operations, from 2013 August 15 to 2016 February 12. The DES DR1 catalogue contains object flags including several that indicate corrupted values due to image artefacts or reduction problems.

For the searches of UCDs, as discussed and presented in Carnero Rosell et al. (2019), we demanded that `FLAGS_z,Y` = 0 (ensures no reduction problems in the z and Y bands) and {\it ISO}_MAGFLAGS_i,z,Y = 0 (ensures the object has not been affected by spurious events in the images in the i, z, and Y bands). We also imposed a magnitude limit cut of $z < 22$ with a detection of 5σ at least in the z and Y to ensure a high completeness in the i band, and therefore allow construction of colour-colour diagrams useful for the selection of UCDs.

For the primary stars, we repeated this same approach, however, we imposed a magnitude limit cut of $i < 24$ and the quality cuts were performed in the g, r, and i bands. The DES DR1 is a public release,[1] but in this work, we used `SOF_PSF_MAG` photometry, which has not been published yet. The SOF photometry is based on a different reduction using the `ngmix` code,[2] which has better point spread function and shape modelling. Even though we used nonpublic photometry, the `COADD_ID` are the same as those in the public release.

In order to extend photometry into the infrared, we matched the DES DR1 to the VHS and AllWISE data using a positional matching radius of 2 arcsec. As discussed in Carnero Rosell et al. (2019), for typical proper motions and a 2 arcsec match between DES and VHS, considering a three-year baseline, our matching should yield a complete combined sample for distances >50 pc, with slowly decreasing completeness for more nearby and higher proper motion sources. After the match, we removed every source that did not pass the DES quality cuts as explained before. The resulting catalogues have 27 249 118 and 27 918 863 sources within a 2374 deg^2 overlap region. These two catalogues were used for the UCD search (Section 2.2) and now to search for primary star candidates (Section 4.2), respectively.

2.2 Sample of ultracool dwarf candidates

As presented in Carnero Rosell et al. (2019), our search of UCD candidates in the combination of DES, VHS and AllWISE data was performed using a colour–colour cut criteria. The adopted cuts to select our candidates was $(i_{\rm AB} - z_{\rm AB}) > 1.2$, $(z_{\rm AB} - Y_{\rm AB}) > 0.15$ and $(Y_{\rm AB} - J_{\rm Vega}) > 1.6$. We used this initial sample, mainly made up of M, L, and T dwarfs, to run our spectral classification code, *classif*, which uses only photometry, to estimate the spectral type of each object of the sample. The *classif* code was implemented using the same method presented in Skrzypek et al. (2015) and Skrzypek, Warren & Faherty (2016), based on a minimization of the χ^2 relative to M, L, and T empirical templates. After running *classif*, we obtain 11 545 sources classified as L dwarfs and 200 as T dwarfs. More details about the selection method, colour cuts and the spectral classification can be found in Carnero Rosell et al. (2019).

2.3 Gaia DR2

The Gaia astrometric mission was launched in December 2013. It is measuring positions, parallaxes, proper motions and photometry for over one billion sources to $G \simeq 20.7$. Its Data Release 2 (Gaia DR2; Gaia Collaboration et al. 2018), has covered the initial 22 months of data taking (from a predicted total of 5 yr), with positions and

[1] https://des.ncsa.illinois.edu/releases/dr1
[2] https://github.com/esheldon/ngmix

Downloaded from https://academic.oup.com/mnras/article/499/4/5302/5920232 by guest on 02 May 2023

photometry for 1.7×10^9 sources and full astrometric solution for 1.3×10^9.

For our purpose, we used Gaia DR2 data to select primary star candidates. Particularly important for this work are the parallaxes, whose precision varies from <0.1 mas for $G \leq 17$ to $\simeq 0.7$ mas for $G = 20$. They allow us to better discern dwarf stars (whose distances will overlap those of the UCDs from DES, VHS, and AllWISE) from much more distant giants of similar colours, $T_{\rm eff}$ and chemistry. For the stars brighter than $G = 18$, the Gaia DR2 sample was cross-matched to the Pan-STARRS1 (Kaiser et al. 2010), 2MASS, and AllWISE catalogues, so as to increase the amount of photometric information available for each star as we did for DES. The photoastrometric distances, derived from precise parallaxes and photometry, are presented in Anders et al. (2019). We refer to this sample as GaiaDR2-18.

3 DISTANCE AND PROPER MOTION MEASUREMENTS

3.1 Distance

3.1.1 Ultracool dwarf candidates

Using our UCD sample described in Section 2.2, we used the spectral type from each candidate and our empirical model grid described in Carnero Rosell et al. (2019) to estimate the absolute magnitude and then obtain the distance modulus for each UCD.

The empirical model grid lists absolute magnitudes in *izYJHKW1W2* for dwarfs ranging from M1 to T9. We computed one distance modulus for each filter with available apparent magnitude. The resulting distance to each UCD was then taken to be the mean value among the available filters and we used the dispersion around the mean as the distance uncertainty. We did not apply any correction for extinction, since this is expected to be small for the passbands we used and towards the relatively high Galactic latitudes covered by our samples.

3.1.2 Primary stars

As mentioned before, we use the Gaia DR2 (Gaia Collaboration et al. 2018) and the combination of DES, VHS, and AllWISE to search for stars located close to our UCD candidates. Anders et al. (2019) ran the `StarHorse` code (Queiroz et al. 2018) on all stars in the Gaia DR2 sample brighter than $G = 18$, in an attempt to better constrain their distances and extinction, yielding what we call the GaiaDR2-18 sample. For DES stars, `StarHorse` was applied by us, but only to the stars that were close enough to the UCD candidates to be considered as a potential companion, as will be discussed in the next section. In this latter case, we use optical and infrared photometry, in addition to parallaxes from Gaia DR2 when available.

The `StarHorse` code uses a Bayesian approach to determine masses, ages, distances, and extinctions for field stars through the comparison of their observed spectroscopic, photometric, and astrometric parameters with those from stellar evolution models. The models used are the `PARSEC` set of isochrones (Bressan et al. 2012). The code assumes spatial priors for each structural component of the Galaxy (thin and thick discs, bulge, and halo). The priors also assume Gaussian metallicity and age distribution functions for each structural component. For all components, the Chabrier IMF (Chabrier 2003) was assumed as a prior. Gaussian likelihood functions were generated using the available observed parameter set and their associated uncertainties. The code then computes the posterior distribution function over distance, marginalized for all other parameters. We take the median of this marginalized posterior as the best distance estimate, while the difference between the median 84th percentile and the (16th percentile) distances is taken as the higher (lower) 1σ uncertainty. For more details, we refer to Queiroz et al. (2018) and Anders et al. (2019).

3.2 Proper motion

The proper motion measurements for the primaries are mostly from Gaia DR2 catalogue. However, for the UCDs, the proper motion measurements are from CatWISE Catalogue (Eisenhardt et al. 2019). CatWISE is a catalogue of selected sources from WISE and NEOWISE data collected from 2010 to 2016 in the *W*1 and *W*2 bands.

However, the majority of the UCDs distances are large and the motions are thus small compared to other samples. Also, the objects are faint and the time baselines relatively short, and so most of the proper motion uncertainties are comparable to the measurements themselves, making them consistent with zero. In this situation, proper motions may turn out to be an inefficient diagnostic of association. None the less, we take into consideration these measurements in our binary and multiple systems search to assess their impact.

4 THE SEARCH FOR BINARY AND MULTIPLE SYSTEM CANDIDATES

Detection of faint sources close to brighter stars is difficult, with detections pushed to larger separations as the difference in brightness increases. We paired UCD candidates to potential primary stars using a search radius that corresponds to 10 000 au as the projected separation between the pair members. Since the distances of our UCD candidates are in the 20–500 pc range, these search radii cover the angular range from 20 to 500 arcsec. Details on how this projected separation is computed vary with the sample of primaries, as discussed in the next subsections. As discussed in Marocco et al. (2017) and Deacon et al. (2014), searches beyond 10 000 au introduce a significant difficulty of disentangling widest binaries from chance alignments from field stars.

To refine our wide binary and multiple systems, we checked if the members that have common distance also share a common proper motion, when available. The common distance criteria were made at the 2σ level. Also, the proper motions had to be within 2σ of each other.

A robust binary or multiple system should satisfy $\Delta_\mu \leq 2\sigma_\mu$ where Δ_μ is the total proper motion difference

$$\Delta_\mu = \sqrt{\Delta^2_{\mu_{\alpha cos\delta}} + \Delta^2_{\mu_\delta}},$$

and $\Delta_{\mu_{\alpha cos\delta}}$ and Δ_{μ_δ} are the differences in proper motion between the pair members in the two directions. In the above criterion,

$$\sigma_\mu = \sqrt{\delta\mu_1^2 + \delta\mu_2^2}$$

is the composite uncertainty in the measured proper motions, where 1, 2 represent the primary and secondary. The individual uncertainties in proper motion also combine in quadrature the uncertainties along each direction.

In the following sections, we describe how the pairing was done for each set, including the common distance and common proper motion requirements, and also discuss the way chance alignment probabilities were computed in each case.

Downloaded from https://academic.oup.com/mnras/article/499/4/5302/5920232 by guest on 02 May 2023

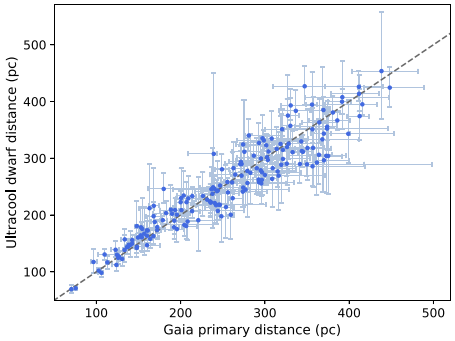

Figure 1. The 174 common distance pair candidates identified using the UCD sample and Gaia DR2 primary candidate stars, taken from the sample by Anders et al. (2019). The horizontal axis represents the primary distance given by StarHorse and the vertical axis shows the secondary's photometric distance. The error bars correspond to an uncertainty of 2σ. The uncertainties in the photometric distances of the UCD sample are usually much larger than those of the stars, which are based on measured parallaxes.

4.1 Ultracool dwarf companions to Gaia DR2 stars

For the GaiaDR2-18 primary candidate stars, we considered their `StarHorse` distances from Anders et al. (2019), and used photometric distances to the UCD candidates. We defined a search radius equal to a projected separation of 10 000 au evaluated at the lower limit in distance of the star, given its smaller distance uncertainty as compared to the UCD. For each star, we then searched for possible UCD companions within this projected radius. By additionally applying the common distance criterion, we found 174 candidate pairs.

For each possible pair, we estimate the chance alignment probability following a similar procedure used by Smart et al. (2017) and Dhital et al. (2015). The chance alignment probability is the probability that we find a physically unrelated object with the same common distance within our uncertainties and within the search radius. To assess the chance alignment probability, we simulate stars within a 2 deg^2 area from the UCD candidate from each pair using `Trilegal` (Girardi et al. 2005). The `Trilegal` simulated stars have a distance modulus without any uncertainty. In order to mimic an uncertainty in their distances, we use the uncertainty computed by `StarHorse` for the GaiaDR2-18 star whose distance is closest to that of the simulated `Trilegal` star. We thus assume that the uncertainty in distance for the simulated stars follows the same distribution as computed by `StarHorse` for real stars. We randomly selected 1000 stars within the 2 deg^2 area and calculated the fraction N/M of common distance stars, where N is the number of simulated stars which have the common distance with the UCD candidate and M is the total number of randomly selected simulated stars. Therefore, N/M gives the probability of a randomly picked simulated star to have a common distance with the UCD. Then we obtain the probability over all stars within the search radius by multiplying N/M by the number of simulated stars and making an area normalization considering the search radius area and the simulated area. We flag every pair with a chance alignment probability $P_a > 5$ per cent as contamination.

In the current sample based on GaiaDR2-18 primaries, all of the 174 common distance pairs survived the $P_a < 5$ per cent cut. These candidate wide binaries are shown in Fig. 1. A simple estimate of the number of chance alignments that still made into the sample may be obtained by adding up the P_a values, yielding a total of 1.078. Among the 174 candidate pairs, 153 UCDs had proper motion in CatWISE catalogue. Applying the common proper motion criteria, a sample of 125 pairs remains. This shows that 82 per cent of the common distance systems survive the proper motion refinement criterion, at the expense of losing a fraction of the objects due to lack of proper motion data. The properties for a subset of these candidate pairs are presented in Table 1. The entire table is available in machine-readable format in https://des.ncsa.illinois.edu/releases/other/y3-lt-widebinaries.

4.2 Ultracool companions to DES DR1 stars

In this case, the search radius corresponds to 10 000 au projected separation evaluated at the lower distance limit for the UCD. We adopt this threshold because we do not have the `StarHorse` distances for the entire DES stars catalogue. Due to computational restrictions, we only obtain the `StarHorse` distance for stars that were inside the UCD search radius. Considering that these UCDs have a large uncertainty in their purely photometric distances, this conservative approach should result in a larger search radius, and the inclusion of several stars within this radius.

As mentioned in the previous section, in this case, `StarHorse` distances for the primary stars were based on photometric measurements, with additional constraint from parallaxes for a small number of DES primary which are common to Gaia DR2. We thus applied the common distance criterion and were able to find 85 possible pairs involving a DES DR1 primary and a UCD as a secondary, as shown in Fig. 2.

As we explain in the previous section, for the chance alignment probabilities, we rely on `Trilegal` simulations. The procedure is the same as described in Section 4.1. We assign distance uncertainties to the simulated stars using the closest DES DR1 star. For each secondary, we randomly selected 5000 stars in the simulated area and require that the distances of the UCD candidate and the simulated star lie within 2σ of each other. Thus, we obtain the probability over all simulated stars within the search radius. In the case of the 85 candidate wide binaries identified with DES DR1, 81 of them have $P_a < 5$ per cent. The sum of the P_a values for this sample yields 1.468 as the expected number of remaining unphysical pairs.

From the 81 candidate pairs, 74 UCDs have proper motion measurements from CatWISE. After applying the common proper motion criteria, 61 pairs remained in the sample, again yielding a fraction of 82 per cent pairs that pass the cut in proper motions. The properties for a subset of these candidate pairs are also presented in Table 1.

4.3 Wide binaries involving two UCDs

We also used the UCD sample to search for candidate binaries among themselves. We computed a search radius for each UCD and checked if another such dwarf appears inside this individual radius. We were able to identify nine possible pairs, which are shown in Fig. 3. The properties of these possible binary pairs are presented in Table 2. The pairs are matched independently of the pair member that we centred on, except for one system. In other words, if source B is found within the search radius of 10 000 au around source A, this latter was also within the same projected separation at B's distance. The entire table is available in https://des.ncsa.illinois.edu/releases/other/y3-lt-widebinaries.

Downloaded from https://academic.oup.com/mnras/article/499/4/5302/5920232 by guest on 02 May 2023

Table 1. The common distance pair candidates identified using the UCD sample combined to Gaia DR2 and DES DR1 data. The ID in *Jhhmm* ± *ddmm* format is based on the primary coordinates.

ID	Position				Photometry			Distance		Spectral type	Binary information		
	α_A	δ_A	α_B	δ_B	$G_{Gaia,A}$	$z_{DES,A}$	$i_{DES,B}$	$z_{DES,B}$	d_A	d_B	B	$\Delta\theta$ (arcsec)	d_P (au)	P_a (%)
J0001−4315[a,b]	00:01:52	−43:15:45	00:01:51	−43:15:41	17.2	15.9	23.0	21.4	295 ± 18	279 ± 8	L1	15.0	4427.4	0.264
J0002 + 0006[a,b]	00:02:10	+00:06:28	00:02:08	+00:07:06	15.4	14.1	22.0	20.4	172 ± 3	179 ± 5	L1	43.1	7440.3	0.222
J0002−0626[a,b]	00:02:24	−06:26:11	00:02:23	−06:26:30	16.7	15.2	20.6	19.1	130 ± 2	123 ± 6	L0	34.3	4482.0	0.391
J0003−5803[a]	00:03:24	−58:03:51	00:03:18	−58:04:06	14.1	12.8	21.2	19.9	154 ± 1	175 ± 24	L0	50.3	7776.1	1.389
J0005 + 0104[b]	00:05:46	+01:04:54	00:05:47	+01:04:43	18.8	17.2	23.0	21.5	393 ± 62	369 ± 13	L0	14.1	5580.9	1.137
J0008−4929[a]	00:08:07	−49:29:27	00:08:08	−49:29:20	17.7	16.4	22.6	21.3	314 ± 8	316 ± 18	L0	16.0	5054.3	0.649
J0008−0437	00:08:15	−04:37:53	00:08:17	−04:37:38	18.1	16.7	22.4	20.8	375 ± 30	265 ± 12	L0	26.6	10017.4	1.100

Notes. The letter A represents the primary star and B the UCD. The angular and the projected separation are indicated by $\Delta\theta$ and d_P, respectively. The P_a refers to the chance alignment probability, as explained in Sections 4.1 and 4.2. The entire table is available in https://des.ncsa.illinois.edu/releases/other/y3-lt-widebinaries. [a]The distance for Gaia DR2 stars was published by Anders et al. (2019). [b]Common proper motion systems.

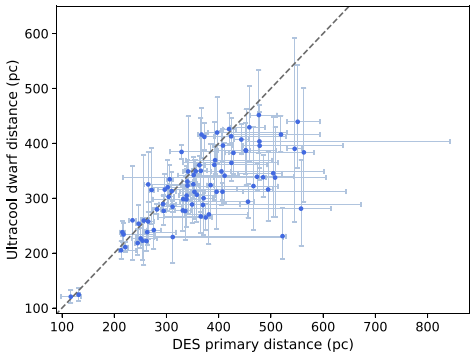

Figure 2. The 85 common distance pair candidates identified using the UCD sample and DES primary stars. The horizontal axis represents the primary photometric distance given by StarHorse and the vertical axis shows the UCD photometric distance. The error bars indicate an uncertainty of 2σ.

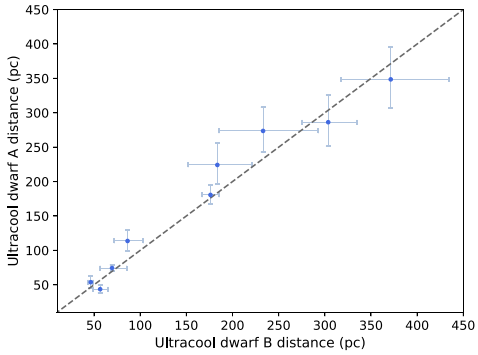

Figure 3. The nine common distances for the pure UCD binary candidates identified. The horizontal and vertical axis show the UCDs photometric distances and the error bars correspond to an uncertainty of 2σ.

To obtain the chance alignment probability, we used the `GalmodBD` simulation code, presented in Carnero Rosell et al. (2019), which computes expected Galactic counts of UCDs, as a function of magnitude, colour, and direction on the sky. `GalmodBD` also creates synthetic samples of UCDs based on the expected number counts for a given footprint, using empirically determined space densities of objects, absolute magnitudes, and colours as a function of spectral type. For the current purpose, we computed the expected number of UCDs in a given direction and within the volume bracketed by the common range of distances and by the area within the angular separation of each possible pair. For all the nine candidate pairs, the probability of chance alignment is $P_a < 0.2$ per cent, as shown in Table 2.

We also used the CatWISE catalogue to obtain the proper motion information for the wide binary involving two UCDs. One L0 member has proper motion from Gaia DR2. All nine pairs have proper motion measurements and seven remain in the sample after application of the proper motion filter. Fig. 4 shows the vector point diagram for these seven pairs. For more details regarding these systems visit https://des.ncsa.illinois.edu/releases/other/y3-lt-widebinaries.

Downloaded from https://academic.oup.com/mnras/article/499/4/5302/5920232 by guest on 02 May 2023

Table 2. The nine common distance pair candidates identified among the UCD sample and the letters A and B represent a different UCD. The ID in *Jhhmm* ± *ddmm* format is based on the primary coordinates.

ID	Position				Photometry			Distance		Spectral type		Binary information		
	α_A	δ_A	α_B	δ_B	$i_{DES,\,A}$	$z_{DES,\,A}$	$i_{DES,\,B}$	$z_{DES,\,B}$	d_A	d_B	A	B	$\Delta\theta$ (arcsec)	d_P (au)	P_a (%)
J0003−0011	00:03:30	−00:11:06	00:03:35	−00:12:59	23.1	21.0	20.6	19.1	70 ± 7	74 ± 2	L7	L2	131.5	9141.83	0.078
J0443−4551[a]	04:43:10	−45:51:55	04:43:04	−45:50:23	25.0	21.9	-	21.7	57 ± 4	44 ± 3	T5	T6	112.0	6345.85	0.020
J0457−4933[a]	04:57:49	−49:33:56	04:57:52	−49:34:02	22.6	21.1	22.4	20.9	304 ± 15	286 ± 19	L0	L0	25.61	7777.43	0.007
J2000−5342[a]	20:00:12	−53:42:38	20:00:12	−53:43:07	23.1	21.3	22.3	20.9	233 ± 27	274 ± 16	L2	L0	29.41	6857.05	0.115
J2251−4959[a]	22:51:57	−49:59:32	22:51:56	−50:00:01	22.9	21.4	23.0	21.4	371 ± 29	349 ± 22	L0	L0	29.51	10961.6	0.170
J2313−4550[a]	23:13:49	−45:50:29	23:13:49	−45:50:25	22.2	20.3	23.3	21.2	86 ± 8	114 ± 8	L4	L5	4.080	352.297	0.000
J2318−5420	23:18:39	−54:20:34	23:19:03	−54:21:49	18.4	17.0	21.4	19.9	46 ± 1	54 ± 4	L0	L5	226.4	10514.6	0.025
J2319−5203[a]	23:19:43	−52:03:55	23:19:48	−52:04:24	21.4	19.9	21.4	19.9	176 ± 5	181 ± 7	L0	L0	59.10	10411.8	0.045
J2319−5607[a]	23:19:50	−56:07:27	23:19:47	−56:07:56	22.1	20.6	22.4	21.0	184 ± 17	224 ± 15	L1	L1	37.21	6832.95	0.066

Notes. The angular and the projected separation are indicated by $\Delta\theta$ and d_P, respectively. The P_a refers to the chance alignment probability. [a]Common proper motion systems.

Figure 4. Vector point diagram for the seven UCD pairs that satisfy the common distance and common proper motion criteria. Each pair is indicated by a different colour. The error bars correspond to an uncertainty of 1σ.

4.4 Multiple systems

In addition to our wide binary candidates presented in Sections 4.1 and 4.2, we find several possible multiple systems: five triple and one quadruple system. All members of the candidate triple systems satisfy the common distance criterion when considered two by two. As for the quadruple candidate, in Dhital et al. (2015) the system is presented as an M1 + M1 binary, but we identified two more members. In this case, the L0 member does not satisfy the common distance criterion with one of the M1 stars in the binary reported by Dhital et al. (2015) and it marginally satisfies this criterion with the other M1.

As for proper motions, all six systems have proper motion measurements for all members. We again use the CatWISE catalogue to obtain the proper motion for the L dwarfs. Applying the common proper motion criteria, we discard the quadruple as a physical system. The M1 + M1 binary does not have a common proper motion with the other stellar member. The proper motion of the L0 is consistent with the brighter three sources, but has an uncertainty comparable to its value and therefore is not very informative. As for the triple systems, the four pairs within them all satisfy the common proper motion criteria presented in the beginning of Section 4, except for J2024-5801, where the binary star has a difference in measured proper motions beyond 2σ. However, the expected motion caused by a physical pair orbiting at their separation is comparable to this observed difference. One of the triple systems, J2342-6135, is composed of two UCDs and a stellar member. Again, the very large uncertainty of the UCD proper motion prevent stronger conclusions about this system. The candidate multiple systems are shown in Fig. 5 and their main characteristics are described in Table 3. For more details regarding the table content visit https://des.ncsa.illinois.edu/releases/other/y3-lt-widebinaries.

For the multiple systems, the chance alignment probability requires estimating and combining the probabilities of random alignment of each of the three (in case of triples) or six (in case of quadruples) pairs involved in the system, as well as the chance alignments of higher orders up to that of the entire system altogether. As this would involve much larger simulations sets, we refrain from computing the chance alignment probabilities for these systems. However, the configurations of the quadruple system, with no clear hierarchy, and of the triple system with two UCDs, are both very uncommon. Combined with the previous discussion based on proper motions, this is a clear indication that these systems are not physical and that the algorithm based on common distances is leading to the

Downloaded from https://academic.oup.com/mnras/article/499/4/5302/5920232 by guest on 02 May 2023

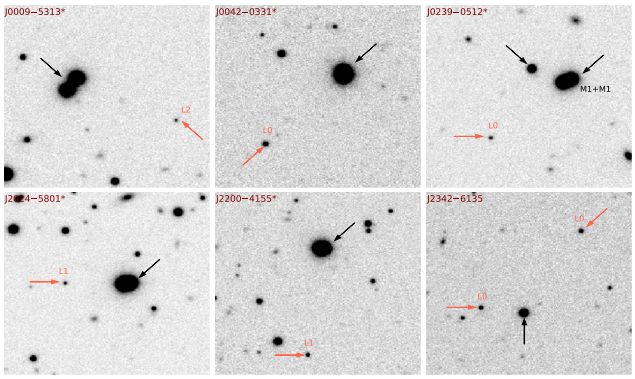

Figure 5. 60 × 60 arcsec^2 z-band images of the multiple systems found. The black arrow indicates the stars, while the UCDs are identified by a red arrow followed by their spectral type. The upper right-hand image corresponds to a quadruple candidate system. The double M1 + M1 were previously identified by Dhital et al. (2015). This quadruple system also contains a common distance between the L0 and a star, indicated by the arrows. The remaining images correspond to candidates of triple systems. The lower right-hand panel corresponds to two UCD companions to a star.

identification of physically unrelated systems of higher order, as in the case of the wide binaries.

5 DISCUSSION

For our 264 common distance pair candidates, we visually inspected the DES images. Fig. 6 shows a sample of some selected binary candidates. The rows show pairs constituted by a UCD companion to a GaiaDR2-18 star, to a DES DR1 star and also systems made up by two UCDs, in this order. All of the images were taken from the DES Science Portal related to the DR1 public release images.[3]

In Table A1, we present the known F/G/K/M + L or T wide systems already published in the literature that were spectroscopically confirmed and have an UCD as a companion. In Table A2, we present the common distance and/or common proper motion known F/G/K/M + L or T wide systems identified so far. Using this information, we searched for matches between our pairs and multiple system candidates presented in this work and the previously known pairs, but none of the 264 pairs and six multiples was identified among them. The main reason is that the majority of the known wide binaries with spectroscopic confirmation are in the Northern hemisphere and/or have a projected separation < 600 au and we are not able to resolve them.

We also perform a search using the catalogue SLoWPoKES I and II presented in Dhital et al. (2011, 2015), respectively, which contains low-mass stars wide binaries identified using common distance and/or common proper motion. In this case, we were able to identify one M1 + M1 common system as discussed in Section 4.4.

Fig. 7 shows the distributions of projected separations from our wide binary candidates sample, the 141 SLoWPoKES-II wide very low-mass binaries, and from Tables A1 and A2. Our sample was divided into binary systems that satisfy the common distance criterion alone and those that satisfy the common distance plus common proper motion criteria. The projected separations in our sample are those listed in Tables 1 and 2 and were computed using the angular separation and the primary's distance. For this reason, they may exceed the 10 000 au limit originally set for the search radius, which was based on the lowest boundary in distance given the uncertainties. The distributions are all different from each other, reflecting selection biases. Spectroscopically confirmed systems containing UCDs are largely restricted to small separations compared to common distance and common proper motions pairs. Our samples, with and without the common proper motion criterion, also span larger separations than those from Dhital et al. (2015). In fact, adding the proper motion constraint barely changes the shape of the distribution of projected separations, but clearly reduces the number of objects due to lack of proper motion data. Furthermore, as discussed in Section 4, the very large uncertainties in the proper motions of most UCDs from CatWISE, indicate that the currently available proper motions are not an efficient diagnostic in this case. Therefore, in the subsequent analyses, we will adopt the common distance objects as our final sample. The abrupt drop in the number of systems with separations > 10 000 au is due to our search radius limit.

Our sample is also the largest of those shown, given the larger photometric and astrometric samples it is derived from. As discussed previously by Dhital et al. (2015), a large number of wide binary low-mass systems in the Galactic field could rule out the proposed formation scenario where very low-mass objects are ejected from the protocluster due to dynamical interactions (Reipurth et al. 2001; Bate & Bonnell 2005). Due to their low binding energy, they are unlikely to survive this dynamical process.

Fig. 8 shows the spectral type of the UCDs versus the projected separation of the common distance pairs. Our sample of wide binary candidates contains 271 L dwarfs companions to stars with projected separations ranging from >1000–24 000 au. We have nine wide systems made up by two UCDs that satisfy the common distance criterion and seven of them also satisfy the common proper motion criterion. If confirmed, these will be the widest systems (>6000 au) involving two L/T dwarfs currently known. Only one candidate double T dwarf system was found, with a projected separation ∼ 6000 au. Deacon et al. (2014) pointed out the paucity of T dwarfs companions wider than 3000 au, which means that this system may be a rare find.

Fig. 9 shows the projected separations against distances for our common distance candidate wide binary sample. It is limited to ∼500 pc, making it the deepest sample of binaries involving UCDs. In total, 82 per cent of our pair candidates concentrate at a distance < 400 pc and projected separation < 10 000 au as shown in the figure.

[3]https://des.ncsa.illinois.edu/releases/dr1/dr1-access

Downloaded from https://academic.oup.com/mnras/article/499/4/5302/5920232 by guest on 02 May 2023

Table 3. The common distance multiple systems found in our search. The letters *A* and *B* represent a star from Gaia DR2 or DES DR1 and the letter *C* the UCD. In the last row, *B*, and *C* represent a different UCD. The ID in *Jhhmm* ± *ddmm* format using the primary coordinates.

ID	Position						Photometry		Distance			Spectral type	
	α_A	δ_A	α_B	δ_B	α_C	δ_C	$G_{Gaia,\,A}$	$G_{Gaia,\,B}$	$z_{DES,\,C}$	d_A	d_B	d_C	B	C
J0009−5313[a,b]	00:09:06	−53:13:30	00:09:06	−53:13:34	00:09:03	−53:13:43	16.8	17.0	23.0	241 ± 3	231 ± 3	235 ± 17		L2
J0042−0331[a,b]	00:42:33	−03:31:29	00:42:33	−03:31:30	00:42:34	−03:31:53	17.9	16.4	21.7	200 ± 10	193 ± 10	195 ± 16		L0
J0239−0512[a]	02:39:43	−05:12:59	02:39:44	−05:12:54	02:39:45	−05:13:17	17.0	20.6	20.9	356 ± 11	345 ± 3	286 ± 15		L0
J2024−5801[a,b]	20:24:13	−58:01:15	20:24:14	−58:01:15	20:24:16	−58:01:15	16.9	16.2	22.3	232 ± 6	222 ± 4	218 ± 7		L1
J2200−4155[a,b]	22:00:25	−41:55:02	22:00:25	−41:55:02	22:00:25	−41:55:37	17.3	17.3	20.9	198 ± 7	202 ± 8	214 ± 3		L1
J2342−6135	23:42:06	−61:35:44	23:42:08	−61:35:42	23:42:04	−61:35:17	20.2	–	20.7	267 ± 28	286 ± 29	279 ± 29	L0	L0

[a]The distance for Gaia DR2 stars was published by Anders et al. (2019). [b]Common proper motion systems.

This is in part due to the fact that the chance alignment probability tends to grow with the projected separation and the heliocentric distance of the primary.

Fig. 9 also shows a lower limit in projected separation, which is related to the typical angular resolution of the DES DR1 and Gaia DR2 images, especially the former, from which the binary sample is drawn. Pairs whose angular separation is of the order or lower than the DES seeing limit will be harder to resolve. At a distance of 480 pc, a 1.3-arcsec resolution limit will translate into a minimum separation of $\simeq$ 620 au, which is roughly what Fig. 9 shows as a lower limit.

Using the wide binary systems presented in Table A1, Table A2 and our sample, we compared the frequency distribution of spectral types, as presented in the left-hand panel of Fig. 10. The L dwarfs dominate all samples. Our common distance sample is particularly biased towards early L types, as expected for the optical data on which our selection of UCDs and of primary stars is based. This sample represents a very significant leap compared to the number of such systems known. Even in a deep optical survey such as DES, we are still bound to detect mainly L types at $\sim$ 500 pc and this selection bias against later types clearly appears in the distributions. The right-hand panel shows the fraction of candidate wide binaries (within the projected separation limits discussed earlier) as a function of spectral type. We observe that the typical wide binary fraction is 2–4 per cent over most of the spectral types, especially among L dwarfs, where we have better statistics. We also have added Poisson uncertainties to the binary fractions for each spectral type as shown in Fig. 10.

As for the candidate triple systems, it is interesting to notice that four of them have a similar configuration, with a tight binary plus a detached third member as a UCD. Systems with a very similar configuration to our findings have been previously reported in the literature, as in Kirkpatrick et al. (2001), Gomes et al. (2013), Dupuy et al. (2018), and Gauza et al. (2019). Regarding the formation scenarios, this type of system is consistent with results of dynamical modelling of three-body interactions including UCDs (Delgado-Donate, Clarke & Bate 2004; Bate 2012).

6 SUMMARY AND CONCLUSIONS

Using the Gaia DR2 and the combination of DES, VHS, and AllWISE data along with a sample of UCD candidates from Carnero Rosell et al. (2019), we identified 264 new wide binary candidates. The projected separations for the wide binary systems are spread within the $\sim$ 1000–24 000 au range. The upper limit in projected distance results from our search strategy, in which we avoided larger separations that are more likely to be affected by contaminants. The lower limit in separation stems from the typical resolution of the DES images on which the original UCD sample is based. A sample of six candidate multiple systems were also identified and the projected separations between the UCD dwarfs and the stellar members of these higher order systems range from $\sim$3000–11000 au.

Our candidates were selected based on common distance criteria and with a chance alignment probability criterion of $P_a < 5$ per cent. We also used proper motions from Gaia DR2 and from the CatWISE Catalogue as an attempt to refine the sample. We found proper motion measurements for about 90 per cent of the sources in the pairs and multiple systems, and 73 per cent of them also satisfy common proper motion criteria as discussed in Section 4. But the proper motion data still have large uncertainties regarding the UCDs. Most of the systems with proper motions available, however, have proper motions within 2σ of each other.

We found 174 common distance candidate pairs with a primary from the Gaia DR2 catalogue limited to $G < 18$, for which distances

Downloaded from https://academic.oup.com/mnras/article/499/4/5302/5920232 by guest on 02 May 2023

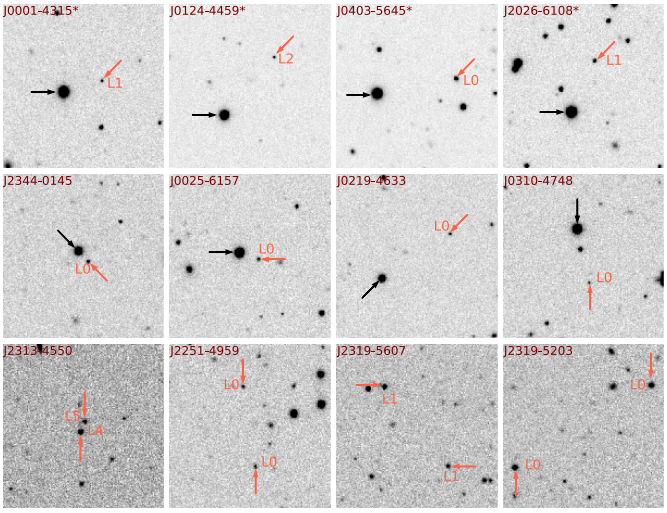

Figure 6. 60 × 60 arcsec^2 z-band images of selected binary candidates systems. In the first row, we present L dwarfs as companions of GaiaDR2-18 stars from Anders et al. (2019). In the second row, the L dwarfs as companions of DES stars. In the last row, we present binary pairs composed by two UCDs. In all images, the primary star is identified by an black arrow and the secondary by a red arrow followed by their spectral type.

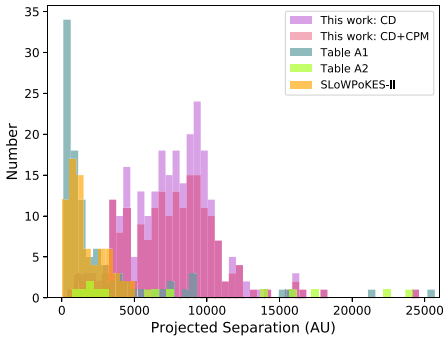

Figure 7. Distribution of projected separations using four different samples, as indicated in the upper right-hand corner. The CD and CPM labels mean common distance and common proper motion, respectively. Our wide binary sample is the most numerous and reaches larger projected separation than the previous known samples. Table A2 has unbound systems with very large projected separations. In order to better understand the distribution of separations, the figure only contains objects with a limiting of 26 000 au in separation.

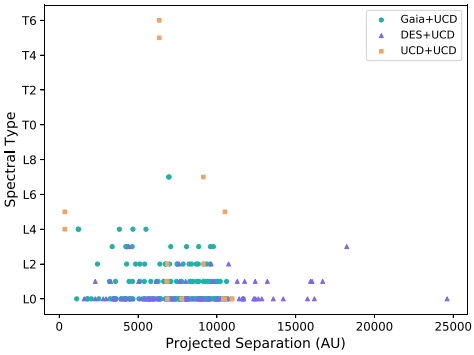

Figure 8. Spectral type of the UCDs plotted against the projected separation of the common distance pairs. The green dots and the purple triangles represent the companions of GaiaDR2-18 and DES stars, respectively. The orange boxes indicate the systems composed by two UCDs.

are estimated from the `StarHorse` code by Anders et al. (2019). We also found 81 common distance candidate pairs with a primary from the DES DR1 sample. These latter tend to be fainter and their `StarHorse` distances are based mostly on photometry, although some have Gaia DR2 parallax information as well. In addition, we found nine systems containing two UCDs. Hence, we found in total 264 new wide binary candidates. This is the largest sample of candidate wide binary systems to date and is also the one that reaches the largest distances. These binary and multiple system candidates involving very low mass and substellar sources are crucial as possible benchmarks to evolutionary models close to or below the hydrogen-burning limit, since properties such as metallicity and age, as well as masses, may be obtained for the primaries. The large number of wide binaries found in this work is inconsistent with the formation of very low-mass stars and brown dwarfs from strong dynamical interactions leading to their ejection of star-forming cores, since the binding energy involved is very low and would lead in most cases to the pair dissolution.

We also found six possible multiple systems, of which five are triples and one is a quadruple. The only potential quadruple system found is composed of an L0 dwarf associated to a star and to an M1 + M1 double found previously by Dhital et al. (2015), but the L0's distance is only marginally consistent with that of the M1 + M1 double, while the third star has a proper motion that is inconsistent with that of the brighter pair. One of the five triples is

Downloaded from https://academic.oup.com/mnras/article/499/4/5302/5920232 by guest on 02 May 2023

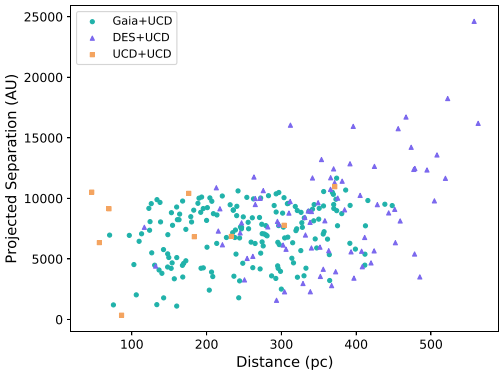

Figure 9. Projected pair separation in au plotted against distance for the 264 common distance binary candidates with $P_a < 5$ per cent. The colours and different symbols represent the three different samples presented previously, as indicated in the upper left-hand corner. The zone of avoidance at small projected separations (<1 au) is caused by spatial resolution limits, while the scarcity of pairs with separations larger than 10 000 au, especially for distances smaller than $\simeq$ 300 pc, is due to the search method.

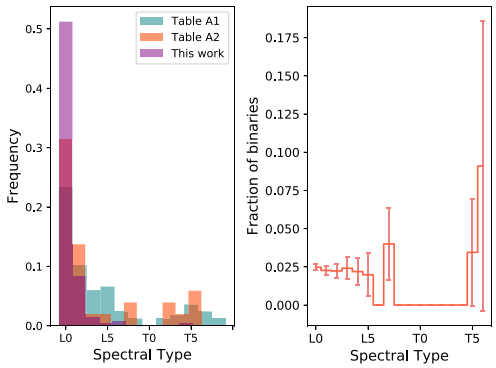

Figure 10. The left-hand panel shows the frequency distribution of UCDs in wide binary systems, considering our sample and the currently known systems. The right-hand panel shows the observed fraction of wide binaries (in the separation range as shown in Fig. 9) as a function of spectral type. The error bars are Poissonian.

composed of two L dwarfs associated with a DES star companion. The configuration of both the quadruple and of this triple is also very atypical of multiple systems, again making their physical reality unlikely. On the other hand, the other four triple systems show a similar configuration, with a tight pair and a detached third object. This is also commonly seen in other triple systems reported in the literature, and is a favoured configuration according to models of three-body encounters (Delgado-Donate et al. 2004; Bate 2012).

Table 4 summarizes all the systems found in this work, regarding its type and the total number of systems, with and without proper motion data available. About 64 per cent of our UCDs found in candidate binary and multiple systems are of the L0 spectral type. Still they make up only $\simeq$ 2 per cent of the total sample of L0 by

Table 4. Summary of the common distance systems found. The systems with chance alignment probability >5 per cent are not included here. CD and CPM stand for common distance and common proper motion, respectively. The PM column indicated how many CD systems have proper motion measurements.

Type of system		Total		
		CD	PM	CD + CPM
Binary	Gaia + UCD	174	153	125
	DES + UCD	81	74	61
	UCD + UCD	9	9	7
Triple		5	5	4
Quadruple		1	1	–

Carnero Rosell et al. (2019). The typical wide binary fraction for the binary candidates over all spectral types ranges from 2–4 per cent in the projected separation range covered by this work. The wide binary systems with UCDs as members presented here comprehend the largest catalogue to date.

Given the measurements of the chance alignment probabilities above, we expect some physically unrelated systems to remain in our sample. The systems here identified, therefore, must all be considered as binary or multiple system candidates, pending on kinematical and spectroscopic confirmation. Still, this catalogue constitutes a significant leap in the number of candidate wide separation systems containing UCDs and in the estimates of the wide binary fraction for UCDs. Evolutionary models predict that our sample dominated by early L sources should include young or intermediate age brown dwarfs, whose benchmarking may also be very useful to constrain models.

ACKNOWLEDGEMENTS

Funding for the DES Projects has been provided by the US Department of Energy, the US National Science Foundation, the Ministry of Science and Education of Spain, the Science and Technology Facilities Council of the United Kingdom, the Higher Education Funding Council for England, the National Center for Supercomputing Applications at the University of Illinois at Urbana-Champaign, the Kavli Institute of Cosmological Physics at the University of Chicago, the Center for Cosmology and Astro-Particle Physics at the Ohio State University, the Mitchell Institute for Fundamental Physics and Astronomy at Texas A&M University, Financiadora de Estudos e Projetos, Fundação Carlos Chagas Filho de Amparo à Pesquisa do Estado do Rio de Janeiro, Conselho Nacional de Desenvolvimento Científico e Tecnológico and the Ministério da Ciência, Tecnologia e Inovação, the Deutsche Forschungsgemeinschaft and the Collaborating Institutions in the DES.

The Collaborating Institutions are Argonne National Laboratory, the University of California at Santa Cruz, the University of Cambridge, Centro de Investigaciones Energéticas, Medioambientales y Tecnológicas-Madrid, the University of Chicago, University College London, the DES-Brazil Consortium, the University of Edinburgh, the Eidgenössische Technische Hochschule (ETH) Zürich, Fermi National Accelerator Laboratory, the University of Illinois at Urbana-Champaign, the Institut de Ciències de l'Espai (IEEC/CSIC), the Institut de Física d'Altes Energies, Lawrence Berkeley National Laboratory, the Ludwig-Maximilians Universität München and the associated Excellence Cluster Universe, the University of Michigan, the NSF's National Optical-Infrared Astronomy Research Laboratory, the University of Nottingham, The Ohio State University, the University of Pennsylvania, the University of Portsmouth, SLAC National Accelerator Laboratory, Stanford

Downloaded from https://academic.oup.com/mnras/article/499/4/5302/5920232 by guest on 02 May 2023

University, the University of Sussex, Texas A&M University, and the OzDES Membership Consortium.

Based in part on observations at Cerro Tololo Inter-American Observatory, NSF's National Optical-Infrared Astronomy Research Laboratory, which is operated by the Association of Universities for Research in Astronomy (AURA) under a cooperative agreement with the National Science Foundation.

The DES data management system is supported by the National Science Foundation under Grant Numbers AST-1138766 and AST-1536171. The DES participants from Spanish institutions are partially supported by MINECO under grants AYA2015-71825, ESP2015-66861, FPA2015-68048, SEV-2016-0588, SEV-2016-0597, and MDM-2015-0509, some of which include ERDF funds from the European Union. IFAE is partially funded by the CERCA program of the Generalitat de Catalunya. Research leading to these results has received funding from the European Research Council under the European Union's Seventh Framework Program (FP7/2007-2013) including ERC grant agreements 240672, 291329, and 306478. We acknowledge support from the Australian Research Council Centre of Excellence for All-sky Astrophysics (CAASTRO), through project number CE110001020, and the Brazilian Instituto Nacional de Ciência e Tecnologia (INCT) e-Universe (CNPq grant 465376/2014-2).

This manuscript has been authored by Fermi Research Alliance, LLC under Contract No. DE-AC02-07CH11359 with the US Department of Energy, Office of Science, Office of High Energy Physics. The United States Government retains and the publisher, by accepting the article for publication, acknowledges that the United States Government retains a non-exclusive, paid-up, irrevocable, world-wide license to publish or reproduce the published form of this manuscript, or allow others to do so, for United States Government purposes.

This publication makes use of data products from the Wide-field Infrared Survey Explorer, which is a joint project of the University of California, Los Angeles, and the Jet Propulsion Laboratory/California Institute of Technology, and NEOWISE, which is a project of the Jet Propulsion Laboratory/California Institute of Technology. WISE and NEOWISE are funded by the National Aeronautics and Space Administration.

The analysis presented here is based on observations obtained as part of the VHS, ESO Programme, 179.A-2010 (PI: McMahon).

This paper has gone through internal review by the DES collaboration.

ACR acknowledges financial support provided by the PAPDRJ CAPES/FAPERJ Fellowship and by 'Unidad de Excelencia María de Maeztu de CIEMAT – Física de Partículas (Proyecto MDM)'.

DATA AVAILABILITY

Data underlying this paper are available in https://des.ncsa.illinois.edu/releases/other/y3-lt-widebinaries.

REFERENCES

Abazajian K. N. et al., 2009, ApJS, 182, 543
Abbott T. M. C. et al., 2018, ApJS, 239, 18
Anders F. et al., 2019, A&A, 628, A94
Anderson E., Francis C., 2012, Astron. Lett., 38, 331
Andrei A. H. et al., 2011, AJ, 141, 54
Artigau É., Gagné J., Faherty J., Malo L., Naud M.-E., Doyon R., Lafrenière D., Beletsky Y., 2015, ApJ, 806, 254
Bailey V. et al., 2014, ApJ, 780, L4
Baraffe I., Homeier D., Allard F., Chabrier G., 2015, A&A, 577, A42
Baron F. et al., 2015, ApJ, 802, 37
Bate M. R., 2012, MNRAS, 419, 3115
Bate M. R., Bonnell I. A., 2005, MNRAS, 356, 1201
Bechtol K. et al., 2015, ApJ, 807, 50
Best W. M. J. et al., 2015, ApJ, 814, 118
Billères M., Delfosse X., Beuzit J.-L., Forveille T., Marchal L., Martín E. L., 2005, A&A, 440, L55
Bonnell I. A., Clark P., Bate M. R., 2008, MNRAS, 389, 1556
Bouy H., Brandner W., Martín E. L., Delfosse X., Allard F., Basri G., 2003, AJ, 126, 1526
Bowler B. P., Liu M. C., Cushing M. C., 2009, ApJ, 706, 1114
Bowler B. P., Liu M. C., Shkolnik E. L., Tamura M., 2012, ApJ, 756, 69
Bressan A., Marigo P., Girardi L., Salasnich B., Dal Cero C., Rubele S., Nanni A., 2012, MNRAS, 427, 127
Burgasser A. J. et al., 2000, ApJ, 531, L57
Burgasser A. J., Reid I. N., Leggett S. K., Kirkpatrick J. D., Liebert J., Burrows A., 2005, ApJ, 634, L177
Burgasser A. J., Luk C., Dhital S., Bardalez Gagliuffi D., Nicholls C. P., Prato L., West A. A., Lépine S., 2012, ApJ, 757, 110
Burningham B. et al., 2009, MNRAS, 395, 1237
Burningham B. et al., 2010, MNRAS, 404, 1952
Burningham B. et al., 2013, MNRAS, 433, 457
Caballero J. A., 2007, ApJ, 667, 520
Carlstrom J. E. et al., 2011, PASP, 123, 568
Carnero Rosell A. et al., 2019, MNRAS, 489, 5301
Casagrande L., Schönrich R., Asplund M., Cassisi S., Ramírez I., Meléndez J., Bensby T., Feltzing S., 2011, A&A, 530, A138
Chabrier G., 2003, PASP, 115, 763
Chauvin G. et al., 2005, A&A, 438, L29
Close L. M., Siegler N., Freed M., Biller B., 2003, ApJ, 587, 407
Cruz K. L. et al., 2007, AJ, 133, 439
Currie T., Burrows A., Daemgen S., 2014, ApJ, 787, 104
Day-Jones A. C. et al., 2011, MNRAS, 410, 705
De Rosa R. J. et al., 2015, ApJ, 814, L3
Deacon N. R. et al., 2012a, ApJ, 755, 94
Deacon N. R. et al., 2012b, ApJ, 757, 100
Deacon N. R. et al., 2014, ApJ, 792, 119
Deacon N. R., Schlieder J. E., Murphy S. J., 2016, MNRAS, 457, 3191
Deacon N. R. et al., 2017, MNRAS, 467, 1126
Delgado-Donate E. J., Clarke C. J., Bate M. R., 2004, MNRAS, 347, 759
Desrochers M.-E., Artigau É., Gagné J., Doyon R., Malo L., Faherty J. K., Lafrenière D., 2018, ApJ, 852, 55
Dhital S., Burgasser A. J., Looper D. L., Stassun K. G., 2011, AJ, 141, 7
Dhital S., West A. A., Stassun K. G., Schluns K. J., Massey A. P., 2015, AJ, 150, 57
Drlica-Wagner A. et al., 2015, ApJ, 813, 109
Dupuy T. J., Liu M. C., 2012, Apjs, 201, 19
Dupuy T. J. et al., 2018, AJ, 156, 57
Eisenhardt P. R. M. et al., 2019, ApJS, 247, 69
Elmegreen B. G., 2011, ApJ, 731, 61
Epchtein N. et al., 1997, The Messenger, 87, 27
Faherty J. K., Burgasser A. J., West A. A., Bochanski J. J., Cruz K. L., Shara M. M., Walter F. M., 2010, AJ, 139, 176
Faherty J. K., Burgasser A. J., Bochanski J. J., Looper D. L., West A. A., van der Bliek N. S., 2011, AJ, 141, 71
Flaugher B. et al., 2015, AJ, 150, 150
Forveille T. et al., 2004, A&A, 427, L1
Gaia Collaboration, Brown A. G. A., Vallenari A., Prusti T., de Bruijne J. H. J., Babusiaux C., Bailer-Jones C. A. L., 2018, A&A, 616, 22
Gálvez-Ortiz M. C., Solano E., Lodieu N., Aberasturi M., 2017, MNRAS, 466, 2983
Gauza B., Béjar V. J. S., Pérez-Garrido A., Rosa Zapatero Osorio M., Lodieu N., Rebolo R., Pallé E., Nowak G., 2015, ApJ, 804, 96
Gauza B. et al., 2019, MNRAS, 487, 1149
Gillon M. et al., 2017, Nature, 542, 456
Girardi L., Groenewegen M. A. T., Hatziminaoglou E., da Costa L., 2005, A&A, 436, 895

Downloaded from https://academic.oup.com/mnras/article/499/4/5302/5920232 by guest on 02 May 2023

Gizis J. E., Monet D. G., Reid I. N., Kirkpatrick J. D., Burgasser A. J., 2000, MNRAS, 311, 385
Gizis J. E., Kirkpatrick J. D., Wilson J. C., 2001, AJ, 121, 2185
Goldman B., Marsat S., Henning T., Clemens C., Greiner J., 2010, MNRAS, 405, 1140
Golimowski D. A. et al., 2004, AJ, 128, 1733
Gomes J. I. et al., 2013, MNRAS, 431, 2745
Jumper P. H., Fisher R. T., 2013, ApJ, 769, 9
Kaiser N. et al., 2010, in Stepp L. M., Gilmozzi R., Hall H. J., eds, Proc. SPIE Conf. Ser. Vol. 7733. Ground-based and Airborne Telescopes III. SPIE, Bellingham, p. 77330E
Kirkpatrick J. D. et al., 2000, AJ, 120, 447
Kirkpatrick J. D., Dahn C. C., Monet D. G., Reid I. N., Gizis J. E., Liebert J., Burgasser A. J., 2001, AJ, 121, 3235
Kirkpatrick J. D. et al., 2011, ApJS, 197, 19
Kirkpatrick J. D. et al., 2016, ApJS, 224, 36
Kraus A. L., Ireland M. J., Cieza L. A., Hinkley S., Dupuy T. J., Bowler B. P., Liu M. C., 2014, ApJ, 781, 20
Lafrenière D., Jayawardhana R., van Kerkwijk M. H., 2008, ApJ, 689, L153
Lawrence A. et al., 2007, MNRAS, 379, 1599
Leggett S. K., Morley C. V., Marley M. S., Saumon D., Fortney J. J., Visscher C., 2013, ApJ, 763, 130
Lépine S., Gaidos E., 2011, AJ, 142, 138
Loutrel N. P., Luhman K. L., Lowrance P. J., Bochanski J. J., 2011, ApJ, 739, 81
Luhman K. L. et al., 2007, ApJ, 654, 570
Luhman K. L., Burgasser A. J., Bochanski J. J., 2011, ApJ, 730, L9
Luhman K. L. et al., 2012, ApJ, 760, 152
Luque E. et al., 2017, MNRAS, 468, 97
McCaughrean M. J., Close L. M., Scholz R. D., Lenzen R., Biller B., Brandner W., Hartung M., Lodieu N., 2004, A&A, 413, 1029
McMahon R. G., Banerji M., Gonzalez E., Koposov S. E., Bejar V. J., Lodieu N., Rebolo R., VHS Collaboration, 2013, The Messenger, 154, 35
Mace G. N. et al., 2013, ApJ, 777, 36
Marocco F. et al., 2017, MNRAS, 470, 4885
Marocco F. et al., 2020, MNRAS, 494, 4891
Martin E. L., Brandner W., Basri G., 1999, Science, 283, 1718
Metchev S. A., Hillenbrand L. A., 2004, ApJ, 617, 1330
Metchev S. A., Hillenbrand L. A., 2006, ApJ, 651, 1166
Mugrauer M., Seifahrt A., Neuhäuser R., Mazeh T., 2006, MNRAS, 373, L31
Mugrauer M., Neuhäuser R., Mazeh T., 2007, A&A, 469, 755
Murray D. N. et al., 2011, MNRAS, 414, 575
Mužić K. et al., 2012, AJ, 144, 180
Naud M.-E. et al., 2014, ApJ, 787, 5
Neuhäuser R., Guenther E. W., Wuchterl G., Mugrauer M., Bedalov A., Hauschildt P. H., 2005, A&A, 435, L13
Phan-Bao N. et al., 2008, MNRAS, 383, 831
Pinfield D. J. et al., 2012, MNRAS, 422, 1922
Queiroz A. B. A. et al., 2018, MNRAS, 476, 2556
Radigan J., Lafrenière D., Jayawardhana R., Doyon R., 2008, ApJ, 689, 471
Raghavan D. et al., 2010, ApJS, 190, 1
Rebolo R., Zapatero Osorio M. R., Madruga S., Bejar V. J. S., Arribas S., Licandro J., 1998, Science, 282, 1309
Reid I. N., Walkowicz L. M., 2006, PASP, 118, 671
Reipurth B., Clarke C., Delgado-Donate E., 2001, preprint (astro-ph/0110481)
Reylé C., 2018, A&A, 619, L8
Reylé C. et al., 2013, Mem. Soc. Astron. Ital., 84, 1050
Sanchis E. et al., 2020, A&A, 633, A114
Scholz R. D., 2010a, A&A, 510, L8
Scholz R. D., 2010b, A&A, 515, A92
Scholz R. D., McCaughrean M. J., Lodieu N., Kuhlbrodt B., 2003, A&A, 398, L29
Seifahrt A., Guenther E., Neuhäuser R., 2005, A&A, 440, 967
Skrutskie M. F. et al., 2006, AJ, 131, 1163
Skrzypek N., Warren S. J., Faherty J. K., Mortlock D. J., Burgasser A. J., Hewett P. C., 2015, A&A, 574, A78
Skrzypek N., Warren S. J., Faherty J. K., 2016, A&A, 589, A49
Smart R. L., Marocco F., Caballero J. A., Jones H. R. A., Barrado D., Beamín J. C., Pinfield D. J., Sarro L. M., 2017, MNRAS, 469, 401
Smart R. L., Marocco F., Sarro L. M., Barrado D., Beamín J. C., Caballero J. A., Jones H. R. A., 2019, MNRAS, 485, 4423
Smith L., Lucas P. W., Burningham B., Jones H. R. A., Smart R. L., Andrei A. H., Catalán S., Pinfield D. J., 2014, MNRAS, 437, 3603
Smith L. C. et al., 2015, MNRAS, 454, 4476
Tokovinin A., Lépine S., 2012, AJ, 144, 102
West A. A., Morgan D. P., Bochanski J. J., Andersen J. M., et al., 2011, aj, 141, 97
Whitworth A. P., Zinnecker H., 2004, A&A, 427, 299
Wilson J. C., Kirkpatrick J. D., Gizis J. E., Skrutskie M. F., Monet D. G., Houck J. R., 2001, AJ, 122, 1989
Wright E. L. et al., 2010, AJ, 140, 1868
York D. G. et al., 2000, AJ, 120, 1579
Zhang Z., 2019, MNRAS, 489, 1423
Zhang Z. H. et al., 2010, MNRAS, 404, 1817

APPENDIX A: TABLES FROM THE LITERATURE

Table A1. Known systems, which contain a L or T dwarf as a secondary, all are spectroscopically confirmed. All the systems presented here have projected separation > 100 au. This table was based on table 12 from Deacon et al. (2014).

Object Name	Separation		Distance	Spectral Type		Mass	References
	(arcsec)	(au)	(pc)	Companion	Primary	($M_\odot$)	
HD65216BC	7.0	253	36.1	M7 + L2	G5	0.08	1
LP213-68Bab	14.0	230	16.4	M8 + L0	M6.5	0.068–0.090	14, 15
BD + 131727B	10.5	380	36.1	M8 + L0.5	K5	–	13
HD221356BC	452.0	11900	26.3	M8 + L3	F8	0.072	27
HD221356D	12.13	2050	169.0	L1	F8+M8 + L3	0.073-0.085	32
DENISJ0551-4434B	2.2	220	100.0	L0	M8.5	0.06	5
Denis-PJ1347-7610B	16.8	418	24.8	L0	M0	–	6
HD89744B	63.0	2460	39.0	L0	F7	0.077–0.080	7
NLTT2274B	23.0	483	21.0	L0	M4	0.081–0.083	8
LP312-49B	15.4	801	52.0	L0	M4	–	9
SDSSJ130432.93 + 090713.7B	7.6	374	49.2	L0	M4.5	–	9
SDSSJ163814.32 + 321133.5B	46.0	2420	52.6	L0	M4	–	9
1RXSJ235133.3 + 312720B	2.4	120	49.9	L0	M2	0.026–0.038	10
2MASS12593933 + 0651255	23.86	1110	46.5	L0	M8	0.21	11
2MASS09411195 + 3315060	7.44	244	32.7	L0	M5	0.23	11

Downloaded from https://academic.oup.com/mnras/article/499/4/5302/5920232 by guest on 02 May 2023

Table A1 *– continued*

Object Name	Separation		Distance	Spectral Type		Mass	References
	(arcsec)	(au)	(pc)	Companion	Primary	($M_\odot$)	
HIP2397B	117.1	3970	33.9	L0.5	K5	–	12
HD253662B	20.1	1252	62.2	L0.5	G8	–	12
2M0858 + 2710	15.6	780	50.0	L0	M4	0.074–0.081	28
2M1021 + 3704	22.2	3000	135.	L0	M4	0.071–0.076	28
2M1202 + 4204	7.3	310	42.4	L0	M6	0.074–0.081	28
2M0005 + 0626	6.1	400	65.5	L0	M4.5	0.079–0.085	28
2M1222 + 3643	20.7	1635	78.9	L0	M3	0.074–0.081	28
GaiaJ0452-36A	115.3	15828	137.2	L0	M1	0.084–0.086	29
2MASS0719-50	58.7	1609	27.4	L0	M3.5	–	75
2M0013-1816	118.1	7400	62.6	L1	M3	0.072–0.078	28
2M1441 + 1856	51.1	4110	80.4	L1	M6	0.072–0.079	28
HIP59933B	38.1	2170	56.9	L1	F8	–	12
HIP63506B	132.8	5640	42.4	L1	M0	–	12
HIP6407B	44.9	2570	57.2	L1 + T3	G5	–	12
GJ1048B	11.9	250	21.0	L1	K2	0.055–0.075	16
ABPicB	5.5	275	50.0	L1	K2	0.01	17
G124-62Bab	44.0	1496	34.0	L1 + L1	dM4.5e	0.054–0.082	18
HD16270	11.9	254	21.3	L1	K3.5	–	2, 16, 4
GQLupB	0.7	103	147.1	L1	K7	0.010–0.020	19
ROX42Bb	1.8	140	77.7	L1	M1	0.006–0.014	20, 21
LSPMJ0241 + 2553B	31.2	2153	69.0	L1	WD	–	12
HIP112422B	16.0	1040	65.0	L1.5	K2	–	12
LSPMJ0632 + 5053B	47.4	4499	94.9	L1.5	G2	–	12
PMI13518 + 4157B	21.6	613	28.3	L1.5	M2.5	–	12
NLTT44368B	90.2	7760	86.0	L1.5	M3	–	12
PMI22118-1005B	204.5	8892	43.4	L1.5	M2	–	12
HIP11161	47.7	3300	69.1	L1.5	F5	–	12
ηTelB	4.20	190	–	L1	A0V	0.04	13
βCir	217.8	6656	30.5	L1	A3V	0.056	22
HD164507AB	25.1	1136	45.2	L1	G5	–	76
V478Lyr	17.05	462	27.0	L1	G8	–	76
2M0122 + 0331	44.8	2222	49.5	L2	G5	0.071–0.076	28
NLTT1011B	58.5	3990	68.2	L2	K7	–	12
G255-34B	38.3	1364	35.6	L2	K8	–	23
2MASSJ05254550-7425263B	44.0	2000	45.4	L2	M3	0.06–0.075	24
G196-3B	16.2	300	18.5	L2	M2.5	0.015–0.04	25
Gl618.1B	35.0	1090	31.1	L2.5	M0	0.06–0.079	7
HD106906b	7.1	650	91.5	L2.5	F5	0.003–0.007	26
HIP73169	29.0	796	27.4	L2.5	M0	–	12
2MASSJ0249-0557AB	39.9	1950	48.8	L2	M6	0.010–0.012	39
CD-288692	50.91	2026	39.7	L2	K5	–	76
2MASSJ1839 + 4424	21.89	811	37.0	L2	M9	–	76
2MASSJ0139 + 8110AB	23.0	959	41.6	L2	L1	–	76
2MASSJ2325 + 4608AB	7.24	378	52.2	L2	M8	–	76
G63-33B	66.0	2010	30.4	L3	K2	0.079–0.081	8
G73-26B	73.0	2774	38.0	L3	M2	0.079-0.081	8, 9
2MASSJ2126-8140	217.0	6900	31.7	L3	M2	0.014–0.011	49
2MASSJ22501512 + 2325342	8.9	518	58.2	L3	M3	–	50
ηCancriB	164.0	15020	91.5	L3.5	K3III	0.063–0.082	9
NLTT27966	15.9	630	39.6	L4	M5	–	12
LSPMJ1336 + 2541	121.7	8793	72.2	L4	M3	–	12
NLTT26746B	18.0	661	36.7	L4	M4	–	12
PMI13410 + 0542B	9.4	484	51.4	L4	M1	–	12
G171-58B	218.0	9200	42.2	L4 + L4	F8	0.045–0.083	8
G200-28B	570.0	25700	45.0	L4	G5	0.077–0.078	8
LHS5166B	8.43	160	18.9	L4	dM4.5	0.055–0.075	18
1RXSJ1609-2105b	2.2	330	150.0	L4	M0	0.009–0.016	33
2MASSJ0219-3925	3.96	156	39.3	L4	M6	–	78
2M1259 + 1001	7.65	345	45.0	L4.5	M5	0.057–0.074	28
GJ1001Bc	18.6	180	9.6	L4.5 + L4.5	M4	0.060–0.075	29, 34, 35
Gl417Bab	90.0	2000	22.2	L4.5 + L6	G0 + G0	0.02–0.05	29, 36
HIP26653	27.0	753	27.8	L5	G5	–	12
2M1115 + 1607	18.1	660	36.4	L5	M4	0.056–0.073	28
G203-50B	6.4	135	21.0	L5.0	M4.5	0.051–0.074	37
GJ499C	516.0	9708	18.8	L5	K5 + M4	–	23
G259-20B	30.0	650	21.6	L5	M2.5	–	38

Downloaded from https://academic.oup.com/mnras/article/499/4/5302/5920232 by guest on 02 May 2023

Table A1 – *continued*

Object Name	Separation		Distance	Spectral Type		Mass	References
	(arcsec)	(au)	(pc)	Companion	Primary	($M_\odot$)	
HD196180	13.51	907	67.1	L5	A3V	–	40
HIP85365B	294.1	8850	30.0	L5.5	F3	–	12
NLTT55219B	9.7	432	44.5	L5.5	M2	–	12
HIP9269B	52.1	1300	24.9	L6	G5	–	12
NLTT31450B	12.3	487	39.5	L6	M4	–	12
LP261-75B	13.0	450	34.6	L6	M4.5	0.019–0.025	41
2MASSJ01303563-4445411B	3.28	130	39.6	L6	M9	0.032–0.076	42
NLTT20346	248.0	7700	31.0	L7 + L6.5	M5 + M6	0.070	47
VHS1256-1257	8.06	102	12.6	L7	M7.5	0.010	43
HD203030B	11.0	487	44.2	L7.5	G8	0.012–0.031	44
NLTT730	233.6	5070	21.7	L7.5	M4	–	12
Gl337CD	43.0	880	20.4	L8 + L8	G8 + K1	0.04–0.074	7, 45
Gl584C	194.0	3600	18.5	L8	G1	0.045–0.075	46
PMI23492 + 3458	34.9	949	27.1	L9	M2	–	12
HD46588B	79.2	1420	17.9	L9	F7	0.045–0.072	48
NLTT51469C	82.27	3800	46.1	L9	M3 + M6	–	77
ϵIndiBaBb	402.0	1460	3.6	T1 + T6	K5	0.06–0.073	53, 54
2MASSJ111806.99-064007.8B	7.7	650	84.4	T2	M4.5	0.06–0.07	55
HNPegB	43.0	795	18.4	T2.5	G0	0.012–0.030	56
2MASSJ0213 + 3648ABC	16.4	360	21.9	T3	M4.5 + M6.5	0.068	51
GUPscB	41.97	2000	47.6	T3.5	M3	0.07–0.13	57
HIP38939B	88.0	1630	18.5	T4.5	K4	0.018–0.058	58
LSPMJ1459 + 0851B	365.0	21500	58.9	T4.5	DA	0.064–0.075	59
SDSSJ0006-0852AB	27.41	820	29.9	T5	M7 + M8.5	0.056	52
LHS2803B	67.6	1400	20.7	T5	M4.5	0.068-0.081	24, 60
HD118865B	148.0	9200	62.1	T5	F5	–	61
HIP63510C	103.0	1200	11.6	T6	M0.5	–	62
HIP73786B	63.8	1230	19.2	T6	K5	–	62, 63
LHS302B	265.0	4500	16.9	T6	M5	–	64
G204-39B	198.0	2685	13.5	T6.5	M3	0.02–0.035	8
Gl570D	258.0	1500	5.8	T7	K4+M2 + M3	0.03–0.07	65
HD3651B	43.0	480	11.1	T7.5	K0	0.018–0.058	56, 66
SDSSJ1416 + 30B	9.0	135	15.0	T7.5	L6	0.03–0.04	67, 68, 69
LHS2907B	156.0	2680	17.1	T8	G1	0.019–0.047	38, 70
LHS6176B	52.0	1400	26.9	T8	M4	–	38, 61
Wolf1130B	188.5	3000	15.9	T8	sdM1.5 + DA	0.020–0.050	71
Ross458C	102.0	1162	11.3	T8.5	M0.5 + M7	0.005–0.0014	72
ξUMaE	510.0	4100	8.0	T8.5	F9 + G0	0.014–0.038	61
Wolf940B	32.0	400	12.5	T8.5	M4	0.02–0.032	73
WD0806-661	130.0	2500	19.2	>Y0	DQ	0.03–0.10	74

References. (1) Mugrauer, Neuhäuser & Mazeh (2007); (2) Anderson & Francis (2012); (3) Forveille et al. (2004); (4) Dupuy & Liu (2012); (5) Billères et al. (2005); (6) Phan-Bao et al. (2008); (7) Wilson et al. (2001); (8) Faherty et al. (2010); (9) Zhang et al. (2010); (10) Bowler et al. (2012); (11) Gálvez-Ortiz et al. (2017); (12) Deacon et al. (2014); (13) Cruz et al. (2007); (14) Gizis et al. (2000); (15) Close et al. (2003); (16) Gizis, Kirkpatrick & Wilson (2001); (17) Chauvin et al. (2005); (18) Seifahrt, Guenther & Neuhäuser (2005); (19) Neuhäuser et al. (2005); (20) Kraus et al. (2014); (21) Currie, Burrows & Daemgen (2014); (22) Smith et al. (2015); (23) Gomes et al. (2013); (24) Mužić et al. (2012); (25) Rebolo et al. (1998); (26) Bailey et al. (2014); (27) Caballero (2007); (28) Baron et al. (2015); (29) Zhang (2019); (30) Casagrande et al. (2011); (31) Metchev & Hillenbrand (2004); (32) Caballero (2007); (33) Lafrenière, Jayawardhana & van Kerkwijk (2008); (34) Golimowski et al. (2004); (35) Martin, Brandner & Basri (1999); (36) Bouy et al. (2003); (37) Radigan et al. (2008); (38) Luhman et al. (2012); (39) Dupuy et al. (2018); (40) De Rosa et al. (2015); (41) Reid & Walkowicz (2006); (42) Dhital et al. (2011); (43) Gauza et al. (2015); (44) Metchev & Hillenbrand (2006); (45) Burgasser et al. (2005); (46) Kirkpatrick et al. (2000); (47) Faherty et al. (2011); (48) Loutrel et al. (2011); (49) Deacon, Schlieder & Murphy (2016); (50) Desrochers et al. (2018); (51) Deacon et al. (2017); (52) Burgasser et al. (2012); (53) Scholz et al. (2003); (54) McCaughrean et al. (2004); (55) Reylé et al. (2013); (56) Luhman et al. (2007); (57) Naud et al. (2014); (58) Deacon et al. (2012a); (59) Day-Jones et al. (2011); (60) Deacon et al. (2012b); (61) Burningham et al. (2013); (62) Scholz (2010b); (63) Murray et al. (2011); (64) Kirkpatrick et al. (2011); (65) Burgasser et al. (2000); (66) Mugrauer et al. (2006); (67) Scholz (2010a); (68) Burningham et al. (2010); (69) Bowler, Liu & Cushing (2009); (70) Pinfield et al. (2012); (71) Mace et al. (2013); (72) Goldman et al. (2010); (73) Burningham et al. (2009); (74) Luhman, Burgasser & Bochanski (2011); (75) Andrei et al. (2011); (76) Marocco et al. (2020); (77) Gauza et al. (2019); (78) Artigau et al. (2015).

Downloaded from https://academic.oup.com/mnras/article/499/4/5302/5920232 by guest on 02 May 2023

Table A2. The common distance and common proper motion wide systems identified in the literature.

Object Name ID	Separation (arcsec)	Separation (au)	Distance (pc)	Spectral type companion	Spectral type primary	$\mu_\alpha \cos\delta$ (mas yr^{-1})	μ_δ (mas yr^{-1})	References
2MASSJ0223–5815	816	400 000	49 ± 10	L0	M5	134.0 ± 10	5.0 ± 19	1
2MASSJ1214+3721	1866	153 000	82 ± 17	L0	–	−122.6 ± 10.6	82.0 ± 17	1
2MASSJ0939+3412	2516	156 000	62 ± 10	L0	–	−107.1 ± 10.4	−64.3 ± 12.6	1
ULASJ0255+0532	207	29 000	140 ± 26	L0	F5	28 ± 30	40 ± 30	2
ULASJ0900+2930	81	16 000	197 ± 37	L0	M3.5	−13 ± 10	−27.8 ± 8.8	2
ULASJ1222+1407	96	6700	70 ± 13	L0	M4	−74 ± 20	−34 ± 20	2
2MASSJ09175035+ 2944455	1684.7	67 388	40.0	L0	F5	-47.54 ± 2.506	−65.776 ± 1.844	5
2MASSJ0626 + 0029	3761	252 000	67 ± 14	L0.5	–	84 ± 15	−92 ± 15	1
2MASSJ1632 + 3505[a]	57	2000	37 ± 8	L0.5	K0	91.6 ± 9.7	−65.3 ± 11.9	1
2MASSJ17073334 + 4301304	917.2	23 847	26 ± 2	L0.5	–	−210.6 ± 8.9	−47.2 ± 7.2	3
2MASSJ16325610 + 3505076	57.0	1938	34.9927	L0.7	K0	89.153 ± 0.51	−60.527 ± 0.615	5
2MASSJ2037–4216	5294	270 000	51 ± 10	L1	–	229 ± 10	−391 ± 10	1
2MASSJ0518461–275645	1007.2	57 399	57.9079	L1.0	–	32.194 ± 1.299	−4.943 ± 1.447	5
SDSSJ124514.95 + 120112.0	96.4	5948	61.7	L1	DA	−10.582 ± 4.067	−53.728 ± 2.44	5
G151-59	46	3100	118	L1	K0	179 ± 9	158 ± 10	6
2MASSJ14493646 + 0533379	246	33 702	137	L1	–	−107 ± 10	−135 ± 10	6
2MASSJ02235464–5815067	1532.6	62 749	40.943	L1.5	M3 + M9	104.21 ± 1.085	−17.379 ± 0.918	5
ULASJ1330 + 0914[b]	409	61 000	149 ± 30	L2	G5	−83 ± 37	10 ± 37	2
WISEAJ134824.42–422744.9	410.1	13 940	34 ± 2	L2	–	−144.3 ± 6.6	−77.1 ± 6.5	3
2MASSJ01415823–4633574	2377.2	86 641	36.4465	L2	–	115.673 ± 0.7	−46.609 ± 0.665	5
2MASSJ08430796 + 3141297	819.5	38 926	47.5	L2.5	–	-52.293 ± 3.438	−43.35 ± 2.189	5
2MASSJ23225299–6151275	16.6	714	43.0283	L2.5	M5	80.092 ± 1.447	−81.969 ± 1.621	5
2MASSJ21265040–8140293	217.5	7436	34.1924	L3	M1.0	56.511 ± 1.656	−115.369 ± 2.441	5
SDSSJ095932.74 + 452330.5	846.7	32175	38 ± 6	L3/L4	M4.5	−97.1 ± 5.2	−144.5 ± 9.4	3
2MASSJ00283943 + 1501418	917.2	36 688	40 ± 3	L4.5	–	199.3 ± 12.8	−34.5 ± 11.7	3
2MASSJ23512200 + 3010540	934.9	22 416	24 ± 3	L5pec	K5	251.7 ± 8.5	4.3 ± 7.1	3
2MASSJ0230-0225	5370	145 000	27 ± 6	L8	K1	329 ± 16.8	51.3 ± 14.9	1
WISEAJ104335.09 + 121312.0	1039.6	17 673	17 ± 8	L9	–	10.5 ± 8.4	−245.2 ± 9.1	3
PSOJ330.3214 + 32.3686	77.1	2313	20.1 ± 2.1	T2.5	M1	105 ± 8	65 ± 9	4
PSOJ334.1193 + 19.8800	52.2	1566	30.7 ± 3.2	T3	M4	120 ± 8	−72 ± 99	4
2MASSJ1244 + 1232	6217	286 000	46 ± 8	T4	–	−104.8 ± 8.6	4.5 ± 7.3	1
2MASSJ0758 + 2225	4758	157 000	33 ± 8	T6.5	–	−105 ± 8	−62.8 ± 8.2	1
2MASSJ1150 + 0949	1283	77 000	60 ± 27	T6.5	–	−107.6 ± 17.1	−31.9 ± 4.5	1
2MASSJ0915 + 0531	5394	178 000	33 ± 6	T7	G + G	−95 ± 5.5	−57.7 ± 4.4	1

References. (1) Smart et al. (2017); (2) Marocco et al. (2017); (3) Kirkpatrick et al. (2016); (4) Best et al. (2015); (5) Smart et al. (2019); (6) Smith et al. (2014).
[a]This is the only bound system in Smart et al. (2017).
[b]Classify as unlikely pair (Marocco et al. 2017).

[1]*Instituto de Física, UFRGS, Caixa Postal 15051, Porto Alegre RS-91501-970, Brazil*
[2]*Laboratório Interinstitucional de e-Astronomia – LIneA, Rua Gal. José Cristino 77, Rio de Janeiro RJ-20921-400, Brazil*
[3]*Centro de Investigaciones Energéticas, Medioambientales y Tecnológicas (CIEMAT), E-28040 Madrid, Spain*
[4]*Center for Astrophysics Research, University of Hertfordshire, Hatfield AL10 9AB, UK*
[5]*Fermi National Accelerator Laboratory, PO Box 500, Batavia, IL 60510, USA*
[6]*George P. and Cynthia Woods Mitchell Institute for Fundamental Physics and Astronomy, and Department of Physics and Astronomy, Texas A&M University, College Station, TX 77843, USA*
[7]*LSST, 933 North Cherry Avenue, Tucson, AZ 85721, USA*
[8]*Physics Department, 2320 Chamberlin Hall, University of Wisconsin-Madison, 1150 University Avenue Madison, WI 53706, USA*
[9]*Center for Cosmology and Astro-Particle Physics, The Ohio State University, Columbus, OH 43210, USA*
[10]*Department of Astronomy, The Ohio State University, Columbus, OH 43210, USA*
[11]*Department of Astrophysical Sciences, Princeton University, Peyton Hall, Princeton, NJ 08544, USA*
[12]*Kavli Institute for Cosmological Physics, University of Chicago, Chicago, IL 60637, USA*
[13]*Observatories of the Carnegie Institution for Science, 813 Santa Barbara St., Pasadena, CA 91101, USA*
[14]*Cerro Tololo Inter-American Observatory, NSF's National Optical-Infrared Astronomy Research Laboratory, Casilla 603 La Serena, Chile*
[15]*Departamento de Física Matemática, Instituto de Física, Universidade de São Paulo, CP 66318, São Paulo, SP 05314-970, Brazil*
[16]*Instituto de Fisica Teorica UAM/CSIC, Universidad Autonoma de Madrid, E-28049 Madrid, Spain*
[17]*CNRS, UMR 7095, Institut d'Astrophysique de Paris, F-75014 Paris, France*
[18]*Sorbonne Universités, UPMC Univ Paris 06, UMR 7095, Institut d'Astrophysique de Paris, F-75014 Paris, France*
[19]*Department of Physics and Astronomy, Pevensey Building, University of Sussex, Brighton, BN1 9QH, UK*
[20]*Department of Physics & Astronomy, University College London, Gower Street, London WC1E 6BT, UK*
[21]*Department of Astronomy, University of Illinois at Urbana-Champaign, 1002 W. Green Street, Urbana, IL 61801, USA*
[22]*National Center for Supercomputing Applications, 1205 West Clark St., Urbana, IL 61801, USA*
[23]*Institut de Física d'Altes Energies (IFAE), The Barcelona Institute of Science and Technology, Campus UAB, E-08193 Bellaterra (Barcelona), Spain*
[24]*Observatório Nacional, Rua Gal. José Cristino 77, Rio de Janeiro RJ-20921-400, Brazil*
[25]*Department of Astronomy/Steward Observatory, University of Arizona, 933 North Cherry Avenue, Tucson, AZ 85721-0065, USA*
[26]*Jet Propulsion Laboratory, California Institute of Technology, 4800 Oak Grove Dr., Pasadena, CA 91109, USA*
[27]*Santa Cruz Institute for Particle Physics, Santa Cruz, CA 95064, USA*
[28]*Institut d'Estudis Espacials de Catalunya (IEEC), E-08034 Barcelona, Spain*
[29]*Institute of Space Sciences (ICE, CSIC), Campus UAB, Carrer de Can Magrans, s/n, E-08193 Barcelona, Spain*
[30]*Department of Astronomy, University of Michigan, Ann Arbor, MI 48109, USA*
[31]*Department of Physics, University of Michigan, Ann Arbor, MI 48109, USA*

Downloaded from https://academic.oup.com/mnras/article/499/4/5302/5920232 by guest on 02 May 2023

[32] *Department of Physics, Stanford University, 382 Via Pueblo Mall, Stanford, CA 94305, USA*
[33] *SLAC National Accelerator Laboratory, Menlo Park, CA 94025, USA*
[34] *School of Mathematics and Physics, University of Queensland, Brisbane, QLD 4072, Australia*
[35] *Department of Physics, The Ohio State University, Columbus, OH 43210, USA*
[36] *Center for Astrophysics | Harvard & Smithsonian, 60 Garden Street, Cambridge, MA 02138, USA*
[37] *Australian Astronomical Optics, Macquarie University, North Ryde, NSW 2113, Australia*
[38] *Lowell Observatory, 1400 Mars Hill Rd, Flagstaff, AZ 86001, USA*
[39] *Department of Physics and Astronomy, University of Pennsylvania, Philadelphia, PA 19104, USA*
[40] *Institució Catalana de Recerca i Estudis Avançats, E-08010 Barcelona, Spain*
[41] *School of Physics and Astronomy, University of Southampton, Southampton, SO17 1BJ, UK*
[42] *Computer Science and Mathematics Division, Oak Ridge National Laboratory, Oak Ridge, TN 37831, USA*
[43] *Institute of Cosmology and Gravitation, University of Portsmouth, Portsmouth, PO1 3FX, UK*
[44] *Max Planck Institute for Extraterrestrial Physics, Giessenbachstrasse, D-85748 Garching, Germany*
[45] *Universitäts-Sternwarte, Fakultät für Physik, Ludwig-Maximilians Universität München, Scheinerstr. 1, D-81679 München, Germany*

This paper has been typeset from a TEX/LATEX file prepared by the author.

Downloaded from https://academic.oup.com/mnras/article/499/4/5302/5920232 by guest on 02 May 2023

Appendix B

Monthly Notices of the ROYAL ASTRONOMICAL SOCIETY

MNRAS **00,** 1 (2023) https://doi.org/10.1093/mnras/stad955
Advance Access publication 2023 March 30

Ultracool dwarfs candidates based on 6 yr of the Dark Energy Survey data

M. dal Ponte [1,2★] B. Santiago,[1,2★] A. Carnero Rosell [2,3,4★] L. De Paris,[1] A. B. Pace [5] K. Bechtol,[6] T. M. C. Abbott,[7] M. Aguena,[2] S. Allam,[8] O. Alves,[9] D. Bacon,[10] E. Bertin,[11,12] S. Bocquet,[13] D. Brooks,[14] D. L. Burke,[15,16] M. Carrasco Kind,[17,18] J. Carretero,[19] C. Conselice,[20,21] M. Costanzi,[22,23,24] S. Desai,[25] J. De Vicente,[26] P. Doel,[14] S. Everett,[27] I. Ferrero,[28] B. Flaugher,[8] J. Frieman,[8,29] J. García-Bellido,[30] D. W. Gerdes,[31,9] R. A. Gruendl,[17,18] D. Gruen,[13] G. Gutierrez,[8] S. R. Hinton,[32] D. L. Hollowood,[33] D. J. James,[34] K. Kuehn,[35,36] N. Kuropatkin,[8] J. L. Marshall,[37,38] J. Mena-Fernández,[26] F. Menanteau,[17,18] R. Miquel,[19,38] R. L. C. Ogando,[39] A. Palmese,[40] F. Paz-Chinchón,[17,41] M. E. S. Pereira,[42] A. A. Plazas Malagón,[43] A. Pieres [2,39] M. Raveri,[44] M. Rodriguez-Monroy,[26] E. Sanchez,[26] V. Scarpine,[8] M. Schubnell,[9] I. Sevilla-Noarbe,[26] M. Smith,[45] M. Soares-Santos,[9] E. Suchyta,[46] M. E. C. Swanson,[19] G. Tarle,[9] D. Thomas,[10] C. To,[47] N. Weaverdyck[9,48] and (DES Collaboration)

Affiliations are listed at the end of the paper

Accepted 2023 March 23. Received 2023 March 23; in original form 2022 November 23

ABSTRACT

We present a sample of 19 583 ultracool dwarf candidates brighter than z ≤23 selected from the Dark Energy Survey DR2 coadd data matched to VHS DR6, VIKING DR5, and AllWISE covering ∼ 480 deg^2. The ultracool candidates were first pre-selected based on their (i–z), (z–Y), and (Y–J) colours. They were further classified using a method that compares their optical, near-infrared, and mid-infrared colours against templates of M, L, and T dwarfs. 14 099 objects are presented as new L and T candidates and the remaining objects are from the literature, including 5342 candidates from our previous work. Using this new and deeper sample of ultracool dwarf candidates we also present: 20 new candidate members to nearby young moving groups and associations, variable candidate sources and four new wide binary systems composed of two ultracool dwarfs. Finally, we also show the spectra of 12 new ultracool dwarfs discovered by our group and presented here for the first time. These spectroscopically confirmed objects are a sanity check of our selection of ultracool dwarfs and photometric classification method.

Key words: surveys – brown dwarfs – stars: low-mass.

1 INTRODUCTION

Ultracool dwarfs (UCDs) are very cool ($T_{\rm eff}$ < 2700 K), low mass (M < 0.1 M$_\odot$) objects, ranging from spectral type M7 and later. They include both very low mass stars and brown dwarfs. Brown dwarfs are not massive enough (∼ 0.072 M$_\odot$) to burn hydrogen in their core. Therefore, they continue to cool and dim over time across spectral types M, L, T, and Y (Kirkpatrick et al. 1999; Cushing et al. 2011). Without sustained hydrogen fusion, there is a degeneracy between mass, age, and luminosity. Their spectra are characterized by the effects of clouds and molecular absorption bands. For the L dwarfs, the spectra in the red optical is characterized by the weakening of TiO and VO, strengthening of FeH, CrH, H_2O, and alkali metals such Na I, K I, Cs I, Rb I (Kirkpatrick et al. 1999). The mid infrared spectra are similar to M dwarfs, with H_2O and CO as the most prominent bands along with the presence of clouds in the photosphere (Burgasser et al. 2002b). The transition sequence to the T dwarfs is characterized by the disappearance of clouds from the photosphere, leading to relatively bluer colours in the near-infrared (NIR) compared to the L sequence. Their spectra is characterized by strong absorption features of H_2O, CH_4, and CIA H_2 (Burgasser et al. 2002a).

Despite UCDs being a very common type of object in the Galaxy, roughly 1/6 of the local stellar population by number density, they are very difficult to detect at larger distances due to their faint luminosities. Large samples of UCDs from wide-field imaging surveys [eg. Two-Micron All-Sky Survey (2MASS; Skrutskie et al. 2006), Deep Near Infrared Survey of the Southern Sky (DENIS; Epchtein et al. 1997), UKIRT Infrared Deep Sky Survey (UKIDSS; Lawrence et al. 2007), Wide-field Infrared Survey Explorer (WISE; Wright et al. 2010), VISTA Hemisphere Survey (VHS; McMahon et al. 2013)] have been discovered and revealed many important features about the ultracool dwarfs population. However, the census is still heterogeneous and shallow. The accurate identification and classification of ultracool dwarfs in wide deep ground-based surveys

★ E-mail: mari.dalponte@gmail.com (MdP); basilio.santiago@ufrgs.br (BS); aurelio.crosell@gmail.com (ACR)

© 2023 The Author(s)
Published by Oxford University Press on behalf of Royal Astronomical Society

using only photometry enables the creation of homogeneous samples without relying on extensive spectroscopic campaigns. These samples are essential to measuring the luminosity and mass functions (Cruz et al. 2007; Bochanski et al. 2010) of the ultracool dwarfs in the Galaxy, the disk scale height (Ryan et al. 2005; Carnero Rosell et al. 2019; Sorahana, Nakajima & Matsuoka 2019), the frequency of close and wide binaries (Luhman 2012; Dhital et al. 2015; Fontanive et al. 2018), and the kinematics (Faherty et al. 2010, 2012; Smith et al. 2014; Best et al. 2018).

Taking advantage of the Dark Energy Survey (DES) depth in the optical bands i, z, and Y, it is possible to select a large homogeneous sample of UCD candidates to greater distances. Carnero Rosell et al. (2019) were able to select a sample of 11 745 L and T dwarf candidates using the first 3 yr of the DES along with VHS and AllWISE (Cutri et al. 2013) data. Here we expand the search for ultracool dwarfs candidates using the full 6 yr of DES observations. Comparing to Carnero Rosell et al. (2019), the DES data are now photometrically deeper, with more reliable/precise photometry. This will allow us to probe fainter candidates, increasing the previous samples of L and T dwarfs. Besides, we have now available a sky coverage of almost the entire DES footprint, whereas in Carnero Rosell et al. (2019) we only had ~ 2400 deg^2. This is due to the new data releases of VHS and VIKING surveys that are also used in the analyses.

The paper outline is as follows. In Section 2 we present the photometric data used in this work. In Section 3 we present the updated colour templates for M dwarfs and UCDs and the colour cuts used to pre-select our candidates. In Section 4 we discuss the photometric classification methodology, where we estimate a spectral type for each target using only their photometry. In Section 5 we compare our photo-type to those of known candidates from the literature and discuss the contamination by extragalactic sources. In Section 6, we present several uses for our L and T dwarf candidates: (i) new young moving group (YMG) and association candidate members; (ii) photometric variable sources; (iii) new binary systems constituted by two ultracool dwarfs. In Section 7 we show the spectra of 12 new ultracool dwarfs presented previously in the Carnero Rosell et al. (2019) catalogue that supports our selection of ultracool dwarfs and photometric classification method. Finally, in Section 8, we present our conclusions.

2 DATA

2.1 DES, VHS, VIKING, and AllWISE

DES is a $\sim$5000 deg^2 optical survey in the *grizY* bands that used the Dark Energy Camera (DECam; Flaugher et al. 2015). DECam is a wide-field (3 deg^2) imager at the prime focus of the Blanco 4-m telescope at Cerro Tololo Inter-American Observatory (CTIO). DES observations started in September 2013 and were completed in January 2019, spanning nearly 6 yr.

DES DR2 is the assembled dataset from 6 yr of DES science operations, with data collected over 681 nights and which includes 691 million astronomical objects detected in 10 169 coadded image tiles of size 0.534 deg^2 produced from 76 217 single-epoch images. The estimated area loss to image defects, saturated stars, satellite trails, etc. is of $\simeq 200$ deg^2. After a basic quality selection, galaxy and stellar samples contain 543 million and 145 million objects, respectively. The typical depths (in AB system) as estimated from the magnitude at S/N $= 10$ in the coadd images are $g = 24.0$, $r = 23.8$, $i = 23.1$, $z = 22.13$, and $Y = 20.7$ (Abbott et al. 2021).

For the purpose of our work, we matched the DES DR2 catalogue to the VHS DR6, VIKING DR5 (Edge et al. 2013), and AllWISE catalogues using a positional matching radius of 2 arcsec, keeping only the best match, i.e, the nearest object found. The DES + VHS coverage area is around 4500 deg^2. The VHS survey is imaged with exposure time per coadded image of 120–240 seconds in J and 120 seconds in K_s. There is also partial coverage in the H band with an exposure time of 120 seconds. The median 5σ point source depths is $J_{AB} \sim 21.4$, $H_{AB} \sim 20.7$, and $K_{s,AB} \sim 20.3$. Since, by design, the VIKING and VHS footprints are complementary, we decided to use also the VIKING DR5 data in regions not covered by VHS. The DES + VIKING coverage is about 500 deg^2, providing along with VHS, almost the entire DES footprint. VIKING has a median depths at 5σ of $J_{AB} \sim 22.1$, $H_{AB} \sim 21.5$, and $K_{s,AB} \sim 21.2$ across all imaged regions (~ 1350 deg^2). Lastly, for the AllWISE survey we will use only $W1$ and $W2$ bands, which is >95 per cent complete for sources with $W1 < 17.1$ and $W2 < 15.7$ (in Vega system).

Some quality cuts were initially applied to the matched catalog, such as `IMAGFLAGS_ISO_i,z,Y` $= 0$ from DES DR2 and `J,H,K_{s}ppErrBits` < 255, to ensure that the object has not been affected by spurious events in the images in i, z, Y, J, H and K_s bands. We also imposed a magnitude limit cut of $z < 23$ (DES) and a simultaneous 5σ level detection in the i, z, Y (DES) and J (VHS + VIKING). We did not apply any standard star/galaxy separation because they are not as efficient for relatively nearby sources with significant signature of proper motions on their coadded DES images. In this work, we adopted the `PSF_MAG_i,z,Y` magnitude type from DES and `apermag3_J,H,Ks` from VHS and VIKING catalogues. Also, all DES magnitudes and colours are in the AB system and the VHS + VIKING and AllWISE magnitudes and colours are in the Vega system.

It is important to mention that for sources with significant proper motions, a matching radius of 2 arcsec may be too small. This matching radius will work except for the very nearby ($<= 6$ pc) or high-velocity (> 50 km s^{-1}) cases. Therefore, a small percentage of ultracool dwarfs will be missing from our catalogue due to this effect. The matching between DES data and others surveys provides a broad photometric baseline, spanning from the optical to the infrared. All these bands will be later used to construct empirical templates, perform the colour selection and photometrically estimate the spectral type of our UCDs candidates. The entire selection and classification process is summarized in Table 1 where every step is highlighted along with the corresponding section in this paper.

2.2 Known ultracool dwarfs

The sample from Best et al. (2020; hereafter B2020 sample) contains the most up-to-date compilation of ultracool dwarfs with spectroscopic confirmation. The complete sample has 2940 sources, with spectral type ranging from M3 to Y2. This compilation includes spectral types from optical and NIR. When both are available for a source, the authors recommend using optical types for M and L dwarfs and NIR types for T dwarfs, given that these are the spectral domains of the dominant features required for spectral classification in each case. From this catalogue there are 388 sources located in the DES footprint, and 292 of them are classified as L or T dwarfs. For the construction of the templates, we excluded objects flagged in the B2020 sample as unresolved binaries and sub-dwarfs. We first matched the B2020 sample of L and T dwarfs with the DES DR2 catalogue and found 227 objects in common. Since we have a small number of objects between the B2020 sample and DES, we decided to adopt only in this step a positional match of

Table 1. Steps used in this paper to select and classify L and T dwarfs using DES+VHS+VIKING + AllWISE.

Step	Description	Number of targets	Section
0	DES Y6 (DR2)	691 483 608	2.1
1	$z < 23$		
	$\mathrm{SNR}_{z,\,Y} > 5\sigma$		
	IMAFLAGS_ISO_i,z,Y = 0	602 366	2.1
	$(i–z)_{AB} > 1.20$		
	$(z–Y)_{AB} > 0.15$		
2	Matching 2 arcsec DES		
	+VHS + VIKING		
	$(Y_{AB}–J_{\mathrm{Vega}}) > 1.55$	164 406	2.1
	$\mathrm{SNR}_J > 5\sigma$		
	J, H, $K_s$ppErrBits > 256		
3	Matching 2 arcsec DES + AllWISE	76 184	3
4	Photo-Type classification $\geq$ L0	53 565	4
5	After removal of extragalactic contamination	19 449	5.2
6	Recover by proper motion criterion	141	5.3
7	From the literature	5484	5.4
8	New candidates	14 099	5.5

Note. First, a magnitude limit is imposed in the z band, quality cuts are applied to the data to remove spurious targets and colour cuts (i–z), (z–Y), and (Y–J) are applied to select only the reddest objects. These are the sources that enter into the classification method. Next, we imposed that every object must have six or more bands and spectral type L0 or later. Then, extragalactic contamination is removed and the proper motion is assessed to recover objects erroneously assigned as extragalactic sources. Finally, we list candidates previously found in the literature and new ones.

3 arcsec. Every matched source was inspected visually using the DES image portal tool. The remaining 65 objects were eliminated in our selection due to quality cuts or for having a positional match beyond the limit. Then we matched B2020+DES DR2 with VHS DR6 and VIKING DR5 resulting in 185 objects in common. The 42 lost objects in the match between DES and VHS + VIKING are due to lack of data or positional match beyond 2 arcsec or the VHS+VIKING quality flag applied. Finally, we matched all the B2020 sample with a combination of VHS+VIKING + AllWISE, regardless of DES data, and we end up with 658 objects. We take these three steps in order to obtain as many objects as possible to construct our colour templates. In comparison with the sample of known ultracool dwarfs in Carnero Rosell et al. (2019), there are more 19 objects with DES magnitudes, 81 more in DES+VHS+VIKING, and 530 more in VHS+VIKING+AllWISE. Here, the difference between the samples with and without DES data is due to the limited area of the south where DES footprint is located. The combination of VHS+VIKING + AllWISE covers almost the entire southern hemisphere.

2.3 Known contaminants

There are two main types of sources that we consider as contaminants at this stage: M dwarfs and quasars at high redshift. In Carnero Rosell et al. (2019) we used a sample of 70 841 visually inspected M dwarfs from West et al. (2011). Here we use the Kiman et al. (2019) compilation of spectroscopic confirmed 73 473 M and 743 L or later dwarfs from SDSS constructed from West et al. (2011) and Schmidt et al. (2015, 2019). The match between Kiman et al. (2019) and DES DR2, VHS DR6, and AllWISE data resulted in 19 355 objects in common. This updated M dwarfs sample, with new DES photometry, is fundamental for the update of our colour templates, used in the classification scheme. Regarding the quasars, we are now using the quasar catalogue from SDSS DR16 presented by Lyke et al. (2020). For this latter, we only kept objects with redshift $z > 4$. The reason is that the low-z quasars have much bluer colours than the UCDs and therefore are not relevant to our contamination analysis.

3 TEMPLATES AND COLOUR SELECTION

We updated our empirical colour templates using the samples of known M, L and T dwarfs described previously. The construction of the templates followed the same methodology described in Carnero Rosell et al. (2019). For the M dwarfs (M0–M9), we used the median colour for each spectral type as the template value. We demanded SNR $> 5\sigma$ in all bands and excluded objects that were $>2\sigma$ from the median. The median was then recalculated after these outliers were removed in an interative process until convergence. For the L and T dwarfs, because of the smaller number of objects, we fit a n order polynomial to each colour vs spectral type relation, using the least squares method. For (i–z), (J–K_s), (H–K_s), and (K_s–$W1$) an order 4 polynomial was used; (Y–J) and ($W1$–$W2$) an order 3 and (z–Y) order 2 polynomial were used.

We re-estimated the intrinsic scatter for each colour index, assuming it to be the same for all spectral types. This intrinsic scatter is the spread in colour due to variations in metallicity, surface gravity, cloud cover, and also the uncertainty in the spectral classification. The procedure to estimate this intrinsic scatter followed the Skrzypek et al. (2015) prescription. We initially adopted a first guess of intrinsic scatter as 0.5 mag and added it in quadrature to the photometric errors to all templates. This new uncertainty was used to weight the points in the polynomial regression to the colour vs spectral type relation. Then, we re-estimated the intrinsic scatter as the variance of the best-fitting residuals with the rms value of the photometric errors subtracted in quadrature from it. This new value was taken as our intrinsic scatter for that colour index, irrespective of spectral type. Finally, we re-fitted the polynomial for L and T dwarfs, using the new intrinsic scatter. The intrinsic scatter values found with this method are the following: $\sigma_{i-z} = 0.34$, $\sigma_{z-Y} = 0.30$, $\sigma_{Y-J} = 0.37$, $\sigma_{J-H} = 0.32$, $\sigma_{H-Ks} = 0.30$, $\sigma_{Ks-W1} = 0.33$, $\sigma_{W1-W2} = 0.34$. These values are slightly smaller than those presented by Dupuy & Liu (2012) but more aligned with those presented recently in Kirkpatrick et al. (2021a). Even though there might be a systematic increase with spectral type, we will adopt a single value of 0.2 mag for each magnitude, corresponding to 0.3 mag for each colour index. These will later to be used to perform the spectral classification of our target sample.

The templates for the several colour indices as a function of the spectral type are shown in Fig. 1. Also shown are the templates presented in Carnero Rosell et al. (2019). In comparison to our previous templates, there are no significant changes for the M and L dwarfs. For the T dwarfs, specially late types, colour indices have changed typically by 0.1–0.2 mag, up to $\simeq 0.5$ mag in a couple of cases for T7 or later. This may be due to the clear increase in the number of objects that now contribute to the updated fit. The redder J–H and H–Ks colours around L4 and T0 types are a known trend caused by the effect of condensate clouds and the variability in the clouds properties. Also, there is a blueward trend for T2 to T7 types in J–H, H–Ks, and Ks–$W1$ due to the loss of the cloud decks and the onset of CH_4 absorption. However, this trend diminishes for the latest types as very little flux remains to be absorbed by CH_4 (Leggett et al. 2010). The scatter for the later T types in H–Ks and Ks–$W1$ is due to the variations in metallicity and gravity. The template colours are shown in Table 2.

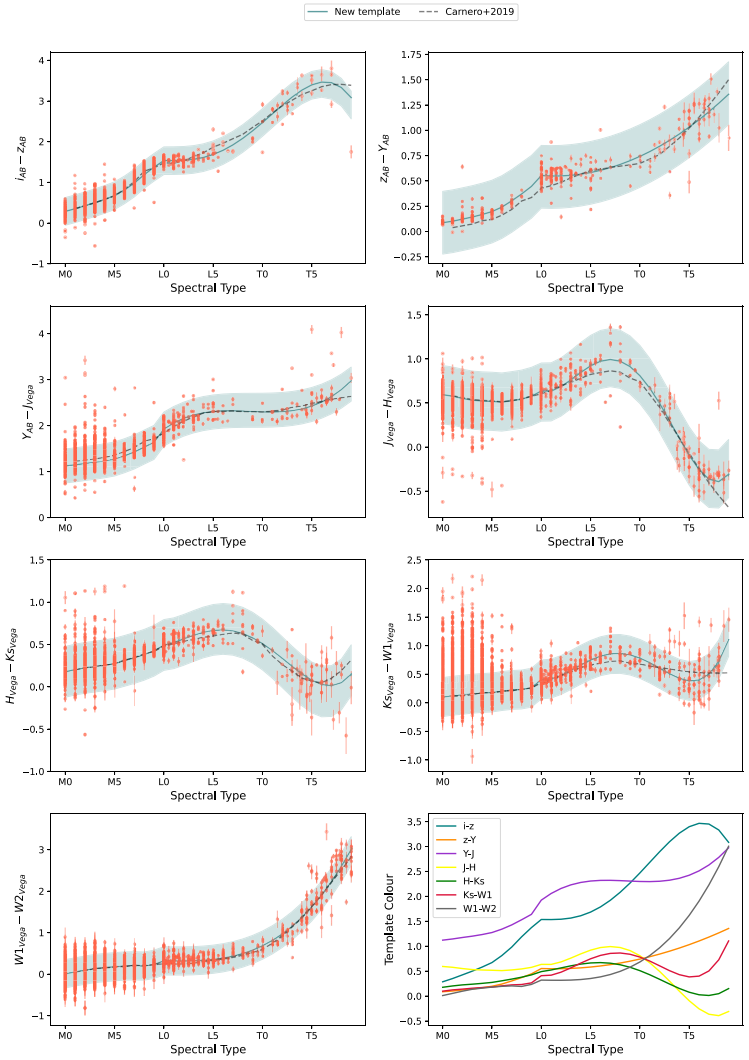

Figure 1. Colours as a function of the spectral type for the enlarged sample of known UCDs as described in the text. The dashed line indicates the new templates, as discussed previously in Section 3, and the solid line refers to the templates presented in Carnero Rosell et al. (2019). The light-shaded area corresponds to the intrinsic scatter of each colour. The last panel shows all the new updated templates for each colour indices used in this work.

For the colour selection of the UCDs, we follow the same methodology presented in Carnero Rosell et al. (2019). We analyse several colour–colour diagrams considering the UCDs and the contaminants samples presented earlier. The colour selection is meant to yield a sample of UCDs sources as complete as possible, at the expense of allowing some contamination by late-M dwarfs and extragalactic sources. The purity of our sample will be later improved using the photo-type classification (see Section 4). We applied an optical band cut $(i–z) > 1.20$, in order to remove the quasars, and also $(z–Y) > 0.15$ and $(Y–J) > 1.55$ to remove M dwarfs and other contamination sources. Fig. 2 shows the colour–colour diagrams where the colour selection was applied for known contaminants, M dwarfs, and UCDs sources. Applying the colour selection discussed above, the initial sample has 164 406 sources in DES+VHS + VIKING data. Among these, 76 184 objects have AllWISE W1 and W2 bands. The next step is to infer a photo-type for each object in the target sample.

4 PHOTO-TYPE CLASSIFICATION

To infer a spectral type for objects in the target sample, we also closely follow the procedure described by Carnero Rosell et al. (2019), originally from Skrzypek et al. (2015). The spectral type

Table 2. Updated template colours of M0–T9 dwarfs.

SpT	i–z	z–Y	Y–J	J–H	H–Ks	Ks–W1	W1–W2
M0	0.28	0.08	1.12	0.59	0.17	0.09	0.01
M1	0.35	0.10	1.14	0.57	0.20	0.12	0.05
M2	0.42	0.12	1.17	0.55	0.22	0.13	0.09
M3	0.50	0.14	1.20	0.53	0.23	0.15	0.13
M4	0.58	0.16	1.23	0.52	0.25	0.17	0.15
M5	0.67	0.19	1.27	0.51	0.27	0.18	0.18
M6	0.81	0.24	1.34	0.51	0.30	0.20	0.19
M7	0.98	0.30	1.42	0.52	0.34	0.22	0.20
M8	1.18	0.37	1.53	0.54	0.37	0.23	0.19
M9	1.37	0.44	1.63	0.57	0.42	0.26	0.23
L0	1.53	0.55	1.92	0.63	0.49	0.40	0.32
L1	1.53	0.54	2.05	0.63	0.52	0.41	0.31
L2	1.54	0.54	2.15	0.68	0.56	0.47	0.31
L3	1.56	0.55	2.23	0.76	0.60	0.56	0.32
L4	1.61	0.56	2.27	0.84	0.64	0.66	0.33
L5	1.68	0.58	2.30	0.92	0.66	0.74	0.35
L6	1.78	0.60	2.32	0.97	0.67	0.81	0.38
L7	1.92	0.63	2.32	0.99	0.65	0.85	0.43
L8	2.08	0.66	2.31	0.97	0.62	0.86	0.49
L9	2.26	0.69	2.30	0.91	0.57	0.83	0.57
T0	2.46	0.74	2.29	0.80	0.50	0.78	0.68
T1	2.68	0.78	2.29	0.66	0.42	0.70	0.81
T2	2.89	0.84	2.30	0.49	0.33	0.60	0.96
T3	3.09	0.90	2.32	0.30	0.24	0.51	1.15
T4	3.26	0.96	2.36	0.09	0.15	0.42	1.36
T5	3.39	1.03	2.42	−0.09	0.07	0.38	1.61
T6	3.46	1.10	2.51	−0.25	0.02	0.40	1.90
T7	3.45	1.18	2.62	−0.36	0.01	0.50	2.22
T8	3.33	1.26	2.78	−0.39	0.04	0.72	2.59
T9	3.08	1.35	2.97	−0.30	0.15	1.10	3.00

will be assigned by the minimization of the χ^2 relative to our new empirical templates presented in Table 2. Only objects that have measurements in a minimum of $N_{\rm bands} = 6$ bands (thus yielding five colour indices) are considered as having a reliable photo-type. We applied this minimum of six bands because we have observed a substantial improvement in photo-type determination with the number of filters available. The χ^2 for the k-th source and the j-th spectral type is

$$\chi^2(\{m_b\}, \{\sigma_b\}, \hat{m}_{z,k,j}, \{c_b\}) = \sum_{b=1}^{N_{bands}} \left(\frac{m_{b,k} - \hat{m}_{z,k,j} - c_{b,j}}{\sigma_{b,k}} \right)^2$$

where $m_{b,k}$ are the measured magnitudes for the source in all available filters, and $c_{b,j}$ are the template colours for the j-th spectral type and for the same bands. These latter are measured for all templates with respect to a reference band (in our case, the z band). The $\sigma_{b,k}$ are the k-th source's photometric errors added in quadrature to the intrinsic scatter (from Section 3). As for $\hat{m}_{z,k,j}$ in equation 2.1, it is the inverse variance weighted estimate of the reference magnitude, computed using all the source's magnitudes, their associated uncertainties and the given template colours for the j-th type as follows:

$$\hat{m}_{z,k,j} = \frac{\sum_{b=1}^{N_{bands}} \frac{m_{b,k} - c_{b,j}}{\sigma^2_{b,k}}}{\sum_{b=1}^{N_{bands}} \frac{1}{\sigma^2_{b,k}}}.$$

4.1 Comparison with the literature

Fig. 3 shows the comparison between the spectral type from the literature and the photo-type method applied to the B2020 sample. As mentioned earlier, only objects with six or more valid magnitudes are shown. Only one object has a misclassification bigger than four spectral types: ULAS J223347 + 002214. However, this object is known as a strong binary candidate (Day-Jones et al. 2013). The accuracy[1] for the B2020 sample is $\sigma_L = 1.7$ and $\sigma_T = 1.1$ for L and T dwarfs, respectively. These values can be considered as an upper limit to the uncertainty in the assigned type. These values are compatible with those obtained by Carnero Rosell et al. (2019) and Skrzypek et al. (2015). After testing the classification code, we obtain a photo-type for each object in our target sample. We used both DES+VHS+VIKING and DES+VHS+VIKING + AllWISE catalogues to estimate a photo-type. Our target sample now have 53 565 objects with photo-type ≥ L0 and six or more bands.

Besides B2020, we also expect to recover in our target sample other UCDs candidates from the literature that are located in the DES footprint. As explained before, the colour selection was made considering objects that have spectroscopic confirmation, but these are currently limited in number. We thus benefit from assessing our sample selection by cross-matching our candidates to other sizeable samples of candidate sources, not only because of the increased numbers but also because this allows a direct comparison of different photo-types.

From the 1361 objects presented by Skrzypek, Warren & Faherty (2016), 154 are located in the DES footprint and 78 of them are present in our target sample. The missing 76 sources are due to three main reasons: (i) a few objects are eliminated due to the colour selection and quality cuts applied to the DES data; (ii) some are eliminated due to separation beyond 2 arcsec match radius; (iii) the main reason, however, is that most of them are eliminated because of our demand on availability of VHS + VIKING data.

Reylé (2018) presented a sample of 14 915 ≥M7 and L candidates from the Gaia DR2 data, of which 2224 are located in the DES footprint. However, only 40 of them are L dwarfs candidates and the remaining objects are M dwarfs. We end up with 248 of their objects in our target sample, 20 of which are L candidates and the remaining are M dwarfs (78 M7/M7.5, 102 M8/M8.5, and 48 M9/M9.5). The missing 20 L dwarfs were eliminated by either one of the reasons we mention above. The reduced number of M dwarfs in our sample is due to the colour cuts imposed, as described in Section 3. Fig. 4 shows the comparison between the photo-types estimated from our classification code and those from these two other samples of UCD candidates. The median photo-type difference is of 0.5 for both Skrzypek et al. (2016) and Reylé (2018) for objects with $z <$ 19. For fainter magnitudes we can only compare to the Skrzypek et al. (2016) sample as Reylé (2018) is limited in $z < 19$ in our DES sample. For $19 < z < 21$ the median discrepancy is also 0.5.

5 TOWARDS THE FINAL SAMPLE: TARGET VALIDATION

5.1 Extragalactic contamination

As in Carnero Rosell et al. (2019), we removed possible extragalactic contamination by running the LEPHARE photo-z code (Arnouts et al. 1999; Ilbert et al. 2006) on the target sample using both a galaxy and quasar templates. We considered as extragalactic all sources that satisfied the following condition: $\chi^2_{\rm Lephare} < \chi^2_{\rm classif}$, where $\chi^2_{\rm Lephare}$ and $\chi^2_{\rm classif}$ are the best-fitting χ^2 values from LEPHARE and from our photo-type code, respectively.

[1] $\sigma = \frac{\sum_{j=1}^{N} |\Delta Sp.T|}{N} \frac{\sqrt{2\pi}}{2}$

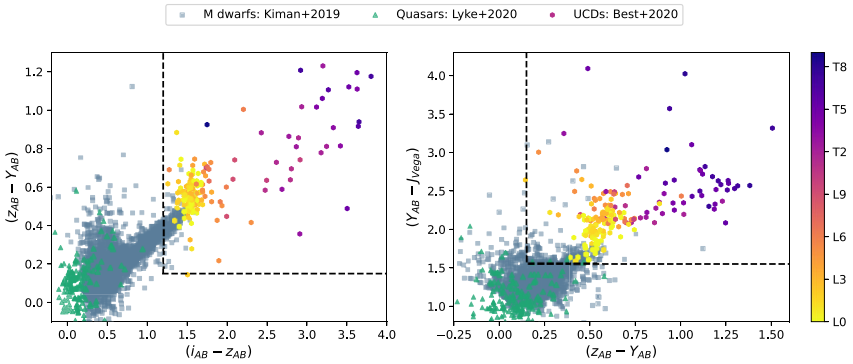

Figure 2. Colour–colour diagrams for the M dwarfs (Kiman et al. 2019; blue squares), L and T dwarfs (Best & et al. 2020), shown as circles, and quasars with z > 4 (Lyke et al. 2020; green triangles). The colour coded represents objects with spectral type L0 and later. The black lines indicate the colour selection.

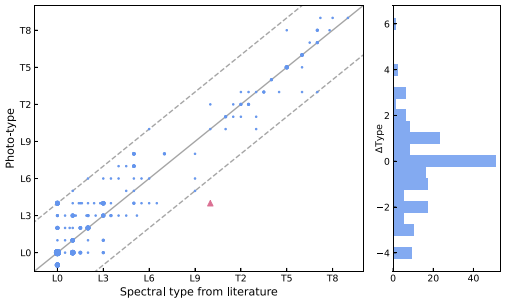

Figure 3. Spectral classification from B2020 compilation against our photo-type classification. The dashed lines represent misclassification by four spectral types. The size of the circles scales as the cube of the number of repeated points. The histogram on the right shows the differences between the spectral types from the literature and our photo-types (ΔType).

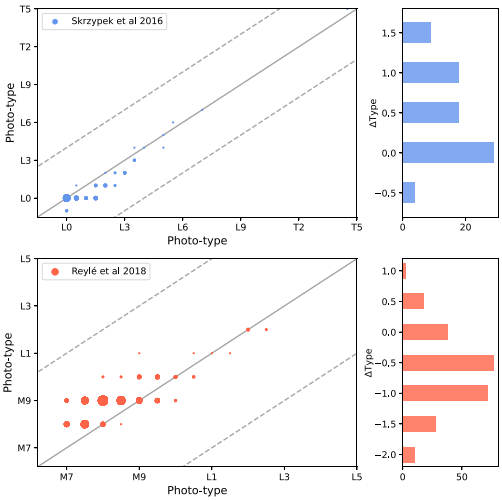

Figure 4. Photo-type classification from Skrzypek et al. (2016) and Reylé (2018; x-axis) and our photo-type classification (y-axis). The dashed lines represent misclassification by four spectral types. The histogram on the right shows the differences between the photo-types from the literature and our photo-types (ΔType).

From the 164 406 objects presented in our initial sample, only 53 565 have six or more bands and have a photo-type L0 and later. From this catalogue of 53 565 L and T candidates, 34 116 were flagged as an extragalatic sources by LEPHARE. Therefore, our final L and T dwarf candidate sample are constituted by a total of 19 449 objects. We also matched the 53 565 L and T dwarf candidates to SIMBAD (Wenger et al. 2000) astronomical database in order to verify if the results provided by LEPHARE were in agreement with the literature. We found 327 objects in common, using a matching radius of 2 arcsec. From this list, only 63 were extragalactic sources and LEPHARE was able to discard 56. The seven objects that remained in the sample were discarded. As discussed in Carnero Rosell et al. (2019), a residual contamination by extragalactic sources is estimated to be ~ 5 per cent.

We also tested running LEPHARE in the B2020 sample to verify the effect of the code on a pure UCD sample and only one object was flagged as an extragalactic: ULAS J222711-004547. ULAS J222711-004547 is known in the literature as a peculiar L dwarf. Since one ultracool dwarf was flagged as extragalatic by LEPHARE we decided to further investigate the 34 116 sources that were flagged as extragalatic sources using their proper motion information. In the next section we will discuss the details.

5.2 Proper motion

In addition to LEPHARE, we used available proper motion catalogues in order to assess the Galactic or extragalactic nature of our candidate L and T dwarfs. If the source has a proper motion significantly different from zero, it is likely a Galactic one. We decided to use the proper motions from Gaia DR3 (Gaia Collaboration 2022), the CatWISE2020 catalogue (Marocco et al. 2021), and the NOIRLab Source Catalog (NSC) DR2 (Nidever et al. 2021). In particular, these last two catalogues extend towards faint enough magnitudes to cover

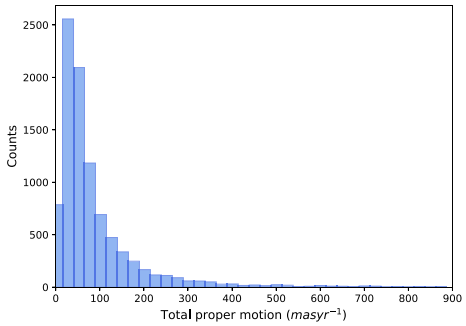

Figure 5. Distribution of total proper motions for ultracool dwarf candidates in our sample. We only show here objects with well-measured proper motion according to our criteria presented in Section 5.2.

a significant fraction (96 per cent) of our target sample of 53 565. These catalogues are responsible for several new discoveries, such as extreme T/Y subdwarfs (Kirkpatrick et al. 2021b; Meisner et al. 2021), new ultracool dwarfs members of the Solar Neighbourhood (Kota et al. 2022), and new wide binary systems (Kiwy et al. 2022; Softich et al. 2022). It is important to mention that in our sample of 53 565 L and T candidates, only 320 sources have Gaia DR3 proper motion measurements (this includes objects with RUWE < 1.4 that ensures a good astrometric solution).

We apply $\sigma_\mu/\mu < 0.5$ for all catalogues as a criterion for them to be considered Galactic sources. In the case of NSC, for some objects with large proper motion errors, $\sigma_\mu > 1000$ mas yr^{-1}, we felt the need to apply a more stringent selection criterion, $\sigma_\mu/\mu < 0.1$. Considering objects with Gaia DR3 proper motion measurements, for instance, only 12 out of the 320 sources are classified as an extragalactic source by LEPHARE. However, 11 of them have proper motion from Gaia DR3 that satisfy our criteria. For the remaining objects flagged as extragalactic, 25 039 have proper motion measurements from CatWISE and NSC catalogues. In this case, 130 satisfies the criteria presented above. In total, 141 objects return to the L and T candidates sample. We conclude that proper motion data in conjunction with our adopted criteria do serve as a means to recover Galactic sources mistakenly classified as extragalactic by other means. Therefore, we have now 19 583 L and T dwarf candidates in the final sample. Fig. 5 shows the distribution of total proper motion ($\mu_{tot} = \sqrt{\mu^2_{\alpha cos\delta} + \mu^2_\delta}$) for the objects that satisfy the condition $\sigma_\mu/\mu < 0.5$ at least in one catalogue (Gaia DR3, CatWISE2020, or NSC DR2). This sample has 9278 objects.

5.3 Comparison with our previous work

From the objects presented in Carnero Rosell et al. (2019), 10 440 L and T dwarfs are present in the initial 164 406 sample of this paper (see Table 1). The missing objects are due to a combination of slight changes in the DES footprint, the quality selection made in the target sample, changes in flags and photometric error criteria, and of lack of data in VHS + VIKING catalogues.

Imposing that the target must have six or more bands, something that was not applied in the past work, we end up with 8512 in common. However, 5342 objects are now classified as L or later. The remaining 3170 are now classified as M9. This large migration across the M9/L0 border is expected due to the larger intrinsic scatter

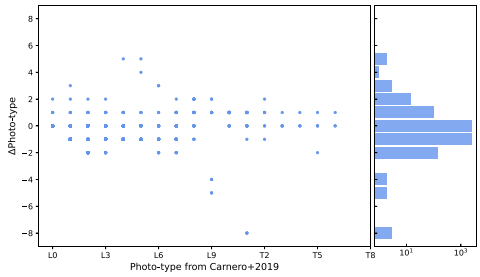

Figure 6. Photo-type comparison between our new classification and the results from Carnero Rosell et al. (2019; ΔType). The histogram in the right shows that the vast majority of the objects have a difference of one spectral type, most now being classified as a slightly earlier type.

adopted here when compared to the previous work, as explained in Section 3. Besides, we used the GalmodBD simulation code (Carnero Rosell et al. 2019) to estimate the reverse effect, namely the contamination of M dwarfs to this new sample. We expect that ~ 30 per cent of our sample is made up of late M dwarfs, the vast majority of them of M9 type. This is again somewhat larger than the 15–20 per cent estimated in our previous work. We should emphasize, however, that that this contamination is from sources of a very similar nature to our target L dwarfs. From the 5342 L and T dwarfs still present on our sample, 24 were flagged as an extragalactic source either by LEPHARE or were listed in SIMBAD database. However, two flagged by LEPHARE have a proper motion measurement that satisfied our criteria. Therefore, in the end, 5320 original L and T dwarfs from Carnero Rosell et al. (2019) remain in the new sample presented here, while most of the missing ones are now classified as late M type. Fig. 6 shows the comparison between the photo-types from the previous work and those of the new candidate sample for objects in common.

5.4 New ultracool dwarf candidates

In total, 19 583 objects remain in our candidate sample, following all the criteria presented earlier. However, from this sample, 142 are included B2020, 5257 additional ones were presented in Carnero Rosell et al. (2019), 26 from Reylé (2018), 5 from Skrzypek et al. (2016), and 54 from SIMBAD (mostly late-M dwarfs from other references, hence surveys, than those used here). There are 14 099 new UCD candidates. The table containing the ultracool dwarf candidates is available at https://des.ncsa.illinois.edu/releases/other/Y6-LTdwarfs.

Fig. 7 shows the photo-type distribution vs photometric distance of the candidate sample of UCDs from this work. The final sample has only objects with six or more bands (used to estimate the photo-type), $\chi^2_{\rm classif} < \chi^2_{\rm Lephare}$ (or otherwise total proper motion significantly different from zero, if available) and a photo-type $\geq$L0. Here we see that this new sample is probing larger distances than those presented in Carnero Rosell et al. (2019). We now reach over 600 pc, while in our previous work we reached ~ 480 pc.

We estimate photometric distances for our candidates following the same procedure explained in Carnero Rosell et al. (2019). We first calculate the absolute magnitudes for the UCD templates discussed in the previous chapter for all photometric bands and spectral types. We do that by using the template colours shown in Table 2 and anchoring the absolute magnitude scale to the M_{W2} values presented by Dupuy &

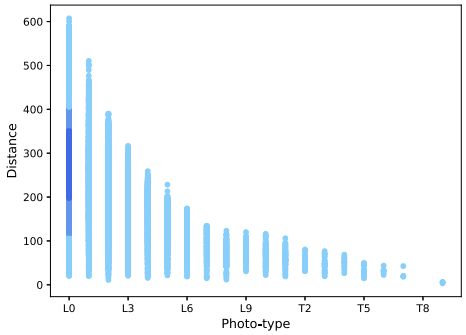

Figure 7. Distances as a function of photo-type. Distances have been calculated using the average value from the distance modulus obtained using all available bands. The colour scale represents the density. Most ultracool dwarf candidates are early L at distances smaller than 650 pc.

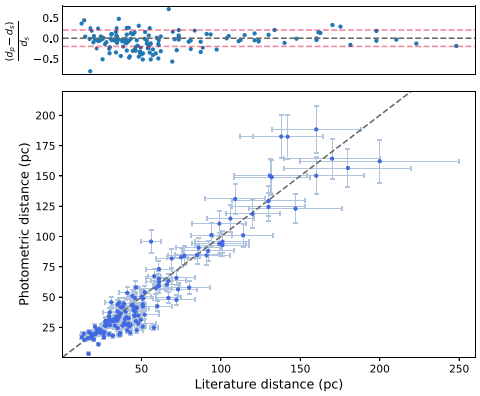

Figure 8. Comparison between our photometric distances (d_p) and distances from the B2020 compilation (d_s), which has a mixture of trigonometric parallaxes and photometric distances. Our photometric distances tend to be slightly underestimated compared to those presented in B2020.

Liu (2012). The distance for each UCD candidate in our sample is then determined from all its available apparent magnitudes and the template absolute magnitudes corresponding to its assigned spectral type. The mean distance over all available bands is assigned as the UCD distance. The distance uncertainty is obtained considering the photometric errors added in quadrature with the intrinsic scatter for each available band. We did not apply any correction for extinction, since this is expected to be small for the passbands we used and towards the relatively high Galactic latitudes covered by our sample.

We checked our photometric distances comparing with those presented in B2020, which comprehends several parallax and photometric measurements from the literature, as shown in Fig. 8. Our photometric distances tend to be slightly underestimated relative to those from B2020. This effect results from a tendency of assigning later types for the objects. Comparing our distance estimates and those from B2020 that have trigonometric parallax distances, the typical error in our photometric distances is ∼28 per cent. Also, the systematic offset seen in the figure, in the sense of our distances being underestimated, is 18 per cent when we considered all objects from B2020, independent of the distance measurement method.

6 UCD CANDIDATES CATALOGUE APPLICATIONS

6.1 Young moving groups and association candidates

Young moving groups and associations contain young stars (∼ 10–100 Myr) and substellar objects whose similar kinematics imply that they originated in the same star-forming region. The members of a young association are a coeval population, where stars can serve as benchmarks to constrain metallicities and ages for substellar objects and to study models of star formation, for instance. Since our search targeted the general ultracool dwarfs population, we used the BANYAN Σ code (Gagné et al. 2018) to estimate if any object in our sample is likely a moving group candidate member. The BANYAN Σ algorithm uses a compiled list of bonafide members of 29 YMGs and associations within 150 pc of the Sun and field stars within 300 pc to compute membership probability given the sky position, proper motion, distance, and radial velocity of targets using Bayesian inference. In our analyses, we divided the sample into: (i) targets with Gaia DR3 information; (ii) targets with CatWISE or NSC proper motion. For these latter, we also demanded that $\sigma_\mu/\mu < 0.5$. Also, we added in the samples radial velocity measurements from the literature when available.

It is important to mention that we ran BANYAN Σ twice if the object has CatWISE2020 and NSC DR2 proper motion. In this case, we only kept candidates whose BANYAN results were the same. We found that 60 objects among our list were already reported in the literature as moving groups candidate members. The recovered members are shown in Table 3 and Table 4 along with new candidates. Table 3 contains only the objects with proper motion and parallax from Gaia DR3. Table 4 contains objects with proper motion from CatWISE2020 and NSC DR2, photometric distances, and BANYAN Σ probabilities according to the catalogue used. We also added in both tables the spectral type from the literature (when available) besides our photo-type. The objects from the literature have added to their spectral type the gravity subtypes α, β, and γ to designate objects of normal gravity, intermediate gravity, and very low gravity, respectively. Also, the δ suffix denotes objects with an even younger age (typically less than a few Myr) and lower surface gravity than those associated with the γ suffix (Kirkpatrick et al. 2006).

The YMGs candidates (new and recovered) that we found are: 20 in AB Doradus (AB Dor, 110–150 Myr; Luhman, Stauffer & Mamajek 2005; Barenfeld et al. 2013), six in β Pictoris (β Pic, 22 ± 6 Myr; Shkolnik et al. 2017), 11 in Columba (Col, 42 $^{+6}_{-4}$ Myr; Bell, Mamajek & Naylor 2015), one in Carina (Car, 45 $^{+11}_{-7}$ Myr; Bell et al. 2015), three in Carina-Near (CarN, 200 ± 50 Myr; Zuckerman et al. 2006), one in Octans (OCT, 35 ± 5 Myr; Murphy & Lawson 2015), and 25 in Tucana-Horologium (THA, 45 ± 4 Myr; Bell et al. 2015). We did not include any candidate member from Argus association considering its high level of contamination (Bell et al. 2015).

We found 20 new candidate members to young associations with Bayesian membership probability above 90 per cent, at least in one catalogue. For objects in common with the literature, we analysed each case individually considering not only the difference in kinematics between this work and previous ones (our work probably making use of more recent and robust proper motion measurements), but also the use of BANYAN Σ (more recent and updated code) results in substitution to those presented by BANYAN II or BANYAN

Table 3. Ultracool dwarfs new candidates and members recovered from the literature of YMGs and associations.

Object Name	RA deg	DEC deg	Ph.T	SpT	$\mu_\alpha\ cos\delta$ mas yr^{-1}	μ_δ mas yr^{-1}	Parallax mas	RV km s^{-1}	Prob.	Ref.
AB Doradus										
Recovered previously candidate members										
J003256-440507	8.2335	−44.0854	L3	L0 γ	127.84 ± 0.28	−96.83 ± 0.31	28.95 ± 0.42	-	99 per cent	2,3,5,6
J013847-345232	24.6981	−34.8756	L0	-	74.99 ± 0.47	−52.01 ± 0.38	18.76 ± 0.63	-	93 per cent	3
J031645-284853	49.1886	−28.8149	L2	L0	103.90 ± 0.22	−94.71 ± 0.30	30.23 ± 0.34	-	98 per cent	1,2,7
J032529-431230	51.3728	−43.2084		M9	66.79 ± 0.26	−20.77 ± 0.30	18.49 ± 0.25	-	88 per cent	1
J043350-421241	68.4578	−42.2114		M9∗	57.23 ± 0.26	−29.37 ± 0.29	22.92 ± 0.24	-	93 per cent	3
J220645-421723	331.6883	−42.2900	L6		128.67 ± 0.90	−184.88 ± 0.93	34.08 ± 1.30	-	99 per cent	1,2,7
β Pictoris										
Recovered previously candidate members										
J045327-175155	73.3605	−17.8652	L3	L3	44.39 ± 0.38	−20.60 ± 0.39	33.06 ± 0.54	-	99 per cent	1,7,8
Carina										
Recovered previously candidate members										
J043531-644956	68.8773	−64.8323	L1	M8.5	49.55 ± 1.33	36.32 ± 0.89	18.49 ± 0.61	19.7 ± 1.0	99 per cent	1,7
Carina-Near										
Recovered previously candidate members										
J051929-450638	79.8699	−45.1106	L0	L2∗	39.43 ± 0.91	66.55 ± 1.20	18.47 ± 0.98	-	96 per cent	3
Columba										
New candidate members										
J051007-530626	77.5307	−53.1072	L0	-	26.57 ± 0.95	20.62 ± 1.31	11.18 ± 0.83	-	90 per cent	
Recovered previously candidate members										
J003443-410228	8.6798	−41.0410	L4	L1 β	107.91 ± 0.80	−59.28 ± 1.56	21.54 ± 1.18	-	82 per cent	1,2,7
J050816-455751	77.0682	−45.9641	L0	M8∗	25.33 ± 0.49	13.94 ± 0.64	11.64 ± 0.45	-	99 per cent	3
J051846-275646	79.6925	−27.9460	L4	L1 γ	33.84 ± 0.51	−4.82 ± 0.60	18.28 ± 0.59	24.35 ± 0.19	99 per cent	2,5,6,7
J055048-302006	87.6999	−30.3351	L1	M9.4	20.46 ± 0.67	−0.59 ± 0.85	18.50 ± 0.74	23.9 ± 1.4	99 per cent	1,6
J055538-413349	88.9064	−41.5635	L2	L0.4	22.65 ± 0.83	15.76 ± 0.80	18.54 ± 0.65	23.5 ± 1.5	99 per cent	1,6
Tucana-Horologium Association										
Recovered previously candidate members										
J000658-643655	1.7423	−64.6154	L0		86.20 ± 0.19	−61.60 ± 0.21	23.17 ± 0.19	-	99 per cent	1,6
J003743-584624	9.4301	−58.7732	L4	L0 γ	86.99 ± 0.91	−49.95 ± 1.05	20.64 ± 0.81	6.62 ± 0.07	99 per cent	2,4,6,7
J003815-640354	9.5629	−64.0649	L1	M9.5 β	86.51 ± 0.30	−47.71 ± 0.29	21.75 ± 0.27	-	99 per cent	2
J011748-340327	19.4485	−34.0574	L3	L1 β	108.27 ± 0.58	−58.06 ± 0.71	25.40 ± 0.70	-	99 per cent	2,4,6
J012051-520036	20.2139	−52.0099	L4	L1 γ	101.59 ± 0.89	−44.85 ± 1.17	24.26 ± 0.94	-	99 per cent	1,6,7
J014158-463358	25.4934	−46.5661	L4	L0 γ	116.73 ± 0.35	−46.62 ± 0.48	27.29 ± 0.44	6.41 ± 1.56	99 per cent	6,7
J021039-301532	32.6612	−30.2589	L2	L0 γ	101.63 ± 0.55	−44.09 ± 0.51	24.65 ± 0.48	7.82 ± 0.27	99 per cent	2,6,7
J022155-541206	35.4799	−54.2016	L0	M9 β	110.74 ± 0.20	−21.91 ± 0.20	26.46 ± 0.19	10.18 ± 0.1	99 per cent	2,4,6,7
J022355-581507	35.9786	−58.2519	L4	L0 γ	105.22 ± 0.51	−16.44 ± 0.50	25.17 ± 0.44	10.36 ± 0.23	99 per cent	2,4,6,7
J022520-583730	36.3320	−58.6250	L0	M9 β	100.88 ± 0.20	−14.97 ± 0.20	24.25 ± 0.17	10.7 ± 2.2	99 per cent	2,4,6,7
J022657-532703	36.7365	−53.4510	L3	L0 δ	92.44 ± 0.47	−18.78 ± 0.59	21.76 ± 0.43	-	99 per cent	1,6,7
J023401-644207	38.5049	−64.7020	L2	L0 γ	87.82 ± 0.65	−4.93 ± 0.75	20.81 ± 0.62	11.76 ± 0.72	99 per cent	2,4,5,6,7
J024012-530553	40.0511	−53.0980	L0	M9.5	96.30 ± 0.24	−14.22 ± 0.28	23.49 ± 0.24	10.9 ± 2.2	99 per cent	6,7
J024106-551147	40.2743	−55.1963	L4	L1 γ	99.14 ± 0.86	−13.3 ± 1.15	23.86 ± 0.80	11.73 ± 2.44	99 per cent	1,7
J024351-543220	40.9634	−54.5388	L0	M9	91.71 ± 0.21	−11.24 ± 0.22	22.29 ± 0.20	11.2 ± 2.2	99 per cent	6,7
J030149-590302	45.4545	−59.0506	L0	M9	81.33 ± 0.17	−2.01 ± 0.19	19.88 ± 0.15	12.3 ± 2.2	99 per cent	6,7
J031143-323945	47.9273	−32.6626	L1	M9.8∗	94.97 ± 0.43	−24.90 ± 0.47	25.63 ± 0.56	10.6 ± 2.2	66 per cent	1
J032310-463124	50.7922	−46.5232	L4	L0 γ	85.55 ± 0.87	−7.32 ± 0.89	23.41 ± 0.70	13.0 ± 0.05	99 per cent	2,5,6,7
J035727-441731	59.3628	−44.2918	L2	L0 β	76.69 ± 0.30	−0.97 ± 0.41	21.28 ± 0.29	10.73 ± 4.6	99 per cent	2,5,6,7
J044010-512654	70.0409	−51.4484	L3	L0 γ	55.98 ± 1.23	18.87 ± 1.94	19.08 ± 1.15	15.6 ± 2.1	99 per cent	1,6
J045521-544616	73.8380	−54.7710	L0	M9∗	54.09 ± 0.40	23.20 ± 0.45	19.09 ± 0.32	-	99 per cent	3
J223536-590632	338.8989	−59.1089	L0	M8.5	60.36 ± 0.20	−84.16 ± 0.22	21.33 ± 0.23	2.9 ± 2.2	99 per cent	2,6,7
J232253-615129	350.7216	−61.8580	L4	L2	79.29 ± 0.80	−80.17 ± 1.09	23.33 ± 0.96	6.75 ± 0.75	99 per cent	1,5,6,7

Note. The objects in this table have proper motion and parallax from Gaia DR3 catalogue. **References:** (1) Gagné et al. (2015); (2) Faherty et al. (2016); (3) Gagné et al. (2018); (4) Naud et al. (2017); (5) Vos et al. (2019); (6) Riedel et al. (2017); (7) Ujjwal et al. (2020).
∗Photo-Type estimated using photometry.

I, for instance. 12 objects are now classified as field members according to our results and are not presented in the following tables. The ambiguous objects were placed in the group indicated by our BANYAN Σ run. The objects with discrepancies in the classification are:

(i) *J003443-410228*: this object was first presented in Faherty et al. (2016) and more recently in Ujjwal et al. (2020) as a THA candidate member. However, using proper motion and parallax measurements from Gaia DR3, we identified it as Col candidate member (83 per cent of probability).

Table 4. Moving groups candidates with CatWISE2020 and NSC DR2 proper motion information.

Object	RA	DEC	Ph.T	SpT	$\mu_\alpha\ cos\delta$	μ_δ	$\mu_\alpha\ cos\delta$	μ_δ	Distance	RV	Prob.
						AB Doradus					
New candidate members											
J020047-510522	30.1975	−51.0894	L8	-	167.11 ± 4.40	−85.81 ± 3.9	175.52 ± 2.28	−68.00 ± 2.33	22.34 ± 2.06	-	99–99 per cent
J022609-161001	36.5383	−16.1669	L8	-	103.18 ± 6.40	−106.56 ± 5.70	109.59 ± 7.99	−128.34 ± 8.22	31.50 ± 2.92	-	98–99 per cent
J023618 + 004852	39.0753	0.8144	L4	-	124.50 ± 7.10	−161.35 ± 6.50	134.52 ± 2.61	−168.00 ± 2.92	37.39 ± 3.45	-	92–75 per cent
J040232-264020	60.6320	−26.6722	T1	-	65.09 ± 24.00	−59.59 ± 25.60	80.81 ± 10.08	−66.82 ± 10.00	46.43 ± 4.40	-	90–81 per cent
J043250-562131	68.2098	−56.3587	L4	-	29.30 ± 7.70	24.86 ± 6.40	33.48 ± 2.22	19.43 ± 2.18	55.04 ± 5.09	-	85–95 per cent
J044842-592802	72.1762	−59.4673	L7	-	22.38 ± 8.60	19.56 ± 7.20	27.27 ± 5.30	12.99 ± 5.30	53.13 ± 4.94	-	94–95 per cent
J050656-251439	76.7333	−25.2442	L8	-	38.45 ± 8.30	−61.19 ± 8.30	36.50 ± 12.26	−64.88 ± 12.25	41.29 ± 3.84	-	98–98 per cent
J050928-311207	77.3671	−31.2018	L5	-	29.91 ± 10.00	−41.56 ± 9.50	25.01 ± 5.77	−32.87 ± 5.87	50.23 ± 4.65	-	96–97 per cent
J051244-502007	78.1825	−50.3351	L4	-	43.30 ± 5.40	14.75 ± 4.90	43.73 ± 2.47	19.18 ± 2.39	35.33 ± 3.26	-	99–98 per cent
J052114-373332	80.3095	−37.5590	L5	-	10.21 ± 7.20	−35.93 ± 7.19	15.46 ± 2.46	−40.04 ± 2.52	35.79 ± 3.31	-	98–99 per cent
J053808-493406	84.5327	−49.5683	L2	-	26.25 ± 7.60	1.05 ± 7.30	13.32 ± 1.86	−2.46 ± 1.88	58.22 ± 5.38	-	81–94 per cent
Recovered previously candidate members											
J032642-210208	51.6765	−21.0356	L8	L5 β	83.09 ± 5.00	−143.70 ± 4.50	90.57 ± 3.42	−144.60 ± 3.13	19.48 ± 1.80	22.91 ± 20.07	65–89 per cent
J040627-381210	61.6117	−38.2028	L4	L0 γ	37.72 ± 7.90	−11.14 ± 7.50	41.90 ± 5.38	1.90 ± 5.53	47.70 ± 4.41	-	66 per cent
J041352-401009	63.4646	−40.1692	L4	L2.5	53.82 ± 7.9	−10.1 ± 7.1	39.45 ± 3.17	4.22 ± 3.19	47.56 ± 4.39	-	76 per cent
						β Pictoris					
New candidate members											
J045544-250107	73.9353	−25.0187	L5	-	43.48 ± 8.20	−0.22 ± 8.00	31.09 ± 4.78	−9.96 ± 4.95	41.72 ± 3.86	-	89–98 per cent
J202436-544944	306.1502	−54.8289	L8	-	37.74 ± 10.60	−86.00 ± 9.90	53.44 ± 11.51	−82.63 ± 11.65	42.28 ± 3.94	-	88–98 per cent
J213422-582853	323.5926	−58.4814	L8	-	61.87 ± 14.10	−93.82 ± 13.00	85.69 ± 5.11	−88.91 ± 5.22	43.14 ± 4.01	-	62–92 per cent
Recovered previously candidate members											
J034209-290432	55.5391	−29.0755	L3	L0 β	37.26 ± 7.2	0.44 ± 6.6	60.95 ± 2.78	−7.79 ± 2.90	42.31 ± 3.91	-	93 per cent
J053620-192040	84.0834	−19.3445	L6	L2 γ	31.73 ± 5.50	−13.04 ± 5.60	33.24 ± 2.48	−18.65 ± 2.54	22.58 ± 2.08	22.06 ± 0.70	99–98 per cent
						Carina-Near					
New candidate members											
J033555-443916	53.9784	−44.6545	T5	-	161.37 ± 17.90	133.76 ± 17.60	209.40 ± 6.07	125.57 ± 5.88	27.03 ± 2.59	-	86–95 per cent
J042013-253924	65.0526	−25.6567	L6	-	90.09 ± 9.30	71.09 ± 9.20	95.23 ± 4.99	63.46 ± 4.85	42.72 ± 4.82	-	79–92 per cent
						Columba					
New candidate members											
J043838-460256	69.6573	−46.0488	L5	-	38.75 ± 8.20	7.94 ± 7.60	39.61 ± 2.85	14.01 ± 2.88	48.05 ± 4.44	-	67–94 per cent
Recovered previously candidate members											
J031819-643322	49.5772	−64.5561	L2	-	48.75 ± 7.80	9.05 ± 7.00	48.62 ± 2.32	8.18 ± 2.28	59.03 ± 5.46	12.6 ± 2.4	54 per cent
J041859-450741	64.7453	−45.1281	L4	L3 γ	60.44 ± 5.90	15.26 ± 5.00	58.56 ± 2.65	8.00 ± 2.51	38.00 ± 3.51	15.1 ± 2.1	83–92 per cent
J051050-184356	77.7070	−18.7321	L3	L2 β	81.77 ± 5.80	−50.12 ± 6.1	83 ± 3.01	−44.10 ± 2.98	31.86 ± 2.94	23.2 ± 1.3	97–55 per cent
J054008-364218	85.0345	−36.7050	L4	L2.3	21.47 ± 6.9	−3.23 ± 6.8	29.45 ± 2.52	4.49 ± 2.56	38.17 ± 3.53	-	99 per cent
						Octans					
New candidate members											
J005503-533413	13.7636	−53.5703	L0	-	31.60 ± 9.30	28.61 ± 8.40	29.23 ± 1.58	16.56 ± 1.67	77.06 ± 7.13	-	96–71 per cent
						Tucana-Horologium Association					
New candidate members											
J024725-492032	41.8555	−49.3423	L8	-	109.25 ± 7.60	−16.97 ± 6.60	106.75 ± 10.08	−28.82 ± 10.09	50.02 ± 4.71	-	92–80 per cent
Recovered previously candidate members											
J203345-563535	308.4365	−56.5931	L3	L0 γ	−3.95 ± 6.7	−74.19 ± 6.6	13.69 ± 2.47	−84.69 ± 2.72	40.66 ± 43.77	-	56 per cent

References: (1) Gagné et al. (2015); (2) Faherty et al. (2016); (3) Naud et al. (2017); (4) Vos et al. (2019); (5) Riedel et al. (2017); (6) Ujjwal et al. (2020). Candidates both new and recovered from the literature are listed.

(ii) *J031645-284853*: Faherty et al. (2016) presented as ambigous AB Dor member by BANYAN II. More recently, Ujjwal et al. (2020) classified as THA candidate member. Here using Gaia DR3 proper motion and parallax we classified as AB Dor candidate member (98 per cent of probability).

(iii) *J040627-381210*: Riedel et al. (2017) classified this object as field member using the LACEwING code. However, Faherty et al. (2016) presented as Col candidate member using BANYAN II, Octans by LACEwING and field object by BANYAN I. Here, the use of NSC proper motion into BANYAN Σ also indicated as field object (66 per cent probability).

(iv) *J041352-401009*: Gagné et al. (2015) classified this object as Col candidate member. The BANYAN Σ classified as β Pic member when we used the NSC DR2 proper motion (32 per cent probability) and as AB Dor member using CatWISE2020 data (76 per cent of probability).

(v) *J034209-290432*: Gagné et al. (2015) and Riedel et al. (2017) classified this object as THA candidate member. Here, BANYAN Σ classified as field member when we used the CatWISE proper motion (94 per cent probability) and as a β Pic using NSC DR2 (93 per cent probability).

(vi) *J041859-450741*: Faherty et al. (2016) presented as ambiguous THA member by BANYAN II and AB Dor candidate by LACEwING and BANYAN I. Both Vos et al. (2019) and Riedel et al. (2017) identified this object as AB Dor candidate member. Here, BANYAN Σ identified as Col candidate member.

(vii) *J031819-643322*: Gagné et al. (2015) presented this object as THA member. Here, BANYAN Σ classified as field using NSC proper motion (99 per cent probability) and Col member using CatWISE2020 (53 per cent probability).

(viii) *J054008-364218*: Gagné et al. (2015) classified this object as Col candidate member. Here, BANYAN Σ classified as β Pic member when we used the CatWISE2020 proper motion (76 per cent probability) and as Col member using NSC DR2 data (99 per cent probability).

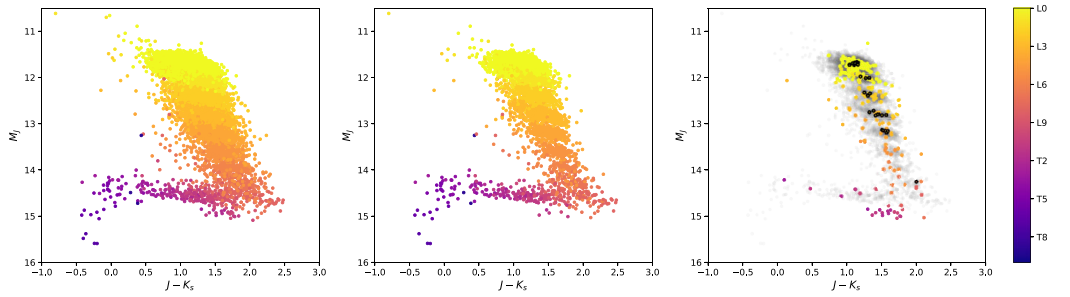

Figure 9. Colour J–K_s vs absolute magnitude in J band. The left-hand panel shows all the 19 583 ultracool dwarf candidates. The mid panel shows only ultracool dwarfs candidates with significant proper motion. The right-hand panel shows the photometric variable objects identified in the Dark Energy Survey Y6 variability catalogue. The points with black contour represent the 28 young candidate objects among the variable sample. The shaded background is made up of all sources from the middle panel.

(ix) *J203345-563535*: Gagné et al. (2015), Faherty et al. (2016), and Riedel et al. (2017) presented this object as THA member. Here BANYAN Σ classified as field member when we used the CatWISE2020 proper motion (99 per cent probability).

Despite the recovered and new candidate members to younger populations, still the vast majority of 99.1 per cent of our sample that has significant proper motion is composed of field objects. Also, it is important to mention that the comparison between our photo-type estimate and spectral type from candidate members of young associations from the literature shows a systematic discrepancy of up to +4 types in some cases. This may be the effect of deviant colours attributed to enhanced dust or thick photospheric clouds, that shift the flux to longer wavelengths in young objects (Faherty et al. 2016).

6.2 Variability

Photometric variability can help to understand atmospheric inhomogeneities in ultracool dwarfs, as it is sensitive to the spatial distribution of condensates as the object rotates. It has been studied in the more massive field L and T dwarfs, but still the variability of the younger and low-gravity objects is less understood. For instance, only a small sample of variability in low-gravity objects (Metchev et al. 2015; Vos et al. 2019) has been detected so far.

Here, we first used DES Y6 variability catalogue described in Stringer et al. (2021) to search for variable sources among our 19 583 ultracool candidates sample and we found 291 of those. There are several available statistics to select variable sources in this particular catalogue. The reduced χ^2 (`RED_CHISQ_PSF_grizy` ≥ 3.3) seems the most efficient to separate variable objects, for instance RR Lyrae, from standard stars. From these 291 variable candidate sources, 130 are also in the Transiting Exoplanet Survey Satellite (TESS) Input Catalog (Stassun et al. 2018), 28 are young objects already identified in the literature and that were discussed in the previous section and are presented in Tables 3 and 4. It is out of the purpose of this work to further analyse in detail these variable candidates. However, this type of sample may be a starting point for studies regarding the cloud formation and dissipation on brown dwarf atmospheres and to assess if low-gravity objects are more likely variable than their field ultracool dwarfs counterparts (Metchev et al. 2015).

Fig. 9 shows colour–magnitude diagrams for the entire sample of ultracool dwarf candidates presented in Section 5 (left-hand panel), for ultracool dwarf candidates that have significant proper motion (satisfy the criteria from Section 5.2; middle panel), and for the photometrically variable candidates identified in the DES variability catalogue (right-hand panel). From these latter, the 28 young candidate objects mentioned above are highlighted. Absolute magnitudes were calculated using our photometric distance estimates. The variable sources seem to roughly follow the same colour–magnitude properties as our full sample of ultracool dwarfs. We may not see subtle redder colours for the highlighted young L types because according to our methodology we tend to attribute later spectral types for young objects, as mentioned in the previous section. Here, 10 per cent of the young (L0–L7) candidate members to moving groups show photometric variability, a lower fraction when compared to Vos et al. (2019) that found 30^{+16}_{-8} per cent for the frequency of variable young objects in L0–L8.5 spectral type range. The remaining variable objects span the L0-T3 range of photo-types. We find that they correspond to 1.3 per cent of the total populations in the range L0–L8, and 7 per cent in the range L9–T3. These numbers are qualitatively similar to Radigan (2014), who found a higher variability of 24^{+11}_{-3} per cent for the L9-T3.5 range as compared to $3.2^{+2.8}_{-1.8}$ per cent outside the L/T transition.

6.3 Wide binary candidate systems

We also search for binary systems constituted by two ultracool dwarfs (L+L,L+T,T + T). This type of system is very interesting, since widely separated ultracool dwarf binaries are quite rare, especially considering field ages. A large number of wide binary systems in the Galactic field could in fact rule out formation scenarios where very low-mass and substellar objects are ejected from the protocluster due to dynamical interactions (Reipurth & Clarke 2001; Bate & Bonnell 2005). Due to their low binding energy, they are unlikely to survive this dynamical process.

A search for this type of binary system was previously presented in dal Ponte et al. (2020) using the sample of UCDs selected with the first DES data release. Here we used the same methodology and presented a new and updated list of this type of system. We used our UCD candidates catalogue to search for binaries, where we computed a search radius for each UCD and checked if another ultracool dwarf appears inside this individual radius. The search radius was defined as a projected separation of 10 000 AU evaluated at the lower limit in distance of the UCD.

Table 5. The common proper motion and distance pair candidates identified among the UCD sample.

ID	Position (deg)				Ph.T		Proper motion (mas yr^{-1})				Distance (pc)		Sep (arcsec)	Ref.	Flag
	α_A	δ_A	α_B	δ_B	A	B	$\mu_\alpha\, cos\delta$	μ_δ	$\mu_\alpha\, cos\delta$	μ_δ	d_A	d_B			
New Candidate Systems															
J004316-320343	10.815	−32.062	10.800	−32.110	T2	L9	−11.17 ± 18.00	46.72 ± 17.00	−19.65 ± 14.20	51.60 ± 13.80	41.86 ± 3.93	41.34 ± 3.85	176.5	5	101
J020903-124420	32.262	−12.739	32.262	−12.738	L0	L0	2.45 ± 4.78	22.89 ± 5.15	0.69 ± 4.92	33.54 ± 5.33	155.46 ± 14.81	151.94 ± 14.45	54.2	5	110
J022636-013744	36.651	−1.629	36.651	−1.629	L0	L0	6.05 ± 4.04	−38.40 ± 4.04	0.79 ± 4.01	−37.45 ± 4.01	166.28 ± 16.12	168.59 ± 16.37	2.4	5	110
J030422-135839	46.090	−13.977	46.049	−14.016	L6	L8	109.39 ± 13.8	45.14 ± 13.4	132.71 ± 36.1	32.35 ± 37.9	55.30 ± 5.15	90.09 ± 9.53	199.4	5	000
Recovered systems															
J013036-444542	22.648	−44.761	22.649	−44.761	L8	L0	124.98 ± 3.84	−33.63 ± 4.83	116.31 ± 1.44	−27.87 ± 1.74	27.00 ± 2.50	27.84 ± 2.57	3.1	2	110
J014611-050851	26.547	−5.147	26.546	−5.147	L4	L7	81.78 ± 1.98	−218.51 ± 1.93	80.51 ± 4.84	−214.01 ± 4.75	29.51 ± 2.73	45.07 ± 4.18	3.2	3	110
J055146-443411∗	87.941	−44.569	87.941	−44.570	L0	L0	−61.01 ± 1.38	−16.71 ± 1.44	−61.02 ± 0.88	−13.07 ± 0.83	76.64 ± 7.08	66.20 ± 6.12	2.2	1	111
J231349-455025	348.455	−45.840	348.455	−45.841	L5	L4	53.76 ± 12.33	6.06 ± 12.36	55.02 ± 4.94	13.36 ± 5.0	106.25 ± 10.25	81.25 ± 7.62	4.1	4	000

References: (1) Billères et al. (2005); (2) Dhital et al. (2011) (3) Softich et al. (2022); (4) dal Ponte et al. (2020); (5) This work.
∗Proper motion from Gaia DR3. The ID in *Jhhmm ± ddmm* format is based on the primary coordinates and the letters A and B represent a different UCD. The flag indicates 0 = common distance and common PM, the latest based on all available catalogues, 0 = common distance and common proper motion according to CatWISE2020, and 0 = common distance and common proper motion according to NSC DR2.

For the initial list of candidates, we required that $\Delta_\mu \leq 2\sigma_\mu$ where Δ_μ is the total proper motion difference,

$$\Delta_\mu = \sqrt{\Delta^2_{\mu_{\alpha cos\delta}} + \Delta^2_{\mu_\delta}}$$

and $\Delta_{\mu_{\alpha cos\delta}}$ and Δ_{μ_δ} are the differences in proper motion between the pair members. In the above criterion,

$$\sigma_\mu = \sqrt{\delta\mu_1^2 + \delta\mu_2^2}$$

is the composite uncertainty in the measured proper motions, where 1,2 represent different objects of the system. We again required that each object has $\sigma_\mu/\mu < 0.5$. The next step was to demand common distances, using a criterion at the 3σ level. The final list has four new candidates and four already known, both with common proper motion and distance. Of these, we note that only one system (J030422-135839) has a common distance beyond 2σ, which was the criterion adopted in dal Ponte et al. (2020). However, this system has proper motions that are in clear agreement with each other. Table 5 shows the new systems and those recovered from the literature. It is important to mention that not all systems presented in dal Ponte et al. (2020) were recovered here. The main reason is that some objects are now classified as M8 or M9 and therefore are not in the sample used for this new search.

To obtain the chance alignment probability we used the GalmodBD simulation code, which computes expected Galactic counts of ultracool dwarfs as a function of magnitude, colour, and direction on the sky. The code also creates synthetic samples based on the expected number counts for a given footprint, using empirically determined space densities of objects, absolute magnitudes and colours as a function of spectral type. We computed the expected number of UCDs in a given direction and within the volume bracketed by the common range of distances and by the area within the angular separation of each system. For all the four new binary candidates, the probability of chance alignment is < 0.004 per cent.

7 SPECTROSCOPIC CONFIRMATION OF 12 ULTRACOOL DWARFS

We undertook a spectroscopic project to further assess our UCDs search and classification methods. We got ∼22 h of Gemini/GMOS time to obtain spectra for a small fraction of our UCD candidates, 12 objects in total. The target sample for the spectrocopic follow up was taken from dal Ponte et al. (2020). We have selected candidates that are more probable to be wide binary systems and for which the technical design will give us the best success rate. We also demanded the pair members to have a difference in distance modulus that was within 1.5 (1.0) from the typical expected difference given their uncertainties. Finally, we avoided the largest physical separation pairs to reach the final target sample. Our targets have magnitudes within the range $19 < z_{\rm DES} < 21.5$ and the preference was given for the systems composed by two L dwarfs. The purpose of this follow up spectroscopy was to confirm their nature, i.e. confront spectral type with our photo-type method and also to re-calculate the distances.

7.1 GMOS observation and data reduction

The selected UCDs were observed using the 8-m Gemini-South telescope with the Gemini Multi-Object Spectrograph (GMOS; Hook et al. 2004). The observations were carried out through the months of September to December 2019 as part of the programs GS-2019B-Q-230 (band 2) and GS-2019B-Q-312 (band 3). We used GMOS with the R150 grating and the OG515 blocking filter to deliver a R∼600 resolution, across the 7000–10 000 Å; range. For all targets, three spectra, centered at 7900, 8000, 8100 Å; at z' filter were taken for each source, to cover the small gaps between the three GMOS detectors, and a focal plane unit of 1 arcsec was selected. We binned both in spatial and spectral direction to 4x4 pixels to increase our signal-to-noise (SNR) ratio. For every change in central wavelength, a flat and a CuAr frame was taken immediately following the science exposure. Table 6 shows the observation log for all the objects observed with GMOS. The individual spectra for the same source were rebinned preserving flux and combined into a single coadded spectrum using standard routines. The typical SNR per pixel for the coadd spectra is ∼ 6.

The objects UCD 1, UCD 3, UCD 10, and UCD 8 are wide binary systems candidates presented previously in dal Ponte et al. (2020) as composed by two L dwarfs. As an observation strategy, we place both objects (L dwarfs) of each system on a single long-slit to obtain two spectra at the same time. The data reduction was carried out using the standard GMOS pipeline contained in the GEMINI IRAF/PYRAF package. The basic steps include bias subtraction, flat-field correction, and wavelength calibration and for the extraction of the spectra we use the APALL pipeline. The spectra have not been flux calibrated and corrected for telluric absorption.

7.2 Ultracool dwarfs spectral types

To determine the spectral type for our UCDs we use a simple χ^2 minimization relative to templates taken from Kirkpatrick et al. (1999). The templates were smoothed down and rebinned to match our resolution and wavelength range of 7200–9400 Å;. We also visually inspected the five best-fitting templates to check the accuracy of the fit. For the instrumental fluxes, we attributed a Poisson fluctuation in the detector counts for every λ. We also multiplied

Table 6. Observation log of the selected ultracool dwarfs.

Name	Obs. Date	Airmass	λ (Å)	Exp. Time
		GS-2019B-Q-230		
UCD 10	2019-09-30	1.35	7900	30.0
	2019-10-07	1.37	7900	30.0
	2019-10-07	1.28	8000	45.0
	2019-10-07	1.22	8100	42.0
UCD 1	2019-10-07	1.16	7900	30.0
	2019-10-07	1.25	8000	68.8
	2019-10-07	1.25	8100	42.0
UCD 3	2019-11-30	1.06	7900	30.0
	2019-11-30	1.07	8000	45.0
	2019-11-30	1.12	8100	42.0
UCD 11	2019-12-01	1.36	7900	26.6
	2019-12-01	1.50	8000	30.0
	2019-12-01	1.73	8100	40.0
		GS-2019B-Q-230		
UCD 36	2019-09-04	1.36	7900	60.0
	2019-09-04	1.21	8000	60.0
	2019-09-04	1.16	8100	45.0
UCD 8	2019-09-22	1.38	7900	30.0
	2019-09-28	1.33	8000	30.0
	2019-09-28	1.25	8100	30.0
UCD 6	2019-09-30	1.17	7900	60.0
	2019-09-30	1.12	8000	22.16
	2019-10-06	1.22	8000	30.0
	2019-10-08	1.26	8100	45.0
UCD 12	2019-10-06	1.13	7900	60.0
	2019-11-20	1.13	8000	15.0
	2019-11-21	1.11	8000	45.0
	2019-11-21	1.11	8100	45.0

Note. The central wavelength is in Å; and the exposure time in minutes.

the templates by a normalization factor before comparing them to each UCD spectrum. This normalization factor is given by

$$N = \frac{\int_{\lambda_1}^{\lambda_2} Flux_{\rm spectra}}{\int_{\lambda_1}^{\lambda_2} Flux_{\rm template}},$$

where the integrals in the numerator and denominator are over the instrumental fluxes of GMOS and template spectra, respectively, within the spectral range of our analysis (λ = 7200–9400 Å).

Fig. 10 shows the spectra and the lowest χ^2 template, along with this best match spectral type. Table 7 shows the photo-type estimated in Carnero Rosell et al. (2019) and the new photo type estimation as presented earlier. The photo-type previously estimated has an typical uncertainty of one or two types due to the method adopted. As discussed previously, to obtain photometric distances we compared the photo-type with our empirical model grid to estimate the absolute magnitude and then obtained the distance modulus for each object. Following the same methodology, but now using the spectral type estimated from the template fitting, new distances were calculated and are shown in the last column of Table. UCD 1, UCD 3, and UCD 10 remain wide binary candidates based on the new distances measurements whereas UCD 8 is discarded as a common distance pair. This latter, in fact, is an interesting pair of sources. Their apparent magnitudes are quite similar in most filters and they are about 1 arcmin apart from each other on the sky. Their proper motion information comes from the CatWISE catalogue and is not precise enough to help assessing the nature of the pair. On the other hand, their Gemini/GMOS spectra are best fitted by an M8 and L0 template, respectively for the a and b components. In Appendix A we compare their spectra to other similar templates, showing the difficulty in attributing a spectral type with precision better than ±2 in some cases.

Also, the comoving candidate systems still have large uncertainties in their proper motion measurements, rendering current kinematical information not an efficient diagnostic. The spectra presented in this section are a basic sanity check that we are in fact selecting ultracool dwarfs and our method to estimate spectral types works as expected, with an accuracy of ±2 types.

8 CONCLUSIONS

Using the recent Dark Energy Survey data release (DR2) combined with VHS DR6, VIKING DR5, and AllWISE data, we were able to identify new ultracool dwarfs candidates, probing faint and more distant objects than those presented in the literature so far. We select these candidates based on their colours (*i*–*z*), (*z*–*Y*), and (*Y*–*J*) up to $z \leq 23$. We applied a classification method where a photo-type can be attributed to each object based only on its photometry. Here we have presented updated colour templates in our classification scheme compared to previous work in Carnero Rosell et al. (2019), and expanded the ultracool dwarf candidate sample to cover almost the entire DES footprint area, thanks to the new VHS DR6 catalogue.

In total, our new sample has 19 583 ultracool dwarf candidates, where 14 099 are presented here for the first time. The complete sample includes 142 spectroscopically confirmed objects from the literature, plus 5342 ultracool dwarf candidates from the literature, where the vast majority (5257 candidates) are from our previous work. The samples from the literature, both with spectroscopic confirmation and candidates were used here as a validation to our method. The method to infer the spectral type consists in a minimization of the χ^2 relative to empirical templates of M, L, and T dwarfs. The comparison between our estimated photo-type with those from the literature showed us that our photo-type is accurate in ±2 spectral types. During the classification step, we also used LEPHARE code with templates from galaxies and quasars in order to identify extragalactic contamination and remove those sources from our final sample.

Our L and T candidates comprise the largest such sample as of today. For instance, Skrzypek et al. (2016) report on finding 1361 L and T dwarfs brighter than J = 17.5 within an effective area of 3070 deg^2 in the Northern Hemisphere. Their UCDs span distances out to 150 pc, whereas our sample goes at least three times farther, out to ∼ 500 pc, and covers a solid angle 60 per cent larger. This much larger volume, coupled with the exponential drop in density in the Galactic disk at the high latitudes we cover, make the two samples quite consistent in terms of the number of objects found.

We also show some applications for our new ultracool dwarf candidates: (i) search for new candidate members to YMG and associations; (ii) photometric variable objects; (iii) search for new wide binary candidate systems. For the first application, we used the BANYAN Σ algorithm to investigate the likelihood of each object in our sample being a member of a YMG. We found 20 new candidate members with membership probability > 90 per cent. We also identify 291 variable candidate sources in our sample, of which 10 per cent are young objects. Also, a higher percentage of the variable sample is concentrated in the L9–T3 range. In addition, as presented previously in dal Ponte et al. (2020), we search for wide binary systems composed of two ultracool dwarfs and here we present four new candidate systems.

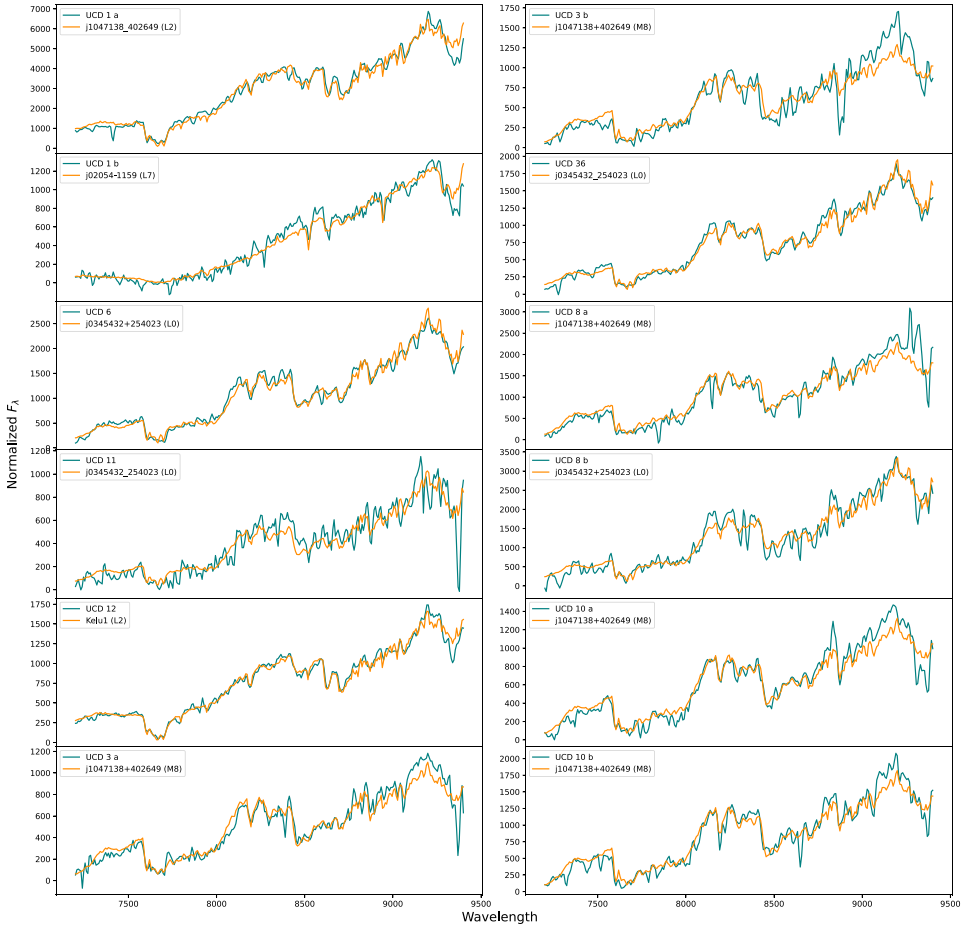

Figure 10. UCD spectra (blue) and the best-fitting template (orange), ordered by right ascension. The fluxes shown are relative F_λ in arbitrary units. The flux of the templates was multiplied by a normalization factor prior to the fit, as explained previously. The individual members of the wide binary candidates are identified by *a,b* labels.

Table 7. Objects z magnitude, photo-type, spectral type, and photometric distances.

Name	RA	DEC	Ph.T	Sp. Type	z	Distance	
UCD 6	10.642	−3.531	L0∗	L0	L0	20.24 ± 0.01	195 ± 33∗	176 ± 17
UCD 11	21.102	−44.986	L2∗	L1	L0	20.92 ± 0.02	173 ± 8∗	219 ± 22
UCD 12	22.886	−5.240	L2∗	L1	L2	20.83 ± 0.01	158 ± 9∗	149 ± 15
UCD 36	321.070	0.484	L0∗	M9	L0	20.63 ± 0.01	246 ± 10∗	222 ± 21
UCD 1 a	0.876	−0.216	L2∗	L1	L2	19.17 ± 0.01	74 ± 2∗	70 ± 6
UCD 1 b	0.876	−0.185	L7∗	L8	L7	21.15 ± 0.02	70 ± 7∗	64 ± 6
UCD 3 a	74.456	−49.567	L0∗	M9	M8	20.96 ± 0.02	349 ± 22∗	429 ± 50
UCD 3 b	74.455	−49.565	L0∗	M9	M8	21.13 ± 0.02	371 ± 29∗	457 ± 49
UCD 8 a	349.952	−52.073	L0∗	M9	M8	19.94 ± 0.01	181 ± 7∗	268 ± 26
UCD 8 b	349.929	−52.065	L0∗	M9	L0	19.95 ± 0.01	176 ± 5∗	160 ± 15
UCD 10 a	355.516	−61.588	L0∗	M9	M8	20.78 ± 0.01	279 ± 29∗	416 ± 41
UCD 10 b	355.533	−61.595	L0∗	L0	M8	21.17 ± 0.02	286 ± 29∗	445 ± 48

Note. The photo-type and the distance column is divided into Carnero Rosell et al. (2019) and new measurements as presented in the earlier sections. All the estimates provided by Carnero Rosell et al. (2019) have ∗ mark.

Finally, we show here the spectroscopic confirmation of 12 new ultracool dwarfs, a basic sanity check of our selection and classification method.

ACKNOWLEDGEMENTS

Funding for the DES Projects has been provided by the U.S. Department of Energy, the U.S. National Science Foundation, the Ministry of Science and Education of Spain, the Science and Technology Facilities Council of the United Kingdom, the Higher Education Funding Council for England, the National Center for Supercomputing Applications at the University of Illinois at Urbana-Champaign, the Kavli Institute of Cosmological Physics at the University of Chicago, the Center for Cosmology and Astro-Particle Physics at the Ohio State University, the Mitchell Institute for Fundamental Physics and Astronomy at Texas A&M University, Financiadora de Estudos e Projetos, Fundação Carlos Chagas Filho de Amparo à Pesquisa do Estado do Rio de Janeiro, Conselho Nacional de Desenvolvimento Científico e Tecnológico (CNPq) and the Ministério da Ciência, Tecnologia e Inovação, the Deutsche Forschungsgemeinschaft, and the Collaborating Institutions in the Dark Energy Survey.

The Collaborating Institutions are Argonne National Laboratory, the University of California at Santa Cruz, the University of Cambridge, Centro de Investigaciones Energéticas, Medioambientales y Tecnológicas-Madrid, the University of Chicago, University College London, the DES-Brazil Consortium, the University of Edinburgh, the Eidgenössische Technische Hochschule (ETH) Zürich, Fermi National Accelerator Laboratory, the University of Illinois at Urbana-Champaign, the Institut de Ciències de l'Espai (IEEC/CSIC), the Institut de Física d'Altes Energies, Lawrence Berkeley National Laboratory, the Ludwig-Maximilians Universität München and the associated Excellence Cluster Universe, the University of Michigan, the NSF's National Optical-Infrared Astronomy Research Laboratory, the University of Nottingham, The Ohio State University, the University of Pennsylvania, the University of Portsmouth, SLAC National Accelerator Laboratory, Stanford University, the University of Sussex, Texas A&M University, and the OzDES Membership Consortium.

Based in part on observations at Cerro Tololo Inter-American Observatory, NSF's National Optical-Infrared Astronomy Research Laboratory, which is operated by the Association of Universities for Research in Astronomy (AURA) under a cooperative agreement with the National Science Foundation.

The DES data management system is supported by the National Science Foundation under Grant Numbers AST-1138766 and AST-1536171. The DES participants from Spanish institutions are partially supported by MINECO under grants AYA2015-71825, ESP2015-66861, FPA2015-68048, SEV-2016-0588, SEV-2016-0597, and MDM-2015-0509, some of which include ERDF funds from the European Union. IFAE is partially funded by the CERCA program of the Generalitat de Catalunya. Research leading to these results has received funding from the European Research Council under the European Union's Seventh Framework Program (FP7/2007-2013) including ERC grant agreements 240672, 291329, and 306478. We acknowledge support from the Australian Research Council Centre of Excellence for All-sky Astrophysics (CAASTRO), through project number CE110001020, and the Brazilian Instituto Nacional de Ciência e Tecnologia (INCT) e-Universe (CNPq grant 465376/2014-2).

This manuscript has been authored by Fermi Research Alliance, LLC under Contract No. DE-AC02-07CH11359 with the U.S. Department of Energy, Office of Science, Office of High Energy Physics. The United States Government retains and the publisher, by accepting the article for publication, acknowledges that the United States Government retains a non-exclusive, paid-up, irrevocable, world-wide license to publish or reproduce the published form of this manuscript, or allow others to do so, for United States Government purposes.

This publication makes use of data products from the Wide-field Infrared Survey Explorer, which is a joint project of the University of California, Los Angeles, and the Jet Propulsion Laboratory/California Institute of Technology, and NEOWISE, which is a project of the Jet Propulsion Laboratory/California Institute of Technology. WISE and NEOWISE are funded by the National Aeronautics and Space Administration.

The analysis presented here is based on observations obtained as part of the VISTA Hemisphere Survey, ESO Programme, 179.A-2010 (PI: McMahon).

This paper has gone through internal review by the DES collaboration.

MDP acknowledges financial support provided by the CNPq Fellowship.

DATA AVAILABILITY

Data underlying this article are available in https://des.ncsa.illinois.edu/releases/other/Y6-LTdwarfs.

REFERENCES

Abbott T. M. C. et al., 2021, ApJS, 255, 20
Arnouts S., Cristiani S., Moscardini L., Matarrese S., Lucchin F., Fontana A., Giallongo E., 1999, MNRAS, 310, 540
Barenfeld S. A., Bubar E. J., Mamajek E. E., Young P. A., 2013, ApJ, 766, 6
Bate M. R., Bonnell I. A., 2005, MNRAS, 356, 1201
Bell C. P. M., Mamajek E. E., Naylor T., 2015, MNRAS, 454, 593
Best W. M. J. et al., 2018, ApJS, 234, 1
Best W. M. J. et al.., 2020, The UltracoolSheet: Photometry, Astrometry, Spectroscopy, and Multiplicity for 3000 + Ultracool Dwarfs and Imaged Exoplanets. Available at: https://doi.org/10.5281/zenodo.4169085
Billères M., Delfosse X., Beuzit J. L., Forveille T., Marchal L., Martín E. L., 2005, A&A, 440, L55
Bochanski J. J., Hawley S. L., Covey K. R., West A. A., Reid I. N., Golimowski D. A., Ivezić Ž., 2010, AJ, 139, 2679
Burgasser A. J. et al., 2002a, ApJ, 564, 421
Burgasser A. J., Marley M. S., Ackerman A. S., Saumon D., Lodders K., Dahn C. C., Harris H. C., Kirkpatrick J. D., 2002b, ApJ, 571, L151
Carnero Rosell A. et al., 2019, MNRAS, 489, 5301
Cruz K. L. et al., 2007, AJ, 133, 439
Cushing M. C. et al., 2011, ApJ, 743, 50
Cutri R. M. et al., 2013, Explanatory Supplement to the AllWISE Data Release Products, Explanatory Supplement to the AllWISE Data Release Products. Available at: http://wise2.ipac.caltech.edu/docs/release/ allwise/expsup
dal Ponte M. et al., 2020, MNRAS, 499, 5302
Day-Jones A. C. et al., 2013, MNRAS, 430, 1171
Dhital S., Burgasser A. J., Looper D. L., Stassun K. G., 2011, AJ, 141, 7
Dhital S., West A. A., Stassun K. G., Schluns K. J., Massey A. P., 2015, AJ, 150, 57
Dupuy T. J., Liu M. C., 2012, ApJS, 201, 19
Edge A., Sutherland W., Kuijken K., Driver S., McMahon R., Eales S., Emerson J. P., 2013, Messenger, 154, 32
Epchtein N. et al., 1997, Messenger, 87, 27
Faherty J. K., Burgasser A. J., West A. A., Bochanski J. J., Cruz K. L., Shara M. M., Walter F. M., 2010, AJ, 139, 176
Faherty J. K. et al., 2012, ApJ, 752, 56

Faherty J. K. et al., 2016, ApJS, 225, 10
Flaugher B. et al., 2015, AJ, 150, 150
Fontanive C., Biller B., Bonavita M., Allers K., 2018, MNRAS, 479, 2702
Gagné J. et al., 2015, ApJS, 219, 33
Gagné J. et al., 2018, ApJ, 856, 23
Gaia Collaboration, 2022, preprint (arXiv:2208.00211)
Hook I. M., Jørgensen I., Allington-Smith J. R., Davies R. L., Metcalfe N., Murowinski R. G., Crampton D., 2004, PASP, 116, 425
Ilbert O. et al., 2006, A&A, 457, 841
Kiman R., Schmidt S. J., Angus R., Cruz K. L., Faherty J. K., Rice E., 2019, AJ, 157, 231
Kirkpatrick J. D. et al., 1999, ApJ, 519, 802
Kirkpatrick J. D., Barman T. S., Burgasser A. J., McGovern M. R., McLean I. S., Tinney C. G., Lowrance P. J., 2006, ApJ, 639, 1120
Kirkpatrick J. D. et al., 2021a, ApJS, 253, 7
Kirkpatrick J. D. et al., 2021b, ApJ, 915, L6
Kiwy F. et al., 2022, AJ, 164, 3
Kota T. et al., 2022, AJ, 163, 116
Lawrence A. et al., 2007, MNRAS, 379, 1599
Leggett S. K. et al., 2010, ApJ, 710, 1627
Luhman K. L., 2012, Araa, 50, 65
Luhman K. L., Stauffer J. R., Mamajek E. E., 2005, ApJ, 628, L69
Lyke B. W. et al., 2020, ApJS, 250, 8
McMahon R. G., Banerji M., Gonzalez E., Koposov S. E., Bejar V. J., Lodieu N., Rebolo R., VHS Collaboration, 2013, Messenger, 154, 35
Marocco F. et al., 2021, ApJS, 253, 8
Meisner A. M. et al., 2021, ApJ, 915, 120
Metchev S. A. et al., 2015, ApJ, 799, 154
Murphy S. J., Lawson W. A., 2015, MNRAS, 447, 1267
Naud M.-E., Artigau É., Doyon R., Malo L., Gagné J., Lafrenière D., Wolf C., Magnier E. A., 2017, AJ, 154, 129
Nidever D. L. et al., 2021, AJ, 161, 192
Radigan J., 2014, ApJ, 797, 120
Reipurth B., Clarke C., 2001, AJ, 122, 432
Reylé C., 2018, A&A, 619, L8
Riedel A. R., Blunt S. C., Lambrides E. L., Rice E. L., Cruz K. L., Faherty J. K., 2017, AJ, 153, 95
Ryan R. E., J., Hathi N. P., Cohen S. H., Windhorst R. A., 2005, ApJ, 631, L159
Schmidt S. J., Hawley S. L., West A. A., Bochanski J. J., Davenport J. R. A., Ge J., Schneider D. P., 2015, AJ, 149, 158
Schmidt S. J. et al., 2019, ApJ, 876, 115
Shkolnik E. L., Allers K. N., Kraus A. L., Liu M. C., Flagg L., 2017, AJ, 154, 69
Skrutskie M. F. et al., 2006, AJ, 131, 1163
Skrzypek N., Warren S. J., Faherty J. K., Mortlock D. J., Burgasser A. J., Hewett P. C., 2015, A&A, 574, A78
Skrzypek N., Warren S. J., Faherty J. K., 2016, A&A, 589, A49
Smith L., Lucas P. W., Burningham B., Jones H. R. A., Smart R. L., Andrei A. H., Catalán S., Pinfield D. J., 2014, MNRAS, 437, 3603
Softich E. et al., 2022, ApJ, 926, L12
Sorahana S., Nakajima T., Matsuoka Y., 2019, ApJ, 870, 118
Stassun K. G. et al., 2018, AJ, 156, 102
Stringer K. M. et al., 2021, ApJ, 911, 109
Ujjwal K., Kartha S. S., Mathew B., Manoj P., Narang M., 2020, AJ, 159, 166
Vos J. M. et al., 2019, MNRAS, 483, 480
Wenger M. et al., 2000, A&AS, 143, 9
West A. A. et al., 2011, AJ, 141, 97
Wright E. L. et al., 2010, AJ, 140, 1868
Zuckerman B., Bessell M. S., Song I., Kim S., 2006, ApJ, 649, L115

APPENDIX: UCD 8 OBJECTS TEMPLATE FITTING

In assessing the nature of binary system candidates involving one or more UCD, it is important to take into account the uncertainties in assigning a spectral type, since our photometric distances are based on template absolute magnitudes for each type. We show here the interesting example of the pair made by UCD 8, for which we obtained Gemini/GMOS spectra of the UCD 8a and UCD 8b candidate members. Fig. A1 we show these spectra along with the templates for M8, M9 and L0. The M8 and M9 templates fit the spectra in a very similar way. The L0 template seems to be the best fit for the UCD 8 b, while for the UCD 8 a, the M8 has the lowest χ^2. As mentioned in Section 7, these two sources are particularly interesting since the objects have very similar magnitudes in all bands and we could expect a more similar spectral type. Because the assigned spectral types differ by two units, however, their distances are now inconsistent with a physical pair. More accurate distance estimates, as well as proper motions, will be required to resolve their nature.

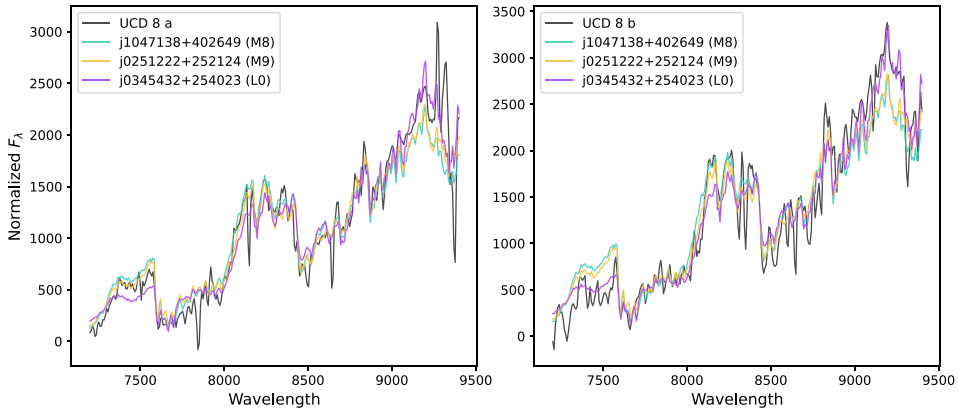

Figure A1. UCD spectra (black) and the M8 (green), M9 (yellow) and L0 (purple) templates. The fluxes shown are relative F_λ in arbitrary units. As in Fig. 10, the flux of the templates was multiplied by a normalization factor.

[1]*Instituto de Física, UFRGS, Caixa Postal 15051, Porto Alegre RS-91501-970, Brazil*
[2]*Laboratório Interinstitucional de e-Astronomia - LIneA, Rua Gal. José Cristino 77, Rio de Janeiro RJ-20921-400, Brazil*
[3]*Instituto de Astrofisica de Canarias, E-38205 La Laguna, Tenerife, Spain*
[4]*Universidad de La Laguna, Dpto. Astrofísica, E-38206 La Laguna, Tenerife, Spain*
[5]*McWilliams Center for Cosmology, Carnegie Mellon University, 5000 Forbes Ave, Pittsburgh, PA 15213, USA*
[6]*Physics Department, University of Wisconsin-Madison, Madison, WI 53706, USA*
[7]*Cerro Tololo Inter-American Observatory, NSF's National Optical-Infrared Astronomy Research Laboratory, Casilla 603, La Serena, Chile*
[8]*Fermi National Accelerator Laboratory, PO Box 500, Batavia, IL 60510, USA*
[9]*Department of Physics, University of Michigan, Ann Arbor, MI 48109, USA*
[10]*Institute of Cosmology and Gravitation, University of Portsmouth, Portsmouth, PO1 3FX, UK*
[11]*CNRS, UMR 7095, Institut d'Astrophysique de Paris, F-75014 Paris, France*
[12]*Sorbonne Universités, UPMC Univ Paris 06, UMR 7095, Institut d'Astrophysique de Paris, F-75014 Paris, France*
[13]*University Observatory, Faculty of Physics, Ludwig-Maximilians-Universität, Scheinerstr. 1, D-81679 Munich, Germany*
[14]*Department of Physics & Astronomy, University College London, Gower Street, London, WC1E 6BT, UK*
[15]*Kavli Institute for Particle Astrophysics & Cosmology, PO Box 2450, Stanford University, Stanford, CA 94305, USA*
[16]*SLAC National Accelerator Laboratory, Menlo Park, CA 94025, USA*
[17]*Center for Astrophysical Surveys, National Center for Supercomputing Applications, 1205 West Clark St., Urbana, IL 61801, USA*
[18]*Department of Astronomy, University of Illinois at Urbana-Champaign, 1002 W. Green Street, Urbana, IL 61801, USA*
[19]*Institut de Física d'Altes Energies (IFAE), The Barcelona Institute of Science and Technology, Campus UAB, E-08193 Bellaterra (Barcelona) Spain*
[20]*Jodrell Bank Center for Astrophysics, School of Physics and Astronomy, University of Manchester, Oxford Road, Manchester, M13 9PL, UK*
[21]*University of Nottingham, School of Physics and Astronomy, Nottingham NG7 2RD, UK*
[22]*Astronomy Unit, Department of Physics, University of Trieste, via Tiepolo 11, I-34131 Trieste, Italy*
[23]*INAF-Osservatorio Astronomico di Trieste, via G. B. Tiepolo 11, I-34143 Trieste, Italy*
[24]*Institute for Fundamental Physics of the Universe, Via Beirut 2, 34014 Trieste, Italy*
[25]*Department of Physics, IIT Hyderabad, Kandi, Telangana 502285, India*
[26]*Centro de Investigaciones Energéticas, Medioambientales y Tecnológicas (CIEMAT), E-28040 Madrid, Spain*
[27]*Jet Propulsion Laboratory, California Institute of Technology, 4800 Oak Grove Dr, Pasadena, CA 91109, USA*
[28]*Institute of Theoretical Astrophysics, University of Oslo. PO Box 1029 Blindern, NO-0315 Oslo, Norway*
[29]*Kavli Institute for Cosmological Physics, University of Chicago, Chicago, IL 60637, USA*
[30]*Instituto de Fisica Teorica UAM/CSIC, Universidad Autonoma de Madrid, E-28049 Madrid, Spain*
[31]*Department of Astronomy, University of Michigan, Ann Arbor, MI 48109, USA*
[32]*School of Mathematics and Physics, University of Queensland, Brisbane, QLD 4072, Australia*
[33]*Santa Cruz Institute for Particle Physics, Santa Cruz, CA 95064, USA*
[34]*Center for Astrophysics | Harvard & Smithsonian, 60 Garden Street, Cambridge, MA 02138, USA*
[35]*Australian Astronomical Optics, Macquarie University, North Ryde, NSW 2113, Australia*
[36]*Lowell Observatory, 1400 Mars Hill Rd, Flagstaff, AZ 86001, USA*
[37]*George P. and Cynthia Woods Mitchell Institute for Fundamental Physics and Astronomy, and Department of Physics and Astronomy, Texas A&M University, College Station, TX 77843, USA*
[38]*Institució Catalana de Recerca i Estudis Avançats, E-08010 Barcelona, Spain*
[39]*Observatório Nacional, Rua Gal. José Cristino 77, Rio de Janeiro, RJ-20921-400, Brazil*
[40]*Department of Astronomy, University of California, Berkeley, 501 Campbell Hall, Berkeley, CA 94720, USA*
[41]*Institute of Astronomy, University of Cambridge, Madingley Road, Cambridge CB3 0HA, UK*
[42]*Hamburger Sternwarte, Universität Hamburg, Gojenbergsweg 112, D-21029 Hamburg, Germany*
[43]*Department of Astrophysical Sciences, Princeton University, Peyton Hall, Princeton, NJ 08544, USA*
[44]*Department of Physics and Astronomy, University of Pennsylvania, Philadelphia, PA 19104, USA*
[45]*School of Physics and Astronomy, University of Southampton, Southampton, SO17 1BJ, UK*
[46]*Computer Science and Mathematics Division, Oak Ridge National Laboratory, Oak Ridge, TN 37831, USA*
[47]*Center for Cosmology and Astro-Particle Physics, The Ohio State University, Columbus, OH 43210, USA*
[48]*Lawrence Berkeley National Laboratory, 1 Cyclotron Road, Berkeley, CA 94720, USA*

This paper has been typeset from a TEX/LATEX file prepared by the author.